Advances in Alignment Based Optically Pumped Magnetometers: Techniques, Characterisation and Applications

Lucy Jade Elson

Orcid iD: 0000-0002-0863-6447
Supervisors: Thomas Fernholz/ Kasper Jensen

School of Physics and Astronomy
University of Nottingham

A thesis presented for the degree of Doctor of Philosophy

January 2025

Abstract

Eddy current induction in objects is a technique that can be used for detection, characterisation and imaging of a sample. By using a primary radio frequency magnetic field eddy currents can be induced in an object which in turn produces a secondary magnetic field. This secondary magnetic field can then be measured using a magnetic field sensor such as a fluxgate magnetometer or an optically pumped magnetometer (OPM). The characteristics of the magnetic field sensor chosen need to be considered in order to ensure the noise floor, operational frequency and bandwidth are sufficient. In this thesis, experiments and numerical simulations for the evaluation of conductive objects are carried out. A commercially available fluxgate magnetometer is used to detect and characterise a non-magnetic (aluminium) and magnetic (steel) sample. The frequency dependence (up to 1 kHz) and positional dependence of the secondary magnetic field is investigated.

Optically pumped magnetometers are capable of measuring oscillating magnetic fields with sensitivities in the $\mathrm{fT}/\sqrt{\mathrm{Hz}}$ range in magnetically shielded and unshielded environments. In this thesis, there is a focus on alignment based magnetometers. Typically, alignment based magnetometers use paraffin coated vapour cells to extend the spin relaxation lifetimes of the alkali vapour. Although this works well, paraffin coated cells have the drawback of being hand-blown making the supply of the cells somewhat unreliable. Buffer gas cells have the ability to be micro-fabricated and hence have the potential to be mass produced. Here, the first implementation of a buffer gas cell in an alignment based OPM is presented. A single laser beam is used to pump and probe the atomic ensemble. Initially, a table-top set up is used to characterise the buffer gas cell's capabilities in an alignment based magnetometer. A sensitivity of 310 $\mathrm{fT}/\sqrt{\mathrm{Hz}}$ with a bandwidth of 800 Hz is found at a Larmor frequency of $\omega_L \approx 2\pi(10\ \mathrm{kHz})$. This data is compared to a paraffin coated cell placed in the same set up.

Characterisation of OPMs and the dynamical properties of their noise is important for applications in real time sensing tasks. The spin noise spectroscopy of an alignment based magnetometer, using a paraffin coated cell, is presented. A stochastic model that predicts the noise power spectra when, as well as the the static magnetic field responsible for the Larmor precession, a white noise field is applied in the beam propagation direction. By experimentally varying the strength of the white noise applied as well as the linear-polarisation angle of incoming light, the theoretical model is verified. This work paves the way for alignment based magnetometers to become operational in real time sensing tasks.

The table-top set up is also used to utilise a spin aligned atomic ensemble for magnetometry at zero-field. An approach is introduced which involves evaluating how the linear polarisation of light rotates as it passes through the atomic vapour to null the magnetic field. Analytical expressions are derived for the resulting spin alignment and photodetection signals. The experimental results show good agreement with the theoretical predictions. The sensitivity and bandwidth of the magnetometer are characterised and the practical utility for medical applications is demonstrated by successfully detecting a synthetic cardiac signal.

The buffer gas vapour cell is then implemented into a compact and portable magnetometer sensor head that was developed. For the development of the portable OPM, a low noise and high bandwidth balanced photodetector (BPD) was designed. The final design had a shot noise limit of ~ 4 μW below 1 MHz, which exceeds that of a commercial BPD that was used for comparison. The use of the home-made detector resulted in a lower overall noise floor in the magnetometer with sensitivities of 230 fT/$\sqrt{\text{Hz}}$ at a Larmor frequency of $\omega_L \approx 2\pi(6\text{ kHz})$ in magnetically shielded conditions and 865 fT/$\sqrt{\text{Hz}}$ in unshielded conditions. Eddy current measurements were then carried out with the sensor in unshielded conditions where aluminium samples with a diameter as small as 1.5 cm were detected at a distance of 26.4 cm from the excitation coil and 23.9 cm from the sensing point of the magnetometer.

The portable OPM was developed with a future goal of imaging the conductivity of the heart with the use of magnetic induction tomography. High frequencies are required to measure induced fields in an object with a low conductivity. The portable OPM has a sensitivity of 825 fT/$\sqrt{\text{Hz}}$ at $\omega_L \approx 2\pi(1.5\text{ MHz})$ in shielded conditions. The use of a buffer gas vapour cell in the prototype OPM is a promising step towards this goal.

Acknowledgements

I would like to start by thanking my supervisors. I would like to thank Kasper Jensen for taking a chance on a student with a theoretical background, allowing me to break into experimental physics, and the wonderful world of OPMs. His patience with my questions as I learned the ropes was very much appreciated. I am also incredibly grateful to Thomas Fernholz, for taking the group on under difficult circumstances, and for being generous with his time when it was needed. I am sure the magnetometry group will continue to do well under his supervision.

I have been fortunate enough to share a Lab with some incredible people throughout the past four years. Adil has always looked after me in the lab, and has been an amazing teacher. He taught me how to use solid works and COMSOL. He is *the* COMSOL wizard, and a good friend. Hopefully I'll get to come and visit you and your family in Colorado soon. Lucas taught me the very basics of optical magnetometry, and helped me to build my first OPM. He has been an amazing friend, and deserves genuine thanks for proof reading not only this thesis, but every piece of written work I produced over the course of this PhD. Vilius drove nearly a thousand miles through Europe on the hottest week of 2024, in a car with no air-conditioning, to deliver my experiment to the University of Copenhagen. For that I will forever be grateful. I shared many pleasant conversations with Ali, after 2PM of course. We were lucky to have some fantastic masters students in the lab over the past three years. To Claire, Ed, Edtya, Reuben, Jeremy, Thomas, and Ailisha; thank you all for your hard work, and best of luck in the future.

During my PhD, I was very fortunate to enjoy a collaboration with Marcin and Janek at the University of Warsaw, they are fantastic theoreticians. In particular, I would also like to thank Marcin for taking us to see the giant Christmas tree in Warsaw.

Towards the end of my PhD, I took an extended trip to Copenhagen to collaborate with the groups of Bo Hjorth Bentzen and Eugene Polzik at the Niels-Bohr Institute. The group was incredibly welcoming, and made me feel safe in a foreign country. Special thanks go out to Nikolaj and Alkis, who stayed in the lab until 4 AM with me on several occasions, and to Luca, who is one of the nicest humans I have ever met. I know the portable OPM is safe in your guys hands and hopefully some amazing results can come out of the end of the project.

I would like to say a special thank you to everyone in the mechanical and electrical workshops in the physics department. In particular I would like to thank Shobita, for endless hours spent helping to design, redesign, and redesign again, the balanced photodetector. Not only was the final product of good quality, but we became good friends in the process. I would also like to thank Ian for his patience with my electronics questions, and lack of expertise.

I would like to thank Dan for being a fantastic housemate, a good friend, and

for always catching the spiders. I miss that. Who would have thought on that first day of university, where we said we'd get a bachelors and then go and get good jobs, that we would both be leaving with PhDs. I would like to thank Niamh and Abs (and Andy), for always supporting me, and always being up for grabbing some good food. I would not be the person I am today, if not for both of your friendships over the last 15 plus years.

I would like to thank my Mum and Dad, I literally would not be here without you. You have always pushed me to do my best, and I hope that I have made you both proud. To my sisters, brothers, brother-in-law, nephews and nieces, thank you for always being there and for being the best family anyone could ever wish for.

Finally, I would like to thank my amazing partner, Jack. Thank you for always believing in, supporting and looking after me. You have always been there when I need you and I would not be who I am or where I am today without you. I am so excited to see what the future has in store for us.

Publications

L. Elson, A. Meraki, L. Rushton, T. Pyragius, and K. Jensen, “Detection and Characterisation of Conductive Objects Using Electromagnetic Induction and a Fluxgate Magnetometer”, MDPI Sensors 22, 5934 (2022). https://doi.org/10.3390/s22165934

L. M. Rushton, T. Pyragius, A. Meraki, **L. Elson**, and K. Jensen, “Unshielded portable optically pumped magnetometer for the remote detection of conductive objects using eddy current measurements”, Review of Scientific Instruments 93, 125103 (2022). https://doi.org/10.1063/5.0102402

L. M. Rushton, **L. Elson**, A. Meraki, and K. Jensen, “Alignment-based optically pumped magnetometer using a buffer gas cell”, Physical Review Applied 19, 064047 (2023). https://doi.org/10.1103/PhysRevApplied.19.064047

A. Meraki, **L. Elson**, N. Ho, A. Akbar, M. Koźbiał, J. Kołodyński, and K. Jensen, “Zero-field optical magnetometer based on spin alignment”, Physical Review A 108, 062610 (2023) https://doi.org/10.1103/PhysRevA.108.062610

M. Koźbiał, **L. Elson**, L. M. Rushton, A. Akbar, A. Meraki, K. Jensen and J. Kołodyński, “Spin noise spectroscopy of an alignment-based atomic magnetometer” Physical Review A 110, 013125 (2024) https://doi.org/10.1103/PhysRevA.110.013125

A. Akbar, M. Koźbiał, **L. Elson**, A. Meraki, J. Kołodyński and K. Jensen, “Optimized detection modality for double resonance alignment based optical magnetometer” (2024) https://doi.org/10.1103/PhysRevApplied.22.054033

The first publication (Ref. [1]) is presented in Chapter 5. I collected and analysed all of the experimental data. Myself and A. Meraki designed the set up. A. Meraki 3D printed the set up and he created and ran the COMSOL data and passed the results on to me for further analysis. The paper was written by myself and A. Meraki. L. Rushton, T. Pyragius and K. Jensen edited it.

The second publication (Ref. [2]) is not presented in this thesis, however the results found in Chapter 10 are directly compared to this paper. My contribution to this publication was assisting in the eddy current detection using the portable OPM. L. Rushton characterised the OPM and wrote the paper.

Results from the third publication (Ref. [3]) are presented in Chapter 6. The original paper was written by L. Rushton and edited by myself, A. Meraki and K. Jensen. I took all of the measurements and analysed all of the data presented with L. Rushton. The D1 Laser system was built by A. Meraki. M. Koźbiał and J. Kołodyński assisted in our understanding of the theory.

The fourth publication (Ref. [4]) is presented in Chapter 8. I wrote the paper alongside A. Meraki and K. Jensen. The experimental data was collected by A.

Meraki, N. Ho and I. I then carried out the data analysis on the data. K. Jensen derived the theoretical model used with help from M. Koźbiał. I have since reproduced these findings.

The fifth publication (Ref. [5]) is presented in Chapter 7. The theoretical stochastic model was developed by M. Koźbiał and J. Kołodyński. I carried out the experimental side of the project. In the early stages of the project I was assisted by L. Rushton. I then analysed all of the data and was responsible for comparing the experimental results to those obtained by M. Koźbiał. The paper was written by M. Koźbiał, J. Kołodyński and I with editing by L. Rushton, A. Meraki, A. Akbar and K. Jensen.

The final publication (Ref. [6]) is not presented in this thesis. The data was collected and the paper was written by A. Akbar. I discussed many of the results and helped with the experiments where needed. The theoretical models were developed by M. Koźbiał, J. Kołodyński and K. Jensen. All of the publications were supervised by K. Jensen who was constantly around to discuss results and provide helpful feedback.

List of Symbols

Symbol	Definition
ω	Optical frequency
ν, f	Frequency
γ_{cs}	Gyromagnetic ratio of caesium (2π(3.5 kHz/μT))
B	Magnetic field
B_0	Static magnetic field
ω_L	Larmor frequency ($\omega_L = \gamma_{\mathrm{cs}} B_0$)
ω_{rf}	RF frequency
$B_1(t)$	Primary magnetic field
$B_{\mathrm{ec}}(t)$	Secondary magnetic field
$B_2(t)$	Compensation magnetic field
σ	Electrical conductivity
ρ	Electrical resistivity ($\rho = 1/\sigma$)
μ	Magnetic permeability
ε	Electrical permittivity
$\delta(\omega)$	Skin depth
S	Signal
X	In-phase lock-in output
Y	Out-of-phase lock-in output
R	Magnitude of the lock-in output ($R = \sqrt{X^2 + Y^2}$)
ϕ	Phase of the lock-in output $\phi = \tan^{-1}(X/Y)$
h	Planck's constant
E_{hfs}	Caesium ground state hyperfine splitting ($E_{\mathrm{hfs}} = h\nu_{\mathrm{hfs}}$) where $\nu_{\mathrm{hfs}} = 9.193$ GHz
τ_{nat}	Natural lifetime of the excited state
Γ	Decay rate of the excited states via spontaneous emission ($\Gamma = 1/\tau_{\mathrm{nat}}$)
R_p	Optical pumping rate
Q	Quenching factor
T_1	Longitudinal relaxation time
Γ_1	Longitudinal relaxation rate ($\Gamma_1 = 1/T_1$)
T_2	Transverse relaxation time
γ	Transverse relaxation rate ($\gamma = 1/T_2$)

List of Abbreviations

Abbreviation	**Definition**
OPM	Optically pumped Magnetometer
RF	Radio frequency
SQUID	Superconducting quantum interference devices
Cs	Caesium
N_2	Nitrogen
SERF	Spin exchange relaxations free
RF-OPMs	Radio-frequency optically pumped magnetometer
MIT	Magnetic induction tomography
BPD	Balanced photodetector
FPGA	Field-programmable gate array
SNR	Signal to noise ratio
FWHM	Full width half maximum
HWHM	Half width half maximum
SNS	Spin noise spectroscopy
PSD	Power spectral density
$\lambda/2$	Half-wave plate
PBS	Polarising beam splitter
MEG	Magnetoencephalography
MCG	Magnetocardiography
NMR	Nuclear magnetic resonance
PCB	Printed circuit board
VNDF	Variable neutral density filter
PID	Proportional–integral–derivative

Contents

List of Figures

List of Tables

Chapter 1

Introduction

The detection of magnetic fields has been an important area of research for nearly two centuries with the first measurements being reported in 1832 by C. Gauss [7]. The magnetic field sensor was made using a bar magnet that was suspended in the air and was designed to measure the Earth's magnetic field. The Earth has a static magnetic field which has been measured and found to have a strength of 25-65 µT (equivalent to 0.25-0.65 Gauss). Since the first magnetic field measurement, magnetic field sensors have developed drastically with multiple different sensor designs that can measure static DC and oscillating radio frequency (RF) fields in the kHz-MHz range. Some examples of magnetic field sensors include Hall-effect probes [8], fluxgate magnetometers [9, 10], inductance coil sensors [11], magneto-resistive sensors [12], proton precession magnetometer [13], superconducting quantum interference devices (SQUIDs) [14] and optically pumped magnetometers (OPMs) [15, 16, 17, 18, 19]. SQUIDs have shown promising potential with sensitivities approaching the fT/$\sqrt{\text{Hz}}$ scale [14]. However, they require cryogenic cooling which makes them bulky and expensive to operate. The OPM shows promising results with the sensitivities outperforming SQUIDs [20, 21]. OPMs can measure static (DC) and oscillating (kHz-MHz) magnetic fields. They can be made into compact sensors with the added advantage of not needing to be kept stationary whilst measuring magnetic fields [22].

Optically pumped magnetometers [15, 16, 17, 18, 19] (also called atomic magnetometers or optical magnetometers) that are based on spin polarised atoms containing e.g. caesium (Cs), rubidium, potassium or helium have shown great potential in reaching high sensitivities in the fT/$\sqrt{\text{Hz}}$ [23, 24, 25, 2, 3] and sub-fT/$\sqrt{\text{Hz}}$ range [20, 21]. The first demonstration of an optically pumped magnetometer by Bloom and Bell was in 1957 [26]. The improvements in the performance and sensitivities of OPMs since then have surpassed the sensitivity of SQUIDs without the need for cryogenic cooling [14]. OPMs have demonstrated their use in a variety of fields where the precise detection of small magnetic fields is essential. Some examples include material characterisation [27], non-destructive testing [28, 29, 30], geophysics, remote sensing [2, 31], dark matter searches [32] and nuclear magnetic resonance gyroscopy [33]. OPMs have also shown their potential in numerous medical applications such as magneto-encephalography [34, 35, 36] and magneto-cardiography [37, 38].

The basic principles behind optically pumped magnetometers depend on measuring the atomic Larmor precession ω_L of the atomic spins in a static magnetic field.

The Larmor frequency is related to the applied static magnetic field by $\omega_L = \gamma_g|\mathbf{B}|$ where γ_g is the gyromagnetic ratio of the atom. The atoms are polarised by optical pumping [39] of the atomic ensemble where angular momentum is transferred from light, that is on resonance with an atomic transition, to the atoms. To create an aligned state, where the atoms are typically pumped to two outer dark states, linearly polarised light is used. Atoms within the dark state cannot absorb a photon and therefore are 'trapped' in these states. In an aligned state the atomic spins have a preferred axis but not a preferred direction. To create an oriented state, where typically the atoms are pumped to a single dark state, circularly polarised light is used. In this case the atomic spins have a preferred direction as well as a preferred axis. The spin polarisation can then be monitored using a linearly polarised probe beam propagating through the atomic ensemble. The change in angle of the light polarisation of the probe beam can then be measured. From this, information about the strength of magnetic fields can be determined allowing for the detection of small fields.

Compact and portable OPMs are highly desirable, especially for the integration of them into densely packed arrays in medical applications [22]. Current commercially available OPMs typically operate in the spin exchange relaxations free (SERF) [40, 41, 42]. SERF magnetometers have proved to be some of the most sensitive magnetometers working close to zero magnetic field with $\mathrm{fT}/\sqrt{\mathrm{Hz}}$ sensitivities being demonstrated [43, 44, 45]. In the SERF regime the vapour cells are heated to high temperatures (100°C - 200°C) [46] leading to high number densities of the alkali atoms. The high number density causes more collisions between the atoms. Upon collisions, spin relaxation occurs and the spins of the atoms are randomised. In the setting of near zero-field magnetic fields, the rate of spin relaxation is much faster than the Larmor precession. Hence the magnetometry signal is a measure of the evolution of the average atomic spin and the system is not subject to decoherences caused by spin exchange. These types of magnetometers are capable of measuring one, two or three components of the magnetic field. In recent years, an alternative zero-field magnetometer has been made commercially available [47]. This magnetometer is based on an ensemble of helium atoms being pumped into an aligned state. This magnetometer has the benefit of working at room temperature and having a larger dynamic range. Although it has shown an impressive sensitivity to magnetic fields, it is not as sensitive to small oscillating magnetic fields when compared to SERF magnetometers [40, 47]. As well as zero-field optical magnetometers, scalar OPMs are also commercially available. These magnetometers have a large enough dynamic range that they can be operated in the Earth's magnetic field [40].

In addition to measuring low frequency magnetic fields (DC - 1 kHz), the detection of radio frequency (RF) magnetic fields is also of interest. RF-OPMs are not yet commercially available but prototypes are becoming more prominent in the literature [29, 2, 48, 49]. Many research groups are focused on the development, characterisation and potential applications of detecting magnetic fields in the kHz-MHz frequency range. There are two common types of RF-OPMs, the first being an orientation based OPM which are typically implemented using two or three laser beams [24, 50, 23]. The other is an alignment based OPM which is typically implemented with a single laser beam [51]. Both show promise for applications and commercialisation. Current prototypes in the literature are based upon orientation based OPMs [29, 2, 48, 49] and utilise two laser beams. Alignment based OPMs show great potential for further miniaturisation due to the use of a single laser beam. Both types of OPMs can operate at room temperature or elevated temperatures that are still much less than a SERF magnetometer.

Measuring oscillating magnetic fields plays a key part in the remote detection and characterisation of electrically conductive and magnetically permeable objects. Electromagnetic induction is commonly used in eddy current testing as a non-destructive technique for flaw detection and material characterisation [52, 53, 54, 55]. Eddy current testing is based upon a primary magnetic field $\mathbf{B}_1(t)$ exciting eddy currents in a sample which induced a secondary magnetic field $\mathbf{B}_{\text{ec}}(t)$ [56, 57]. The secondary magnetic field contains information about the sample including its position, shape, electrical conductivity and magnetic permeability [58, 1]. This technique can be used to detect a wide range of objects, as it is sensitive to both the electrical conductivity σ and the magnetic permeability $\mu = \mu_0\mu_r$ of the object, where μ_0 is the vacuum permeability and μ_r is the relative permeability. Hence, the potential and use of eddy current testing has already shown great potential in numerous applications including, but not limited to, remote sensing [31, 2], defect detection and non-destructive testing [28, 59].

Eddy current detection can image samples using magnetic induction tomography (MIT) [56]. MIT can be used to detect objects as well as construct 2D and 3D maps of the structure and electromagnetic properties [56, 58, 60, 61]. In order to create 3D images of the objects the frequency of the primary magnetic field needs to be varied as each object has a frequency dependent skin depth. The skin depth determines the distribution of the eddy currents in an object. Hence by varying the frequency different penetration depths can be obtained for the primary magnetic field in the object [62]. This method is of potential importance in medical applications in the non-invasive diagnosis of atrial fibrillation [61]. Atrial fibrillation is a common heart condition where the heartbeat is irregular. Currently, details about the causes are unknown. It is thought that a potential cause is due to permanent anomalies in the electrical conductivity σ of the heart [61]. As the causes are not known, current treatment methods are less than optimal and often fail in treating the irregularities [63]. If permanent anomalies in the conductivity of the heart are the issue, the use of magnetic induction tomography could prove promising in creating a 3D map of the conductivity as a diagnostic tool [61]. The heart has a low conductivity of ~ 0.5 S/m so a sensitive magnetometer needs to be used to detect the small secondary magnetic field with a sufficient signal to noise ratio. Optically pumped magnetometers are a good option with their $\text{fT}/\sqrt{\text{Hz}}$ sensitivities. Their potential has already been shown with the detection and imaging of low conductivity phantoms [30, 25].

This thesis is structured as follows: to begin with, the theoretical background that underpins radio frequency OPMs is then presented in Chapter 2. This includes the atomic structure of caesium, atomic interactions with magnetic fields and light, before finally looking at how the atomic ensemble can be optically pumped into an aligned state.

Following on from this, the basic principles needed to understand how electromagnetic induction imaging can be used to image samples with electromagnetic properties are then discussed in Chapter 3. These principles are experimentally demonstrated throughout the thesis.

This is followed by the theory of an alignment magnetometer, which is presented in Chapter 4. This shows how a single laser beam can be used to pump and probe an atomic ensemble. The theory takes into account the difference between using a paraffin coated cell and a buffer gas cell, where appropriate, to measure oscillating magnetic fields.

Chapter 5 focuses on eddy current testing with a study of how the secondary magnetic field produced in a non-magnetic and magnetic sample vary with the frequency of the primary magnetic field and position of the object. In this chapter, a commercial fluxgate that is well calibrated and known to perform well in unshielded conditions is used. This data is used as a point of reference for experimental data taken using a prototype portable OPM and to characterise the materials extracting the conductivity and relative magnetic permeability. The data presented in this chapter is verified using COMSOL which shows good agreement with the experimental data. The findings are first detailed in Ref. [1].

The thesis will then turn to the experimental results obtained over the course of the PhD with a focus on alignment based OPMs. In Chapter 6, a table-top magnetometer is shown. The magnetometer is characterised with two different vapour cells being used. Initially, a paraffin coated cell is placed into the experimental setup. The magnetometer is characterised to determine the minimal detectable field and the non-linear Zeeman splitting is observed. This magnetometer is then used to perform eddy current measurements on an aluminium sample. The vapour cell is then replaced with a 65 Torr nitrogen (N_2) buffer gas cell. This is the first demonstration of a buffer gas cell being used in an alignment based OPM [3] as in previous work anti-relaxation coated vapour cells are used [51, 64]. The magnetometer is then characterised to determine the minimum detectable field and the non-linear Zeeman splitting is observed with the use of the buffer gas cell. It is noted that for a fair comparison vapour cells of comparable size are used. The advantage of using a buffer gas cell is the ability for them to be produced on a mass scale using micro-fabrication techniques [65, 66, 67]. These techniques are not currently comparable with anti-relaxation coated cells that have to be hand-made. Combining the micro-fabrication techniques with the use of a single laser beam makes buffer gas alignment magnetometers well-suited for further miniaturisation of RF-OPMs.

Using the table-top alignment based magnetometer in Chapter 6 with the paraffin coated cell, the setup is further characterised. In Chapter 7, a stochastic model of the spin noise spectroscopy is presented. How the power spectral density of the alignment based magnetometer, in the presence of a static magnetic field, is affected by white noise is presented [5]. This work paves the way for exploring alignment based magnetometers in real time sensing tasks, in which it is possible to track time-varying signals beyond the nominal bandwidth dictated by the magnetometer. In Chapter 8, the alignment based magnetometer is used to investigate how to use a spin aligned atomic ensemble for zero-field magnetometry [4]. A modulation free technique for nulling the magnetic field is presented. The method involves evaluating how the linear polarisation of the light is rotated as it is transmitted through the atomic ensemble. Having presented the method for nulling the magnetic field, the magnetometer is then characterised and the sensitivity and bandwidth are determined.

Finally, the development of a portable alignment based magnetometer prototype is presented. In order to create a portable device, a high bandwidth low noise balanced photodetector (BPD) with a small footprint needed to be designed. The design procedure and performance of the final balanced photodetector are presented in Chapter 9. Chapter 10 shows the use of this BPD, along with the buffer gas cell, in a portable OPM prototype. The development and characterisation of the OPM in shielded and unshielded conditions is presented. The OPM has a sub-$\mathrm{pT}/\sqrt{\mathrm{Hz}}$ performance in unshielded conditions. The use of the OPM for eddy current detection is also presented, with samples as small as 1.5 cm being detected with a good signal to noise ratio at a distance of 26.4 cm from the excitation coil and 23.9 cm from the sensing point of the magnetometer. The findings in this thesis are then summarised in Chapter 11.

Chapter 2

Atomic physics and magnetometry

2.1 Caesium

2.1.1 Atomic structure

Caesium (Cs) only has one stable isotope which is Cs-133 [68]. Caesium has an atomic number 55 and an electronic configuration of [Xe] $6^2\mathrm{S}_{1/2}$ where Xenon (Xe) is a noble gas. The electronic shells in Xe are full resulting in it being non-reactive. Caesium has a single electron in the outer shell. This outer electron makes caesium useful for magnetometry. The electron is described by $6^2\mathrm{S}_{1/2}$ where the '6' is the principal quantum number n and 'S' represents the orbital angular momentum L of the outer electron. The superscript '2' results from $2S + 1$ where $S = 1/2$ is the intrinsic spin of the electron and the subscript of '1/2' is the total angular momentum J of the electron. The higher the quantum number n the less tightly bound the electron is to the nucleus. For the orbital angular momentum of the electron 'S' corresponds to $L = 0$ and 'P' corresponds to $L = 1$.

The outer electron prefers to be in the lowest energy configuration which corresponds to $L = 0$. In the excited state there is a fine structure doublet with possible levels of $6^2\mathrm{P}_{1/2}$ and $6^2\mathrm{P}_{3/2}$. The fine structure arises from the coupling between the orbital angular momentum $\mathbf{L}$ and the spin angular momentum $\mathbf{S}$ and can be calculated from the total angular momentum $\mathbf{J}$ [68]. This can be used to determine the possible quantum numbers that J can take. The total electronic angular momentum $\mathbf{J}$ needs to be calculated as

$$\mathbf{J} = \mathbf{L} + \mathbf{S}. \tag{2.1}$$

The quantum number J can take values of $|L - S| \leq J \leq L + S$ in steps of 1. For the caesium atom in the ground state the electron has $L = 0$, $S = 1/2$ and hence $J = 1/2$. In the excited state the electron has $L = 1$ and hence $J = 1/2$ or $3/2$. The energy level structure can be seen in Figure 2.1. The energy level transition (D-line) from the ground state to the excited state is split into two. The transition from $6^2\mathrm{S}_{1/2} \rightarrow 6^2\mathrm{P}_{1/2}$ is called the D1 transition and $6^2\mathrm{S}_{1/2} \rightarrow 6^2\mathrm{P}_{3/2}$ is known as the D2 transition. In order for a Cs atom to be excited from the ground state it must absorb a photon of the correct wavelength that matches the transition. For the D1 transition ($6^2\mathrm{S}_{1/2} \rightarrow 6^2\mathrm{P}_{1/2}$) the photon needs a wavelength of $\sim$ 895 nm and for the D2 transition ($6^2\mathrm{S}_{1/2} \rightarrow 6^2\mathrm{P}_{3/2}$) the photon needs a wavelength of $\sim$ 852 nm.

Each sublevel further splits into the hyperfine states which arise from the coupling between the total electronic angular momentum $\mathbf{J}$ and the total nuclear angular

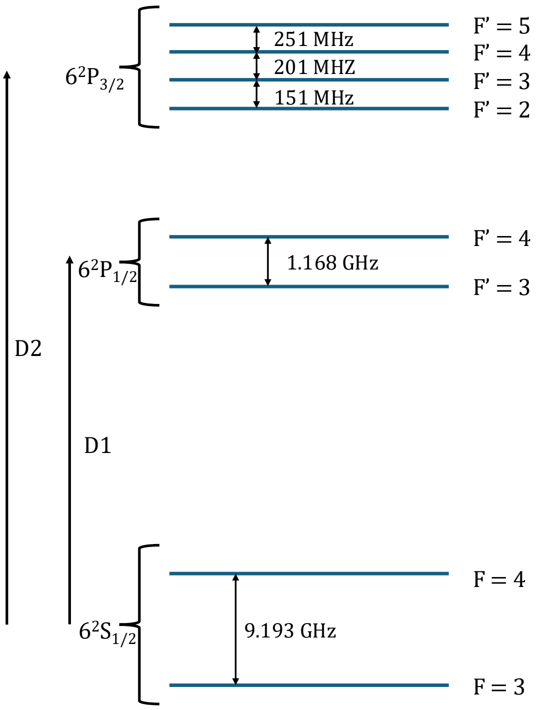

Figure 2.1: Caesium energy level diagram with the ground states $F = 3$ and $F = 4$. The two energy transitions are shown with the $6^2\mathrm{S}_{1/2} \rightarrow 6^2\mathrm{P}_{1/2}$ (D1) transition having excited states $F' = 3, 4$ and the $6^2\mathrm{S}_{1/2} \rightarrow 6^2\mathrm{P}_{3/2}$ (D2) transition having excited states $F' = 2, 3, 4, 5$. An atom must absorb a photon of wavelength 894 nm and 852 nm to become excited for the D1 and D2 transitions, respectively.

momentum **I**. This results in a total angular momentum **F** which is given by

$$\mathbf{F} = \mathbf{J} + \mathbf{I}. \tag{2.2}$$

The values of F can take the values of $|J - I| \leq F \leq J + I$ in steps of 1. Caesium has a total nuclear angular momentum $I = 7/2$ and hence for the ground state level which has a total electronic angular momentum $J = 1/2$ the total angular momentum can take the values $F = 3, 4$. For the excited states the couplings result in a total angular momentum of $F' = 3, 4$ for $6^2\mathrm{P}_{1/2}$ which has $J = 1/2$ and $F' = 2, 3, 4, 5$ for $6^2\mathrm{P}_{3/2}$ which has $J = 3/2$. Here F' is used to distinguish the excited state from the ground state which is denoted by F. For the hyperfine splitting, the atomic energy levels are shifted according to the value of F.

Due to the Heisenberg uncertainty principle, only one of the components of the total angular momentum **F** can be measured with 100% certainty. The total angular momentum components F_x, F_y and F_z are spin operators, for simplicity in the text the ‘hats’ are dropped. In this thesis the F_z component will be measured. The F_z component can take possible values in the range of $m_F = [-F, -F+1, ..., F-1, F]$. When measuring the F_z component the F_x and F_y components cannot be known with 100% certainty as they do not commute $[F_x, F_y] = i\hbar F_z$. The uncertainties can be determined using the Heisenberg uncertainty principle

$$\Delta F_x \Delta F_y \geq \frac{\hbar}{2} \langle F_z \rangle . \tag{2.3}$$

In order to describe the interactions of the atomic states with magnetic fields and light it is convenient to describe the different sublevels in vector form. For a simple model with the transition of $F = 1 \rightarrow F' = 0$, the ground state sublevels can be defined as $|F, m_F\rangle = \{|1,1\rangle, |1,0\rangle, |1,-1\rangle\}$ with the excited state being defined as $\left|F', m'_F\right\rangle = |0', 0'\rangle$.

2.1.2 Number density

In a magnetometer a vapour cell containing a small amount of caesium is utilised. The amount of caesium vapour depends on the temperature and pressure of the cell. Caesium has a low melting point of 301.6 K (28.44°C). For temperatures below the melting point, $T < 301.6$ K, the pressure P_v is calculated from

$$\log_{10}(P_v) = -219.482 + \frac{1088.676}{T} - 0.083362T + 94.888\log_{10}T. \tag{2.4}$$

Above the melting point, $T > 301.6$ K, the pressure P_v is given by

$$\log_{10}(P_v) = 8.22127 + \frac{4006.048}{T} - 0.00060194T - 0.19623\log_{10}T. \tag{2.5}$$

The pressure P_v here is given in units of Torr [68]. The relation between the pressure of the atomic vapour as temperature increases can be seen in Figure 2.2a. From the pressure, the number density in the Cs vapour cell can be calculated as

$$n = \frac{\tilde{P}_v}{k_B T}, \tag{2.6}$$

where $\tilde{P}_v$ is the vapour pressure in units of Pascals. The pressure is converted from Torr to Pascals using the conversion factor 133.322 Pa/Torr. The number density as a function of temperature is shown in Figure 2.2b. Two key temperatures used in this thesis are 18.5°C and 50°C which have a corresponding number density of 2.2×10^{16} m^{-3} and 4.1×10^{17} m^{-3}, respectively.

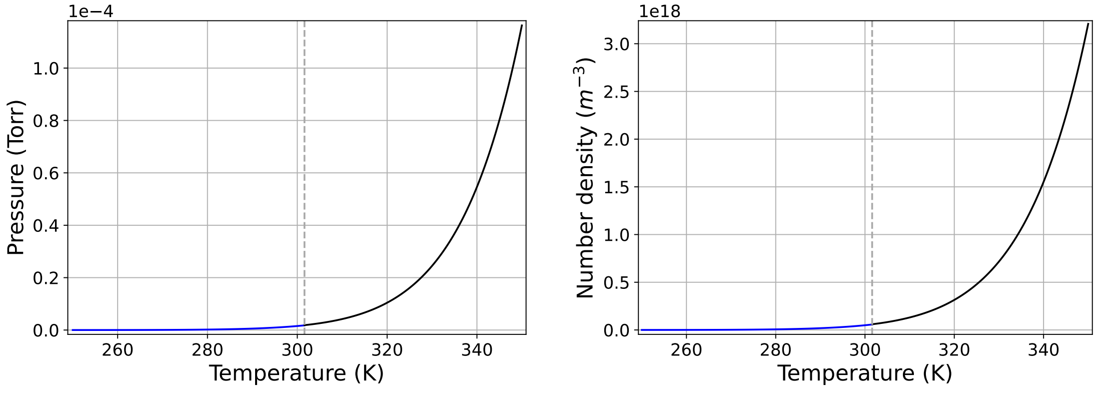

(a) (b)

Figure 2.2: The atomic (a) pressure and (b) number density of the caesium vapour as a function of temperature.

2.2 The Zeeman effect

When a static magnetic field is applied to the atomic ensemble, the magnetic-field-atom-interaction Hamiltonian is determined from

$$H_B = -\mu \cdot \mathbf{B}, \tag{2.7}$$

where $\mu = g_F \mu_B (F_x \hat{\mathbf{x}} + F_y \hat{\mathbf{y}} + F_z \hat{\mathbf{z}})/\hbar$ is the atom's magnetic dipole operator while g_F is the hyperfine Landé g-factor [68] and μ_B is the Bohr magneton. Hence the Hamiltonian is calculated from

$$H_B = \frac{g_F \mu_B}{\hbar}(F_x B_x + F_y B_y + F_z B_z). \tag{2.8}$$

This holds for a generic magnetic field but the focus will now move to a static magnetic field B_0 applied in the z-direction. Hence, only the F_z component in Equation 2.8 remains and can be determined from

$$F_z \left|F, m_F\right\rangle = \hbar m_F \left|F, m_F\right\rangle. \tag{2.9}$$

For simplicity, a simple model with a ground state of $F = 1$ which has sublevels $\left|F, m_F\right\rangle = \{\left|1,-1\right\rangle, \left|1,0\right\rangle, \left|1,-1\right\rangle\}$ and an excited state $F' = 0$ with $\left|F', m'_F\right\rangle = \left|0,0\right\rangle$, as shown in Figure 2.3, will be used. In this case, F_z can be defined as

$$F_z = \hbar \begin{pmatrix} 1 & 0 & 0 & 0 \\ 0 & 0 & 0 & 0 \\ 0 & 0 & -1 & 0 \\ 0 & 0 & 0 & 0 \end{pmatrix}, \tag{2.10}$$

and hence in a static magnetic field the magnetic-field-atom-interaction Hamiltonian is given by

$$H_B = g_F \mu_B \begin{pmatrix} B_0 & 0 & 0 & 0 \\ 0 & 0 & 0 & 0 \\ 0 & 0 & -B_0 & 0 \\ 0 & 0 & 0 & 0 \end{pmatrix}. \tag{2.11}$$

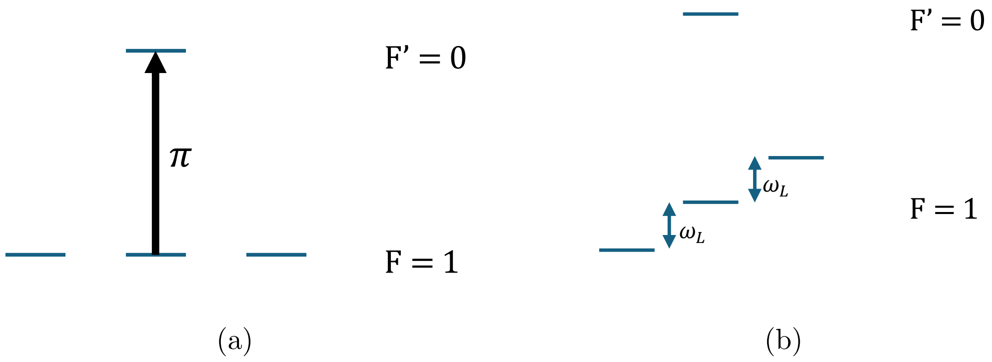

(a) (b)

Figure 2.3: A simple energy level model with a single ground state level $F = 1$ and a single excited state $F' = 0$. (a) A π-polarised light drives the $F = 1 \rightarrow F' = 0$ transition to excite atoms. (b) In the presence of a weak static field the ground state energy levels are equally split by the Larmor frequency ω_L.

The application of this static magnetic field causes perturbations in the hyperfine structure. This is described by the Zeeman effect. For a weak static magnetic field, the energy sublevels are displaced by an even amount with the energy difference proportional to the magnetic field strength,

$$\Delta E_{F,m_F} = g_F \mu_B m_F B_0. \tag{2.12}$$

From this the operational frequency of a magnetometer can be determined as

$$\nu_L = \frac{\Delta E_{F,m_F} - \Delta E_{F,m_F-1}}{\hbar}. \tag{2.13}$$

Hence, it can be seen that in the weak field regime the Larmor frequency can be calculated as $\nu_L = \tilde{\gamma}_{\text{cs}} B_0$ where $\tilde{\gamma}_{\text{cs}} = 3.5$ kHz/μT is the gyromagnetic ratio of caesium in units of Hz. The Zeeman splitting is shown for the ground state of caesium in Figure 2.4.

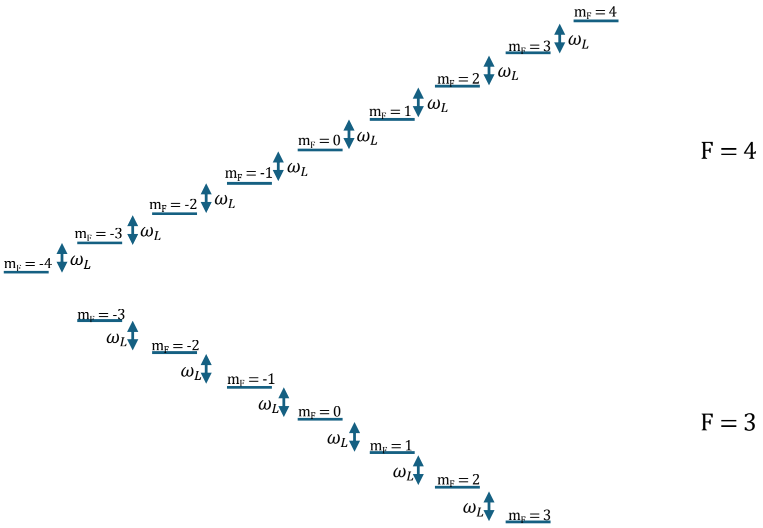

Figure 2.4: Zeeman splitting of the caesium ground state levels in a weak static magnetic field which splits neighbouring levels by the Larmor frequency ω_L.

2.2.1 The non-linear Zeeman effect

When a strong magnetic field is applied to the system the splitting of the hyperfine levels is no longer equal and hence Equation 2.13 is not valid. As the linear response is no longer valid second order corrections need to be considered. For a system where $J = 1/2$ the energy splitting is described by the Breit-Rabi formula [68] which is given by

$$E = -\frac{E_{\text{hfs}}}{2(2I+1)} - g_I \mu_B m_F B_0 \pm \frac{E_{\text{hfs}}}{2}\sqrt{1 + \frac{4m_F}{(2I+1)}x + x^2}, \tag{2.14}$$

where $E_{\text{hfs}} = h\nu_{\text{hfs}}$ is the hyperfine splitting of the ground state, $g_I = \mu_I/(\mu_N I)$ is the nuclear g-factor, μ_I is the nuclear magnetic moment, $g_J \sim 2$ and

$$x = \frac{(g_J - g_I)\mu_B}{E_{\text{hfs}}} B_0. \tag{2.15}$$

The choice of the sign factor ± is determined from $F_{\pm} = I \pm 1/2$ where $F_{\pm}$ represented the hyperfine splitting.

Expanding the final term up to second order of B_0 and substituting in $I = 7/2$ for caesium Equation 2.14 becomes

$$E = \frac{7E_{\text{hfs}}}{16} + \mu_B \left(\frac{m_F}{4} - g_I\right) B_0 + \frac{\mu_B^2(16 - m_F^2)}{16E_{\text{hfs}}} B_0^2. \tag{2.16}$$

By calculating the energy difference between the m_F and $m_F - 1$ state, for some arbitrary F, the frequency difference between two adjacent sublevels can be calculated as

$$\Delta\nu_{m,m-1} = \nu_L + \frac{2\nu_L^2}{\nu_{\text{hfs}}}\left(m - \frac{1}{2}\right). \tag{2.17}$$

As is shown in Section 6.4.5, for the $F = 4$ caesium ground state the difference between the two outer states is $\Delta\nu_{m=4,m=3} - \delta\nu_{m=-3,m=-4} = -7(2\nu_L^2)/\nu_{\text{hfs}}$.

2.3 Light-atom interactions

The optical electric field for light that is polarised in the z-direction can be written as

$$\mathbf{E} = E_0 \cos(\omega t)\hat{\mathbf{z}}, \tag{2.18}$$

where E_0 is the electric field amplitude and ω is the angular frequency of the light. The light-atom interaction Hamiltonian H_l is

$$\begin{aligned} H_l &= -\mathbf{E} \cdot \mathbf{d} && (2.19)\\ &= -E_0 \cos(\omega t) d_z, && (2.20) \end{aligned}$$

where $\mathbf{d} = d_x\hat{\mathbf{x}} + d_y\hat{\mathbf{y}} + d_z\hat{\mathbf{z}}$ is the dipole operator. The components of the dipole operator can be defined as

$$\begin{aligned} d_x &= \frac{d_{-1} - d_1}{\sqrt{2}}, && (2.21)\\ d_y &= -i\frac{d_{-1} - d_1}{\sqrt{2}}, && (2.22)\\ d_z &= d_0. && (2.23) \end{aligned}$$

Here d_1, d_0 and d_{-1} are rank-1 spherical tensor components that are used to describe the dipole operator vector [16]. The Wigner-Eckart Theorem can be used to calculate d_0 [16]. The Wigner-Eckart formula for a rank-1 tensor is given by

$$\langle F_1, m_1| d_q |F_2, m_2\rangle = (-1)^{F_1 - m_1} \begin{pmatrix} F_1 & 1 & F_2 \\ -m_1 & q & m_2 \end{pmatrix} \langle F_1| |d| |F_2\rangle, \tag{2.24}$$

where the matrix in the equation is the Wigner-3j symbol and $\langle F_1| |d| |F_2\rangle$ is the reduced matrix elements for the transition. The Wigner-3j symbol is related to the Clebsch-Gordon coefficient $\langle F_1, 1, m_1, q|F_2, -m_2\rangle$ [68] by

$$\begin{pmatrix} F_1 & 1 & F_2 \\ -m_1 & q & m_2 \end{pmatrix} = \frac{(-1)^{F_1 - 1 - m_2}}{\sqrt{2F_2 + 1}} \langle F_1, 1, m_1, q|F_2, -m_2\rangle. \tag{2.25}$$

For a simple model with the transition $F = 1 \longrightarrow F' = 0$, d_0 is calculated as

$$d_0 = \begin{pmatrix} 0 & 0 & 0 & 0 \\ 0 & 0 & 0 & -1 \\ 0 & 0 & 0 & 0 \\ 0 & -1 & 0 & 0 \end{pmatrix} \frac{\langle 1| \, |d| \, |0' \rangle}{\sqrt{3}}. \tag{2.26}$$

The derivation of d_1 and d_{-1} are not of use to the geometries used in this thesis but can be found in Ref. [16]. For light that is linearly polarised along the the quantisation axis in the z-direction the d_z component is equal to the d_0 component calculated here. Therefore, the light-atom interaction Hamiltonian is found to be

$$H_l = E_0 \cos(\omega t) \begin{pmatrix} 0 & 0 & 0 & 0 \\ 0 & 0 & 0 & -1 \\ 0 & 0 & 0 & 0 \\ 0 & -1 & 0 & 0 \end{pmatrix} \frac{\langle 1| \, |d| \, |0' \rangle}{\sqrt{3}} \tag{2.27}$$

$$= \hbar \Omega_R \cos(\omega t) \begin{pmatrix} 0 & 0 & 0 & 0 \\ 0 & 0 & 0 & -1 \\ 0 & 0 & 0 & 0 \\ 0 & -1 & 0 & 0 \end{pmatrix}, \tag{2.28}$$

where $\Omega_R = (\langle 1| \, |d| \, |0' \rangle \, E_0)/(\hbar\sqrt{3})$ is the Rabi frequency.

2.3.1 Selection rules

With the use of linearly polarised light, as shown here, the atom can change its total angular momentum ΔF when in the excited state such that $\Delta F = F - F' = 1$ without changing the projection of the angular momentum along the quantisation axis. In general, the allowed transitions can be calculated from the Wigner-3j symbol (Equation 2.25) and they show that for a transition $F \longrightarrow F' = F \pm 1$, $\Delta m_F = -1, 0, +1$ are allowed. Where as for a transition $F \longrightarrow F' = F$, $\Delta m_F = -1, +1$ are only allowed. Here the polarisation type of light couples to the different Δm_F level with π-polarised light coupling to $m_F \longrightarrow m'_F$, σ^+-polarised light coupling to $m_F \longrightarrow m'_F + 1$ and σ^--polarised light coupling to $m_F \longrightarrow m'_F - 1$. Hence for the experiments presented in this thesis the allowed transition is $\Delta m_F = 0$.

2.4 Vapour cells

In this thesis there are three vapour cells of interest. The first is a vapour cell only containing caesium vapour which is used as a reference cell. The next is a paraffin coated cell which is used in the table-top setup, for the spin noise measurements and as a zero-field magnetometer. The paraffin coated cell is hand-blown and cubic with a volume of (5 mm)^3. The paraffin coated vapour cell is not heated and remains at room temperature ($\sim 18.5^\circ$C) for all measurements. The final cell is a 65 Torr buffer gas cell which is used in the table-top setup as well as in the portable prototype that was developed. The buffer gas used in the cell is nitrogen (N_2) which is heated to $\sim 50^\circ$C. The cell is heated using a Shapal ceramic cover that is wrapped in a non-magnetic resistive heating wire. This is then surrounded by a heat insulator aerogel and Kapton tape to keep the wires in place. The tip of the cell is not heated to keep the solid Cs in the stem. All three cells can be seen in Figure 2.5.

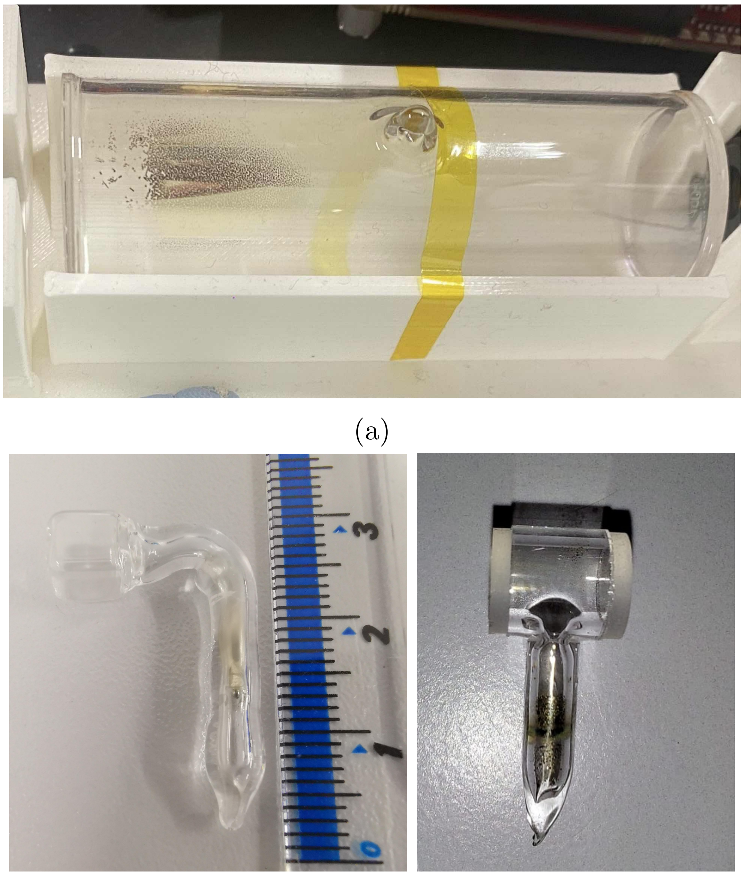

(a)

(b) (c)

Figure 2.5: Caesium filled vapour cells: (a) a 7 cm long reference cell containing only Cs, (b) a (5 mm)^3 paraffin coated cell, (c) a 5 mm diameter and 5 mm long nitrogen buffer gas cell.

2.4.1 Quantum noise

Optically pumped magnetometers have a fundamental noise floor limit that are imposed by quantum mechanics. There are two typical sources of noise that arise from the quantum fluctuations in the atomic ensemble and probe beam known as the spin projection noise δB_{spin} and photon shot noise δB_{shot}, respectively. The total quantum noise limit is given by

$$\delta B_{\text{quantum}} = \sqrt{\delta B_{\text{spin}}^2 + \delta B_{\text{shot}}^2}. \tag{2.29}$$

The theoretical values for the spin projection noise and photon shot noise can be derived following the reasoning in Ref. [21].

Starting with the derivation of the spin projection noise which arises from the uncertainty relation

$$\Delta F_x \Delta F_y \geq \frac{|F_z|}{2}, \tag{2.30}$$

for non-commuting operators with total angular momentum $\left[F_x, F_y\right] = iF_z$. As there is no squeezing used here it can be assumed that $\Delta F_x = \Delta F_y$ and hence the relation simplifies to

$$\Delta F_x \geq \sqrt{\frac{|F_z|}{2N}}, \tag{2.31}$$

where there are N atoms in the system. For a continuous measurement over a time t the uncertainty of F_x can be adapted to have the form [21, 69]

$$\Delta F_x = \sqrt{\frac{2F_zT_2}{N}}, \tag{2.32}$$

where T_2 is the transverse relaxation time. The uncertainty on the measurement of ΔF_x can also be related to the uncertainty on the measurement of the oscillating magnetic field. With the light polarised in the z-direction and a resonant oscillating magnetic field along the y-direction given by $B_{\mathrm{rf}} \cos{(\omega_L t)}\hat{\mathbf{y}}$, the transverse polarisation can be calculated as

$$P_x = \frac{F_x}{F_z} = \frac{1}{2}\gamma_{\mathrm{cs}}B_{\mathrm{rf}}T_2 \sin{(\omega_0 t)}. \tag{2.33}$$

Hence the uncertainty on F_x can be calculated from

$$\Delta P_x = \frac{\Delta F_x}{F_z} = \frac{\gamma_{\mathrm{cs}}T_2}{2}\delta B_{\mathrm{spin}}. \tag{2.34}$$

Combining Equations 2.32 and 2.34 results in the spin projection noise being calculated as [21]

$$\delta B_{\mathrm{spin}} = \frac{1}{\gamma_{\mathrm{cs}}}\sqrt{\frac{8}{F_z n V T_2}}, \tag{2.35}$$

where n is the number density of atoms and V is the volume of atoms being probed.

In order to determine the photon shot noise limit the angle at which the linear polarisation of the probe beam is tilted, due to the transverse spin polarisation of the RF field, needs to be considered. The angle of rotation is given by [21]

$$\phi = \frac{1}{2} l r_e f_{\mathrm{osc}} n P_x D(\nu), \tag{2.36}$$

where l is the length of the vapour cell, $r_e = 2.8 \times 10^{-13}$ cm is the classic electron radius, $f_{\mathrm{osc}} \approx 1/3$ is the typical oscillator strength for the D1 transition and $D(\nu)$ is the dispersion profile which is given by $D(\nu) = (\nu - \nu_0)/[(\nu - \nu_0)^2 + (\Delta\nu/2)^2]$. Here ν_0 is the frequency of the D1 transition and $\Delta\nu$ is the optical full width half maximum. The uncertainty of the measured rotation arises from the uncertainty in the number of photons hitting each photodiode in the balanced photodetector and is given by

$$\delta\phi = \sqrt{\frac{1}{2\Phi\eta}}, \tag{2.37}$$

where Φ is the flux of the photons and η is the quantum efficiency of the photodiodes. Using Equations 2.33, 2.36 and 2.37, the photon shot noise can be calculated as

$$\delta B_{\mathrm{spin}} = \frac{2\sqrt{2}}{\pi l r_e c f n D(\nu)\sqrt{\Phi\eta}}. \tag{2.38}$$

In an ideal case the photon shot noise limit will be equal to the spin projection noise such that the total quantum noise can be determined by $\delta B_{\mathrm{quantum}} = \sqrt{2}\delta B_{\mathrm{spin}}$.

2.5 Absorption spectroscopy

The hyperfine levels that are shown in Figure 2.1 can be seen experimentally by performing absorption spectroscopy measurements. This method involves shining laser light through a vapour cell and detecting the transmitted light using a single photodiode detector. A reference cell with a length of 7 cm filled with caesium vapour is used to see the hyperfine transitions on the D1-line. A custom-made laser as described in Section 6.3 is used with the wavelength being ramped up and down around 894.5 nm. The wavelength is varied in order to match the different energy transitions between the hyperfine levels. The amplitude of the transmitted light is detected as the wavelength of the laser is ramped up and down around 894.5 nm. The signal is then normalised such that the light power before the vapour cell $I(0)$ is equal to the light power after the vapour cell $I(l)$ when the laser light is off resonance. The resulting signal can be seen in Figure 2.6. It can be seen that the four expected transitions are detected and separated by the expected frequency differences.

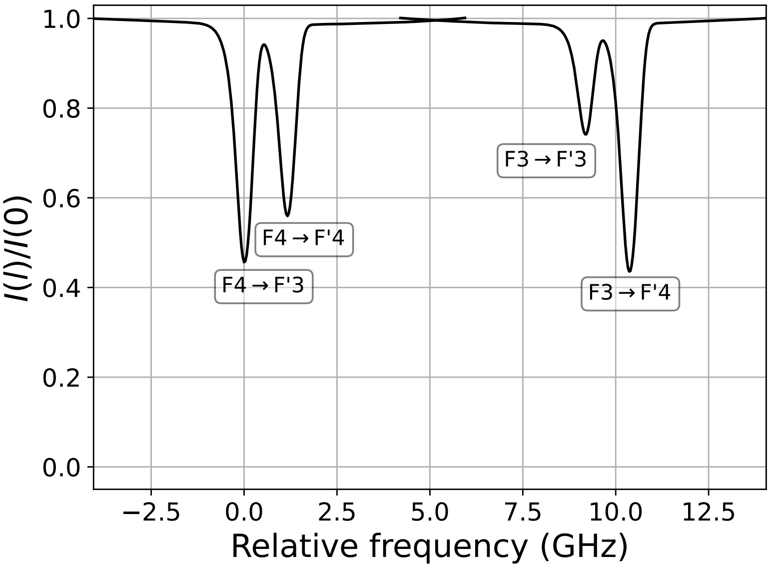

Figure 2.6: Absorption spectrum of the D1 line for caesium reference cell normalised to the light power before the vapour cell $I(0)$.

2.5.1 Doppler broadening

In temperatures above 0 K, atoms move with a velocity $\mathbf{v}$. The atom has a speed component v_x along the laser propagation direction, this causes the frequency of the laser that the laser experiences to be shifted due to the Doppler effect as given by,

$$\nu(v_x) = \nu_0 \left(1 \pm \frac{v_x}{c}\right), \tag{2.39}$$

where c is the speed of light and ν_0 is the resonant frequency between the ground and excited states. The atoms can take a range of velocities with the speed distribution $f(v)$ being given by the Maxwell-Boltzmann distribution

$$f(v) = \sqrt{\frac{2}{\pi}} \left(\frac{m_{\mathrm{cs}}}{k_B T}\right)^{3/2} v^2 \exp\left\{\frac{-m_{\mathrm{cs}} v^2}{2 k_B T}\right\}, \tag{2.40}$$

where m_{cs} is the mass of a caesium atom, k_B is the Boltzmann constant, T is the temperature and v is the speed of the atom. The Doppler effect causes broadening of the atomic resonance. The resulting signal takes the form of a Gaussian lineshape with a full width at half maximum given by

$$\Gamma_G = \frac{2\nu_0}{c}\sqrt{\frac{2\ln(2)k_B T}{m_{\mathrm{cs}}}}. \tag{2.41}$$

For the caesium D1 line the Doppler broadening can be calculated to be $\Gamma_G =$ 356 MHz at a temperature of $20^{\circ}C$. As the excited states are separated by a frequency of 1.168 GHz the two F' transitions can be resolved individually for $F = 3 \rightarrow F'$ and $F = 4 \rightarrow F'$ as is shown in Figure 2.6.

2.5.2 Pressure broadening

The measurement time of an OPM is determined by the spin relaxation time resulting in a longer T_2 time being desirable. Factors affecting the spin-relaxation time in vapour cells containing buffer gas are discussed in Refs. [70, 71]. In the OPM presented in this thesis, the main contribution to the spin relaxation limit is from alkali-wall collisions. Buffer gas is added to the caesium vapour cell in order to slows the diffusion of the caesium atoms causing a longer T_2 time reducing the alkali-wall collision rate. Hence improving the performance of the OPM. However, the addition of the buffer gas causes the atoms in the excited states to rapidly collide with the buffer gas molecules. This leads to rapid collisional mixing in which the atoms in the excited state are redistributed among the sublevels in the short time they are there. This causes the linewidth of the absorption spectroscopy to be broadened from the expected ~ 5 MHz in a purely caesium cell. For typical buffer gas pressures used in magnetometry the broadening is on the order of $1 - 100$ GHz [72]. This broadening also alters the lineshape of the absorption spectroscopy with the data needing to be fitted to a Voigt profile [73]. In complex form, the Voigt profile is defined as [72]

$$V(\nu - \nu_0) = \frac{2}{\Gamma_G}\sqrt{\frac{\ln(2)}{\pi}}\mathrm{e}^{-(\alpha(\nu))^2}(1 - \mathrm{erf}(-i\alpha(\nu))), \tag{2.42}$$

where Γ_G is the full width half maximum of the Gaussian profile, Γ_L is the full width half maximum of the Lorentzian profile, erf is the complex error function and

$$\alpha(\nu) = \frac{2\sqrt{\ln(2)}[(\nu - \nu_0) + i(\Gamma_L/2)]}{\Gamma_G}. \tag{2.43}$$

By determining the Voigt profile, the absorption cross section can be determined by

$$\sigma_V(\nu) = \pi r_e c f_{\mathrm{osc}} \mathrm{Re}\left[V(\nu - \nu_0)\right], \tag{2.44}$$

where r_e is the classical electron radius, c is the speed of light and f_{osc} is the oscillator strength.

Figure 2.7 shows the absorption spectroscopy of the 65 Torr N_2 buffer gas cell used in this thesis. The data is plotted on top of the reference cell that contains only caesium vapour. By fitting the Voigt profile to the data, the pressure broadening and frequency shifts can be used to determine the buffer gas pressure in the cell as 65(1) Torr, see Section 6.5.1 for further details.

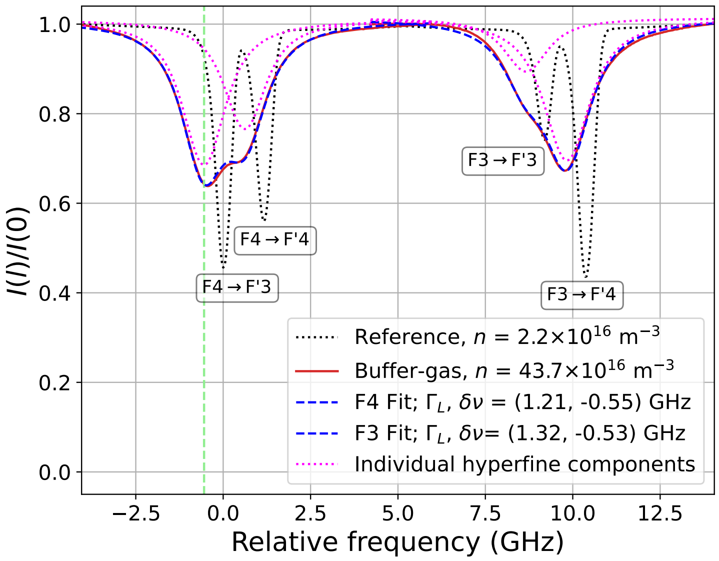

Figure 2.7: The D1 absorption spectrum for a pure caesium cell (black dotted line) and a 65 Torr buffer gas cell (red line) at a temperature of 51°C. This corresponds to a number density of atoms of 43.7×10^{16} m^{-3}. A Voigt profile is fitted to the $F = 3 \longrightarrow F' = 3, 4$ and $F = 4 \longrightarrow F' = 3, 4$ transitions with the Gaussian linewidth fixed at $\Gamma_G = 374$ MHz so the Lorentzian linewidths, Γ_L, and the pressure shifts, $\delta\nu$, can be extracted.

2.5.3 Calculating the number density

The absorption spectroscopy can be used to experimentally determine the number density of a vapour cell. This is an accurate method to measure the temperature of the atomic ensemble. The expected light intensity after the vapour cell can be determined by the Beer-Lambert law where

$$I(l) = I(0) \exp\{-n\sigma(\nu)l\}. \tag{2.45}$$

Here n is the number density and $\sigma(\nu)$ is the absorption cross section which is given by [72],

$$\sigma(\nu) = \pi r_e c f_{\mathrm{osc}} V(\nu). \tag{2.46}$$

The number density can then be calculated as

$$n = -\frac{1}{\pi r_e c f_{\mathrm{osc}} l} \int_{-\infty}^{\infty} \ln \frac{I(l)}{I(0)} d\nu. \tag{2.47}$$

In Figure 6.5.1 it can be seen that the number density for the reference cell is found to be $n = 2.2 \times 10^{16}$ m^{-3} and $n = 43.7 \times 10^{16}$ m^{-3} for the buffer gas cell. The temperature of the atomic ensemble can then be determined by substituting the results for the number density into Equation 2.6 and rearranging for T.

2.6 Optical pumping

The size of the signal from a magnetometer is proportional to the polarisation of the atomic vapour. Assuming negligible spin-exchange collisions, the vapour is initially unpolarised with an equal population in each of the ground state sublevels. It is noted that if the spin-exchange collisions are not negligible then the population of the ground state sub-levels are defined by the spin temperature. For the theory presented here it is assumed that the spin-exchange collisions are negligible. Optical pumping can be used to create a polarised ensemble. On resonance laser light can be used to transfer angular momentum and drive transitions, creating a polarised sample. In this thesis, light that is linearly polarised along the z-axis is used to create an aligned state using two different types of cells, a paraffin coated cell and a buffer gas cell. A single laser beam that is tuned to the $F = 4 \rightarrow F' = 3$ transition is used to pump and probe the ensemble, as shown in Figure 2.8.

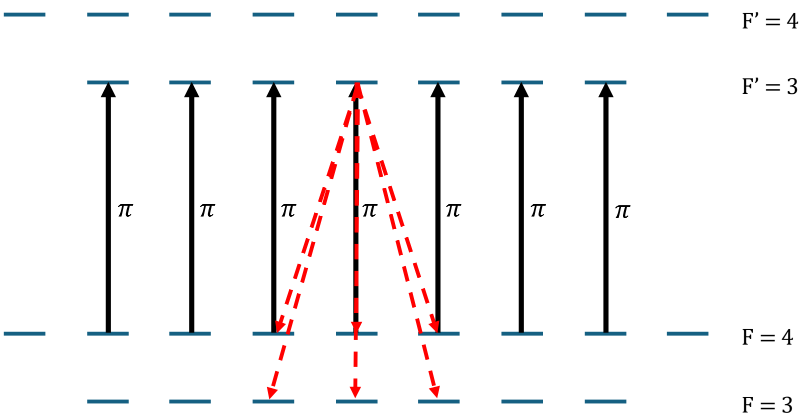

Figure 2.8: Optical pumping of the caesium D1 transition using linearly (π) polarised light to drive the $F = 4 \rightarrow F' = 3$ transition. The allowed states that the atom can decay to, when in the excited state, is represented by the red dashed arrows.

Initially, the optical pumping of a paraffin coated cell will be studied. For a paraffin coated cell the main de-excitation is from spontaneous emission. The use of linearly polarised (π-polarised) light results in no change in the angular momentum with $\Delta m_F = 0$. This can be seen by looking at a single atoms. If an atom that is in the $|F, m_F\rangle = |4, 3\rangle$ sublevel absorbs a photon it is excited to the $\left|F', m'_F\right\rangle = |3', 3'\rangle$. The atoms remains in the excited state for a short period of time as the natural lifetime of the excited states is very short ($\tau_{\text{nat}} = 34.9$ ns for the $6^2\text{P}_{1/2}$ excited state). The atom then decays back to the ground state. It can decay to any one of five allowed $|F, m_F\rangle$ sublevels of either $F = 3$, $m_F = 2, 3$ or $F = 4$, $m_F = 2, 3, 4$. Note that, if the atom decays into the $F = 3$ state it is not re-excited due to the laser being resonant with the $F = 4$ ground state transition. The probability of the atom decaying into each of these states is determined by the square of the Clebsch-Gordan coefficients [68]. The square of the Clebsch-Gordan coefficients are represented as $\left\langle F, 1, m_F, q \middle| F', m'_F\right\rangle^2$ for the transition $|F, m_F\rangle \leftrightarrow \left|F', m'_F\right\rangle$. For linearly polarised light $q = 0$. The rate equations that describe how the population of the magnetic sublevels vary with time can be written in a general form, for light that is tuned to the $F = 4 \rightarrow F' = 3$ transition, as

$$\frac{dp_{3,m_F}}{dt} = R_p \sum_{\alpha=-1}^{1} p_{4,m_F+\alpha} \left\langle 4, 1, m_F+\alpha, 0 \middle| 3', m'_F = m_F+\alpha \right\rangle^2 - \Gamma_1 p_{3,m_F} + \frac{\Gamma_1}{16}, \quad (2.48)$$

and

$$\begin{aligned}\frac{dp_{4,m_F}}{dt} =&R_p \sum_{\alpha=-1}^{1} p_{4,m_F+\alpha} \left\langle 4,1,m_F+\alpha,0 \middle| 3',m'_F=m_F+\alpha \right\rangle^2 \\ &-\Gamma_1 p_{4,m_F} + \frac{\Gamma_1}{16} - R_p p_{4,m_F} \left\langle 4,1,m_F,0 \middle| 3',m'_F=m_F \right\rangle\end{aligned} \tag{2.49}$$

for the $F = 3$ and $F = 4$ ground states, respectively. Note that when exciting to the $F' = 3$ state, $m'_F = -3, -2, ..., 2, 3$. If in Equations 2.48 and 2.49 m'_F does

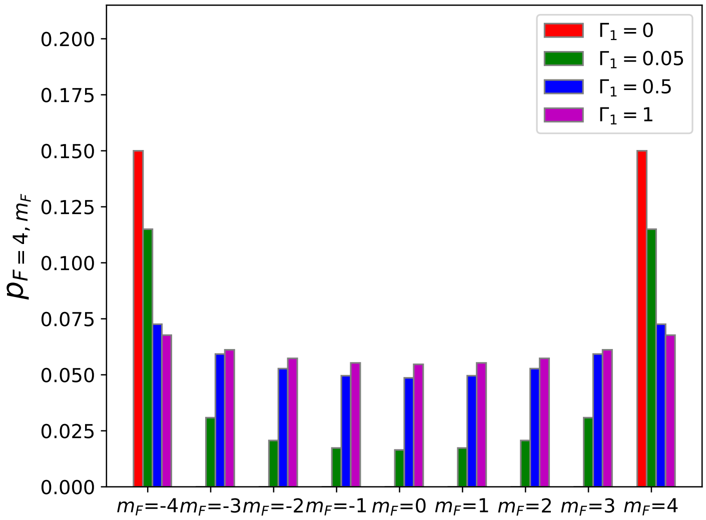

(a)

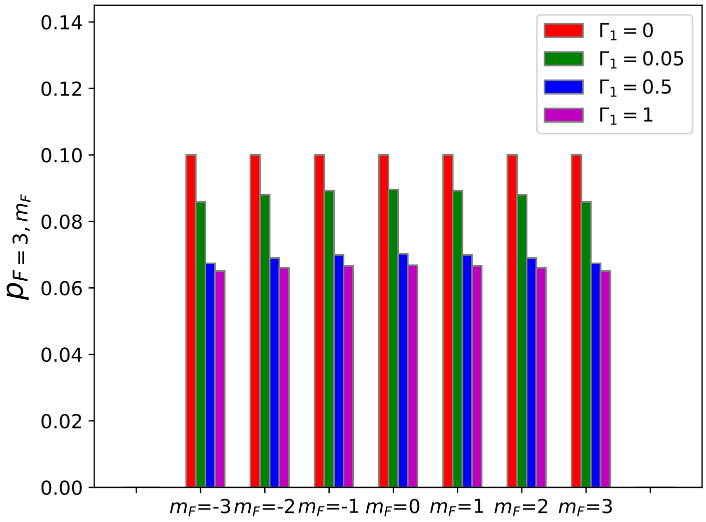

(b)

Figure 2.9: Optical pumping into an aligned state when spontaneous emission is the dominant de-excitation mechanism, as is the case in a paraffin coated cell. The populations of the states in the steady state are presented for (a) $F = 4$ and (b) $F = 3$ ground state levels with longitudinal relaxation rates $\Gamma_1 = 0, 0.05, 0.5, 1$ with the optical pumping rate $R_p = 1$.

not obey this condition angular momentum is not conserved, and as a result the

Clebsch-Gordan coefficient vanishes setting this term to zero. Here R_p is the optical pumping rate, Γ_1 is the longitudinal relaxation rate and p_{F,m_F} is the population of the magnetic sublevel. All 16 equations are explicitly defined in Appendix A. Solving the 16 differential equations determines the populations p_{F,m_F} of each of the sublevels. The populations of the ground state levels in the steady state are plotted in Figure 2.9 for a range of longitudinal relaxation rates $\Gamma_1 = 0, 0.05, 0.5, 1$. For simplicity it is assumed that $R_p = 1$. It can be seen in Figure 2.9a that the bigger the value of Γ_1 the weaker the alignment in the steady state.

The addition of a buffer gas to a vapour cell causes rapid collisional mixing of the caesium atoms in the excited states. This causes the state that the Cs atom is in, in the excited state, to be randomised. The molecules of the buffer gas have many vibrational and rotational states which, upon interacting with the excited states of the Cs atoms, quenches the ensemble. These quenching collisions become the dominant decay mode for Cs excited states in the presence of a buffer gas. The rate R_Q at which an excited atom undergoes a quenching collision is given by

$$R_Q = n_Q \sigma_Q \tilde{v}, \tag{2.50}$$

where n_Q is the number density of quenching gas molecules, σ_Q is the quenching cross section and $\tilde{v} = \sqrt{8k_B T/\pi M_{\text{eff}}}$ is the relative velocity between an alkali atom, caesium, and the quenching molecule with M_{eff} being the effective mass. For the buffer gas used in this thesis (see Section 2.4) the number density of the $\mathrm{N_2}$ molecules is $n_Q = P/(k_B T) = 1.91 \times 10^{24}$ m^{-3} at a temperature of 55°C. The quenching cross section at 100°C is $\sigma_Q = 5.5 \times 10^{-19}$ m^2 for Cs and $\mathrm{N_2}$ [72] and $\tilde{v} = 548$ m/s. Substituting these values into Equation 2.50 it can be found that $R_Q = 5.9 \times 10^8$ s^{-1}. The probability that an atom will decay via spontaneous emission instead of quenching is known as the quenching factor Q [72]. This is given by the ratio of the quenching rate and the spontaneous emission rate and defined as

$$Q = \frac{1}{1 + R_Q \tau_{\text{nat}}}. \tag{2.51}$$

When $Q = 1$ the atom will decay by spontaneous emission where as when $Q = 0$ it will decay by quenching. For the 65 Torr nitrogen buffer gas cell presented in this thesis $Q = 0.05$ and hence the dominant de-excitation mechanism is quenching. This means that the decay probabilities to the ground states are no longer governed by the Clebsch-Gordan coefficients but now there is an equal probability of 1/16 that the atom will decay to any of the ground state sublevels. Hence the optical pumping equations need to be defined such that this is taken into considerations. The rate equations in the presence of a quenching gas are given by

$$\frac{dp_{3,m_F}}{dt} = R_p \left[\frac{1}{16} \sum_{m=-3}^{3} p_{4,m} \left\langle 4, 1, m_F = m, 0 \middle| 3', m_F' = m \right\rangle^2 \right] - \Gamma_1 p_{3,m_F} + \frac{\Gamma_1}{16}, \tag{2.52}$$

and

$$\begin{aligned} \frac{dp_{4,m_F}}{dt} =& R_p \left[\frac{1}{16} \sum_{m=-3}^{3} p_{4,m} \left\langle 4, 1, m_F = m, 0 \middle| 3', m_F' = m \right\rangle^2 \right] \\ & - \Gamma_1 p_{4,m_F} + \frac{\Gamma_1}{16} - R_p p_{4,m_F} \left\langle 4, 1, m_F, 0 \middle| 3', m_F' = m_F \right\rangle . \end{aligned} \tag{2.53}$$

It is noted that when exciting to the $F' = 3$ state, $m'_F = -3, -2, ..., 2, 3$. If in Equations 2.48 and 2.49 m'_F does not obey this the Clebsch-Gordan coefficient and hence the term is equal to zero. The 16 differential equations can then be solved, in the steady-state, to determine the populations of each sublevel. The populations of the ground state levels are presented in Figure 2.10 for translational relaxation rates $\Gamma_1 = 0, 0.05, 0.5, 1$ with $R_p = 1$. Again here, it can be seen that for larger values of Γ_1

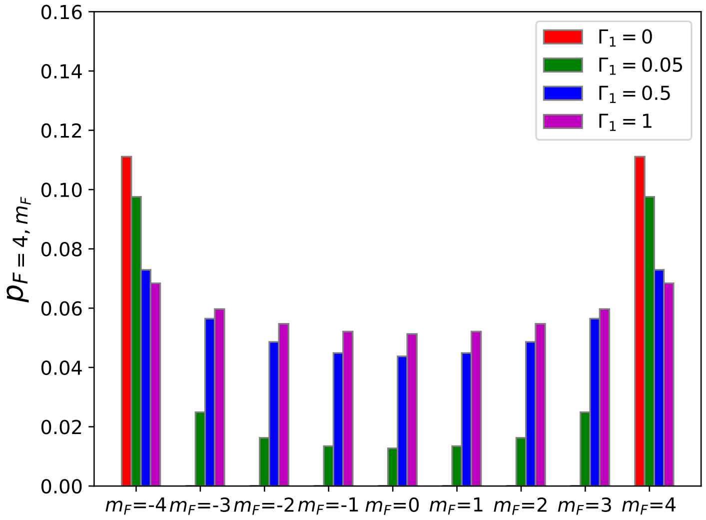

(a)

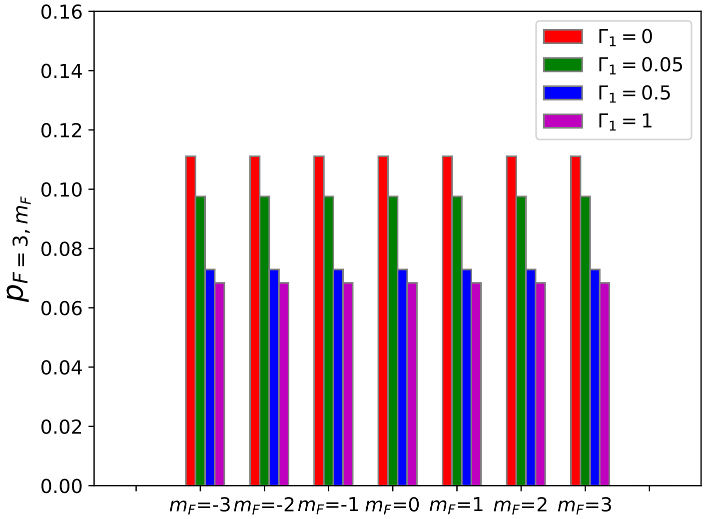

(b)

Figure 2.10: Optical pumping into an aligned state when quenching is the dominant de-excitation mechanism, as is the case in the buffer gas cell. The populations of the states in the steady state are presented for (a) $F = 4$ and (b) $F = 3$ ground state levels with longitudinal relaxation rates $\Gamma_1 = 0, 0.05, 0.5, 1$ with the optical pumping rate $R_p = 1$.

the optical pumping into the $m_F = \pm 4$ states is weaker. In all values presented these states do have the highest population, in the steady state, however it is much more efficient for $\Gamma_1 = 0$. By comparing this data to that presented in Figure 2.9, the optical pumping efficiency can be compared for the two scenarios where the atoms decay via spontaneous emission ($Q = 1$) and when the atoms decay via quenching ($Q = 0$). The optical pumping will be compared when $\Gamma_1 = 0.05$. For $Q = 1 \sim 12\%$ of the atoms are pumped into the $m_F = \pm 4$ state where as for $Q = 0$ a lower percentage of $\sim 10\%$ of the atoms are pumped into the outer most states. For all values of Γ_1 the optical pumping produces a better aligned state when spontaneous emission is the dominating de-excitation mechanism. Hence, the alignment produced is better in the paraffin coated cell than in the buffer gas vapour cell.

Chapter 3

Eddy currents

3.1 Motivation

A primary oscillating magnetic field $\mathbf{B}_1(t)$ can be used to induce eddy currents in a sample using the general principals of electromagnetic induction. Eddy currents are generated in electrically conductive objects due to changing magnetic fields. They are produced in closed loops as a result of Faraday's law of induction. The magnitude and density of the induced eddy currents are related to the primary magnetic field strength, dielectric properties and geometry of the sample. This results in a secondary magnetic field $\mathbf{B}_{\mathrm{ec}}(t)$ being produced as a result of Lenz's law which opposes the primary magnetic field. This magnetic field can then be measured using a magnetic field sensor [74, 75, 56]. As the secondary magnetic field produced is related to the dielectric properties of the sample, the properties can be determined from the measured signal. These properties include the conductivity, σ, magnetic permeability, μ, and the electrical permittivity, ε. These measurements are often referred to as eddy current testing, electromagnetic induction imaging, or magnetic induction tomography (MIT), to name a few. It is noted that although electrically conductive objects are of interest in this thesis, electromagnetic induction imaging can also be used with magnetically permeable objects where the primary magnetic field magnetises the sample which in turn produces a secondary magnetic field [76].

In the literature there are a few approaches to calculate the theoretical strength of the induced magnetic field $\mathbf{B}_{\mathrm{ec}}(t)$. One method is through Maxwell's equations as shown in Refs. [60, 58]. An alternative approach is presented in Ref. [56]. Here eddy currents are induced in a cylindrical sample and individual current loops are calculated. This is then integrated over the sample to gain the total induced field. Both of these theories are used to characterise a magnetic and non-magnetic sample in Section 5.

A main difficulty found in magnetic induction tomography, for low conductivity samples, is deciphering the secondary (induced) magnetic field component from the total magnetic field detected. This is due to the amplitude of the secondary magnetic field typically being much weaker than the primary magnetic field. In order to over come this issue a highly sensitive OPM which uses the differential technique [30] is required to detect low conductivity objects. In this configuration a compensation magnetic field $\mathbf{B}_2(t)$ is introduced which cancels the primary magnetic field at the sensing point of the magnetic field sensor. Hence the sensor measures $\mathbf{B}_1(t)+\mathbf{B}_{\mathrm{ec}}(t)+\mathbf{B}_2(t) \approx \mathbf{B}_{\mathrm{ec}}(t)$. This technique means that a larger primary magnetic field can be used without saturating the magnetic field sensor when no object is present. As the primary field is proportional to the secondary induced magnetic field, larger signals can be detected and hence it is easier to obtain the information about the dielectric properties of the sample.

A main dielectric property of the samples that is of interest is the conductivity. From the measured secondary magnetic field a 2D or 3D image of the electrical conductivity of the sample can be mapped. This technique is important for imaging the conductivity of the human heart in order to improve the understanding of the causes of atrial fibrillation and to act as a potential new diagnostic tool for the damaged tissue [61]. It is also important in the diagnosis of brain haemorrhages [77, 78] with the use of MIT playing an important role in both applications. The properties and principals of inducing eddy currents and magnetic induction tomography will now be discussed further.

3.2 Skin depth

The skin effect is the tendency for eddy currents to flow and be distributed in an object which results in the current density being largest near the surface. The current density in the object drops off exponentially with depth. The skin depth depends on the frequency of the alternating current where higher frequencies result in the current density being more concentrated at the surface of the object. At a depth of d from the surface of the object, the current density is given by

$$J(d) = J_0 e^{-d/\delta(\omega)}, \tag{3.1}$$

where J_0 is the current density at the surface of the object and $\delta(\omega)$ is the skin depth. The skin depth is the point at which the current density value has dropped to $J_0 e^{-1}$. The skin depth parameter is calculated from

$$\delta(\omega) = \sqrt{\frac{2\rho}{\omega\mu}\left(\sqrt{1 + (\rho\omega\varepsilon)^2} + \rho\omega\varepsilon\right)}, \tag{3.2}$$

where $\omega = 2\pi\nu_{\mathrm{rf}}$ is the angular frequency of the magnetic field, $\mu = \mu_0\mu_r$ is the magnetic permeability, $\varepsilon = \varepsilon_0\varepsilon_r$ is the electric permittivity, and $\rho = 1/\sigma$ is the resistivity of the medium. The skin depth controls the amount an RF magnetic field can penetrate a medium.

The skin depth is a key factor in eddy current detection of conductive/ magnetic objects as it is used to calculate the appropriate operational frequency to set the penetration depth of the primary magnetic field. This plays an important role in the goal of 3D imaging as the penetration depth can be varied by varying the frequency of the primary field resulting in different skin depths.

3.2.1 High conductivities

Highly conductive samples are easily detectable using low frequencies. In the regime where $\sigma >> \omega\varepsilon$ the bracket in Equation 3.2 tends to 1 and the skin depth equation simplifies to

$$\delta(\omega) = \sqrt{\frac{2\rho}{\omega\mu}}. \tag{3.3}$$

This simplified form of the skin depth equation is used throughout the work presented here when detecting metal samples.

3.2.2 Low conductivities

For a poor conductor, like a human heart, high frequencies are needed to detect the objects as will be discussed in Section 3.3. In the case where high frequencies are used such that $\sigma << \omega\varepsilon$ the skin depth is given by

$$\delta(\omega) = \frac{1}{\omega}\left[\frac{\mu\varepsilon}{2}\left(\sqrt{1+\left(\frac{1}{\rho\omega\varepsilon}\right)^2}-1\right)\right]^{-1/2}. \tag{3.4}$$

Asymptotically, as $\omega\varepsilon\rho \to \infty$, the skin depth tends to

$$\delta(\omega) = 2\rho\sqrt{\frac{\varepsilon}{\mu}}. \tag{3.5}$$

3.3 Magnetic induction tomography (MIT)

Magnetic induction tomography is an imaging technique that provides a non-invasive, direct mapping of the electrical and magnetic properties of an object. This includes the conductivity, σ, magnetic permeability, μ, and the electrical permittivity, ε. This method uses an excitation coil to produce a primary oscillating magnetic field, $\mathbf{B_1}(t)$ which induces eddy currents in a conductive sample. This in turn produces a secondary magnetic field, $\mathbf{B}_{\mathrm{ec}}(t)$. The secondary field is produced such that it opposes the primary field. The secondary field can then be detected. This method is carried out without the need for the sensor to be in contact with the sample. The relationship between the two fields and the total field can be seen in Figure 3.1. If the skin depth of $\mathbf{B}_1$ is larger than the object's thickness, the relationship of the two fields is

$$\mathbf{B}_{\mathrm{ec}}(\omega) = \{Q\omega\mu_0[\omega\varepsilon_0(\varepsilon_r-1)-i\sigma]+P(\mu_r-1)\}\mathbf{B}_1(\omega), \tag{3.6}$$

where ω is the oscillation frequency, Q and P are geometric factors [56], ε_r is the relative permittivity and μ_r is the relative permeability. In Equation 3.6 the conductivity σ is the only imaginary term and hence can be isolated from the other parameters. This can be used to map the conductivity of an object. The imaginary term is dependent on the frequency as well as the conductivity so it can be seen that for objects with low conductivities higher frequencies for the excitation coil are desirable to obtain a larger secondary field that can be detected.

Standard magnetic induction tomography uses a driving coil to produce the primary magnetic field, $\mathbf{B_1}(t)$, and then an additional set of coils which detects the overall magnetic field after it has been perturbed by the object. The sensing coils detect both the primary magnetic field and the induced secondary magnetic field $\mathbf{B}_{\mathrm{ec}}(t)$ at their position. However there are limits to this method. At low frequencies the sensitivity is limited and the coils do not have a large enough bandwidth to detect low- or non-conductive objects. The size of the coils also limits the spatial resolution of the imaging and the miniaturisation of the system [61]. These factors have prevented the work of using MIT for medical imaging.

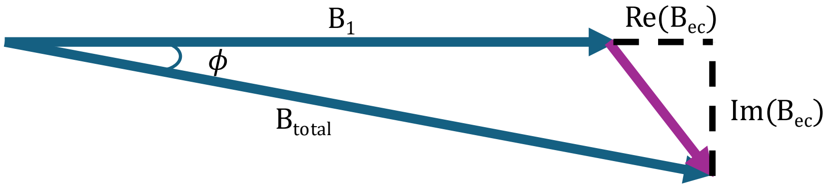

Figure 3.1: Magnetic induction imaging with a primary magnetic field $\mathbf{B_1}(t)$ inducing a secondary magnetic field $\mathbf{B}_{\text{ec}}(t)$ in an object. The total magnetic field can then be measured with the primary and secondary magnetic field having a phase difference of ϕ.

3.3.1 OPM based MIT

Replacing the coils that detect the response field in standard MIT measurements with a highly sensitive OPM could improve the performance of MIT for low conductive objects [37, 25]. The MIT primary field, $\mathbf{B_1}(t)$, can be produced by an array of coils that are placed above the object. Using commercial devices, an AC current supply can be used to drive the excitation coils with a tuneable frequency in the range of $\nu_{\text{rf}} = 1$ MHz - 100 MHz. The induced magnetic field $\mathbf{B}_{\text{ec}}(t)$ can then be detected by radio-frequency OPMs instead of a pick up coil. The development of portable OPM sensors would allow for this technique to be used in applications outside of the lab. The induced magnetic field interacts with the precessing atoms. This causes the probe laser beam's polarisation to be rotated. A balanced photodetector then measures the change in the oscillations of the polarisation and from this the magnetic field can be calculated. The output of the OPM can be selectively amplified by a lock-in amplifier which can extract the signal from a noisy environment. Using the differential technique [30], changes in the induced secondary magnetic field can be measured. The relative phase of the imaginary component of the signal is directly related to the conductivity. From this a map the conductivity of the object can be produced. For larger objects or time sensitive measurements, an array of OPMs could be used [61].

3.4 MIT detection of the heart

3.4.1 Benefits of imaging the heart

Cardiac arrhythmias are characterised by irregular, slow or accelerated beating of the heart. Atrial fibrillation is a common example that affects 10% of the population who are over 70 [79]. The causes are related to the conduction of electrical pulses in the heart. However, the causes are unknown and hence treatment is sub-optimal. It is common in people with other heart conditions and is also associated with other medical conditions such as pneumonia, asthma, diabetes, COPD, and lung cancer [80]. However, it is not always linked to another health condition, as many athletes have also suffered from atrial fibrillations and other cardiac arrhythmias. There are also a number of known triggers such as binge drinking, being overweight, caffeine, drug usage and smoking. Currently there are very limited diagnostic tools. The most common to be used are checking the pulse and ECGs. If an arrhythmia is present then the heart rate will be irregular and can beat at a rate over 100 beats/minute, which can be seen by simply checking the pulse. However, in this case the arrhythmia has to be present at the time of testing which is hard to detect as they can be unpredictable. To try and detect this better most patients are asked to wear an ECG for 24 hours. Even in this case an arrhythmia can be missed [81]. The diagnostic tools are poor as even if they detect unusual behaviour they do not give any information about the cause, or location of what is causing the abnormal heart beat. The cause is thought to be linked to the abnormal generation and conduction of electrical pulses that control the heart [82]. It is thought that OPM-MIT can be used to diagnose and locate the source of the issue by creating a conductivity map of the heart. If the arrhythmia is caused by a conductivity issue this would be detectable and the image would also show the location of the issue. If successful, this could improve the number of arrhythmias detected as well as potentially improving the success rate of operations to correct for these issues.

3.4.2 Dielectric properties of the heart

In order to calculate the desired frequency range that an OPM needs to operate in, the resistivity, ρ, permeability, ε_r and the skin depth, σ of human tissues need to be determined as these are all involved in the resultant signal from imaging the heart. These tissues typically include skin, fat, muscle and bone. The resistivity and relative permeability can be determined theoretically from the complex relative permittivity $\tilde{\varepsilon}$ which is determined from the Cole-Cole equation,

$$\tilde{\varepsilon} = \varepsilon_\infty + \frac{\sigma_i}{i\omega\varepsilon_0} + \sum_n \frac{\Delta\varepsilon_n}{1 + (i\omega\tau_n)^{(1-\alpha_n)}} \tag{3.7}$$

where ε_∞ is the electrical permittivity at high frequencies ($\omega\tau >> 1$), $\Delta\varepsilon_n = \varepsilon_s - \varepsilon_\infty$ with ε_s being the quasi-static permittivity ($\omega\tau << 1$), τ_n is the n-th relaxation time and α_n is a phenomenological parameter describing the broadening of the n-th contribution. From this the dependence of the resistivity ρ and relative permittivity ε_r on frequency can be determined as

$$\rho = -\frac{1}{\omega\varepsilon_0 \mathrm{Im}[\tilde{\varepsilon}(\omega)]}, \tag{3.8}$$

and

$$\varepsilon_r = \mathrm{Re}[\tilde{\varepsilon}(\omega)], \tag{3.9}$$

respectively. Using the values stated in Ref. [83], the dependence of the resistivity ρ and relative permittivity ε_r are calculated for a heart. The results for the resistivity were then scaled to match average values that are determined across multiple experiments with frequencies between 100 Hz to 10 MHz being used. For the relative permittivity there is insufficient literature on the expected value and so the results from Equation 3.9 are assumed to be true. The average data is summarised in Ref. [84] and the theoretical results calculated from Equations 3.8 and 3.9 are shown in Figure 3.2. The results match the predictions in Ref. [61].

The frequency relations predicted in Figure 3.2 can then be substituted into Equation 3.2 to determine how the skin depth varies with the frequency of the primary magnetic field when detecting a heart. Figure 3.3 shows the predicted

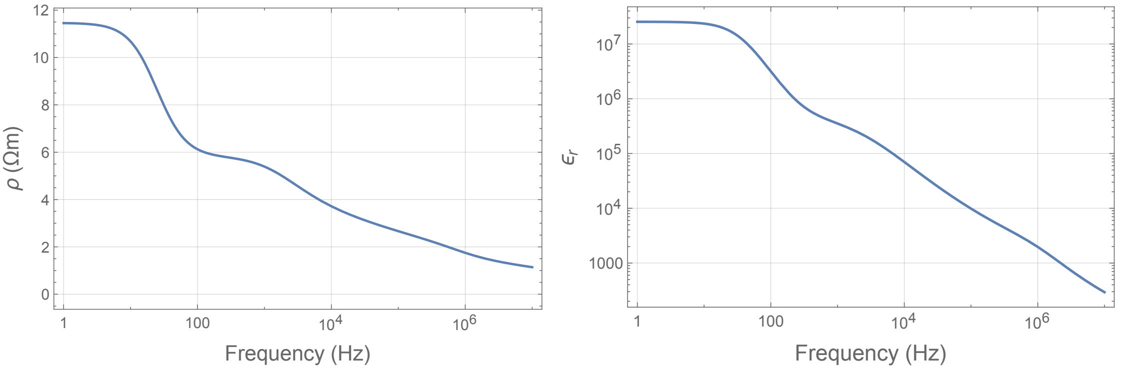

(a) (b)

Figure 3.2: The computed (a) resistivity ρ and the (b) relative permeability ϵ_r of healthy human heart tissue in the frequency range between 1 Hz and 10 MHz.

frequency dependence for frequencies between 1 MHz and 10 MHz. As the frequency increases the skin depth decreases. By varying the frequency of the primary magnetic field, eddy currents can be induced at various depths of the heart. Tuning of the primary magnetic field frequency can hence be used to produce a 3D map of the object of interest i.e. a heart. With the use of an OPM, the tuning of ν_{rf} can be finely controlled over the penetration depth. This makes the technique suitable for locating areas of abnormal conductivity in the heart.

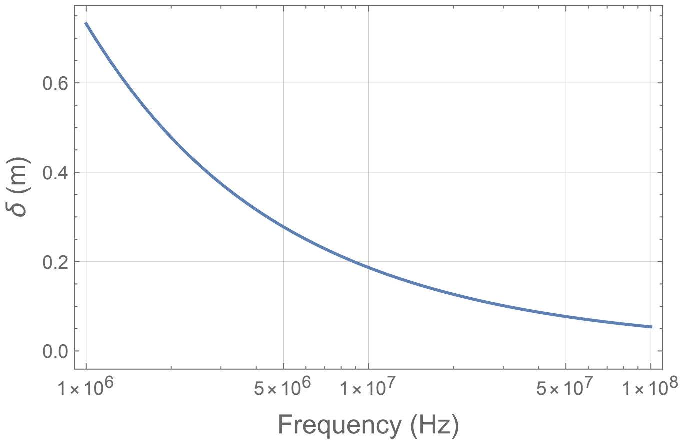

Figure 3.3: Predicted skin depth of the eddy currents induced in heart tissue, using the computed resistivity and relative permittivity, as a function of frequency.

The same calculations can be carried out to determine the predicted values for other tissues that will need to be considered when imaging a heart. Table 3.1 shows the predicted values for these tissues at 3 MHz. From Table 3.1 it can be seen that the resistivity of bones and fat are much higher than the other surrounding tissue. In particular, the significant difference in the heart's values means that the other tissue has an almost negligible contribution to the signal observed. This supports the feasibility of using OPM-MIT for mapping the conductivity of the heart.

The final consideration is how the magnetic field is attenuated as it propagates through a body to the heart. A primary magnetic field, $\mathbf{B_1}(t)$, that is penetrating

	ρ (Ωm)	ε_r	h (mm)
Skin	15.84	745.67	1.8
Fat	38.54	20.92	4.8
Muscle	1.76	522.35	7.2
Bone	12.22	83.25	12
Heart	2.43	759.81	

Table 3.1: Calculated values for the resistivity ρ and relative permittivity ε_r, as well as the expected thickness h of human tissues that surround the heart at a frequency of 3 MHz.

inside a patient's chest, will have an attenuation along the $\hat{\mathbf{z}}$ direction given by

$$\Delta(\omega) = \frac{|\mathbf{B_1}(z)|}{|\mathbf{B_1}(0)|} = \sum_{i=layer} e^{-(z_i^b - z_i^t)/\delta_i(\omega)}, \tag{3.10}$$

where the sum is over the different layers of tissue that the primary field encounters as it travels to the heart is calculated. Each of these layers is located between a top position, z_i^t, and a bottom position, z_i^b, such that $z_i^b - z_i^t = h_i$ where h_i is given in Table 3.1. A prediction of how the attenuation varies with distance, at different frequencies, is shown in Figure 3.4. These results demonstrate how feasible the MIT measurements of the human heart are. As the frequency is increased the attenuation of the primary field becomes larger. It can be seen that $\mathbf{B_1}(t)$ is reduced by $\sim$ 20% by the time it reaches the surface of the heart when using the highest frequency of 100 MHz. This can potentially induce additional eddy currents in other biological materials. Despite this, a sufficiently large primary magnetic field is still present at the heart leading to the effective excitation of eddy currents. As there is only a little change in the attenuation of the primary magnetic field, bones and fat appear almost completely transparent so the OPM based MIT is insensitive to these screening effects. At all frequencies presented, air does not alter the attenuation of the primary magnetic field as it acts as a transparent medium in the MHz band. The largest attenuation is in the heart itself, meaning that the device is highly sensitive to the heart's response to the primary magnetic field. This allows for control over the skin depth by altering the frequency of the field, ν_{rf}. The secondary field will undergo a comparable attenuation as the signal travels to the sensor position due to it oscillating at the same frequency as the primary field. As a relative measurement of the conductivity is desired, the possible diffraction effects at the boundaries of materials do not cause an issue. Hence systematic effects due to the patient's anatomy should not impact the experiment [61], supporting the feasibility of using OPM-MIT for imaging the heart.

3.4.3 Simulation

A simulation of an experimental setup in which a salt water sample is detected was designed using the AC/DC module in COMSOL multiphysics. The simulation conditions are the same as that shown in Appendix C.1, with full details about the model shown in Appendix C.2. A rectangular object with a conductivity of 0.5 S/m, which is comparable to that theoretically determined for a heart, with a

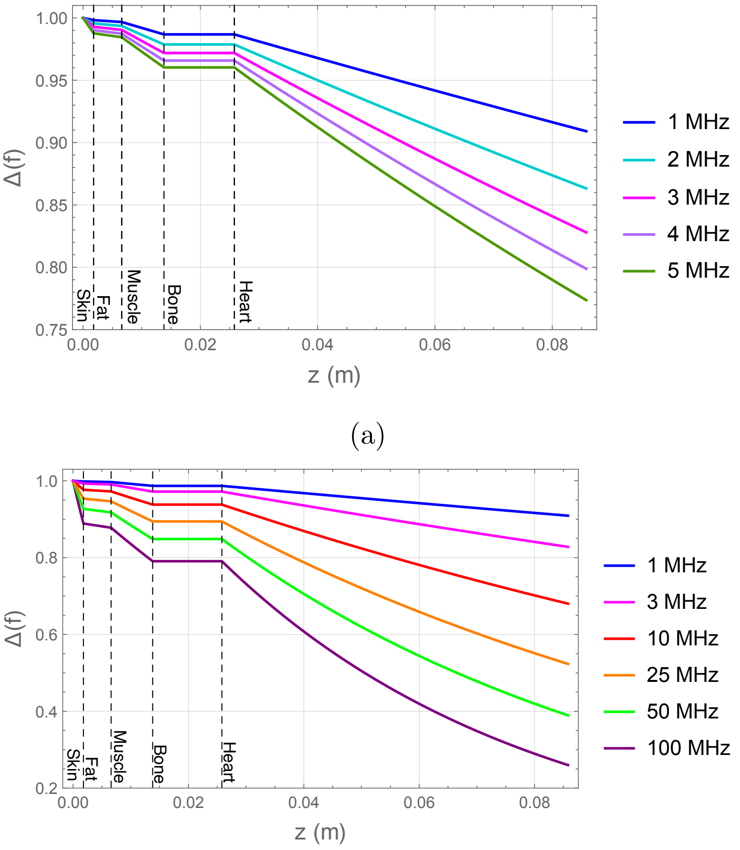

(a)

(b)

Figure 3.4: Relative attenuation of the primary magnetic field as it propagates through the human body near the heart at (a) 1 MHz to 5 MHz and (b) 1 MHz to 100 MHz as s function of distance.

6 cm × 4 cm size and a 1 cm thickness is modelled. The relative permittivity was set to 1. The excitation coil and OPM were aligned along the z-axis. The coil has a radius of 5 mm and is placed 3 cm from the centre of the object. The sensing point, i.e. the position of the OPM sensing point, is 5 cm from the centre of the object on the opposite side to the coil, as shown in Figure 3.5a. A defect is placed in the centre of the object with a 5 mm radius and a conductivity of 0 S/m. The object is moved from −5 cm to 5 cm along the x-axis and between −4 cm and 4 cm along the y-axis, with respect to the centre of the object. The position of the coil and sensing point remains constant. An oscillating primary magnetic field with a frequency of 3 MHz is applied to the coil with a dipole moment of 0.00157 Am^2. The results of the induced secondary magnetic field are shown in Figure 3.5b. It can be seen that the largest signal is induced at the centre of the object despite the defect that was placed there. This is due to the coil radius being the same size as the defect. Signals will also be induced due to the edges where the properties change. A smaller coil would be required for experiments. The dipole moment of the coil matches what could be realistically achieved with a smaller coil of radius 1.5 mm. The secondary magnetic field strength is at least 5 pT where the low conductive object is, and so for a signal to noise ratio of at least 2 a minimal detectable field of at least 2.5 pT is required.

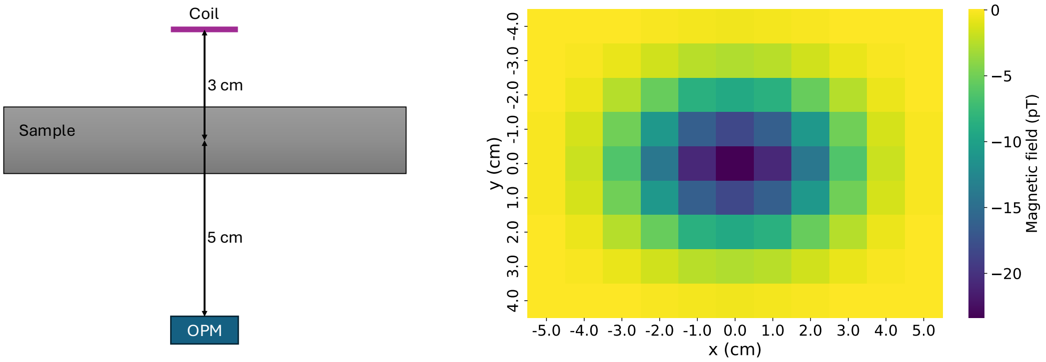

(a) (b)

Figure 3.5: (a) Simulation setup for the imaging of a low conductive object. (b) Simulation results of the induced magnetic field heat map of a rectangular sample of dimensions 6 cm×4 cm and a 1 cm thickness. The sample has a 0.5 S/m conductivity. A 1 cm diameter defect is placed at the centre of the object with a conductivity of 0 S/m. The sample's position is varied whilst the excitation coil and magnetic field sensor are kept at a constant position.

3.5 Conclusion

In this chapter, the basic principals behind eddy current testing and how it can be used for detection, characterisation and imaging are presented. There is a focus on how eddy current testing can be used to image biological tissue such as the heart, with findings agreeing with those in the literature [61]. Using a COMSOL simulation predicted values of the induced magnetic field size, using realistic experimental parameters, is obtained. As arythmias are caused by local variations in the heart's conductivity, the simulation shows how feasible OPM-MIT is with the sensor described in Section 10. This gives a base goal for the sensitivities required, in magnetic field sensors, to reconstruct a 2D image of a sample with low conductivities, such as heart tissue. The resolution of the detected signal here is set by the size of the excitation coil. This could be improved by using a smaller excitation coil and further data analysis techniques [69].

Chapter 4

Alignment based magnetometry theory

4.1 Motivation

Throughout this thesis, alignment based magnetometers are used for a variety of experiments that look at the characterisation, miniaturisation and potential applications. They use a single laser beam that 'pumps' and 'probes' the atomic ensembles. The theory presented in this chapter is a combination and revision of theories presented in Refs. [85, 16, 64, 4, 5].

4.2 Hamiltonian of the system

In order to determine the Hamiltonian for the system a simplified model will be used. Atoms with a $F = 1 \rightarrow F' = 0$ optical transition are considered. Here the ground state sublevels are defined as $|F, m\rangle = \{|1, 1\rangle, |1, 0\rangle, |1, -1\rangle\}$ and an excited sublevel of $|F', m'\rangle = |0, 0\rangle$. A static magnetic field is applied in the z-direction and the polarisation of the laser light is assumed to be along the same direction. The laser light is linearly polarised (π-polarised) leading to the atoms being pumped into $m = \pm 1$ with an equal probability of being pumped into either sublevel. This creates an aligned state as the spins are aligned along a preferred axis but do not have a preferred direction. With the optical pumping this creates a dark state which, assuming all atoms are pumped into the $m = \pm 1$ sublevels, leads to all of the laser light being transmitted through the vapour cell. An additional magnetic field is applied to the system along the y-direction. This is an oscillating magnetic field that has to be applied perpendicular to the static field. This field is detectable and affects the light that is transmitted from the cell as it affects the atomic polarisation, creating an oscillating component of the polarisation. In this thesis, this field is detected by measuring the absorption or polarisation rotation of the transmitted light.

The total Hamiltonian that describes this system is given by

$$H = H_0 + H_l + H_B, \tag{4.1}$$

where H_0 is the unperturbed Hamiltonian, H_l is the light-atom Hamiltonian and H_B is the magnetic-field-atom-interaction Hamiltonian. Assuming that the energy of the lower state is zero, the unperturbed Hamiltonian is defined as

$$H_0 = \begin{pmatrix} 0 & 0 & 0 & 0 \\ 0 & 0 & 0 & 0 \\ 0 & 0 & 0 & 0 \\ 0 & 0 & 0 & \hbar\omega_0 \end{pmatrix}, \tag{4.2}$$

where $\omega_0 = 2\pi c/\lambda$ is the transition frequency, c is the speed of light and λ is the wavelength.

The optical electric field for light that is polarised in the z-direction can be written as

$$\mathbf{E} = E_0 \cos(\omega t)\hat{\mathbf{z}}, \tag{4.3}$$

where E_0 is the electric field amplitude and ω is the frequency of the light. The light-atom interaction Hamiltonian H_l is

$$\begin{aligned} H_l &= -\mathbf{E} \cdot \mathbf{d} && (4.4) \\ &= -E_0 \cos(\omega t) d_z, && (4.5) \end{aligned}$$

where $\mathbf{d} = d_x\hat{\mathbf{x}} + d_y\hat{\mathbf{y}} + d_z\hat{\mathbf{z}}$ is the dipole operator. The derivation of d_z and H_l in detail can be seen in Section 2.3 where the light-atom interaction Hamiltonian is found to be

$$\begin{aligned} H_l &= E_0 \cos(\omega t) \begin{pmatrix} 0 & 0 & 0 & 0 \\ 0 & 0 & 0 & -1 \\ 0 & 0 & 0 & 0 \\ 0 & -1 & 0 & 0 \end{pmatrix} \frac{\langle 1 \| d \| 0' \rangle}{\sqrt{3}} && (4.6) \\ &= \hbar\Omega_R \cos(\omega t) \begin{pmatrix} 0 & 0 & 0 & 0 \\ 0 & 0 & 0 & -1 \\ 0 & 0 & 0 & 0 \\ 0 & -1 & 0 & 0 \end{pmatrix}, && (4.7) \end{aligned}$$

where $\mathbf{\Omega}_R = (\langle 1 \| d \| 0' \rangle E_0)/(\hbar\sqrt{3})$ is the Rabi frequency.

Finally, the magnetic-field-atom-interaction Hamiltonian H_B needs to be derived for the setup described here. As stated previously, there are two applied magnetic fields in the setup: a static magnetic field $\mathbf{B_0}$ applied along the z-direction and an oscillating magnetic field $\mathbf{B}_{\mathrm{rf}}(t)$ applied along the y-direction. It will be assumed that there are no magnetic fields along the x-direction. The total magnetic field is $\mathbf{B} = B_{\mathrm{rf}} \cos(\omega_{\mathrm{rf}} t)\hat{\mathbf{y}} + B_0\hat{\mathbf{z}}$. Hence, the magnetic-field-atom-interaction Hamiltonian is given by

$$H_B = -\boldsymbol{\mu} \cdot \mathbf{B}, \tag{4.8}$$

where $\boldsymbol{\mu} = g_F \mu_B (F_x\hat{\mathbf{x}} + F_y\hat{\mathbf{y}} + F_z\hat{\mathbf{z}})/\hbar$ is the atom's magnetic dipole operator with g_F being the hyperfine Landé g-factor [68] and μ_B the Bohr magneton. Substituting this into Equation 4.8 the Hamiltonian can be written as

$$H_B = \frac{g_F \mu_B}{\hbar}(F_y B_y + F_z B_z) = \frac{g_F \mu_B}{\hbar}(F_y B_{\mathrm{rf}} \cos(\omega_{\mathrm{rf}} t) + F_z B_0). \tag{4.9}$$

In the model setup being described here, only one of the magnetic fields is along the quantisation axis. The oscillating magnetic field is orthogonal to the quantisation axis meaning that radio frequency coherences are expected between the sublevels in the ground state. These are expected to occur between $|1,1\rangle$ and $|1,0\rangle$ as well as between $|1,0\rangle$ and $|1,-1\rangle$. As a result, the various components of the total angular momentum vector need to be determined. The F_y component can be calculated using raising and lowering operators using

$$F_y = \frac{-i(F_+ - F_-)}{2}, \tag{4.10}$$

where F_+ is the raising operator and F_- is the lowering operator. These operators are defined as follows:

$$F_+ |F,m\rangle = \hbar\sqrt{F(F+1) - m(m+1)}\, |F, m+1\rangle\,, \tag{4.11}$$

and

$$F_- |F,m\rangle = \hbar\sqrt{F(F+1) - m(m-1)}\, |F, m-1\rangle\,. \tag{4.12}$$

By substituting these operators into Equation 4.10 the F_y component can be calculated from

$$\begin{aligned} F_y |F,m\rangle &= \frac{F_+ |F,m\rangle - F_- |F,m\rangle}{2i} \\ &= \frac{\hbar}{2i}\Big(\sqrt{F(F+1) - m(m+1)}\, |F,m+1\rangle \\ &- \sqrt{F(F+1) - m(m-1)}\, |F,m-1\rangle\Big)\,, \end{aligned} \tag{4.13}$$

which in matrix form is given by

$$F_y = \frac{\hbar}{i\sqrt{2}} \begin{pmatrix} 0 & 1 & 0 & 0 \\ -1 & 0 & 1 & 0 \\ 0 & -1 & 0 & 0 \\ 0 & 0 & 0 & 0 \end{pmatrix}. \tag{4.14}$$

The F_z component is determined from

$$F_z |F,m\rangle = \hbar m\, |F,m\rangle\,, \tag{4.15}$$

which, as a matrix, is defined as

$$F_z = \hbar \begin{pmatrix} 1 & 0 & 0 & 0 \\ 0 & 0 & 0 & 0 \\ 0 & 0 & -1 & 0 \\ 0 & 0 & 0 & 0 \end{pmatrix}. \tag{4.16}$$

Hence substituting the matrices for the total angular momentum into Equation 4.8 gives the magnetic-field-atom-interaction Hamiltonian as

$$H_B = \frac{g_F \mu_B}{\hbar} \left[\frac{\hbar}{i\sqrt{2}} \begin{pmatrix} 0 & 1 & 0 & 0 \\ -1 & 0 & 1 & 0 \\ 0 & -1 & 0 & 0 \\ 0 & 0 & 0 & 0 \end{pmatrix} B_{\text{rf}} \cos(\omega_{\text{rf}} t) + \hbar \begin{pmatrix} 1 & 0 & 0 & 0 \\ 0 & 0 & 0 & 0 \\ 0 & 0 & -1 & 0 \\ 0 & 0 & 0 & 0 \end{pmatrix} B_0 \right] \tag{4.17}$$

$$= g_F \mu_B \begin{pmatrix} B_0 & \frac{B_{\text{rf}} \cos(\omega_{\text{rf}} t)}{i\sqrt{2}} & 0 & 0 \\ -\frac{B_{\text{rf}} \cos(\omega_{\text{rf}} t)}{i\sqrt{2}} & 0 & \frac{B_{\text{rf}} \cos(\omega_{\text{rf}} t)}{i\sqrt{2}} & 0 \\ 0 & -\frac{B_{\text{rf}} \cos(\omega_{\text{rf}} t)}{i\sqrt{2}} & -B_0 & 0 \\ 0 & 0 & 0 & 0 \end{pmatrix}, \tag{4.18}$$

which, by defining the strength of the RF magnetic field as $\Omega_{\text{rf}} = g_F \mu_B B_{\text{rf}}/\hbar$, can be rewritten as

$$H_B = \hbar \begin{pmatrix} \omega_L & \frac{\Omega_{\text{rf}} \cos(\omega_{\text{rf}} t)}{i\sqrt{2}} & 0 & 0 \\ -\frac{\Omega_{\text{rf}} \cos(\omega_{\text{rf}} t)}{i\sqrt{2}} & 0 & \frac{\Omega_{\text{rf}} \cos(\omega_{\text{rf}} t)}{i\sqrt{2}} & 0 \\ 0 & -\frac{\Omega_{\text{rf}} \cos(\omega_{\text{rf}} t)}{i\sqrt{2}} & -B_0 & 0 \\ 0 & 0 & 0 & 0 \end{pmatrix}. \tag{4.19}$$

Hence, the total Hamiltonian $H = H_0 + H_l + H_B$ is

$$H = \hbar \begin{pmatrix} \omega_L & \frac{\Omega_{\text{rf}} \cos(\omega_{\text{rf}} t)}{i\sqrt{2}} & 0 & 0 \\ -\frac{\Omega_{\text{rf}} \cos(\omega_{\text{rf}} t)}{i\sqrt{2}} & 0 & \frac{\Omega_{\text{rf}} \cos(\omega_{\text{rf}} t)}{i\sqrt{2}} & -\Omega_R \cos(\omega t) \\ 0 & -\frac{\Omega_{\text{rf}} \cos(\omega_{\text{rf}} t)}{i\sqrt{2}} & -\omega_L & 0 \\ 0 & -\Omega_R \cos(\omega t) & 0 & \omega_0 \end{pmatrix}. \tag{4.20}$$

4.3 The rotating-wave approximation

The Hamiltonian for the system has time dependencies at the optical frequency ω and the RF frequency ω_{rf}. These oscillations are a vital part of the setup, however it is preferable for the time dependants to be removed from direct consideration in the theory. This can be done by using the rotating wave approximation [16]. The approximation is valid when the optical frequency ω is close to the atomic transition frequency ω_0. In an alignment based magnetometer, the laser light is on resonance with the atomic transition and hence the optical frequency is tuned to the atomic transition frequency such that $\omega \approx \omega_0$. Hence for the system described here the rotating wave approximation is valid. The total Hamiltonian that is derived above is in the lab frame. This Hamiltonian can be transformed into a rotating frame. Initially, the Hamiltonian will be transformed to a rotating frame at the optical frequency ω around the z-axis. This transformation is carried out using a transformation matrix [16]

$$U = \begin{pmatrix} 1 & 0 & 0 & 0 \\ 0 & 1 & 0 & 0 \\ 0 & 0 & 1 & 0 \\ 0 & 0 & 0 & \mathrm{e}^{i\omega t} \end{pmatrix}, \tag{4.21}$$

which is unitary, i.e. $U^\dagger U = U U^\dagger = \mathbb{1}$. Typically, under a change of basis an operator O transforms as $O' = U^\dagger O U$. However, as the rotating frame that the Hamiltonian is being transformed to is not inertial, the transformation equation needs to be modified and an effective Hamiltonian can be calculated. The modified effective Hamiltonian is calculated from

$$H'_{\text{eff}} = U^\dagger H U - i\hbar U^\dagger \frac{\partial U}{\partial t}. \tag{4.22}$$

Substituting in the total Hamiltonian presented in Equation 4.20, the first and second term are found to be

$$U^{\dagger}HU = \hbar \begin{pmatrix} \omega_L & \frac{\Omega_{\mathrm{rf}}\cos(\omega_{\mathrm{rf}}t)}{i\sqrt{2}} & 0 & 0 \\ -\frac{\Omega_{\mathrm{rf}}\cos(\omega_{\mathrm{rf}}t)}{i\sqrt{2}} & 0 & \frac{\Omega_{\mathrm{rf}}\cos(\omega_{\mathrm{rf}}t)}{i\sqrt{2}} & -\Omega_R\cos(\omega t)\mathrm{e}^{i\omega t} \\ 0 & -\frac{\Omega_{\mathrm{rf}}\cos(\omega_{\mathrm{rf}}t)}{i\sqrt{2}} & -\omega_L & 0 \\ 0 & -\Omega_R\cos(\omega t)\mathrm{e}^{-i\omega t} & 0 & \omega_0 \end{pmatrix}, \tag{4.23}$$

and

$$i\hbar U^{\dagger}\frac{\partial U}{\partial t} = \hbar \begin{pmatrix} 0 & 0 & 0 & 0 \\ 0 & 0 & 0 & 0 \\ 0 & 0 & 0 & 0 \\ 0 & 0 & 0 & \omega \end{pmatrix}, \tag{4.24}$$

respectively. The effective Hamiltonian H' in the rotating frame is given by

$$H'_{\mathrm{eff}} = \hbar \begin{pmatrix} \omega_L & \frac{\Omega_{\mathrm{rf}}\cos(\omega_{\mathrm{rf}}t)}{i\sqrt{2}} & 0 & 0 \\ -\frac{\Omega_{\mathrm{rf}}\cos(\omega_{\mathrm{rf}}t)}{i\sqrt{2}} & 0 & \frac{\Omega_{\mathrm{rf}}\cos(\omega_{\mathrm{rf}}t)}{i\sqrt{2}} & -\frac{\Omega_R(1+\mathrm{e}^{2i\omega t})}{2} \\ 0 & -\frac{\Omega_{\mathrm{rf}}\cos(\omega_{\mathrm{rf}}t)}{i\sqrt{2}} & -\omega_L & 0 \\ 0 & -\frac{\Omega_R(1+\mathrm{e}^{-2i\omega t})}{2} & 0 & \omega_0-\omega \end{pmatrix}, \tag{4.25}$$

where the substitution $\cos(\omega t) = (\mathrm{e}^{i\omega t} + \mathrm{e}^{-i\omega t})/2$ has been used. The optical frequency ω is tuned to the transition frequency ω_0 and so the detuned, fast oscillating, terms that contain 2ω can be dropped. The use of the rotating frame approximation here results in the effective Hamiltonian being

$$H'_{\mathrm{eff}} = \hbar \begin{pmatrix} \omega_L & \frac{\Omega_{\mathrm{rf}}\cos(\omega_{\mathrm{rf}}t)}{i\sqrt{2}} & 0 & 0 \\ -\frac{\Omega_{\mathrm{rf}}\cos(\omega_{\mathrm{rf}}t)}{i\sqrt{2}} & 0 & \frac{\Omega_{\mathrm{rf}}\cos(\omega_{\mathrm{rf}}t)}{i\sqrt{2}} & -\frac{\Omega_R}{2} \\ 0 & -\frac{\Omega_{\mathrm{rf}}\cos(\omega_{\mathrm{rf}}t)}{i\sqrt{2}} & -\omega_L & 0 \\ 0 & -\frac{\Omega_R}{2} & 0 & \omega_0-\omega \end{pmatrix}. \tag{4.26}$$

In this frame there are still time dependencies coming from the RF magnetic field so a second transformation needs to be carried out on the Hamiltonian. In the second transformation, the transformation matrix is given by

$$U_{\mathrm{rf}} = \begin{pmatrix} \mathrm{e}^{-i\omega_{\mathrm{rf}}t} & 0 & 0 & 0 \\ 0 & 1 & 0 & 0 \\ 0 & 0 & \mathrm{e}^{i\omega_{\mathrm{rf}}t} & 0 \\ 0 & 0 & 0 & 1 \end{pmatrix}. \tag{4.27}$$

The effective Hamiltonian in the RF rotating frame is calculated using

$$\tilde{H}_{\mathrm{eff}} = U_{\mathrm{rf}}^{\dagger}H'U_{\mathrm{rf}} - i\hbar U_{\mathrm{rf}}^{\dagger}\frac{\partial U_{\mathrm{rf}}}{\partial t}. \tag{4.28}$$

In this case the effective Hamiltonian (Equation 4.26) in the rotating frame is used. The first and second terms for this transformation are given by

$$U_{\mathrm{rf}}^{\dagger} H' U_{\mathrm{rf}} = \hbar \begin{pmatrix} \omega_L & \frac{\mathrm{e}^{i\omega_{\mathrm{rf}} t}\Omega_{\mathrm{rf}} \cos{(\omega_{\mathrm{rf}} t)}}{i\sqrt{2}} & 0 & 0 \\ -\frac{\Omega_{\mathrm{rf}} \cos{(\omega_{\mathrm{rf}} t)} \mathrm{e}^{-i\omega_{\mathrm{rf}} t}}{i\sqrt{2}} & 0 & \frac{\mathrm{e}^{i\omega_{\mathrm{rf}} t}\Omega_{\mathrm{rf}} \cos{(\omega_{\mathrm{rf}} t)}}{i\sqrt{2}} & -\frac{\Omega_R}{2} \\ 0 & -\frac{\Omega_{\mathrm{rf}} \cos{(\omega_{\mathrm{rf}} t)} \mathrm{e}^{-i\omega_{\mathrm{rf}} t}}{i\sqrt{2}} & -\omega_L & 0 \\ 0 & -\frac{\Omega_R}{2} & 0 & \omega_0 - \omega \end{pmatrix}, \tag{4.29}$$

and

$$i\hbar U_{\mathrm{rf}}^{\dagger} \frac{\partial U_{\mathrm{rf}}}{\partial t} = \hbar \begin{pmatrix} \omega_{\mathrm{rf}} & 0 & 0 & 0 \\ 0 & 0 & 0 & 0 \\ 0 & 0 & -\omega_{\mathrm{rf}} & 0 \\ 0 & 0 & 0 & 0 \end{pmatrix}, \tag{4.30}$$

respectively. Hence the effective Hamiltonian takes the form,

$$\tilde{H}_{\mathrm{eff}} = \hbar \begin{pmatrix} \omega_L - \omega_{\mathrm{rf}} & \frac{\mathrm{e}^{i\omega_{\mathrm{rf}} t}\Omega_{\mathrm{rf}} \cos{(\omega_{\mathrm{rf}} t)}}{i\sqrt{2}} & 0 & 0 \\ -\frac{\Omega_{\mathrm{rf}} \cos{(\omega_{\mathrm{rf}} t)} \mathrm{e}^{-i\omega_{\mathrm{rf}} t}}{i\sqrt{2}} & 0 & \frac{\mathrm{e}^{i\omega_{\mathrm{rf}} t}\Omega_{\mathrm{rf}} \cos{(\omega_{\mathrm{rf}} t)}}{i\sqrt{2}} & -\frac{\Omega_R}{2} \\ 0 & -\frac{\Omega_{\mathrm{rf}} \cos{(\omega_{\mathrm{rf}} t)} \mathrm{e}^{-i\omega_{\mathrm{rf}} t}}{i\sqrt{2}} & -\omega_L + \omega_{\mathrm{rf}} & 0 \\ 0 & -\frac{\Omega_R}{2} & 0 & \omega_0 - \omega \end{pmatrix}. \tag{4.31}$$

Using the same technique as was done for the effective Hamiltonian and neglecting the fast oscillating terms at $2\omega_{\mathrm{rf}}$, the Hamiltonian in the (RF) rotating frame is found to be

$$\tilde{H}_{\mathrm{eff}} = \hbar \begin{pmatrix} \omega_L - \omega_{\mathrm{rf}} & \frac{\Omega_{\mathrm{rf}}}{i2\sqrt{2}} & 0 & 0 \\ -\frac{\Omega_{\mathrm{rf}}}{i2\sqrt{2}} & 0 & \frac{\Omega_{\mathrm{rf}}}{i2\sqrt{2}} & -\frac{\Omega_R}{2} \\ 0 & -\frac{\Omega_{\mathrm{rf}}}{i2\sqrt{2}} & -\omega_L + \omega_{\mathrm{rf}} & 0 \\ 0 & -\frac{\Omega_R}{2} & 0 & \omega_0 - \omega \end{pmatrix}. \tag{4.32}$$

The Hamiltonian describing the system is now independent of time as desired.

4.4 Relaxation and repopulation of the state

How the atoms decay from the excited states to the ground states is not included in the derived Hamiltonian, but these dynamics need to be taken into account when studying the dynamics of the system. Each sublevel undergoes relaxation due to atoms exiting from the light beam at a rate γ. Atoms in the excited state also undergo spontaneous decay at a rate Γ. Hence, the relaxation matrix is given by

$$\bar{\Gamma} = \begin{pmatrix} \gamma & 0 & 0 & 0 \\ 0 & \gamma & 0 & 0 \\ 0 & 0 & \gamma & 0 \\ 0 & 0 & 0 & \gamma + \Gamma \end{pmatrix}. \tag{4.33}$$

The relaxation matrix is the same in the rotating and lab frame. In order to conserve the number of atoms in the system, a repopulation of states must also be considered. The first term that contributes to the repopulation of the states is the fact that as atoms leave the laser beam, it is assumed that other atoms that are in the ground state enter the beam. The atoms in the ground state are unpolarised so, as the atom density is normalised to unity, the three ground state sublevels are repopulated at a rate $\gamma/3$. The second term that repopulates the states results from the spontaneous decay of atoms in the excited state. In the simplified model here the atoms can decay to any of the three ground states with an equal probability so the repopulation rate from the spontaneous decay is $\Gamma\rho_{0'0'}/3$ where $\rho_{0'0'}$ is the density matrix element corresponding to the population of the excited state. For systems with multiple excited sublevels, rapid collisional mixing and the allowed ground sublevels that the atoms can decay to need to be considered (see Section 2.6). For the system with a single excited state the repopulation matrix is hence given by

$$\Lambda = (\gamma + \Gamma\rho_{0'0'})\begin{pmatrix} \frac{1}{3} & 0 & 0 & 0 \\ 0 & \frac{1}{3} & 0 & 0 \\ 0 & 0 & \frac{1}{3} & 0 \\ 0 & 0 & 0 & 0 \end{pmatrix}. \tag{4.34}$$

4.5 Liouville equation for a density matrix

In order to study the dynamics of the atomic state a density matrix $\tilde{\rho}$ is constructed in the rotating frame

$$\tilde{\rho} = \begin{pmatrix} \tilde{\rho}_{1,1} & \tilde{\rho}_{1,0} & \tilde{\rho}_{1,-1} & \tilde{\rho}_{1,0'} \\ \tilde{\rho}_{0,1} & \tilde{\rho}_{0,0} & \tilde{\rho}_{0,-1} & \tilde{\rho}_{0,0'} \\ \tilde{\rho}_{-1,1} & \tilde{\rho}_{-1,0} & \tilde{\rho}_{-1,-1} & \tilde{\rho}_{-1,0'} \\ \tilde{\rho}_{0',1} & \tilde{\rho}_{0',0} & \tilde{\rho}_{0',-1} & \tilde{\rho}_{0',0'} \end{pmatrix}. \tag{4.35}$$

The diagonal elements of the density matrix represent the populations of the different sublevels and the off diagonal elements represent the coherences between the different sublevels. The density matrix in the lab frame can be found by the transformation $\rho = U\tilde{\rho}U^{\dagger}$. In the rotating frame, the density matrix elements can be found by solving the Liouville equation

$$i\hbar\frac{\partial\tilde{\rho}}{\partial t} = \left[\tilde{H}, \tilde{\rho}\right] - \frac{i\hbar}{2}\left(\bar{\Gamma}\tilde{\rho} + \tilde{\rho}\bar{\Gamma}\right) + i\hbar\Lambda. \tag{4.36}$$

Substituting in the derived effective Hamiltonian, relaxation matrix and repopulation matrix results in 16 differential equations that need to be solved. The solutions to these equations determines the 16 matrix elements of the density matrix which describe the atomic state.

4.6 Description of the atomic state as a spherical tensor

An atom that has a hyperfine quantum number F can be described by a density matrix of size $(2F+1) \times (2F+1)$. The density matrix can be written in terms of the eigenbasis of the angular momentum operators $\hat{F}^2$ and $\hat{F}_z$ [39]

$$\rho = \sum_{M,M'=-F}^{F} \rho^{(F)}_{MM'} \left|F, M\right\rangle\!\left\langle F, M'\right| . \tag{4.37}$$

An alternative and more convenient approach is to decompose the density matrix into the basis of spherical tensor operators of rank $\kappa = 0, 1, ..., 2F$ due to their properties under rotations. Each operator transforms independently in each κ subspace under rotations. Equation 4.37 can be rewritten in the general form as

$$\rho = \sum_{\kappa=0}^{2F} \sum_{q=-\kappa}^{\kappa} m_{\kappa q} \hat{\mathcal{T}}_q^{(\kappa)}, \tag{4.38}$$

where $m_{\kappa q}$ are multipole components with rank $\kappa = 0, 1, ..., 2F$, $q = -\kappa, ..., \kappa$ and $\hat{\mathcal{T}}_q^{(\kappa)}$ are spherical tensor operators [85, 16, 18]. Each multipole represents an item in the density matrix so in total there are $(2F+1)^2$ multipoles. Given that a system has a fixed F a basis forms from $\hat{\mathcal{T}}_q^{(\kappa)}$ that satisfies the condition $\mathrm{Tr}\{\hat{\mathcal{T}}_q^{(\kappa)}(\hat{\mathcal{T}}_{q'}^{(\kappa')})^{\dagger}\} = \delta_{\kappa\kappa'}\delta_{qq'}$. In order to ensure that the density matrix given by Equation 4.38 is Hermitian, it is convenient to impose $\hat{\mathcal{T}}_q^{(\kappa)\dagger} = (-1)^q \hat{\mathcal{T}}_{-q}^{(\kappa)}$, leading to the conditions $m_{\kappa,q} = (-1)^q m^*_{\kappa,-q}$ and $\mathrm{Im}\{m_{\kappa,0}\} = 0$. Using the condition that $\mathrm{Tr}(\rho) = 1$ the coefficient $m_{0,0}$ can be determined as $m_{0,0} = \frac{1}{\sqrt{2F+1}}$ and the corresponding tensor operator for a rank $\kappa = 0$ is given by $\hat{\mathcal{T}}_0^{(0)} = \frac{1}{\sqrt{2F+1}}\mathbb{1}_{2F+1}$. $\hat{\mathcal{T}}_0^{(0)}$ is the only operator with a non-zero trace and is invariant under any rotation.

As is the case with the caesium D1-line used in this thesis, the atomic steady state may include various F levels. For the D1-line of caesium there are two values with $F = 3, 4$. If the laser light is tuned on resonance to a single F level and there are no coherent couplings between the different F levels, the coherences can be disregarded and the atomic state can be generally defined as

$$\rho = \bigoplus_{F} p_F \rho^{(F)}, \tag{4.39}$$

where p_F is the effective fraction of atoms having the total angular momentum F. The focus can then be on a single $\rho^{(F)}$ for the F level that is contributing to the light-atom interaction. For simplicity, the F superscript will be dropped.

How the spin is orientated is defined by the multipoles with rank $\kappa = 1$,

$$\mathbf{m}_1 = (m_{1,-1}, m_{1,0}, m_{1,1})^T, \tag{4.40}$$

where 'T' represents the transpose. How the spin of the atoms is aligned along some axis is defined by the multipoles with rank $\kappa = 2$,

$$\mathbf{m}_2 = (m_{2,-2}, m_{2,-1}, m_{2,0}, m_{2,1}, m_{2,2})^T. \tag{4.41}$$

As the density matrix is described using the multipoles, atoms that are optically pumped using circularly polarised light (creating an orientation state) are described by $\mathbf{m}_1$. For linearly polarised light used for optical pumping, only the even rank κ components are altered by the light [86]. With the pump in the system being relatively strong, the atomic state which is described by Equation 4.38, reads as

$$\rho = \frac{1}{\sqrt{2F+1}}\mathbb{1}_{2F+1} + \sum_{q=-2}^{2} m_{2,q}\hat{\mathcal{T}}_q^{(2)} + \sum_{q=-4}^{4} m_{4,q}\hat{\mathcal{T}}_q^{(4)} + \cdots . \tag{4.42}$$

However, as only the orientation ($\kappa = 1$) and alignment ($\kappa = 2$) components can be probed, by resorting to electric dipole light-atom interactions [39, 86], any signal obtained by probing the atoms with light is determined by $\mathbf{m} = \mathbf{m}_2$ whose dynamics can be tracked.

If the quantisation axis is chosen to be along the z-direction and the light polarisation along the quantisation axis, then by symmetry, the atomic steady state must be invariant to any rotations around z (see Figure 4.1a). Only the coefficient with $q = 0$ acquires some value $m_{2,0} \longrightarrow m_{2,0}^{\text{in}}$, whose maximum value is constrained by the theoretical positivity of $\rho \geq 0$. Practically the constraint arises from the efficiency of the optical pumping being counteracted by relaxation. This is the case for the experiments in this thesis, with the exception of Section 7, and hence the vector in the steady state $\mathbf{m}^{\text{eq}}$ is given by

$$\mathbf{m}^{\text{eq}} = m_{2,0}^{\text{in}} \, (0, 0, 1, 0, 0)^T \, . \tag{4.43}$$

If the light polarisation is at an arbitrary angle θ to the xz-plane then the steady state vector can be determined by rotating the above solution (for $\theta = 0$) around the direction of the light-propagation (x-direction). The $\mathbf{m}^{\text{eq}}$ vector generated by the linearly polarised light at a polarisation angle θ, with respect to the quantization axis, reads as

$$\mathbf{m}^{\text{eq}} = m_{2,0}^{\text{in}} \left(-\frac{\sqrt{6}}{4} \sin^2\theta, i\frac{\sqrt{6}}{4} \sin 2\theta, 1 - \frac{3}{2} \sin^2\theta, i\frac{\sqrt{6}}{4} \sin 2\theta, -\frac{\sqrt{6}}{4} \sin^2\theta \right)^T . \tag{4.44}$$

Applying a strong static field $\mathbf{B}_0$ causes the atomic state to precess around the z-axis much faster than the time it takes to reach the steady state. Hence, as the Larmor frequency $\omega_L = \gamma_g |\mathbf{B}_0|$ is much larger than the overall relaxation rate, all of the multipoles which have $q \neq 0$ average to zero. According to the Secular approximation [39] the steady state vector is simplified to

$$\mathbf{m}^{\text{eq}} = m_{2,0}^{\text{in}} \left(0, 0, 1 - \frac{3}{2} \sin^2\theta, 0, 0 \right)^T . \tag{4.45}$$

Note that $\gamma_g = g_F \mu_B / \hbar$ where g_F is the Landé g-factor for an atom of total spin F and μ_B is the Bohr magneton.

4.6.1 Visualising the state

It is useful to think about the atomic states in terms of the angular-momentum probability surfaces. These are defined by the probability of detecting the state of maximum angular momentum in a given direction and are useful for the visualisation of the states. They are defined by

$$r(\mathbf{n}) = {}_{\mathbf{n}}\langle F, F|\, \rho \,|F, F\rangle_{\mathbf{n}} \, , \tag{4.46}$$

where $\mathbf{n}$ is defined as the quantisation direction. When the light is vertically polarised ($\theta = 0^\circ$) the probability surface takes on a ‘peanut’ shape (see Figure 4.1a) and when it is horizontally polarised ($\theta = 90^\circ$) the probability surface has a ‘doughnut’ shape (see Figure 4.1b). The surface that corresponds to $\hat{\mathcal{T}}_0^{(2)}$ has a rotational symmetry relative to the z-axis. The surfaces that correspond to $\hat{\mathcal{T}}_{\pm1}^{(2)}$ and $\hat{\mathcal{T}}_{\pm2}^{(2)}$ return to the original state after rotations by 2π and π respectively. This results in peaks being seen at $\mathbf{\Omega}_L$ and $2\mathbf{\Omega}_L$ in the predicted spectra discussed in Section 7.2.

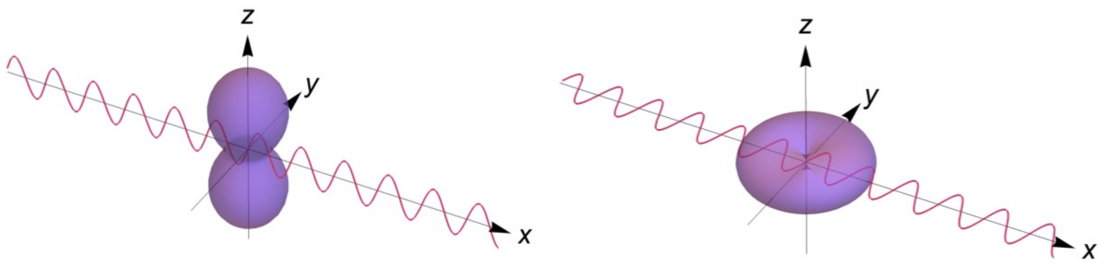

(a) (b)

Figure 4.1: The angular momentum probability surfaces in the steady state for an alignment based magnetometer with the light propagating along the x-direction and polarised along the (a) z-axis and (b) y-direction.

4.7 Evolution of the atomic state

In order to study the evolution of the atomic state when defined in terms of the multipole moments an arbitrary magnetic field will initially be considered. It is assumed that the atoms are placed in a magnetic field

$$\mathbf{B} = B_x\hat{\mathbf{x}} + B_y\hat{\mathbf{y}} + B_z\hat{\mathbf{z}}. \tag{4.47}$$

To see the dynamics of the system, the Liouville equation (see Equation 4.36) for the density matrix can be rewritten as a matrix equation for the multipoles. This is possible due to the properties of spherical tensors under rotations. The matrix equations can be written as

$$\dot{\mathbf{m}}_2 = \left(-i\omega_x J_x^{(2)} - i\omega_y J_y^{(2)} - i\omega_z J_z^{(2)}\right)\mathbf{m}_2 - \Gamma\mathbf{m}_2 + \Gamma\mathbf{m}_2^{\mathrm{eq}}, \tag{4.48}$$

where $\dot{\mathbf{m}}_2 = d\mathbf{m}_2/dt$ and a single ground state relaxation rate (Γ) has been included for simplicity. Here $\omega_x = \gamma_g B_x$, $\omega_y = \gamma_g B_y$ and $\omega_z = \gamma_g B_z$, where γ_g is the gyromagnetic ratio of the atom. $J_x^{(2)}$, $J_y^{(2)}$ and $J_z^{(2)}$ are the rank-2 angular momentum operators given by

$$J_x^{(2)} = \hbar\begin{pmatrix} 0 & 1 & 0 & 0 & 0 \\ 1 & 0 & \sqrt{\frac{3}{2}} & 0 & 0 \\ 0 & \sqrt{\frac{3}{2}} & 0 & \sqrt{\frac{3}{2}} & 0 \\ 0 & 0 & \sqrt{\frac{3}{2}} & 0 & 1 \\ 0 & 0 & 0 & 1 & 0 \end{pmatrix}, \tag{4.49}$$

$$J_y^{(2)} = \hbar\begin{pmatrix} 0 & i & 0 & 0 & 0 \\ -i & 0 & i\sqrt{\frac{3}{2}} & 0 & 0 \\ 0 & -i\sqrt{\frac{3}{2}} & 0 & i\sqrt{\frac{3}{2}} & 0 \\ 0 & 0 & -i\sqrt{\frac{3}{2}} & 0 & i \\ 0 & 0 & 0 & -i & 0 \end{pmatrix}, \tag{4.50}$$

$$J_z^{(2)} = \hbar \begin{pmatrix} -2 & 0 & 0 & 0 & 0 \\ 0 & -1 & 0 & 0 & 0 \\ 0 & 0 & 0 & 0 & 0 \\ 0 & 0 & 0 & 1 & 0 \\ 0 & 0 & 0 & 0 & 2 \end{pmatrix}. \tag{4.51}$$

By substituting in the angular momentum operators and setting $\dot{\mathbf{m}}_2^{\text{ss}} = 0$, a set of linear equations can be solved to find the steady state solutions of the rank-2 multipoles. The steady state solutions are given by

$$\begin{pmatrix} m_{2,-2}^{\text{ss}} \\ m_{2,-1}^{\text{ss}} \\ m_{2,0}^{\text{ss}} \\ m_{2,1}^{\text{ss}} \\ m_{2,2}^{\text{ss}} \end{pmatrix} = \frac{m_{2,0}^{\text{eq}}}{\left(\Gamma^2 + \omega_x^2 + \omega_y^2 + \omega_z^2\right)\left[\Gamma^2 + 4\left(\omega_x^2 + \omega_y^2 + \omega_z^2\right)\right]}$$
$$\times \begin{pmatrix} -\sqrt{\frac{3}{2}}\left(\omega_x + i\omega_y\right)^2 \left(\Gamma^2 + \omega_x^2 + \omega_y^2 + 3i\Gamma\omega_z - 2\omega_z^2\right) \\ -\sqrt{\frac{3}{2}}\left(\omega_x + i\omega_y\right)\left(i\Gamma + 2\omega_z\right)\left(\Gamma^2 + \omega_x^2 + \omega_y^2 + 3i\Gamma\omega_z - 2\omega_z^2\right) \\ \Gamma^4 + \left(\omega_x^2 + \omega_y^2 - 2\omega_z^2\right)^2 + \Gamma^2\left[2\left(\omega_x^2 + \omega_y^2\right) + 5\omega_z^2\right] \\ \sqrt{\frac{3}{2}}\left(\omega_x - i\omega_y\right)\left(-i\Gamma + 2\omega_z\right)\left(\Gamma^2 + \omega_x^2 + \omega_y^2 - 3i\Gamma\omega_z - 2\omega_z^2\right) \\ -\sqrt{\frac{3}{2}}\left(\omega_x - i\omega_y\right)^2 \left(\Gamma^2 + \omega_x^2 + \omega_y^2 - 3i\Gamma\omega_z - 2\omega_z^2\right) \end{pmatrix}. \tag{4.52}$$

It can be seen that $(m_{2,-2}^{\text{ss}})^* = m_{2,-2}^{\text{ss}}$ and $(m_{2,-1}^{\text{ss}})^* = m_{2,-1}^{\text{ss}}$ where * represents the complex conjugate.

4.8 Observables of interest

From the steady state solution of the multipoles the expected lineshapes of the observable signals can be calculated. Throughout this thesis the main observable measured is the polarisation rotation of the light. In this case, how the polarisation of the light changes after it has exited the atomic ensemble is measured using a balanced photodetector. In Section 8 the intensity of the transmitted light, referred to as the absorption measurement, is also of interest. Here the amount of light that is transmitted from the vapour cell is measured using a single diode photodetector. For a vapour cell with a length l the intensity of the light after the vapour cell is given by $I(l) = I(0)\mathrm{e}^{-S^{\text{abs}}l}$ where $I(0)$ is the intensity of the light before the vapour cell and S^{abs} is the absorption coefficient being measured. In both cases it will be assumed that the laser light is polarised along the z-direction and propagates along the x-direction. This is in order to match that previously defined when calculating the Hamiltonian of the system (see Section 4.2) and the experimental geometry. This means that $\theta = 0$ and hence $m_{2,0}^{\text{eq}} = m_{2,0}^{\text{in}}$.

In order to derive the forms of the equations of the expected signals the symmetry properties that these observables have need to be identified. The symmetry arguments then allow for the linear combinations of the spherical tensor components $m_{\kappa,q}$ (with $\kappa \leq 2$) that make up the observable signals to be determined. In terms of the spherical tensor components, the absorption coefficient and polarisation rotation signal can be generally written as

$$S^{\mathrm{abs}} = C_0 m_{0,0} + \sum_{q=-1}^{1} C_{1q} m_{1q} \quad + \sum_{q=-2}^{2} C_{2q} m_{2q} \tag{4.53}$$

$$= C_0 m_{0,0} + \mathbf{C}_1^T \mathbf{m}_1 + \mathbf{C}_2^T \mathbf{m}_2, \tag{4.54}$$

and

$$S^{\mathrm{PR}} = D_0 m_{0,0} + \sum_{q=-1}^{1} D_{1,q} m_{1,q} + \sum_{q=-2}^{1} D_{2,q} m_{2,q}, \tag{4.55}$$

$$= D_0 m_{0,0} + \mathbf{D}_1^T \mathbf{m}_1 + \mathbf{D}_2^T \mathbf{m}_2, \tag{4.56}$$

respectively. Here C_0, C_{1q} and C_{2q} are complex coefficients for the absorption signal and D_0, D_{1q} and D_{2q} are complex coefficients for the polarisation rotation signal. These coefficients are rewritten as row vectors such that $\mathbf{C}_1^T$ contains the coefficients C_{1q}, $\mathbf{C}_2^T$ contains the coefficients C_{2q}, $\mathbf{D}_1^T$ contains the coefficients D_{1q} and $\mathbf{D}_2^T$ contains the coefficients D_{2q}.

Due to properties of the system, rotating the atomic state around the light propagation axis (x-axis) by π must be equivalent to rotating the light polarisation around the x-axis by $-\pi$. As the light is linearly polarised, the rotation of the light around the x-axis by $-\pi$ does not affect the system. This means that both the absorption and polarisation rotation signal are not affected by either of these rotation operations. The operators have a matrix form of

$$\mathbf{R}_x^{(1)} = \exp\left[-i\pi J_x^{(1)}/\hbar\right] = \begin{pmatrix} 0 & 0 & -1 \\ 0 & -1 & 0 \\ -1 & 0 & 0 \end{pmatrix}, \tag{4.57}$$

$$\mathbf{R}_x^{(2)} = \exp\left[-i\pi J_x^{(2)}/\hbar\right] = \begin{pmatrix} 0 & 0 & 0 & 0 & 1 \\ 0 & 0 & 0 & 1 & 0 \\ 0 & 0 & 1 & 0 & 0 \\ 0 & 1 & 0 & 0 & 0 \\ 1 & 0 & 0 & 0 & 0 \end{pmatrix}, \tag{4.58}$$

when acting on the $\mathbf{m}_1$ and $\mathbf{m}_2$ multipoles, respectively. The $m_{0,0}$ component remains constant and unchanged. The matrices $J_x^{(1)}$ and $J_x^{(2)}$ are the $\kappa = 1$ and $\kappa = 2$ representations of the x-component of the angular momentum operators. For the $\kappa = 2$ case the matrix is given in Equation 4.49. For the signals to be invariant under the transformations it must be imposed that

$$\mathbf{C}_1^T \mathbf{m}_1 + \mathbf{C}_2^T \mathbf{m}_2 = \mathbf{C}_1^T \mathbf{R}_x^{(1)} \mathbf{m}_1 + \mathbf{C}_2^T \mathbf{R}_x^{(2)} \mathbf{m}_2, \tag{4.59}$$

$$\mathbf{D}_1^T \mathbf{m}_1 + \mathbf{D}_2^T \mathbf{m}_2 = \mathbf{D}_1^T \mathbf{R}_x^{(1)} \mathbf{m}_1 + \mathbf{D}_2^T \mathbf{R}_x^{(2)} \mathbf{m}_2. \tag{4.60}$$

This must hold true for any $\mathbf{m}_1$ and $\mathbf{m}_2$. Hence, $\mathbf{C}_1$ and $\mathbf{D}_1$ must be eigenvectors of $(\mathbf{R}_x^{(2)})^T$ as well as $\mathbf{C}_2$ and $\mathbf{D}_2$ being eigenvectors of $(\mathbf{R}_x^{(1)})^T$. These must all correspond to an eigenvalue of 1 meaning that

$$\mathbf{C}_1, \mathbf{D}_1 \in \operatorname{span}\left\{\begin{pmatrix}1\\0\\-1\end{pmatrix}\right\}, \tag{4.61}$$

$$\mathbf{C}_2, \mathbf{D}_2 \in \operatorname{span}\left\{\begin{pmatrix}1\\0\\0\\0\\1\end{pmatrix}, \begin{pmatrix}0\\1\\0\\1\\0\end{pmatrix}, \begin{pmatrix}0\\0\\1\\0\\0\end{pmatrix}\right\}. \tag{4.62}$$

Specific symmetry properties arising from the the observables individually will now be considered.

4.8.1 Absorption coefficient

When measuring the light absorption coefficient S^{abs}, the light polarisation direction does not depend on the direction that the laser light is propagating in. So, a rotation of the atomic state around the light polarisation axis (z-axis), at an angle of φ, can be calculated using the operators

$$\mathbf{R}_\varphi^{(1)} = \exp\left[-i\varphi J_z^{(1)}/\hbar\right] = \begin{pmatrix}\mathrm{e}^{i\varphi} & 0 & 0\\ 0 & 1 & 0\\ 0 & 0 & \mathrm{e}^{-i\varphi}\end{pmatrix}, \tag{4.63}$$

$$\mathbf{R}_\varphi^{(2)} = \exp\left[-i\varphi J_z^{(2)}/\hbar\right] = \begin{pmatrix}\mathrm{e}^{2i\varphi} & 0 & 0 & 0 & 0\\ 0 & \mathrm{e}^{i\varphi} & 0 & 0 & 0\\ 0 & 0 & 1 & 0 & 0\\ 0 & 0 & 0 & \mathrm{e}^{-i\varphi} & 0\\ 0 & 0 & 0 & 0 & \mathrm{e}^{-2i\varphi}\end{pmatrix}. \tag{4.64}$$

It can be seen that $\mathbf{C}_1$ and $\mathbf{C}_2$ must be eigenvectors of $(\mathbf{R}_\varphi^{(1)})^T$ and $(\mathbf{R}_\varphi^{(2)})^T$, respectively, and both correspond to an eigenvalue of 1. As a result of this $\mathbf{C}_1$ and $\mathbf{C}_2$ can be defined as

$$\mathbf{C}_1 \in \operatorname{span}\left\{\begin{pmatrix}0\\1\\0\end{pmatrix}\right\}, \tag{4.65}$$

$$\mathbf{C}_2 \in \operatorname{span}\left\{\begin{pmatrix}0\\0\\1\\0\\0\end{pmatrix}\right\}. \tag{4.66}$$

Again here, the $m_{0,0}$ component remains unchanged. When also taking into account the expressions presented in Equations 4.65 and 4.66 it can be seen that $\mathbf{C}_1 = \begin{pmatrix}0 & 0 & 0\end{pmatrix}^T$ and $\mathbf{C}_2 \propto \begin{pmatrix}0 & 0 & 1 & 0 & 0\end{pmatrix}^T$ and there are no constraints on the value of C_0. Substituting these results into Equation 4.53 the formula for the signal when measuring the absorption coefficient is given by

$$S^{\mathrm{abs}} = C_0 m_{0,0} + \begin{pmatrix}0, 0, 0\end{pmatrix} \begin{pmatrix} m_{1,-1} \\ m_{1,0} \\ m_{1,1} \end{pmatrix} + \begin{pmatrix}0, 0, 1, 0, 0\end{pmatrix} \begin{pmatrix} m_{2,-2} \\ m_{2,-1} \\ m_{2,0} \\ m_{2,1} \\ m_{2,2} \end{pmatrix}. \tag{4.67}$$

Carrying out the multiplication the absorptive signal, in terms of the multipoles, takes the form

$$S^{\mathrm{abs}} \propto \left(m_{0,0} - \chi \cdot m_{2,0}\right), \tag{4.68}$$

where χ depends on the hyperfine quantum number F. By substituting in the steady state solutions found in Equation 4.52, the absorption signal is given by

$$S^{\mathrm{abs}} \propto m_{0,0} - \chi \frac{m_{2,0}^{\mathrm{eq}} \{\Gamma^4 + (\omega_x^2 + \omega_y^2 - 2\omega_z^2)^2 + \Gamma^2[2(\omega_x^2 + \omega_y^2) + 5\omega_z^2]\}}{(\Gamma^2 + \omega_x^2 + \omega_y^2 + \omega_z^2)[\Gamma^2 + 4(\omega_x^2 + \omega_y^2 + \omega_z^2)]}. \tag{4.69}$$

It is noted that although this model uses the simplified 'toy model' of a $F = 1$ ground state, the theory still holds valid for a caesium atom with a ground state of $F = 3, 4$. In general, the $F = 4$ state can have multipoles with values $\kappa = 0, 1, 2, ..., 8$. As low light power is assumed in this setup only the $\kappa = 2$ multipole is relevant as the light only probes multipoles with $\kappa \leq 2$. This is also not an issue when carrying out rotations as this does not cause any couplings between different values of κ.

4.8.2 Polarisation rotation signal

Now, the symmetry arguments arising from the polarisation rotation measurements will be determined. If the light propagates in the opposite direction, in the case presented here in the $-x$-direction, the polarisation-rotation signal has the same magnitude but with the opposite sign. Hence a clockwise light polarisation rotation around the x-axis becomes an anti-clockwise rotation. Flipping the direction that the light propagates in is equivalent to rotating the atomic system around the z-axis by π. The matrix for this rotation is given by

$$\mathbf{R}_z^{(1)} = \exp\left[-i\pi J_z^{(1)}/\hbar\right] = \begin{pmatrix} -1 & 0 & 0 \\ 0 & 1 & 0 \\ 0 & 0 & -1 \end{pmatrix}, \tag{4.70}$$

$$\mathbf{R}_z^{(2)} = \exp\left[-i\pi J_z^{(2)}/\hbar\right] = \begin{pmatrix} 1 & 0 & 0 & 0 & 0 \\ 0 & -1 & 0 & 0 & 0 \\ 0 & 0 & 1 & 0 & 0 \\ 0 & 0 & 0 & -1 & 0 \\ 0 & 0 & 0 & 0 & 1 \end{pmatrix}. \tag{4.71}$$

In order for the detected signal amplitude to maintain the same magnitude but with the opposite sign it is imposed that

$$D_0 m_{0,0} + \mathbf{D}_1^T \mathbf{m}_1 + \mathbf{D}_2^T \mathbf{m}_2 = -(D_0 m_{0,0} + \mathbf{D}_1^T \mathbf{R}_z^{(1)} \mathbf{m}_1 + \mathbf{D}_2^T \mathbf{R}_z^{(2)} \mathbf{m}_2), \tag{4.72}$$

for any $m_{0,0}$, $\mathbf{m}_1$ and $\mathbf{m}_2$. From this, it can be calculated that $D_0 = 0$ and

$$\mathbf{D}_1 \in \operatorname{span}\left\{\begin{pmatrix}1\\0\\0\end{pmatrix},\begin{pmatrix}0\\0\\1\end{pmatrix}\right\}, \tag{4.73}$$

$$\mathbf{D}_2 \in \operatorname{span}\left\{\begin{pmatrix}0\\1\\0\\0\\0\end{pmatrix},\begin{pmatrix}0\\0\\0\\1\\0\end{pmatrix}\right\}. \tag{4.74}$$

$\mathbf{D}_1$ is an eigenspace of $(\mathbf{R}_z^{(1)})^T$ and $\mathbf{D}_2$ is an eigenspace of $(\mathbf{R}_z^{(2)})^T$ respectively, and both correspond to the eigenvalue of -1. By taking into account the conditions determined previously in Equations 4.65 and 4.66 it can be concluded that $\mathbf{D}_1 \propto \begin{pmatrix}-1 & 0 & 1\end{pmatrix}^T$ and $\mathbf{D}_2 \propto \begin{pmatrix}0 & 1 & 0 & 1 & 0\end{pmatrix}^T$. Hence the polarisation rotation signal can be calculated using Equation 4.55 and reads

$$S^{\mathrm{PR}} = D_{1,1}(m_{1,1} - m_{1,-1}) + D_{2,1}(m_{2,1} + m_{2,-1}). \tag{4.75}$$

For the signal to be real $D_{2,1}$ needs to be purely imaginary. As linearly polarised light is used to create an aligned state $m_{1,q} = 0$ for all q so the detected signal is given by

$$S^{\mathrm{PR}} \propto i\left(m_{2,1} + m_{2,-1}\right). \tag{4.76}$$

By substituting in the steady state solutions found in Equation 4.52, the polarisation rotation signal is found to be

$$S^{\mathrm{PR}} \propto \frac{\sqrt{6}m_{2,0}^{\mathrm{eq}}[\Gamma^3\omega_x - \Gamma^2\omega_y\omega_z + 2\omega_y\omega_z(\omega_x^2 + \omega_y^2 - 2\omega_z^2) + \Gamma\omega_x(\omega_x^2 + \omega_y^2 + 4\omega_z^2)]}{(\Gamma^2 + \omega_x^2 + \omega_y^2 + \omega_z^2)[\Gamma^2 + 4(\omega_x^2 + \omega_y^2 + \omega_z^2)]}. \tag{4.77}$$

4.9 RF magnetometry signals

The main focus of this thesis is on RF magnetometry in which the system has an RF magnetic field as well as a static magnetic field. It is convenient to here define the equations for the expected signals in this case. The general form of the expected signal in terms of the multipoles (Equation 4.77) will be used with the magnetic field components defined to match the experimental setup as was initially described in Section 4.2. The system has a static magnetic field $\mathbf{B}_0$ being applied in the z-direction and an oscillating magnetic field $\mathbf{B}_{\mathrm{rf}}\cos(\omega_{\mathrm{rf}}t)$ along the y-direction. It will be assumed that the magnetic field along the x-direction is zero. Due to the time dependence of the oscillating magnetic field it is convenient to use the rotating wave approximation when calculating the multipole components. In the rotating frame, the ensemble is rotating around the z-axis (around $\mathbf{B}_0$) at the RF frequency. In the rotating frame the multipoles are given by

$$\tilde{m}_{\kappa,q} = \mathrm{e}^{iq\omega_{\mathrm{rf}}t} m_{\kappa,q}. \tag{4.78}$$

Assuming the rotating wave approximation, described in Section 4.3, holds true and dropping the fast oscillating terms, the equation that describes the evolution of the multipoles is given by

$$\dot{\tilde{\mathbf{m}}}_2 = \left(-i\frac{\Omega_{\mathrm{rf}}}{2}J_y^{(2)} + i\Delta_{\mathrm{rf}}J_z^{(2)}\right)\tilde{\mathbf{m}}_2 - \Gamma\tilde{\mathbf{m}}_2 + \Gamma\tilde{\mathbf{m}}_2^{\mathrm{eq}}, \tag{4.79}$$

where $\Delta_{\mathrm{rf}} = \omega_{\mathrm{rf}} - \omega_L$. The steady state solutions are found by solving Equation 4.79 when $\dot{\tilde{m}}_2 = 0$ and are found to be

$$\widetilde{m}_{2,-2}^{\mathrm{ss}} = \frac{-\sqrt{\frac{3}{2}}m_{2,0}^{\mathrm{eq}}\Omega_{\mathrm{rf}}^2\left[4\left(\Gamma - i\Delta_{\mathrm{rf}}\right)\left(\Gamma - 2i\Delta_{\mathrm{rf}}\right) + \Omega_{\mathrm{rf}}^2\right]}{4\left(\Gamma^2 + 4\Delta_{\mathrm{rf}}^2 + \Omega_{\mathrm{rf}}^2\right)\left[4\left(\Gamma^2 + \Delta_{\mathrm{rf}}^2\right) + \Omega_{\mathrm{rf}}^2\right]}, \tag{4.80}$$

$$\widetilde{m}_{2,-1}^{\mathrm{ss}} = \frac{-\sqrt{\frac{3}{2}}m_{2,0}^{\mathrm{eq}}\left(\Gamma + 2i\Delta_{\mathrm{rf}}\right)\Omega_{\mathrm{rf}}\left[4\left(\Gamma - i\Delta_{\mathrm{rf}}\right)\left(\Gamma - 2i\Delta_{\mathrm{rf}}\right) + \Omega_{\mathrm{rf}}^2\right]}{2\left(\Gamma^2 + 4\Delta_{\mathrm{rf}}^2 + \Omega_{\mathrm{rf}}^2\right)\left[4\left(\Gamma^2 + \Delta_{\mathrm{rf}}^2\right) + \Omega_{\mathrm{rf}}^2\right]}, \tag{4.81}$$

$$\widetilde{m}_{2,0}^{\mathrm{ss}} = \frac{m_{2,0}^{\mathrm{eq}}\left[16\left(\Gamma^2 + \Delta_{\mathrm{rf}}^2\right)\left(\Gamma^2 + 4\Delta_{\mathrm{rf}}^2\right) + 8\left(\Gamma^2 - 2\Delta_{\mathrm{rf}}^2\right)\Omega_{\mathrm{rf}}^2 + \Omega_{\mathrm{rf}}^4\right]}{4\left(\Gamma^2 + 4\Delta_{\mathrm{rf}}^2 + \Omega_{\mathrm{rf}}^2\right)\left[4\left(\Gamma^2 + \Delta_{\mathrm{rf}}^2\right) + \Omega_{\mathrm{rf}}^2\right]}, \tag{4.82}$$

$$\widetilde{m}_{2,1}^{\mathrm{ss}} = \frac{\sqrt{\frac{3}{2}}m_{2,0}^{\mathrm{eq}}\left(\Gamma - 2i\Delta_{\mathrm{rf}}\right)\Omega_{\mathrm{rf}}\left[4\left(\Gamma + i\Delta_{\mathrm{rf}}\right)\left(\Gamma + 2i\Delta_{\mathrm{rf}}\right) + \Omega_{\mathrm{rf}}^2\right]}{2\left(\Gamma^2 + 4\Delta_{\mathrm{rf}}^2 + \Omega_{\mathrm{rf}}^2\right)\left[4\left(\Gamma^2 + \Delta_{\mathrm{rf}}^2\right) + \Omega_{\mathrm{rf}}^2\right]}, \tag{4.83}$$

$$\widetilde{m}_{2,2}^{\mathrm{ss}} = \frac{-\sqrt{\frac{3}{2}}m_{2,0}^{\mathrm{eq}}\Omega_{\mathrm{rf}}^2\left[4\left(\Gamma + i\Delta_{\mathrm{rf}}\right)\left(\Gamma + 2i\Delta_{\mathrm{rf}}\right) + \Omega_{\mathrm{rf}}^2\right]}{4\left(\Gamma^2 + 4\Delta_{\mathrm{rf}}^2 + \Omega_{\mathrm{rf}}^2\right)\left[4\left(\Gamma^2 + \Delta_{\mathrm{rf}}^2\right) + \Omega_{\mathrm{rf}}^2\right]}. \tag{4.84}$$

Rotating the steady state solutions of the multipoles back to the lab frame and substituting them into Equation 4.76 results in the polarisation rotation signal being

$$S^{\mathrm{PR}}(t) \propto A\cos(\omega_{\mathrm{rf}}t) + D\sin(\omega_{\mathrm{rf}}t), \tag{4.85}$$

where A and D correspond to the absorptive and dispersive lineshapes corresponding to the in-phase ($X = A$) and quadrature ($Y = D$) components of the detected signal. These take the form of

$$A\left(\Delta_{\mathrm{rf}}, \Omega_{\mathrm{rf}}\right) = \frac{\sqrt{\frac{3}{2}}m_{2,0}^{\mathrm{eq}}\Gamma\Omega_{\mathrm{rf}}\left[4\left(\Gamma^2 + 4\Delta_{\mathrm{rf}}^2\right) + \Omega_{\mathrm{rf}}^2\right]}{4(\Gamma^2 + 4\Delta_{\mathrm{rf}}^2 + \Omega_{\mathrm{rf}}^2)\left[4\left(\Gamma^2 + \Delta_{\mathrm{rf}}^2\right) + \Omega_{\mathrm{rf}}^2\right]}, \tag{4.86}$$

and

$$D(\Delta_{\mathrm{rf}}, \Omega_{\mathrm{rf}}) = \frac{\sqrt{\frac{3}{2}}m_{2,0}^{\mathrm{eq}}\Delta_{\mathrm{rf}}\Omega_{\mathrm{rf}}\left[2\left(\Gamma^2 + 4\Delta_{\mathrm{rf}}^2\right) - \Omega_{\mathrm{rf}}^2\right]}{2(\Gamma^2 + 4\Delta_{\mathrm{rf}}^2 + \Omega_{\mathrm{rf}}^2)\left[4\left(\Gamma^2 + \Delta_{\mathrm{rf}}^2\right) + \Omega_{\mathrm{rf}}^2\right]}. \tag{4.87}$$

As the magnetometers presented in this thesis are primarily operated in the regime of weak RF magnetic field strengths, the signal can be simplified. In the limit of a low RF magnetic field strength ($\Omega_{\mathrm{rf}} \approx 0$) the components of the signal simplify to

$$A\left(\Delta_{\mathrm{rf}}, \Omega_{\mathrm{rf}} \approx 0\right) = \frac{\sqrt{\frac{3}{2}}m_{2,0}^{\mathrm{eq}}\Gamma\Omega_{\mathrm{rf}}}{4\left(\Gamma^2 + \Delta_{\mathrm{rf}}^2\right)}, \tag{4.88}$$

and

$$D(\Delta_{\mathrm{rf}}, \Omega_{\mathrm{rf}} \approx 0) = \frac{\sqrt{\frac{3}{2}} m_{2,0}^{\mathrm{eq}} \Delta_{\mathrm{rf}} \Omega_{\mathrm{rf}}}{4\left(\Gamma^2 + \Delta_{\mathrm{rf}}^2\right)}. \tag{4.89}$$

The signal amplitude is given by $R = \sqrt{X^2 + Y^2} = \sqrt{A^2 + D^2}$ which in the weak RF field regime can be calculated as

$$R\left(\Delta_{\mathrm{rf}}, \Omega_{\mathrm{rf}} \approx 0\right) = \frac{\sqrt{\frac{3}{2}} m_{2,0}^{\mathrm{eq}} \Omega_{\mathrm{rf}}}{4\sqrt{\Gamma^2 + \Delta_{\mathrm{rf}}^2}}. \tag{4.90}$$

These predictions will be compared to experimental data throughout this thesis.

Chapter 5

Eddy current measurements using a commercial fluxgate

5.1 Motivation

The remote detection and characterisation of conductive objects is useful in many areas including medical, defence, aerospace and quality control applications [87, 88, 89, 90, 91]. The use of eddy currents has the added benefit of not needing to be in contact with the object being investigated and hence is a non-destructive method of measurement [52, 53, 54, 55]. The use of eddy currents for flaw detection has already shown its potential in the aerospace, transport and power supply industries [92]. Additional applications include subsurface crack and corrosion detection with current technologies that are used in the kHz to MHz range to detect cracks ~ 0.1 mm or less in depth [52, 92]. This is done using an oscillating primary magnetic field to detect and characterise conductive objects. The primary field induces eddy currents in the object resulting in a secondary magnetic field that can be measured using a magnetic field sensor such as a fluxgate magnetometer. This method has also been applied to the monitoring of fuel cells [93, 94].

Although there has been a lot of research in this area over the years there are still a number of challenges. This includes being able to differentiate the object from the noisy background it is in. In the case of an unexploded ordnance (UXO) it takes time and multiple resources to be able to distinguish the object from false signals [95]. The detection of the secondary magnetic field that results from the eddy currents in an electrically conductive object when placed in an oscillating/oscillatory primary magnetic field, contains distinct characteristics such as the electrical conductivity, magnetic permeability, object geometry, and size of the object. This can help with the identification of the correct object. The work in this chapter shows a method of characterising both non-magnetic and magnetic objects in low frequency magnetic fields. The response of the secondary magnetic field is measured as a function of frequency, by varying the primary magnetic field from 10 Hz to 1 kHz. How the secondary induced field varies with the placement of the conductive object is also looked at with the position being varied on- and off-axis from the fluxgate magnetometer. The findings are verified using COMSOL simulations and theory.

5.2 Experimental setup

Figure 5.1a shows the experimental setup used to detect and characterise aluminium and steel samples (see Figure 5.1b). The setup is 3D printed with ridges to place the object's position with a high level of precision. A Bartington Mag690 fluxgate is used to detect the magnetic fields induced in the samples. Further details about the sensor can be found in Section 5.3. The sensor can measure the field components in all three directions, however for simplicity only the on-axis component (z-direction) of the induced magnetic field is investigated. The experiment is controlled by a sbRIO-9627 field-programmable gate array (FPGA) programmed in LabVIEW. The FPGA can output oscillating signals, record and save data, apply real time feedback, perform lock-in amplification and analyse data.

A primary magnetic field oscillating at a particular frequency ν, induces eddy currents in a conductive object which then induces a secondary magnetic field that can be detected. The signal detected is of the form $S = R\cos(2\pi\nu t + \phi)$. This can be given in terms of the in-phase X, and out-of-phase components Y such that $S = X\cos(2\pi\nu t) + Y\sin(2\pi\nu t)$. The in-phase and out-of-phase components of the signal are detected and tracked using the lock-in amplifier implemented in the FPGA.

An excitation coil is used to produce a primary magnetic field $\mathbf{B_1}(t)$ that is oscillating at a set frequency ν ranging between 10 Hz and 1000 Hz. For the primary field the phase of the lock-in amplifier was adjusted such that the field is all in the in-phase component. The excitation coil has a radius of 8 cm with 60 coil windings. The wire used on this coil has a diameter of 1 mm to prevent heating and results in a small resistance. A 10 Ω power resistor is placed in series with the coil. The centre of the coil is positioned 48.4 cm from the detection point of the fluxgate magnetometer. The primary magnetic field was produced using a sinusoidal voltage with an amplitude of $\approx$ 7.2 $\mathrm{V_{pp}}$ which generates a current of $I_e = 0.53$ A. This corresponds to a magnetic dipole moment of $\mu_e = 0.64$ $\mathrm{Am^{-2}}$ in the z-direction. The primary magnetic field induced has an amplitude of $B_1 = 1.09$ μT at the detection point of the magnetometer.

A second coil is used in the experiment to compensate the magnetic field when no object is present. The compensation coil consists of a one turn Helmholtz coil with a radius of 3 cm and is placed around the sensing point of the magnetometer. A 6 Ω power resistor was placed in series with the coil. The compensation coil produces a second magnetic field $\mathbf{B_2}(t)$ which oscillates at the same frequency as the primary field. A 0.24 $\mathrm{V_{pp}}$ oscillating voltage is applied to the compensation coil. This generates a current of $I_c = 0.036$ A corresponding to a magnetic dipole moment of $\mu_c = 1.02\times10^{-4}$ $\mathrm{Am^{-2}}$. This cancels the primary field such that when no object is present the total magnetic field at the position of the magnetometer reads $\mathbf{B_1}(t) + \mathbf{B_2}(t) \approx 0$.

When a conductive object is placed between the excitation coil and the magnetometer, eddy currents are induced in the object which in turn creates a secondary magnetic field that oscillates at the same frequency as the primary field ν. As the compensation field amplitude is much smaller than the magnetic field generated by the excitation coil (the primary field), the eddy currents are primarily induced by the primary field and hence the amplitude of the induced secondary field is proportional to the primary field. As the field is cancelled when no object is present the total magnetic field detected by the magnetometer is the secondary

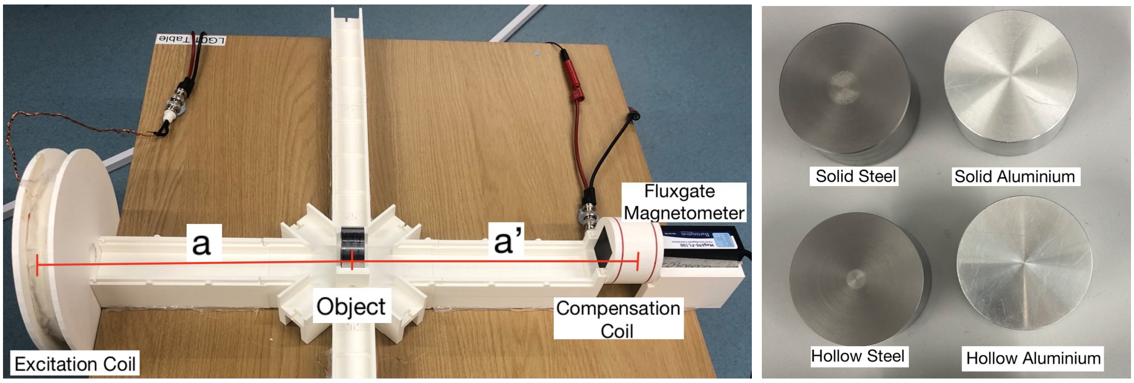

(a) (b)

Figure 5.1: Experimental setup for detecting and characterising metal samples. (a) An image of the active detection system, consisting of an excitation coil, a sensor, a compensation coil, and an object, of thickness t, which can be placed either on-axis or off-axis. The object is placed at a distance a from the excitation coil and a distance a' from the detection point of the magnetometer. (b) The samples detected in this setup. These are solid and hollow samples of 6061 T6 aluminium and 440c steel.

field, $\mathbf{B_{total}}(t) = \mathbf{B_1}(t) + \mathbf{B_2}(t) + \mathbf{B_{ec}}(t) \approx \mathbf{B_{ec}}(t)$. Cancelling the primary field allows the secondary field to be directly measured. Unlike for optically pumped magnetometers (OPMs) [30] this technique does not have any added stability, as can be seen in Section 5.3.1.

Figure 5.1b shows the four objects that were detected and characterised. They are all cylinders with a 2 cm radius and a 2 cm width. A solid and hollow cylinder of two different materials were used. The hollow cylinders had a wall thickness of 4 mm. The cylinders were made of either 6061 T6 aluminium or 440c steel; 6061 T6 aluminium has an electrical conductivity of $\sigma = 24.6$ MSm^{-1}, is non-magnetic, and has a relative magnetic permeability of $\mu_r = 1$ [96], while the electrical properties of 440c steel are not well defined [97]. While the electrical conductivity and permeability are unknown they can be determined experimentally [58]. In Ref. [58] a 440C sample is used where they experimentally determined the conductivity to be $\sigma = 1.51(1)$ MS/m and a relative permeability of $\mu_r = 16.7(1)$. It is expected that similar values should be obtained experimentally in this chapter.

The experimental setup is used to determine how the frequency response of the induced magnetic fields in a non-magnetic and magnetic object differ. How the signal changes with distance on- and off-axis is also analysed with the findings being verified using simulations (COMSOL) and theoretical models [56, 60, 58]. When varying the frequency of the primary field, the frequency was varied from 10 to 1000 Hz. The object was placed 22.4 cm from the excitation coil. When varying the distance of the object, both on- and off-axis, the frequency of the primary coil was set to 500 Hz. For the on-axis measurement the distance of the object was placed at approximately 5 cm intervals, beginning from 5 cm in front of the excitation coil to 39.5 cm. For the off-axis measurements the sample was placed 22.4 cm away from the front of the coil in the z-direction. The sample was then varied from 0 to 34 cm off-axis in the x-direction.

5.3 Sensor details

The sensor used in this chapter is a commercially available Bartington Mag690-FL100 Fluxgate magnetometer (see Figure 5.2a) [98]. The magnetometer has a 3 dB bandwidth of 1.5 kHz, a dynamic range of ±100 μT and a calibration factor of 100 mV/μT.

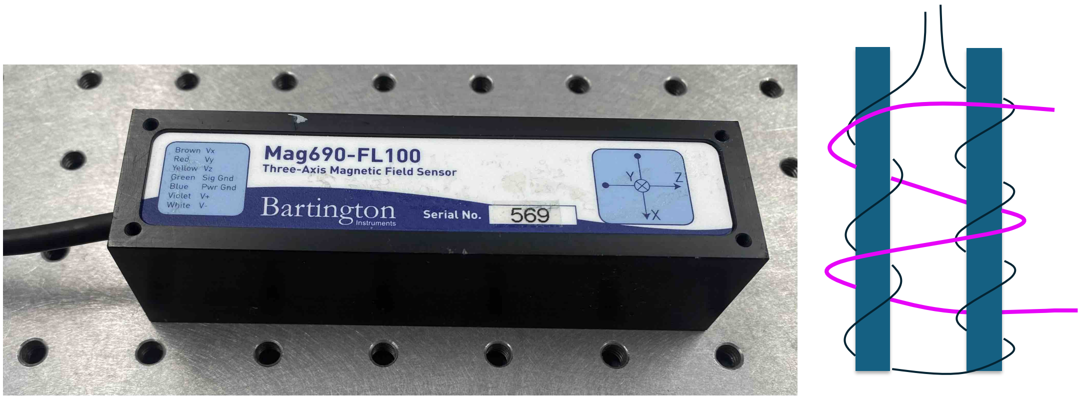

(a) (b)

Figure 5.2: (a) Image of the Bartington Mag690 Fluxgate magnetometer. (b) A simple drawing of how a fluxgate magnetometer works. The magnetometer is made up of two coils, an excitation/ driving coil (black coil) and a pick up coil (pink coil), wrapped around a magnetically permeable alloy core (blue).

Fluxgate magnetometers measure the strength of a magnetic field along a particular direction. They operate well in the Earth's magnetic field. A fluxgate magnetometer is made up of two coils, an excitation/ driving coil and a pick up coil, wrapped around a magnetically permeable alloy core, as shown in Figure 5.2b. A magnetically permeable core is used as it has a high magnetic susceptibility so it aligns easily with a magnetic field. A fluxgate magnetometer can have either one core or two. The fluxgate explained here will be based on the magnetometer having two cores [98, 99]. A driving coil surrounds the cores (see Figure 5.2b) and an alternating current is passed through it. This repeatedly magnetises and demagnetises the core. Each core has an opposite direction of the excitation flux. The magnetic field from the driving coil induces a current in the sensing coil. When there is no ambient magnetic field present the current in the driving coil and sensing coil is equal [10]. When the core is placed in a magnetic field it will be more easily saturated in the direction of the magnetic field and less easy to saturate in the opposite direction. This results in the currents in the driving coil and sensing coils to no longer be equal and hence the difference in the current of the two coils can be integrated over to give a signal as a voltage. This voltage output is the magnetometer signal and can be used to determine the magnetic field that the sensor is in. The use of three fluxgate magnetometer configurations with in a sensor head allows vector measurements to be measured. Hence, many commercially available fluxgate magnetometers are able to measure the strength and direction of magnetic fields.

5.3.1 Performance

In order to determine the stability and sensitivity of the magnetometer in the experimental setup, 10 minute time traces were taken and the Allan deviation was calculated. The data in Figure 5.3 shows the Allan deviation for the applied magnetic field at various frequencies (10 Hz, 120 Hz, 500 Hz and 1 kHz) in unshielded conditions. All four sets of data were taken using the setup shown in Figure 5.1a with no object present. Figure 5.3 shows the Allan deviation of the in-phase component of the signal. For each frequency a set of four 10 minute time traces were obtained with one being when both coils are connected to the voltage source (referred to as 'on'), one with the excitation coil on, one with the compensation coil on and finally one with both of the coils disconnected (referred to as 'off'). It can be seen in all four figures that having both coils on does not affect the stability of the setup compared to only using one coil. The configuration of two coils on has the benefit of being able to apply larger magnetic fields to induce eddy currents without saturating the fluxgate magnetometer. With both coils on the smallest detectable fields are 51 pT at 10 Hz, 35 pT at 120 Hz, 62 pT at 500 Hz, and 70 pT at 1 kHz, and are in the gate time frame of 1 to 10 seconds. It can be seen that with the coils off the Allan deviation of the signal is smaller - this is most likely due to drifts in the current generating the magnetic field. The Allan deviation of the stability at 10 Hz picks up further noise when both of the coils are on due to flicker noise. To improve the sensitivity the current source could be replaced with a less noisy supply. The out-of-phase component can be found in Appendix B and has a similar stability to the in-phase component of the signal.

In order to see the how the magnetometer's noise floor changes when in shielded conditions compared to unshielded conditions, 2×1 second time traces were taken. The first time trace is in unshielded (blue data in Figure 5.4) conditions that the experiments were carried out in, where the fluxgate is placed in the setup shown in Figure 5.1a but with no coils on or samples present. The second time trace (red data in Figure 5.4) was taken with the fluxgate placed inside a mu-metal shield (Twinleaf MS-2). These time traces were then Fourier transformed to produce the spectral density of the signals, as shown in Figure 5.4. It can be seen that in the area of interest the noise floor remains relatively flat with peaks at 50 Hz and its harmonics. The sensitivity in unshielded conditions here can be seen to be higher than that in shielded conditions. This shows that the experiment is limited by environmental noise and not the intrinsic noise of the sensor. The unshielded sensitivities agrees well with that determined in the Allan deviation data (Figure 5.3) with the sensitivities reading ~ 25 pT/$\sqrt{\text{Hz}}$, ~ 30 pT/$\sqrt{\text{Hz}}$, ~ 40 pT/$\sqrt{\text{Hz}}$, and ~ 50 pT/$\sqrt{\text{Hz}}$ at 10 Hz, 120 Hz, 500 Hz, and 1000 Hz, respectively.

5.4 Example traces

Figure 5.5 shows two example time traces of the detection of conductive objects. The signals show the object is initially not present in the setup and this remains the case for ~ 5 seconds and then the object is placed into the setup for ~ 10 seconds. Three repeats were taken for each sample in all data sets. The conductive objects were placed at a distance of 22.4 cm from the excitation coil. The example traces show the demodulated signals from the output of the fluxgate when an aluminium

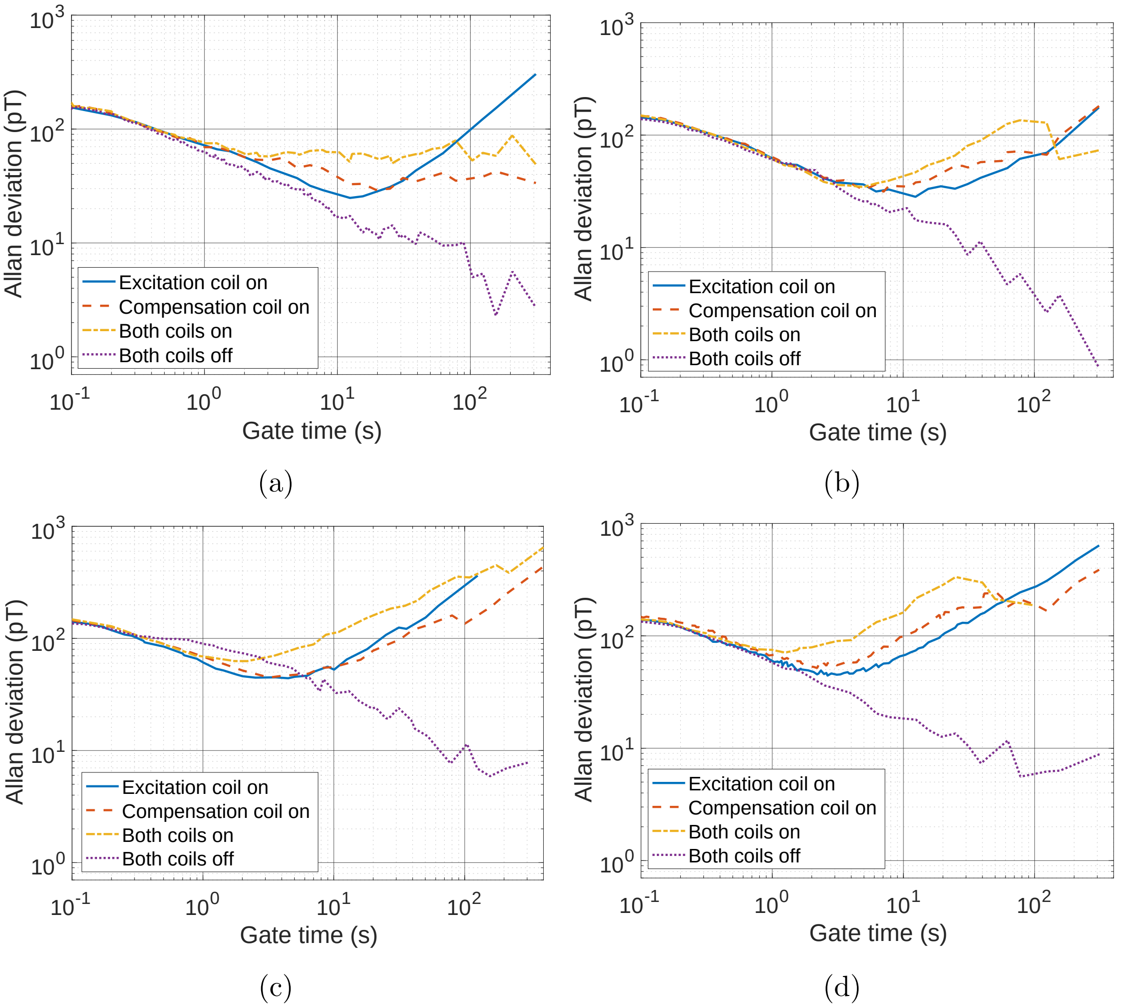

Figure 5.3: Allan Deviation of the in-phase response of the fluxgate at (a) 10 Hz, (b) 120 Hz, (c) 500 Hz and (d) 1000 Hz

(Figure 5.5a) and a steel sample (Figure 5.5b) are placed in the setup with an excitation frequency of 500 Hz. Using these traces the change in the in-phase (ΔX) and the out-of-phase (ΔY) can be calculated by subtracting the averages of the trace with and without the objects present. The standard deviation of the time traces (with and without the object) was found to be ~ 0.03 mV for both components of the signal. For the Aluminium sample at 500 Hz (Figure 5.5a) the signal to noise ratio (SNR) of ΔX is ~ 17 and for ΔY the SNR is ~ 7. The SNR is also calculated for the steel sample where for ΔX a SNR of ~ 24 can be seen and for ΔY a SNR of ~ 4.

The extracted ΔX and ΔY are used to calculate the magnitude of the secondary (induced) field relative to the primary field that is applied ($|B_{\mathrm{ec}}|/|B_1|$) at the sensing point of the magnetometer. In order to take the bandwidth of the magnetometer into account, the primary field was measured at all frequencies used in the experiments. Time traces were recorded for various frequencies between 10 Hz and 1 kHz, as shown in Section 5.5.

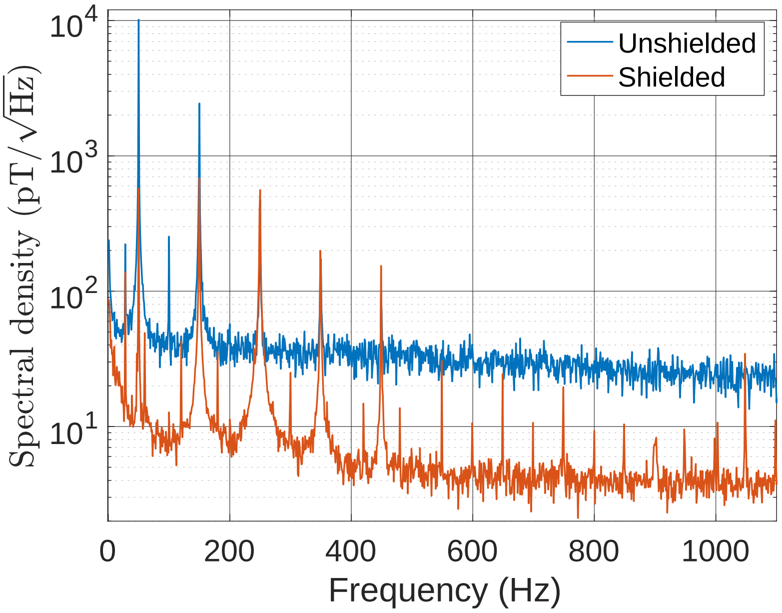

Figure 5.4: Fourier transform of one second time traces of a Bartington Mag690 fluxgate magnetometer noise floor in unshielded (blue) and shielded (red) conditions.

5.5 Varying frequency

How the secondary magnetic field induced in the conductive cylinders varies with the frequency of the primary field, f, can be seen in Figure 5.6. The signals are normalised to the amplitude of the primary excitation field. Figures 5.6a and 5.6b show the in-phase (ΔX) and out-of-phase (ΔY) signals of the field ratio for the aluminium and steel samples, respectively. Figures 5.6c and 5.6d show the signal amplitude, R and Figs. 5.6e and 5.6f show the phase, $\phi = \tan^{-1}(\Delta Y/\Delta X)$, of the secondary magnetic field relative to the primary excitation field. The dependence of the secondary signal on the frequency of the primary field is studied in a range between 10 Hz and 1 kHz. All data is presented alongside the simulated results produced using the COMSOL AC/DC module. See Appendix C.1 for further details about the simulation model.

For the aluminium cylinder (see Figure 5.6a) the signal can be seen to be primarily in the out-of-phase component at frequencies below $\sim$ 150 Hz, with the signal being linear up to $\sim$ 50 Hz. For non-magnetic conductive samples the conductivity of the sample can be determined (see Section 5.5.2.1). The overall magnetic field ratio saturates at 350 Hz, which can be seen in Figure 5.6c. This is due to the skin effect of the aluminium sample. The skin effect is important when the skin depth, $\delta = 1/\sqrt{\pi\mu\sigma f}$, becomes less than or equal to the thickness of the object, t, being detected. For the 6061 T6 Aluminium cylinder used here, with a thickness of $t = 2$ cm, $\mu = \mu_0$ and $\sigma = 24.6$ MS/m [96], the corresponding frequency at which the skin effect becomes significant is when $f \geq 1/(t^2\pi\mu\sigma) = 26$ Hz. For non-magnetic samples the signal is out of phase with respect to the primary field and hence the phase $|\phi| \sim 90^{\circ}$ for low frequencies, as can be seen in Figure 5.6e. As the frequency increases the signals phase approaches 180° and the in-phase component of the signal dominates. From this it can be seen that at high frequencies the secondary field is induced in the opposite direction to the primary field.

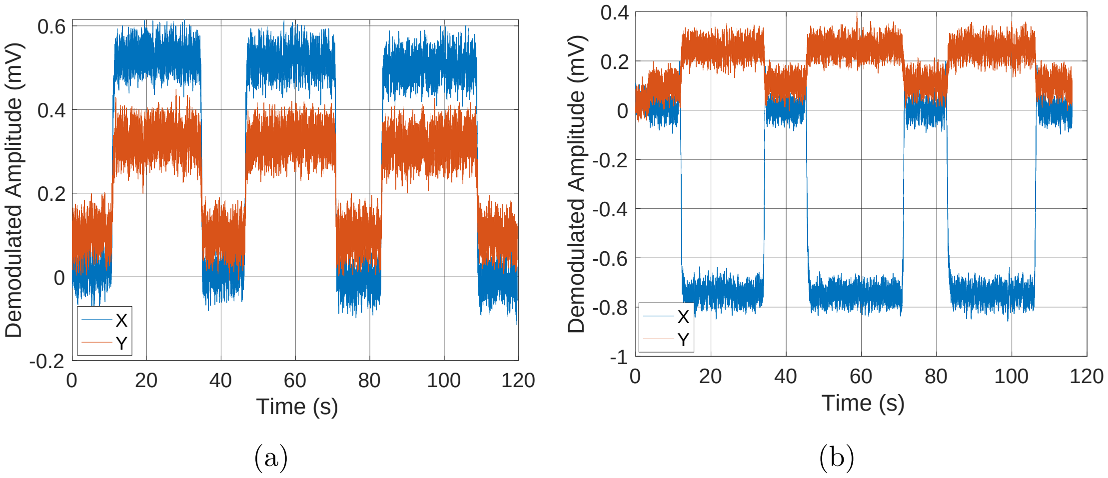

Figure 5.5: Example demodulated time traces for the detection of (a) 6061 T6 aluminium and (b) 440c steel samples in an active detection setup. For these data sets, the primary magnetic field measured 1.09 μT at the position of the magnetometer and had a frequency of 500 Hz, with the conductive objects 22.4 cm away from the excitation coil.

The conductivity of the non-magnetic sample can be determined from the gradient ($|B_{\mathrm{ec}}|/|B_1|/f$) of the signal amplitude at low frequencies, where the signal response is linear as a function of frequency. The experimental results presented in Figure 5.6c can be compared to an analytical formula valid for a non-magnetic conductive cylinder [58]. These equations are presented in detail in Section 5.5.2.1. The gradient of the magnetic field ratio in Figure 5.6c in the range up to 20 Hz was used to determined the conductivity of the aluminium sample presented here to be 25.5 (±1.8) MS/m, which is in agreement with the published value for 6061 T6 aluminium of 24.6 MS/m [96].

For a magnetic sample, such as the 440c steel shown in Figures (5.6b, 5.6d, and 5.6f), the largest signal is found at low frequencies. This is due to steel being magnetically permeable. From the phase response of the secondary field with respect to the primary field, shown in Figure 5.6f, it can be seen that the secondary field is produced in the same direction as the primary field at low frequencies ($|\phi| \sim 0^{\circ}$). The in-phase component of the signal is much larger than the out-of-phase component. It can be seen that as frequency increases the in-phase component decreases as the out-of-phase component increases. However, the in-phase component remains dominant and this results in the phase difference between the secondary and primary field (Figure 5.6f) remaining relatively small, $|\phi| \leq 20^{\circ}$ and the magnetic field ratio (Figure 5.6b) being very similar to the in-phase component of the signal. Whilst it can be seen that the magnetic field amplitude decreases with frequency it remains larger than the signal detected for aluminium in the frequency range presented.

The conductivity and permeability of the steel sample used was unknown due to the lack of studies presenting the relative permeability of 440c steel. In Ref. [58], a sample of 440c steel is studied where the relative permeability of the sample is found to have a value of $\mu_r = 16 - 17$. Aside from this study, no other studies were found so it is unknown how this value changes between different samples. When the relative permeability is low, a small change in the relative permeability leads to a large change in the signal that is detected [58, 60]. In order to determine

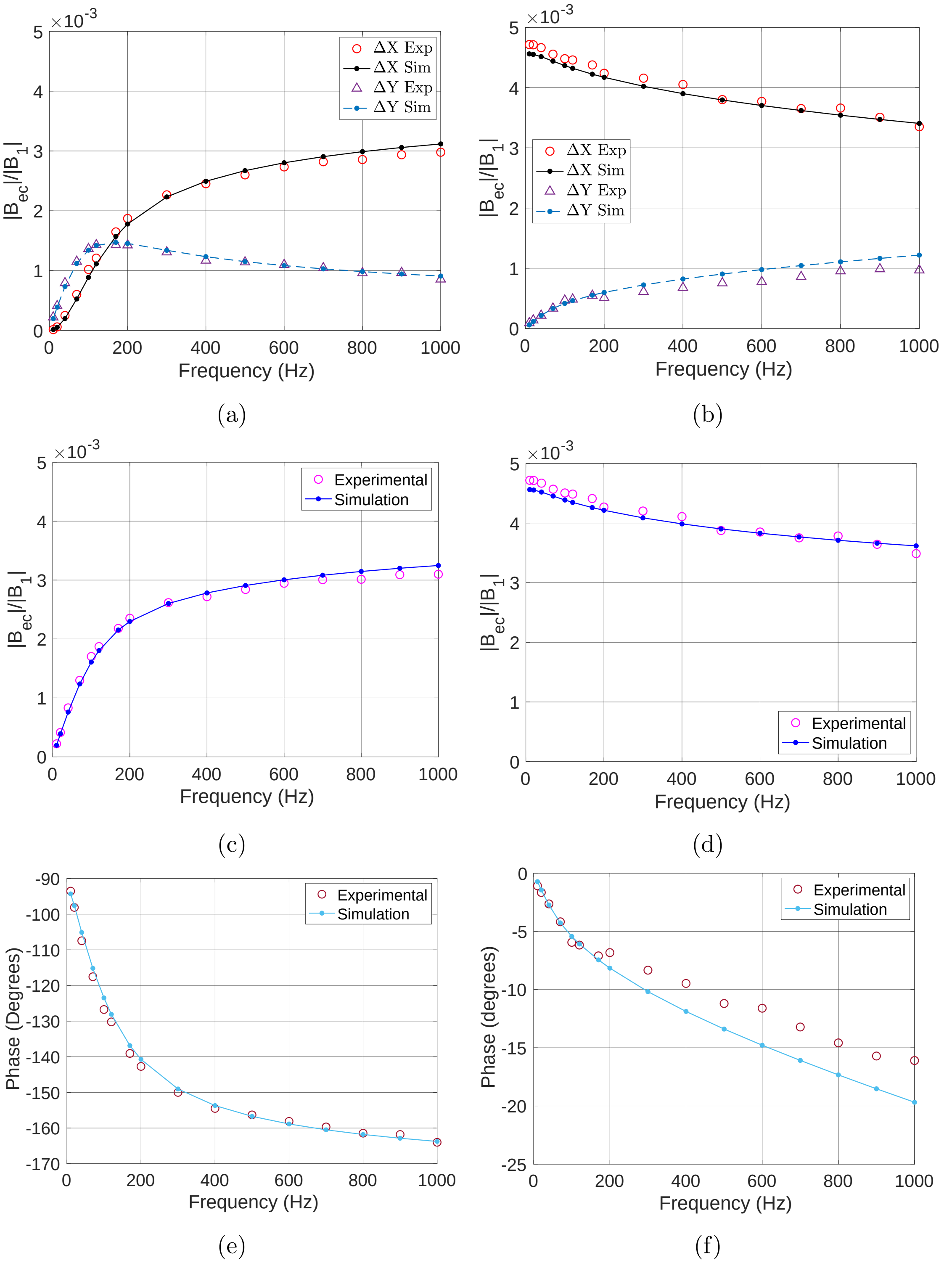

Figure 5.6: Frequency response of the induced secondary magnetic field produced from (a, c, e) a solid 6061 T6 aluminium cylinder and (b, d, f) a solid 440c steel cylinder. The frequency of the field was varied from 10 Hz to 1 kHz. (a, b) The in-phase ΔX and out-of-phase ΔY components normalised to the primary field. (c, d) The ratio of the magnetic field amplitude of the secondary field to the primary field at the sensing point of the magnetometer. (e, f) The phase (degrees) of the secondary magnetic field with respect to the primary magnetic field.

the conductivity and relative permeability of the sample, the theory presented in Ref. [58] was adapted to the setup presented in Figure 5.1a. These values will then be used to produce the simulated data in COMSOL. Fitting these equations to the experimental data for steel in Figure 5.6 the conductivity of the 440c steel sample used here was found to be $\sigma = 1.67(\pm 0.2)$ MS/m and the relative permeability to be $\mu_r = 50(\pm 15)$. Full details can be found in Section 5.5.2.2. These values were used for the simulation model in which the data was found to agree within $\sim 5\%$ of the experimental data, with both sets following the same trends. Hence, these values were used throughout the simulations.

Figure 5.6 shows the frequency response of the secondary fields produced by the two cylinders side by side. It can be seen that by varying the frequencies the magnetic and non-magnetic samples can be distinguished, especially if the phase of the induced field is looked at (Figure 5.6e and Figure 5.6f). At low frequencies the phase of the secondary magnetic field produce is approximately 0° for the steel sample (magnetic), while the phase is around 90° for the aluminium sample (non-magnetic).

5.5.1 Hollow cylinders

As well as testing the frequency response of solid cylinders, the response of hollow cylinders with a wall thickness of 4 mm were tested. Both cylinders are shown in Figure 5.1b and have the same outer dimensions as the solid samples. They are made from the same materials as the solid cylinders. Figure 5.7 shows a comparison for the 6061 T6 aluminium cylinders (Figure 5.7a) and the 440c steel cylinders (Figure 5.7b). It can be seen that the signals are very similar for both the hollow and solid cylinders. This is due to the cylinders having the same dimensions. Hence results presented in the remainder of this chapter will only focus on the solid cylinders.

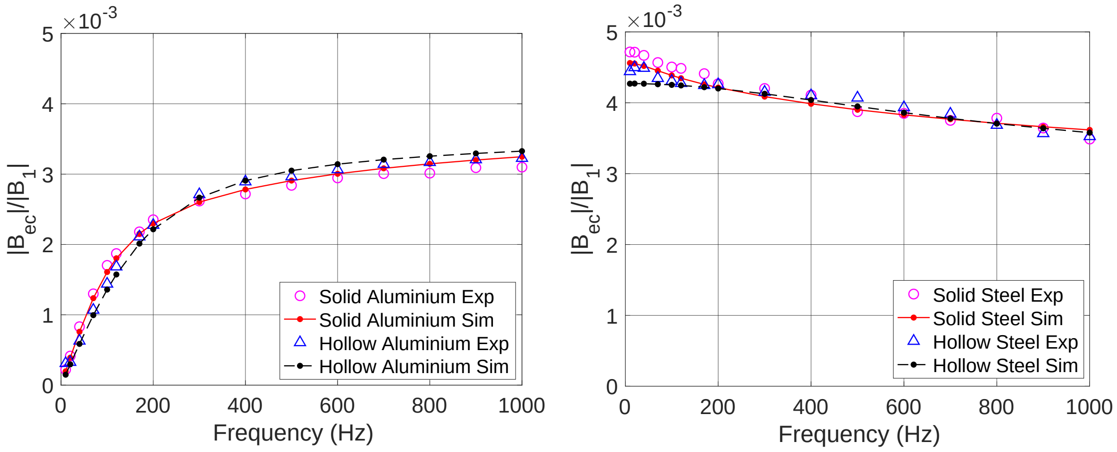

(a) (b)

Figure 5.7: Comparison of the experimental and simulated frequency response of hollow and solid cylinders made from (a) 6061 T6 aluminium and (b) 440c steel cylinders. The frequency was varied from 10 Hz and 1 kHz.

5.5.2 Characterising conductive objects

The conductivity of the aluminium and steel sample can be determined theoretically. The permeability can also be determined using theory for sources with an unknown value [56, 58]. Figure 5.1a shows the experimental setup with the corresponding theoretical parameters for a sample of radius r and thickness t. The distance from the centre of the excitation coil to the centre of the sample is denoted by a and the distance from the centre of the sample to the detection point of the magnetometer is a'.

5.5.2.1 Aluminium

Using the low frequency limit of the data presented in Figure 5.6c, the conductivity of the aluminium sample can be determined. Equations presented here are of the form of those found in [56] that have been altered to match the setup described in Section 5.2.

The current that is induced in a thin area, from ρ to $\rho+d\rho$, of a cylinder is given by

$$dI = \frac{mt}{2\pi\delta^2}\frac{\rho}{(a^2+\rho^2)^{3/2}}d\rho, \tag{5.1}$$

where m is the magnetic dipole moment of the coil and δ is the skin depth. This current induces a magnetic field that at the detection point of the sensor reads

$$dB_{\text{ec}} = \frac{\mu_0 dI}{2}\frac{\rho^2}{(\rho^2+a'^2)^{3/2}}. \tag{5.2}$$

Integrating from the centre of the cylinder $\rho = 0$ to the outer radius of the cylinder $\rho = r$ gives the total magnetic field induced by the eddy currents at the magnetometer. For the setup in this thesis, $a \neq a'$ and hence

$$B_{\text{ec}} = \frac{mt\mu_0}{4\pi\delta^2}\left(\frac{a^2(2a'^2+r^2)+a'^2r^2}{(a^2-a'^2)^2\sqrt{a^2+r^2}\sqrt{a'^2+r^2}} - \frac{2aa'}{(a^2-a'^2)^2}\right). \tag{5.3}$$

Note that if $a = a'$ then Equation 5.3 is not defined. This is due to the integral simplifying before the integral, which is presented in [56]. Both of the equations tend to the same limit as $a \rightarrow a'$. By substituting in the equation for the skin depth, $\delta^2 = 1/(f\pi\mu\sigma)$, and dividing through by $fB_1 = f\mu_0 m/2(a+a')^3\pi$ at the detection point of the magnetometer it can be found that

$$\frac{B_{\text{ec}}}{B_1 f} = \frac{t\pi\mu\sigma}{2}\frac{(a+a')^3}{(a^2-a'^2)^2}\left(\frac{a^2(2a'^2+r^2)+a'^2r^2}{\sqrt{a^2+r^2}\sqrt{a'^2+r^2}} - 2aa'\right). \tag{5.4}$$

Here the only unknown parameter is σ and the left hand side of the equation is given by the gradient of the magnetic field ratio in the low frequency limit where the relationship is linear. By using a fit function in MATLAB and the experimental data for the aluminium source in Figure 5.6c the conductivity of 25.5 (±1.8) MS/m can be extracted, which is in agreement with the data sheet for 6061 T6 aluminium [96].

5.5.2.2 Steel

A similar method to that described above can be used to calculate the conductivity and magnetic permeability of magnetic objects, such as the 440c steel used in this thesis. The theory presented here is built upon from the equations found in [58, 60] that have been altered to match the experimental setup presented here (see Figure 5.1a). Note a key difference from the theories presented in [58, 60] is that in this case a cylindrical sample is used instead of a spherical sample. Using the data in Figure 5.6d the conductivity and permeability of the steel cylinder presented can be extracted.

The primary magnetic field at the centre of the cylinder is given by

$$B_1(z=a)=\frac{\mu_0 m}{2\pi a^3}, \tag{5.5}$$

where m is the magnetic moment of the excitation coil, a is the distance from the centre of the excitation coil to the centre of the object and μ_0 is the vacuum permeability. This induces a secondary magnetic field at the sensing point of the magnetometer, which is equal to

$$B_{\mathrm{ec}}(z=a+a')=\frac{\mu_0 m_{\mathrm{ec}}}{2\pi a'^3}. \tag{5.6}$$

Here m_{ec} is the magnetic moment that is induced in the conductive object. For a sphere of radius r the magnetic moment is given by

$$m_{\mathrm{ec}}=\frac{2\pi r^3 B_1(z=a)}{\mu_0}\frac{2(\mu_r-1)j_0(kr)+(2\mu_r+1)j_2(kr)}{(\mu_r+2)j_0(kr)+(\mu_r-1)j_2(kr)}, \tag{5.7}$$

where j_0 and j_2 are spherical Bessel functions and μ_r is the relative permeability [58]. The propagation constant is given by $k=\sqrt{\mu\varepsilon\omega^2+i\mu\sigma\omega}$ where ε is the permittivity of the sample, $\mu=\mu_0\mu_r$ and $\omega=2\pi\nu$.

By dividing Equation 5.6 by Equation 5.5, at the detection point of the magnetometer ($z=a+a'$), the magnetic field ratio can be determined. Simplifying this equations gives

$$\frac{B_{\mathrm{ec}}(z=a+a')}{B_1(z=a+a')}=\frac{r^3(a+a')^3}{(aa')^3}\frac{2(\mu_r-1)j_0(kr)+(2\mu_r+1)j_2(kr)}{(\mu_r+1)j_0(kr)+(\mu_r-1)j_2(kr)}, \tag{5.8}$$

which can be used as a function to fit the experimental data to. This equation assumes a uniform magnetic field is induced across the spherical object. However, due to the fact that the cylindrical sample has a finite size the primary field will not be perfectly uniform across the sample.

Figure 5.8 shows how the theory compares to the simulated and experimentally obtained data. It can be seen that Equation 5.8 shows good agreement with the experimental data if a scale factor is introduced. Using a fit function in MATLAB, and the parameters that match the experimental setup (see Section 5.2), it is possible to determine μ_r, σ and the scale factor for the 440c steel cylinder used in this chapter. The scale factor was calculated to be 0.56 (±0.01). Hence the theory overestimates the experimental results of $|B_{\mathrm{ec}}|/|B_1|$ by 79 (±3)%. The values for the permeability and conductivity were determined as $\mu_r = 50$ (±15) and $\sigma =$ 1.67 (±0.20) MS/m. The function was fitted to the real and imaginary components of the field ratio $|B_{\mathrm{ec}}|/|B_1|$ (see Figure 5.6b). This method can also be used to calculate the conductivity of non-magnetic samples, such as aluminium, using the known relative magnetic permeability of $\mu_r = 1$.

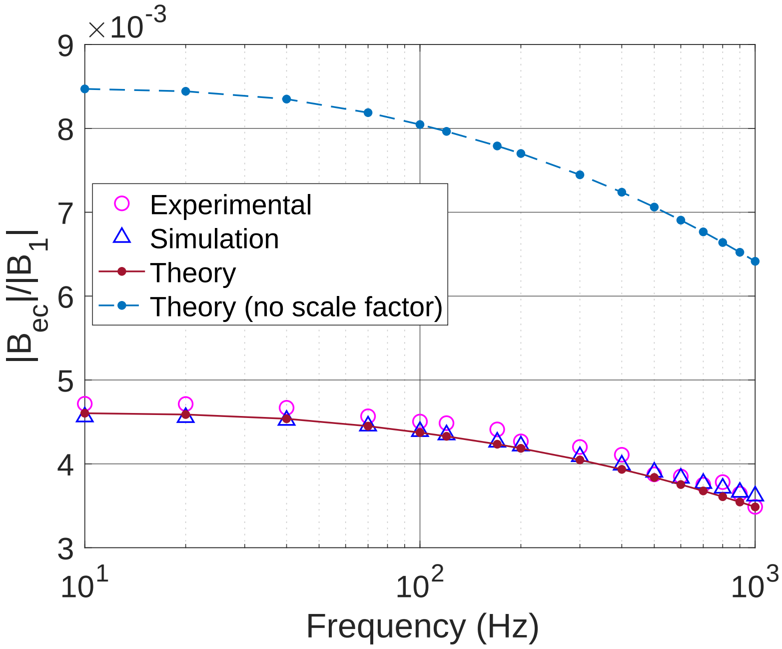

Figure 5.8: Fitting the theoretical model to experimental data to extract the conductivity (σ) and relative permeability (μ_r) of the 440c steel cylinder.

5.6 Varying distance

How the signal changes with distance was studied for the objects being moved on-axis and off-axis, with the object 22.4 cm away from the excitation coil in the z-direction. These results are compared to COMSOL numerical simulations (see Ap. C.1). The measurements were taken at a fixed frequency of 500 Hz as at this frequency large signals are seen for both conductive objects.

5.6.1 On-axis

Figure 5.9 shows how the magnetic field detected by the magnetometer changes as the object is moved along the z-axis. The excitation coil is placed at 0 cm and the object is placed at different positions between 5 cm to 39.5 cm, with respect to the excitation coil's position. For both conductive objects presented in Figure 5.9 the magnetic field ratio detected by the magnetometer is smallest when the object is halfway between the excitation coil and fluxgate detection point. The signals are the largest when closest to the excitation coil or the magnetometer. When comparing the response of the aluminium cylinder (Figs. 5.9a and 5.9c) to the steel cylinder (Figs. 5.9b and 5.9d) it can be seen that the steel cylinder produces a larger signal amplitude, as expected from Section 5.5. It can also be seen that the in-phase and out-of-phase signals have an opposite signs for the steel cylinder. For both conductive cylinders the numerical simulations can be seen to be in good agreement with the experimental data.

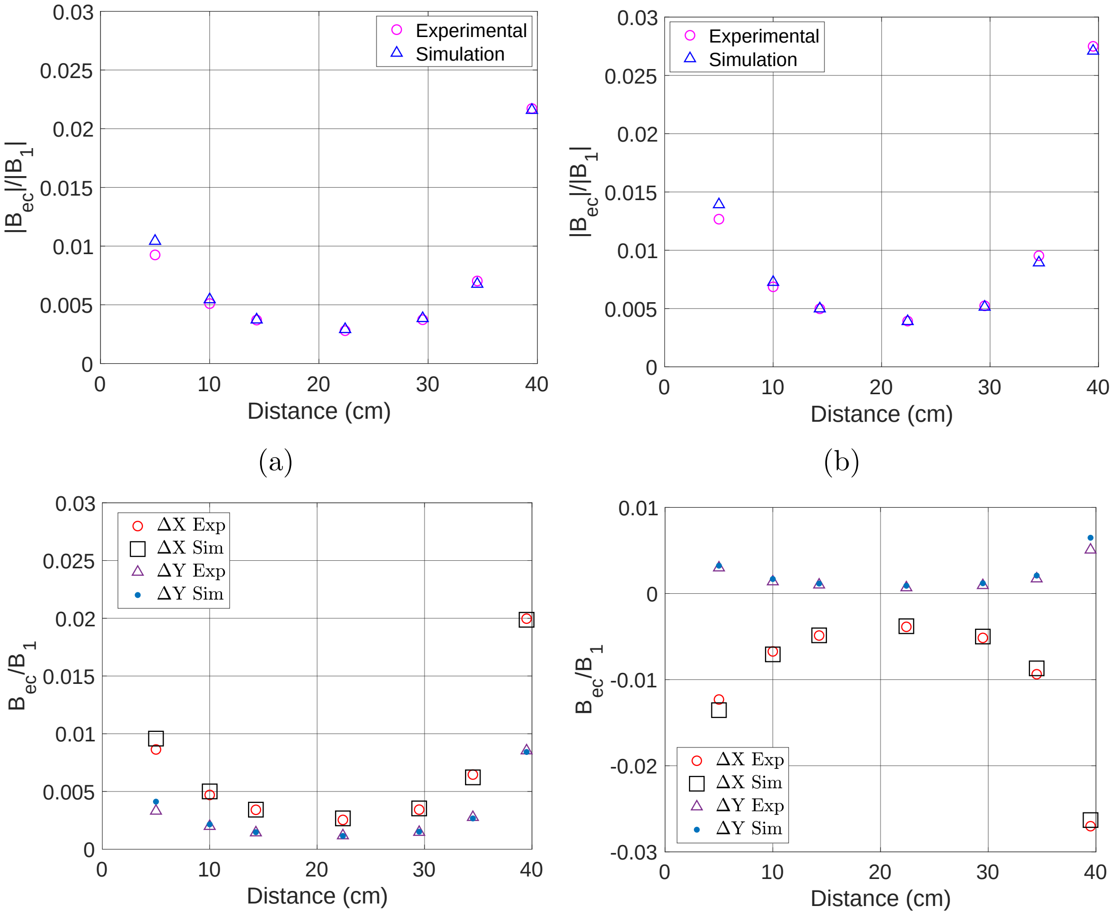

(a) (b)

(c) (d)

Figure 5.9: On-axis detection of conductive cylinders at varying distances between 5 cm to 39.5 cm, with respect to the position of the excitation coil. The amplitude of the magnetic field ratio for (a) 6061 T6 aluminium and (b) 440c steel. (c) and (d) represent the change in the in-phase and out-of-phase components of the demodulated signal when aluminium and steel cylinders are present, respectively.

5.6.2 Off-axis

As well as looking at how the induced field changes with the position of the object on-axis, how the field changes with distance off-axis is also of interest. For the detection of objects in real world conditions the chance of the object being on-axis might be out of the control of the experiment. Hence, studying the response of the signal as the objects distance is varied off-axis is of interest. The conductive objects were varied from $x = 0$ cm (on-axis) to $x = 34.5$ cm off-axis. The object was placed at a fixed distance from the excitation coil in the z-direction of 22.4 cm. The frequency of the primary field was set to 500 Hz. Figure 5.10 shows that as both the aluminium and steel objects are moved off-axis their signal amplitudes drop and the sign of the signal changes. For the aluminium sample (Figure 5.10c) the signals change their sign when the cylinder is approximately 16 cm off-axis. Similarly, the signal for the steel cylinder changes sign when the object is approximately 12 cm off-axis. These findings are validated by the simulated results. The change in sign of the magnetic field is due to the orientation of the induced dipole. Only the z-

component of the field was recorded experimentally however, the magnetic field will also have a x-component when the object is moved off-axis. The COMSOL model was used to study how all three components of the magnetic field change as the conductive objects are moved off-axis. Figure 5.11 shows the simulated results for the $|\mathbf{B_x}|$, $|\mathbf{B_y}|$ and $|\mathbf{B_z}|$ components of the induced magnetic field. In the simulation an excitation frequency of 500 Hz was used to match the experimental conditions. It can be seen that for both the non-magnetic and magnetic cylinders the z-component of the induced magnetic field is maximal when the object is on-axis ($x = 0$ cm). The x-component of the field is at a maximum around 5 to 10 cm for both of the conductive samples. The y-component of the field remains at zero for all distances, as the induced dipole is in the (x, z)-plane.

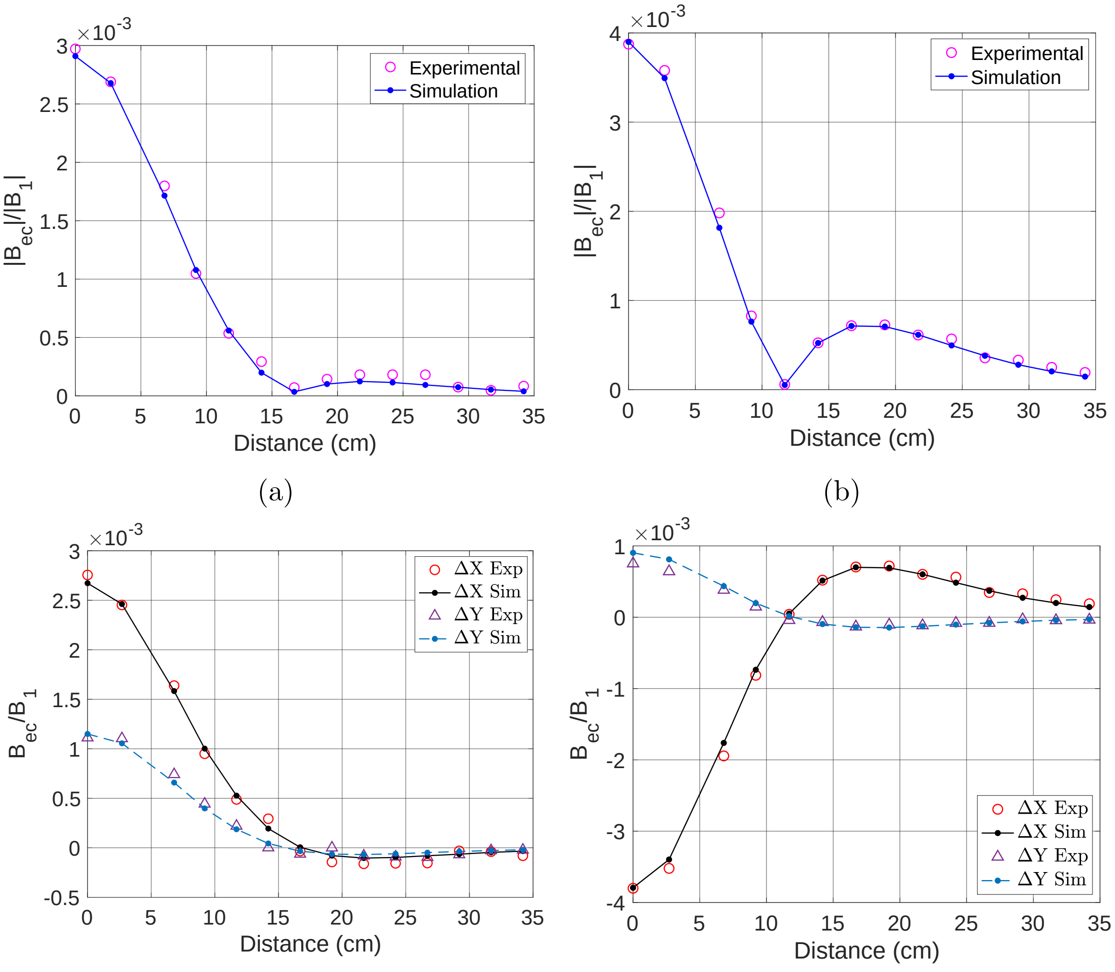

(a) (b)

(c) (d)

Figure 5.10: Magnetic field response as (a, c) an aluminium cylinder and (b, d) a steel cylinder is placed at varying distances between 0 cm and 34.5 cm off-axis. (a, b) is the induced field amplitude with respect to the primary field and (c, d) the in-phase and out-of-phase components of the induced field.

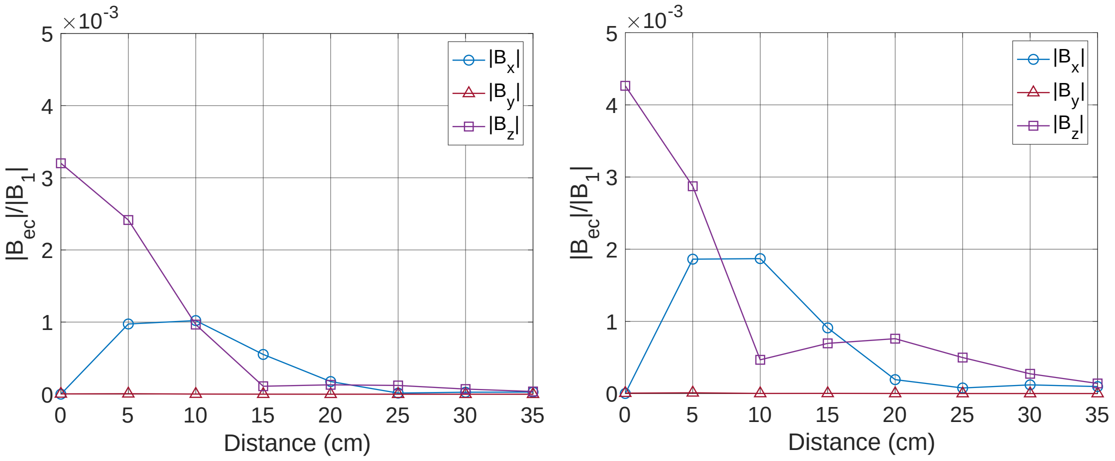

(a) (b)

Figure 5.11: COMSOL simulation results of the $\boldsymbol{B}_x$, $\boldsymbol{B}_y$ and $\boldsymbol{B}_z$ components of the induced field as a function of distance as non-magnetic (aluminium) and magnetic (steel) objects are moved off-axis.

5.7 Conclusion

In this chapter it has been demonstrated how commercially available magnetic field sensors can be used to detect and characterise conductive and magnetic objects at low frequencies. With varying the frequency the non-magnetic (aluminium) and magnetic (steel) samples have different responses so can be easily distinguished with both samples matching the theoretical predictions [56, 60, 58]. The experimental results are in good agreement with the COMSOL simulations. By varying the distance of the objects on- and off-axis the capability of the setup to detect objects at a variety of positions is shown. Using COMSOL for the off-axis measurements shows how not only the z-component of the magnetic field changes with distance off-axis, along the y-direction, but also the x-component. So, as the signal in the z- component is low the component in the x-direction is larger so could be used to also track the object. Although these measurements were carried out in a laboratory environment the setup could easily be modified and scaled for 'real world' applications as all data was taken in an unshielded environment with no active feedback system to cancel residual fields. As long as the residual fields are within the operating range of the magnetometer (±1 Gauss) then the setup works well in the Earth's magnetic field. In order to improve the detectable distance and object size that could be detected in the setup a magnetic field sensor with an improved sensitivity could be used in place of the fluxgate magnetometer. An optically pumped magnetometer has the improved sensitivity required for the detection of smaller secondary magnetic fields [2, 29, 100].

Chapter 6

Table-top alignment based magnetometry

6.1 Motivation

Optically pumped magnetometers [15, 16] are highly sensitive magnetic field sensors with typical sensitivities in the fT/$\sqrt{\text{Hz}}$ range [20, 50, 24, 23, 101]. OPMs are based upon spin polarised atomic ensembles and their interaction with light. Current commercially available OPMs operate near to zero magnetic field in the spin-exchange relaxation free (SERF) regime [40, 41, 47, 42], or in the Earth's magnetic field as a scalar magnetic field sensor measuring the total magnetic field amplitude. These OPMs use one or two laser beams that are typically circularly polarised and are generated from a signal laser diode inside the sensor head. This makes them compact and robust. These detectors have shown great potential in numerous areas, especially in magneto-encephalography [102, 22, 19].

In order to detect oscillating magnetic fields in the kHz-MHz frequency range, radio frequency (RF) magnetometers need to be used [21, 103, 104, 31, 105]. The atomic ensemble can be polarised in either an oriented [50, 24, 23] or aligned state [85, 51, 64, 106, 18]. RF-OPMs have many potential applications in areas such as medical physics [61, 37, 25], remote sensing [31, 2] and non-destructive testing [28, 100, 59, 107]. The focus in this thesis, and in this chapter, is of atomic ensembles optically pumped into an aligned state. This is known as an alignment based magnetometer (also referred to as 'double resonance alignment magnetometer' or 'RF-OPM based on non-linear magneto-optical rotation') where the atomic spins have a preferred axis but not direction. Alignment based magnetometers use a single linearly (π) polarised laser beam to pump and probe the atoms.

Long spin coherence times are required to gain high sensitivities in an OPM. This is achieved by using anti-relaxation coatings or adding a buffer gas to vapour cells. Anti-relaxation coated cells are hand-blown and typically lined with paraffin. The coating allows moving alkali atoms to bounce off the cell walls multiple times without losing their spin coherence [108, 109]. Adding a buffer gas to a vapour cell also prolongs the spin coherence as the collisions between the buffer gas atoms and the alkali atoms result in the alkali atoms diffusing slowly. Hence reducing the collisions the alkali atoms have with the vapour cell walls which destroys the spin coherence. Buffer gas cells can be made via micro-fabrication techniques [65, 66] meaning they can be mass produced which is ideal for the commercialisation of

RF-OPMs.

Current demonstrations of alignment based magnetometry have used anti-relaxation coated cells [51, 64]. These show promising results with high sensitivities however, due to the cells being handmade, there are limitations in the potential for commercialisation with the use of anti-relaxation coated cells. Buffer gas cells are a viable alternative but also come with their own issues that need to be considered. The addition of a buffer gas, in this case N_2, causes pressure broadening in the absorption spectrum which affects the optical pumping that prepares the aligned state. The pressure needs to be carefully selected such that the spin-coherence time is sufficiently prolonged but the $F = 4 \rightarrow F' = 3$ and $F = 4 \rightarrow F' = 4$ peaks are still clearly distinguishable in the spectrum. The buffer gas also acts as a quenching gas which causes rapid collisional mixing in the excited states [72]. This also affects the optical pumping into an aligned state (see Section 2.6).

In this chapter, it will be demonstrated that despite the added complexities it is possible to use a buffer gas cell in an alignment magnetometer and obtain high sensitivities. It is experimentally demonstrated that using a 65 Torr N_2 buffer gas cell a sensitivity of 310 $\mathrm{fT}/\sqrt{\mathrm{Hz}}$ is obtained at 10 kHz. A paraffin coated cell of similar dimensions is also placed into the experimental setup in place of the buffer gas cell. The results from both vapour cells are then compared. These results open up the possibility for miniaturisation [29, 2, 49] and commercialisation of RF-OPMs.

6.2 Experimental setup

Figure 6.1 shows an image and a schematic of a table-top alignment based magnetometer. Linearly polarised light with a wavelength of 895 nm is passed through an optical fibre from a home-made laser diode system (see Section 6.3). The laser light is locked on resonance with the $F = 4 \rightarrow F' = 3$ transition on the caesium D1 line (see Figure 2.1) using the absorption spectroscopy of a caesium reference cell. The output is collimated and propagates along the x-direction. The first set of a half wave plate ($\lambda/2$) and polarising beam splitter (PBS) is used to ensure that the output polarisation is vertically polarised such that the electric field amplitude $\boldsymbol{E}_0\hat{\mathbf{z}}$ passes through the vapour cell. This prevents fluctuations in the laser from small changes in the polarisation at the output of the fibre. These small fluctuations can be caused by temperature changes in the lab. The second set of a half wave plate ($\lambda/2$) and polarising beam splitter (PBS) is to vary the light power of the laser before it enters the vapour cell. A caesium vapour cell is placed inside a mu-metal magnetic shield (Twinleaf MS-1 shown is Figure 6.1a). In this chapter two different caesium vapour cells are used. Figure 6.2a shows a paraffin coated cell which has an anti-relaxation coating on the windows. The cell is a (5 mm)^3 cubic vapour cell at room temperature (~ 18°C). Figure 6.2b is a caesium cell filled with a nitrogen buffer gas. The cell has a diameter of 5 mm and an optical path length of 5 mm. The buffer gas cell is surrounded by a Shapal cover and heating wires which are fixed in place using kapton tape, as shown in Figure 6.2c. The Shapal cover allows uniform heat distribution over the cell from the heating wires. The buffer gas cell is heated to between 50°C and 55°C.

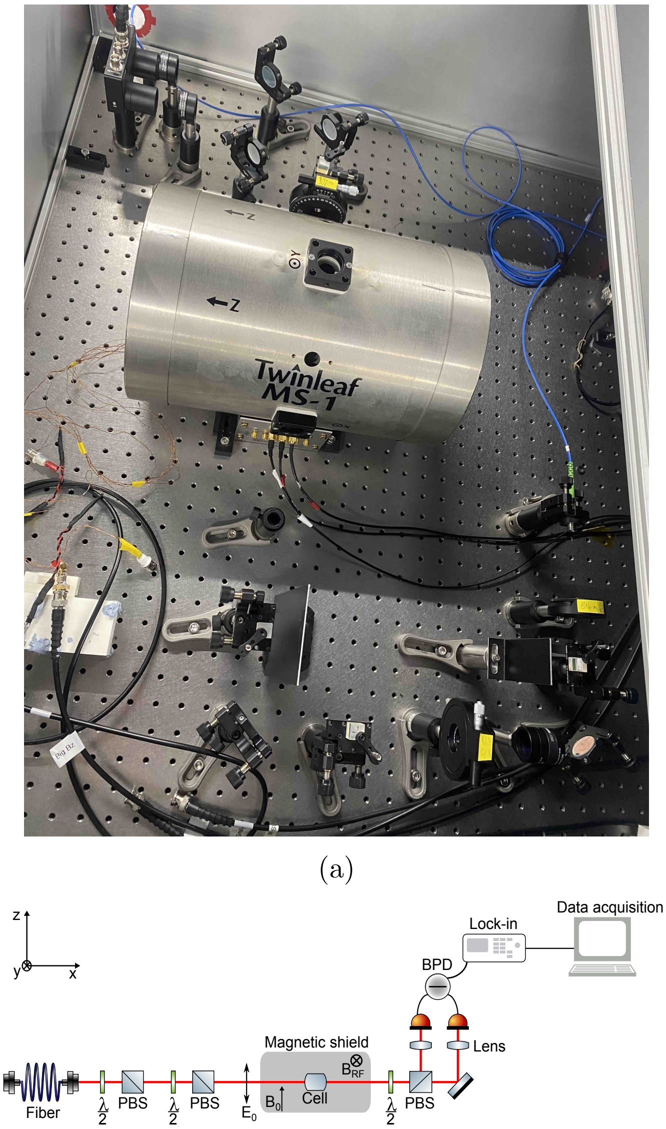
(a)

(b)

Figure 6.1: (a) Image of an experimental setup of a table-top alignment based magnetometer with a (b) schematic of the setup shown. The laser light propagates along the x-direction with its light polarisation in the z-direction. The light is passed through two sets of half wave plate ($\lambda/2$) and polarising beam splitter (PBS). The first set is to maintain the correct polarisation and the second is to set the light power. The light then passes through a caesium vapour cell that is placed inside a magnetic field. Inside the shield a static field $\mathbf{B}_0$ is applied along the z-direction and an oscillating field $\mathbf{B}_{\mathrm{rf}}(t)$ is applied along the y-direction. After the cell, polarisation rotation measurements are detected using a balanced photodetector. The output is demodulated using a lock-in amplifier.

A static magnetic field $\mathbf{B_0} = B_0\hat{\mathbf{z}}$ is applied along the z-direction using the coils built into the Twinleaf MS-1 magnetic shield. An oscillating magnetic field $\mathbf{B}_{\mathrm{rf}}(t) = B_{\mathrm{rf}}\cos(2\pi\nu_{\mathrm{rf}}t)\hat{\mathbf{y}}$ is applied along the y-direction where ν_{rf} is the RF frequency in Hertz. This can also be written in terms of rads^{-1} as $\omega_{\mathrm{rf}} = 2\pi\nu_{\mathrm{rf}}$. In the case of the paraffin coated cell, the oscillating magnetic field is produced using a home-made single coil with a diameter of 3 mm that is placed 1.5 cm away from the vapour cell.

In order to create a uniform field for the buffer gas cell, the oscillating magnetic field was produced using a square home-made Helmholtz coil placed in the y-direction.

After the vapour cell, polarisation rotation of the transmitted light is measured. This is done using a half wave plate and a polarising beam splitter. The half wave plate is used to rotate the polarisation of the light to a 45° angle. When this light is then passed through a polarising beam splitter half of the light is horizontally polarised so is transmitted and the other half of the light is vertically polarised and is reflected. The two components of the laser light are then directed to two photodiodes on a balanced photodetector. The photodetector used for the majority of this chapter is a Thorlabs PDB210A/M. The photodetector has a 1 MHz bandwidth. Where noted in this chapter a home-made balanced photodetector, presented in Section 9.4.1, is used in place of the commercial detector. The light incident on each detector is balanced when no magnetic fields are present in the magnetic shield. The photodiodes convert the laser power into a current. The two current outputs of the photodiodes are then subtracted, amplified and converted into an output voltage. The signal oscillates at the driving RF frequency. The oscillating output signal from the balanced photodetector is fed into a lock-in amplifier (Stanford Research Systems SR830 Lock-In Amplifier) which is then demodulated at the RF frequency. This produces two signal which are the in-phase (X) and out-of-phase (Y) components of the demodulated signal.

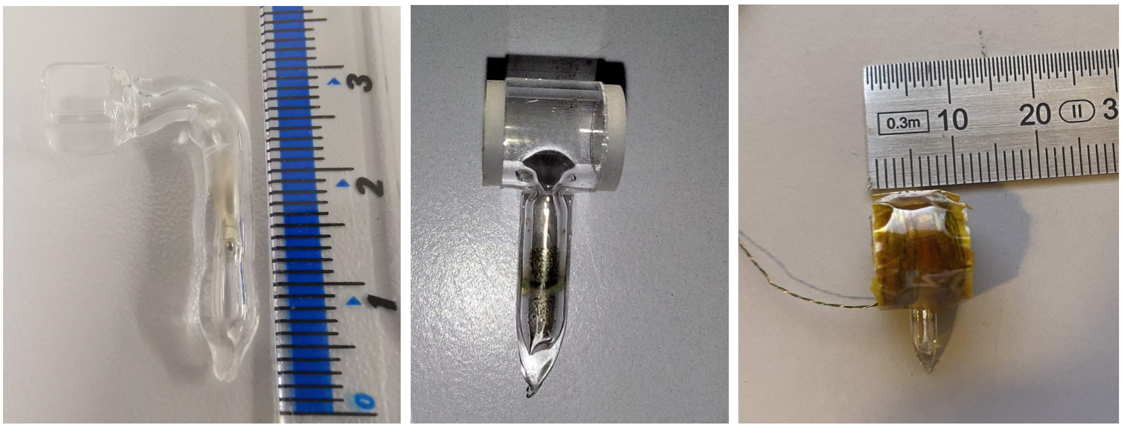

(a) (b) (c)

Figure 6.2: Caesium filled vapour cells used in the alignment based magnetometers presented in this thesis: (a) a $(5\text{ mm})^3$ paraffin coated cell, (b) a 5 mm diameter and 5 mm long nitrogen buffer gas cell, (c) buffer gas cell from (b) with a Shapal cover and heating wires that are surrounded by kapton tape.

6.3 Laser system

Throughout this thesis a home constructed laser system is used, as shown in Figure 6.3, that is housed inside a 30 cm × 20 cm × 11 cm enclosure. The entire system is mounted on an aluminium bread board, is light in weight and hence completely portable. The laser system is made up from a butterfly DBR laser (Thorlabs DBR895PN, shown in Figure 6.3bi) which is controlled by a CTL200 Koheron laser controller. The laser setup is fibre coupled with the output from the DBR laser being split into three using a custom made fibre splitter from Thorlabs (see Figure 6.3bii).

Two of the outputs of the splitter carry 25 % of the laser light and the third carries 50 %. Two of the fibre outputs (25 % and 50 %) are coupled directly as outputs from the laser box to be used in the experiments. The other 25 % fibre output is used to perform absorption spectroscopy in the enclosure.

The absorption signal is used to lock the laser to the $F = 4 \to F' = 3$ D1 transition. The laser is passed through a reference caesium vapour cell with a diameter of 2.5 cm and a length of 7.5 cm, which can be seen in Figure 6.3a. The transmitted light is detected using a photodiode (Thorlabs SM05PD1A) and the signal is amplified using a transimpedance amplifier (Koheron PD10TIA). The amplified photodiode signal is then sent to a Red Pitaya. A Red Pitaya can be used as an alternative to many lab instruments, such as data acquisition, function generation and lock-in amplification [110]. The Red Pitaya modulates the signal to give the absorption spectra and an error signal that can be used to lock the laser to the correct transition.

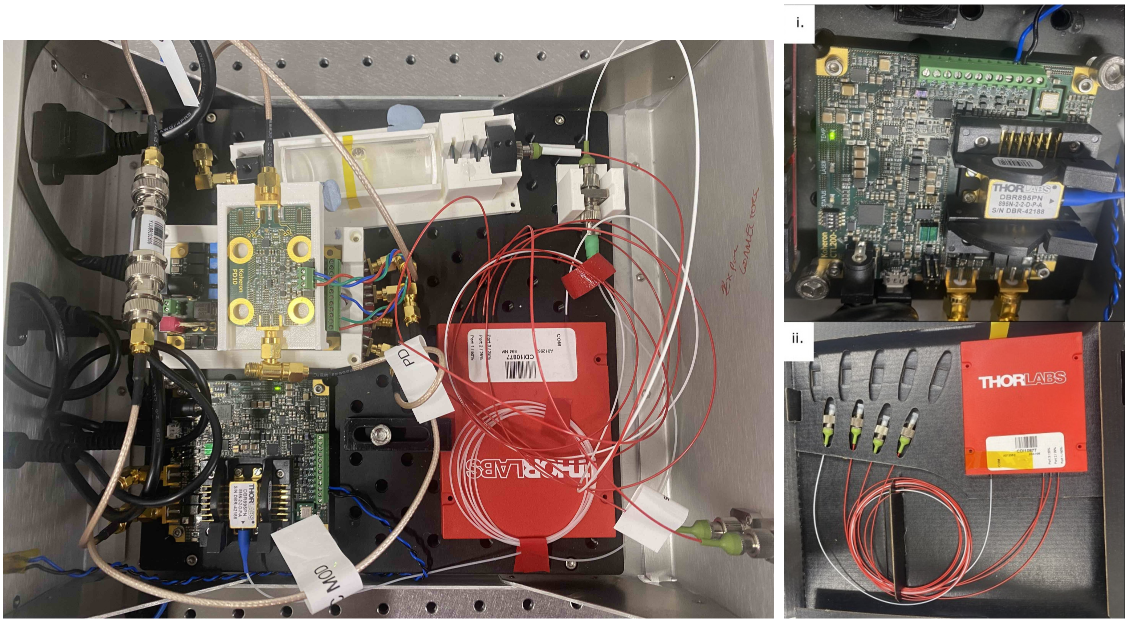

(a) (b)

Figure 6.3: (a) Image of the inside of the D1 laser system used throughout this thesis. (b) Key components of the laser setup are (i) the Thorlabs DBR895PN butterfly laser embedded on the Koheron CTL200 Digital butterfly laser diode controller and (ii) the Thorlabs custom made fibre splitter that is compatible with the D1 caesium line. The fibre splitter has three outputs of 25%, 25% and 50%.

6.4 Characterisation of a paraffin coated cell

To obtain the maximal sensitivity from an optically pumped magnetometer, the laser light power need to be optimised and the maximal RF magnetic field that can be used, whilst still in the linear regime, needs to be determined. The conversion from the RF voltage applied to the coil to the magnetic field that the atoms see needs to be calibrated so that the signal amplitude can be determined in terms of the magnetic field amplitude that the atomic ensemble measures. Carefully tuning these factors optimises the sensitivity of the magnetometer allowing smaller magnetic fields to be detected.

6.4.1 Calibrating RF coils

In order to calculate the sensitivity of an optically pumped magnetometer the RF field ($\mathrm{B_{rf}}$) that the atoms see needs to be calibrated. A conversion from voltage to field is obtained by calibrating the two RF coils, excitation and compensation, with the paraffin cell. The voltage is supplied to the coil either using a function generator (Rigol DG1032Z) or the sinusoidal output on a lock-in amplifier (Stanford lock-in SR830), both of which have an output impedance of 50 $\boldsymbol{\Omega}$. One coil is placed above the vapour cell and one below. Both are approximately 1.5 cm from the centre of the cell and both produce a field in the y-direction. It is noted that for the sensitivity measurements only the excitation coil is used. The compensation coil is used for eddy current detection and hence also needs to be calibrated. As both coils are calibrated in this section either can be used to obtain the sensitivity of the magnetometer.

In order to calibrate the excitation coil a small oscillating magnetic field is applied to the compensation coil. This acts as the RF field for the magnetometer and a small amplitude is used (40 $\mathrm{mV_{rms}}$). The residual magnetic field in the x- and y-direction should then be nulled as $\omega_L \propto \sqrt{B_x^2 + B_y^2 + B_z^2}$. In the case presented here this was done using the coils integrated into the magnetic shield (Twinleaf MS-1). With the field nulled in two directions the Larmor frequency now only depends on the magnetic field in the direction that the static field is being applied, i.e. $\omega_L = \gamma_{\mathrm{cs}} B_z$, where γ_{cs} is the gyromagnetic ratio of caesium, and the RF coils can now be calibrated. DC voltages of amplitudes varying from −1 V to 1 V are applied to the excitation coil using a function generator. The magnetic resonance signal from the lock-in amplifier is recorded for each DC voltage applied, as can be seen in Figure 6.4a, with the 'R' amplitude being fitted to a Lorentzian function. The central frequency, $\nu_L = \omega_L/(2\pi)$, of each of the Lorentzians is extracted from the fit function and is plotted against the applied DC voltage for each data set. Figure 6.4b shows how this is then fitted to a quadratic equation and the fit parameters determined here can be used to determine the calibration from voltage to magnetic field.

If it is assumed that $B_x \approx 0$ then the magnetic field in the shield can be written as $\nu_L = \tilde{\gamma}_{\mathrm{cs}} \sqrt{B_y^2 + B_z^2}$. Then using the fact that $B_y > B_z$ and the binomial expansion $(1+x)^n = 1 + nx$, to first order, when $x << n$ the field can be written as

$$\nu_L = \tilde{\gamma}_{\mathrm{cs}} \left(1 + \frac{1}{2} \frac{B_z^2}{B_y^2} \right). \tag{6.1}$$

To find the calibration this can be rewritten in terms of the applied voltage and the central frequency of the signal:

$$\nu = \nu_0 \left(1 + \frac{1}{2} \frac{(k \times V_{\mathrm{DC}})^2}{\nu_0^2} \right), \tag{6.2}$$

where V_{DC} is the applied DC voltage to the coil to be calibrated, k is the conversion factor and ν_0 is the central frequency when the total magnetic field is minimal.

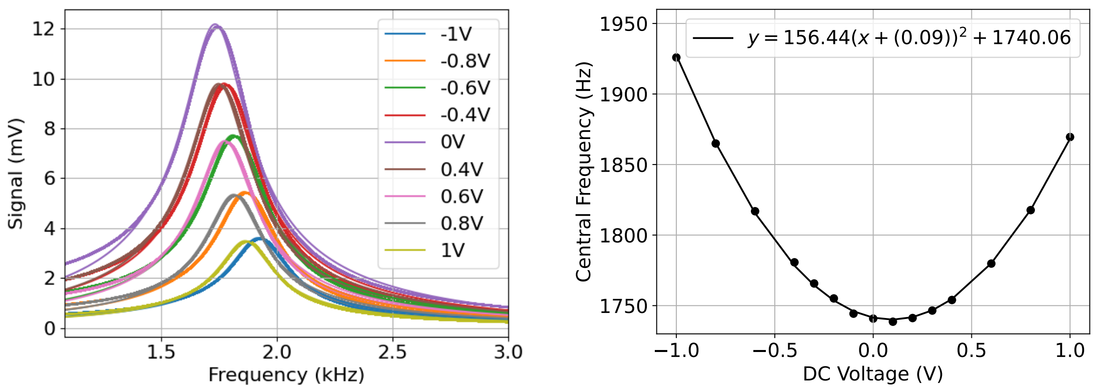

(a) (b)

Figure 6.4: Calibrating the excitation (RF) coil by applying various DC voltages through the coil to see how the (a) magnetic resonances and (b) central frequency depends on the voltage applied.

Equation 6.2 is of the same form as the fitted parabola in Figure 6.4b. By comparison it can be seen that $\nu_0 = 1740.06$ Hz and $b_0 = k^2/2\nu_0 = 156.44$ Hz/V^2. Rearranging b_0 it can be determined that $k = \sqrt{2\nu_0 b_0} = 737.85$ Hz/V. Using the gyromagnetic ratio for caesium ($\tilde{\gamma}_{\text{cs}} = 3.5$ kHz/μT) this is found to be equivalent to $k = 210.8$ nT/V. The same process was followed to calibrate the compensation coil (Figure 6.5) and a conversion factor of 208.6 nT/V was determined. This calibration can now be used to determine the sensitivity of the alignment magnetometer when the single coil is used for the RF field.

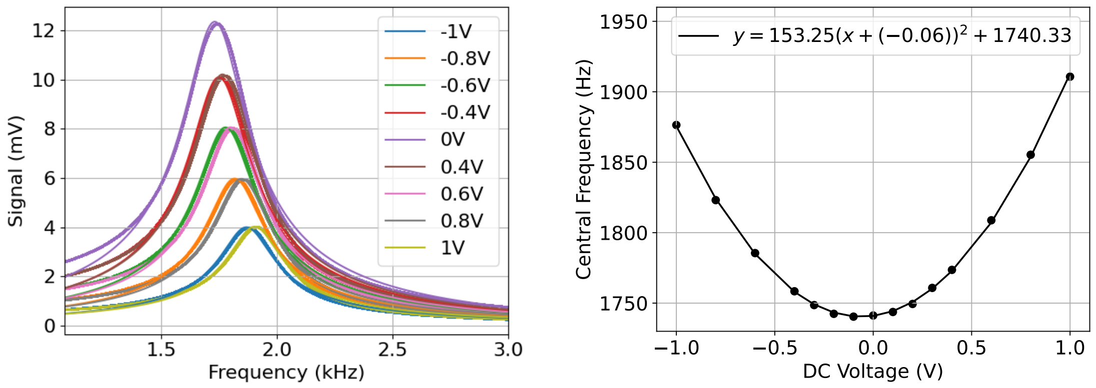

(a) (b)

Figure 6.5: Calibrating the compensation (RF) coil by applying various DC voltages through the coil to see how the (a) magnetic resonances and (b) central frequency depends on the voltage applied.

6.4.2 RF amplitude

In order to optimise the sensitivity of a magnetometer the amplitude of the RF magnetic field needs to be chosen such that it is maximal but the atoms still has a linear response to the magnetic field. This is done by varying the amplitude of the RF field sent to the excitation coil (see Figure 6.4) and recording a magnetic resonance sweep. These sweeps are then fitted to an absorptive Lorentzian curve (see Figure 6.6a):

$$R = \sqrt{X^2 + Y^2} \propto B_{\mathrm{rf}} \sqrt{\left(\frac{1}{\gamma^2 + (\nu_{\mathrm{rf}} - \nu_L)^2}\right)^2 + \left(\frac{(\nu_{\mathrm{rf}} - \nu_L)}{\gamma^3 + \gamma(\nu_{\mathrm{rf}} - \nu_L)^2}\right)^2}, \tag{6.3}$$

where γ is the half width half maximum, ν_{rf} is the RF frequency which is varied and ν_L is the Larmor frequency. From the fitting of this function the full width half maximum (FWHM) and the amplitude of the Lorentzian can be extracted. Due to the low probe power utilised in the alignment based magnetometer, the peak amplitude is the point at which the RF frequency is equal to the Larmor frequency. It is noted that in general the signal peak frequency can differ from the Larmor frequency from effects such as light shift. The sensitivity is optimal when the amplitude/FWHM is at its maximum. For the data set presented in Figure 6.6 the light power was set to 10 μW. It can be seen in Figure 6.6b that for the paraffin

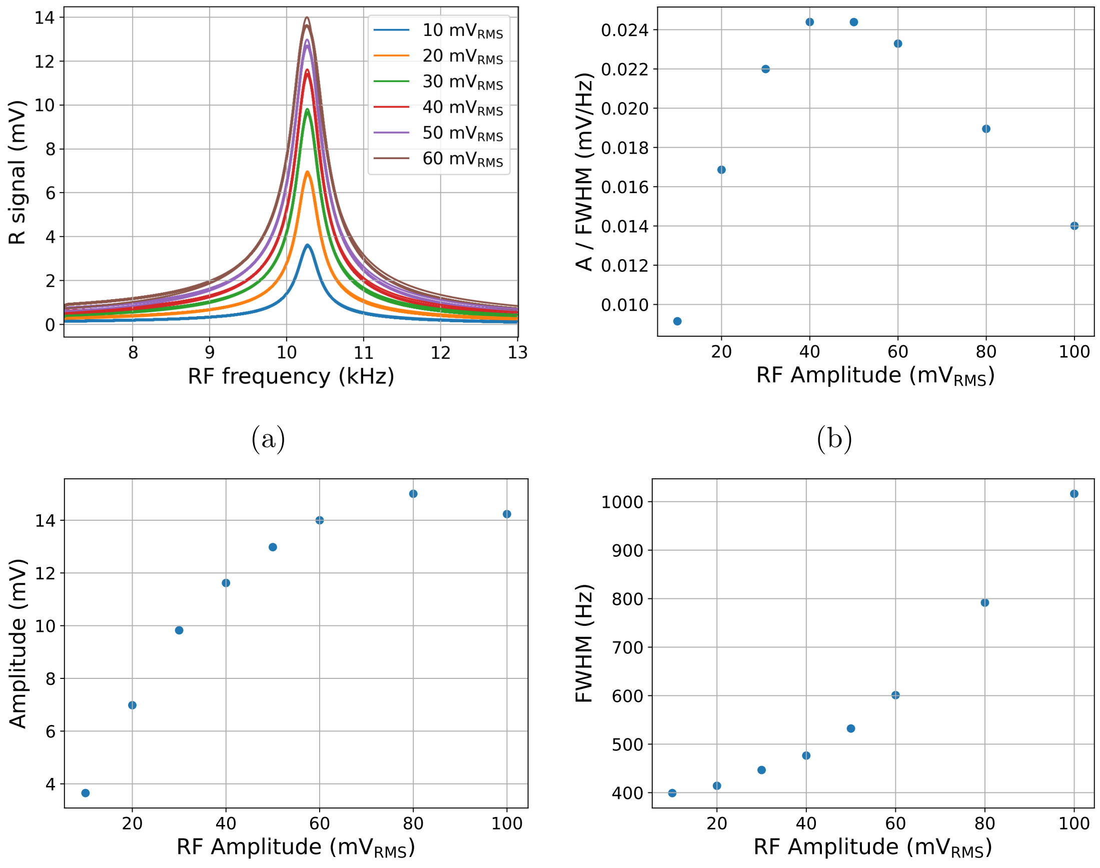

(a) (b)

(c) (d)

Figure 6.6: Magnetic resonance signal at various RF magnetic field amplitudes, which are produced for a paraffin coated caesium cell, with a light power of 10 μW. (a) The R signal of the magnetic resonance sweep is fitted to an absorptive Lorentzian to obtain the (b) A/FWHM dependence on the RF amplitude applied. The (c) amplitude and (d) full width half maximum (FWHM) of the signals are also presented.

coated cell in the alignment setup this is maximal at around 40-50 mV$_{\mathrm{rms}}$. However, the optimal RF power selected needs to still be within the linear regime. Figure 6.6c shows that the signal amplitude is only linear with magnetic field amplitudes up to ~ 20 mV$_{\mathrm{rms}}$. Hence an RF amplitude of 20 mV$_{\mathrm{rms}}$ is used as this is the RF amplitude, in the linear regime, with optimal amplitude/ FWHM. Figure 6.6d shows that with the use of 20 mV$_{\mathrm{rms}}$ there is only a slight increase in the FWHM. With no RF broadening it can be seen that the linewidth of the magnetometer would be ~ 400 Hz. This can be calculated from Figure 6.6d by extracting the full width at half maximum when V$_{\mathrm{rf}}$ = 0 mV$_{\mathrm{rms}}$.

6.4.3 Optimal light power

As sensitivity is determined by the signal to noise ratio, how the signal changes with light power also needs to be studied. Similarly to the RF amplitude, the optimal light power is when the demodulated signal has maximal amplitude whilst maintaining a narrow linewidth. The R signals for a number of light powers were recorded and are shown in Figure 6.7. The demodulated signals are fitted to an absorptive Lorentzian (see Figure 6.7a) with the amplitude and full width half maximum being extracted. From these fits the dependence of A/FWHM on the light power can be found. Figure 6.7b shows that the maximal value of A/FWHM is at a light power of 10 μW.

With a light power of 10 μW and the optimal RF amplitude of 20 mV$_{\mathrm{rms}}$ it can be seen in Figure 6.7d that the R signal has a full width half maximum of ~ 400 Hz. The magnetometer's bandwidth is given by 400 Hz/$\sqrt{3}$ = 230 Hz which corresponds to the full width half maximum of the in-phase (X) signal [64]. It is noted that this linewidth does have some broadening from the light power and RF amplitude. Without broadening, the R signal has a full width half maximum of ~ 200 Hz which corresponds to a linewidth of 200 Hz/$\sqrt{3}$ = 115 Hz. The bandwidth is significant as $\gamma \propto 1/T_2$ where T_2 is the transverse relaxation rate. The larger T_2 is the better the sensitivity of the magnetometer. The T_2 time is used to determine the theoretical maximal sensitivity of a magnetometer.

6.4.4 Sensitivity

Using the optimised parameters determined from characterising the magnetometer with a paraffin coated caesium cell, the sensitivity can be determined. To obtain the sensitivity, four measurements were taken as shown in Figure 6.8. The first data set is a magnetic resonance sweep where the frequency of the RF field is swept around the Larmor frequency. The signal amplitude is extracted from this data and using the coil calibration (see Section 6.4.1) the conversion between the detected field and the demodulated signal can be found. This is done by extracting the maximal signal amplitude and dividing this by the coil calibration. Figure 6.8a shows the demodulated output of the lock-in amplifier when the RF field is varied. A Larmor frequency of $\omega_L \approx 2\pi(10.65\text{ kHz})$ is obtained. The RF field is then fixed at the Larmor frequency, such that $\omega_{\mathrm{rf}} = \omega_L$, and a 4 minute time trace of the lock-in output is recorded, as presented in Figure 6.8b. The data is sampled at a rate of 10 kHz. The RF field amplitude is then set to zero and another 4 minute time trace is recorded (see Figure 6.8c). The time trace with the RF field off (set to zero)

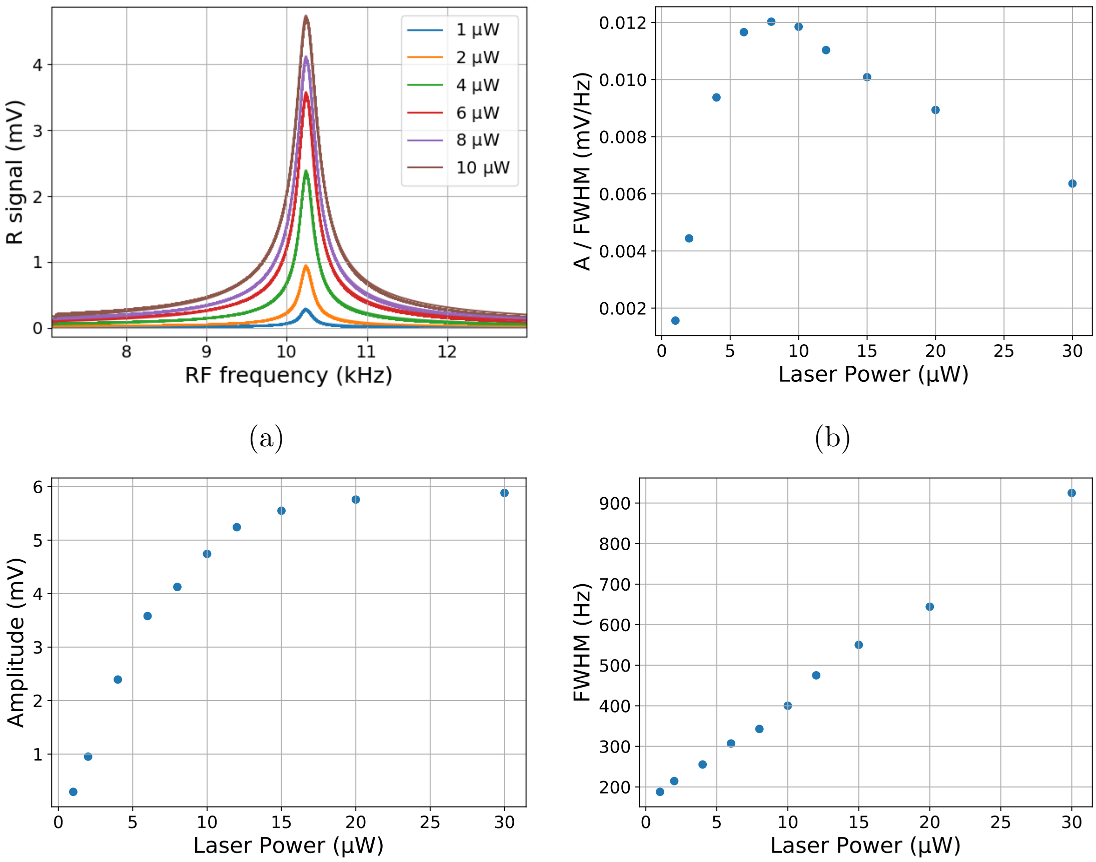

(a) (b)

(c) (d)

Figure 6.7: Characterising the optimal light power for the paraffin coated caesium cell, an RF amplitude of 20 $\mathrm{mV_{rms}}$ is used. (a) The R signal of the magnetic resonance sweep is fitted to an absorptive Lorentzian to obtain the (b) A/FWHM dependence on light power. The (c) amplitude and (d) full width half maximum (FWHM) of the signals are also presented.

represents the intrinsic noise of the magnetometer. Figure 6.8d shows a final four minute data set is taken with the laser light hitting the photodetector, in this case the Thorlabs PDB210A/M, being blocked. This is the electronic noise contribution of the setup resulting from the photodetector, lock-in amplifier and data acquisition card.

In order to obtain the sensitivity of the time traces, the time traces are divided into one second chunks which are then averaged over, see the dashed lines in Figure 6.8. The standard deviation of the one second averages is then calculated, giving the sensitivity of the trace. Alternatively, as shown in Figure 6.8e, the Allan Deviation of the time traces can be computed. At a gate time of 1 second the sensitivity agrees with that obtained by computing the standard deviation. The benefit of calculating the Allan Deviation of the sample is that it also shows the systems stability over time. Figure 6.8c shows the sensitivity of the magnetometer to small oscillating fields. The in-phase (X) component of the signal has a sensitivity of 410 fT and the out-of-phase (Y) component has a sensitivity of 420 fT. Figure 6.8b shows that the magnetometer has a higher sensitivity of 14.9 pT for the X component of the signal and 1.6 pT for the Y component of the signal. This is due to

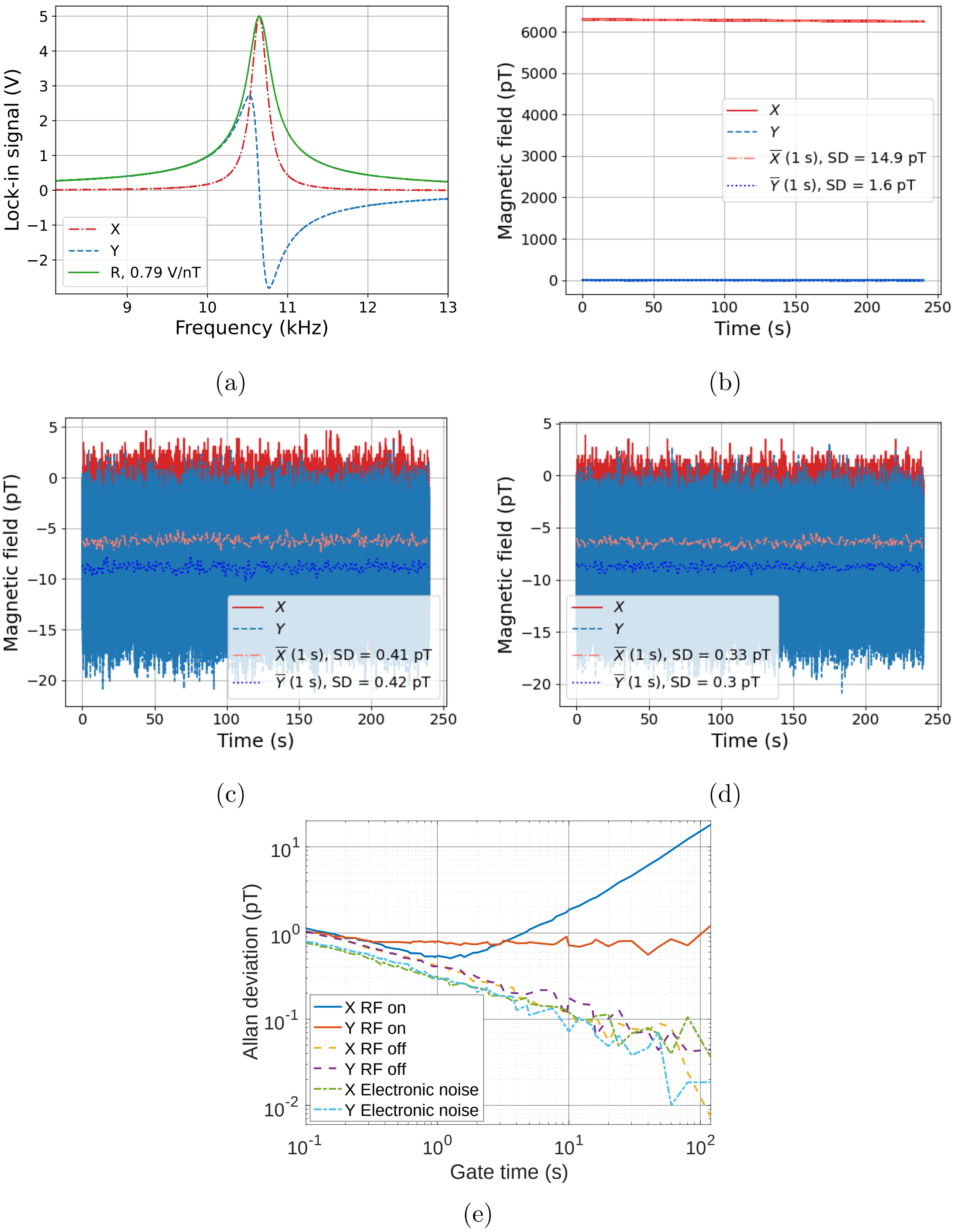

(a) (b) (c) (d) (e)

Figure 6.8: Sensitivity of a (5 mm)^3 Paraffin coated cell at a Larmor frequency of approximately 10 kHz. The cell is at room temperature ($\sim 18^\circ$C). (a) The magnetic resonance signal from sweeping the frequency of the RF magnetic field from 8 kHz to 13 kHz. Four minute time traces are then recorded with the frequency set to to the peak value in (a) at which $\omega_L \approx 2\pi(10.65 \text{ kHz})$ with (b) the RF field amplitude on (c) the RF amplitude set at zero which represents the intrinsic noise of the OPM and (d) the electronic noise of the setup. The standard deviation of one second averages are found and the (e) Allan deviation is also calculated for the time traces.

noise from the voltage supplier that drives the RF coils. It would be expected that the Y component should have a worse sensitivity than the X component due to the dispersive-Lorentzian shape. However, here it can be seen that the X component is less sensitive to small oscillating fields. This is due to temperature fluctuations in the lab affecting the optical fibres and changing the light power through the cell. Improved shielding of the fibre from the environment would improve the sensitivity of the X component. It is noted that in Figure 6.8d it can be seen that the electronic noise is comparable to the intrinsic sensitivity. The noise that is not caused by the electronics can be found to be $\sqrt{410^2 - 330^2} = 243$ fT for the X component and $\sqrt{420^2 - 300^2} = 294$ fT for the Y component of the signal. Hence, the electronic noise is the dominant source of noise in the setup. In order to obtain the optimal sensitivity for an optically pumped magnetometer the photodetector should be replaced with a lower noise detector.

To test if the noise of the OPM setup is reduced if a balanced photodetector with a lower noise floor is used in position of the Thorlabs PDB210A/M a home-made balanced photodetector was used. Further details on the performance of the home-made balanced photodetector can be found in Section 9.4.1. The same data sets as described above were taken with the new detector and the results can be seen in Figure 6.9. A different Larmor frequency of $\omega_L \approx 2\pi(4.2 \text{ kHz})$ is used as the noise floor is lowest around this frequency (see Figure 9.6a). Figure 6.9c shows that using a balanced photodetector with a lower noise floor improves the sensitivity. The X component of the signal has a sensitivity of 360 fT and the Y component has a sensitivity of 370 fT. When the lower electronic noise floor of ~ 200 fT is taken into account it is found that in this case the system is no longer dominated by the electronic noise but now by the photon shot noise which contributes a noise floor of ~ 300 fT. Note that although the electronic noise is no longer the dominating factor of the sensitivity in this configuration, a lower noise detector would still further improve the sensitivity.

The quantum noise limit for an optically pumped magnetometer depends on two main fundamental limits which are the spin projection noise δB_{spin} and the photon shot noise δB_{shot}. These result in a total quantum noise of $\delta B_{\text{quantum}} = \sqrt{\delta B_{\text{spin}}^2 + \delta B_{\text{shot}}^2}$. The theoretical noise floor of an alignment based magnetometer can be calculated for the setup [51, 111]

$$\delta B_{\text{spin}} = \frac{2\hbar}{g_F \mu_B \sqrt{nVT_2}}, \tag{6.4}$$

where $g_F = 1/4$ for the F = 4 caesium ground state, n is the number density of Cs atoms, $T_2 \approx 1/(\pi(230Hz)) \approx 1.4$ ms is the transverse relaxation time. For paraffin coated cells, the effective volume is the volume of the entire cell. This is due to the atoms travelling at high velocities and being able to bounce off the vapour cell walls up to 10,000 times without depolarising [111] meaning that the laser light is able to probe all of the atoms. Hence in the setup presented here the volume is given by $V = (5 \text{ mm})^3$. The cell is kept at room temperature ($T \approx 18.5^{\circ}$C) leading to a number density of $n \approx 2.2 \times 10^{16}$ m^{-3}. The spin projection noise is theoretically calculated to be $\delta B_{\text{spin}} \approx 50$ fT/$\sqrt{\text{Hz}}$. An ideal optically pumped magnetometer has $\delta B_{\text{shot}} = \delta \text{B}_{\text{spin}}$ such that $\delta \text{B}_{\text{quantum}} = \sqrt{2}\delta \text{B}_{\text{spin}}$ [21]. Hence the theoretical quantum noise limit of the magnetometer is $\delta B_{\text{quantum}} \approx 70$ fT/$\sqrt{\text{Hz}}$. When comparing the

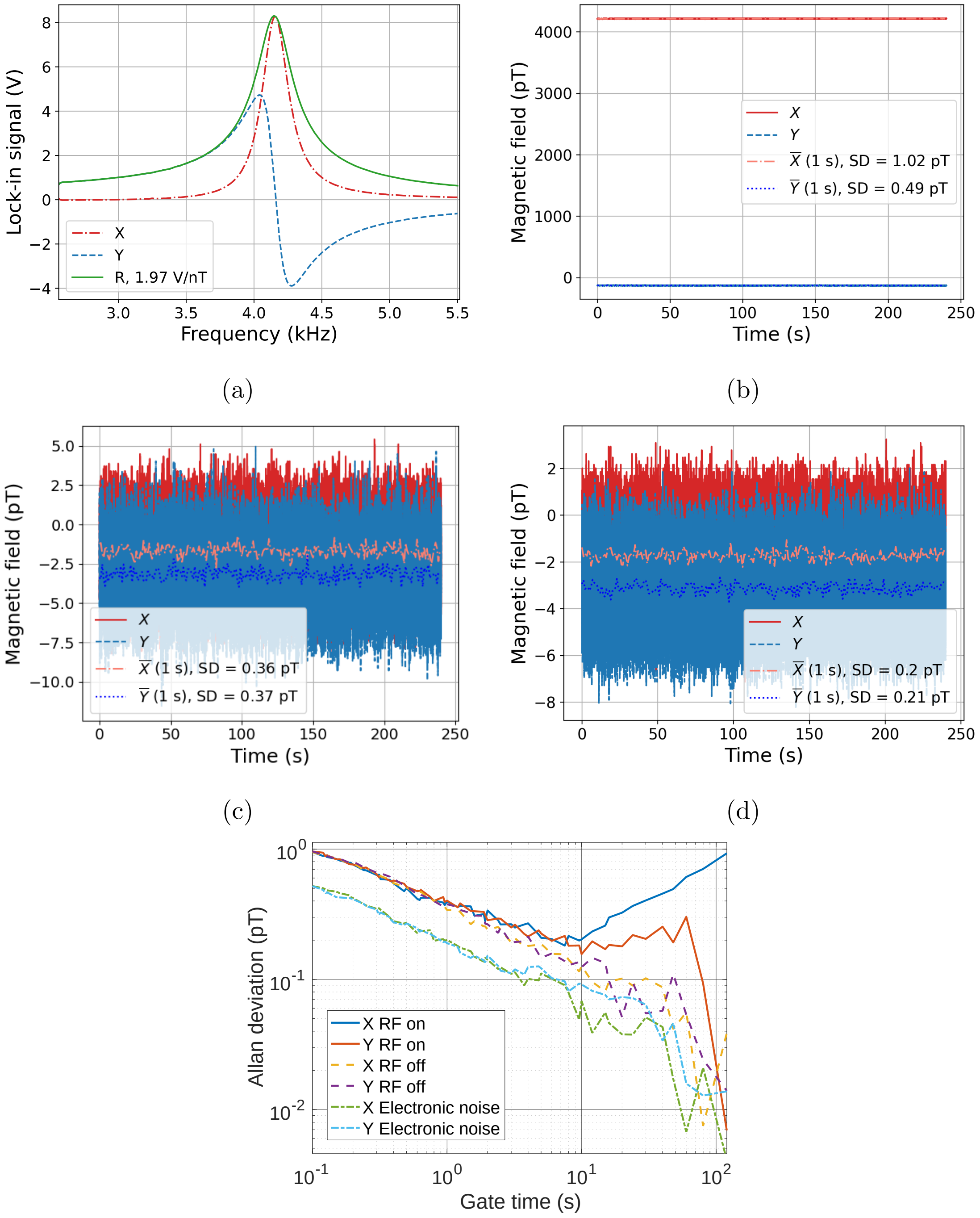

(a)

(b)

(c)

(d)

(e)

Figure 6.9: Sensitivity of a (5 mm)^3 Paraffin coated cell at a Larmor frequency of approximately 4 kHz with a home-made balanced photodetector (see Section 9.4.1) used in place of a commercial Thorlabs detector. The cell is at room temperature ($\sim 18^{\circ}$C). (a) The magnetic resonance signal from sweeping the frequency of the RF magnetic field from 2.5 kHz to 5.5 kHz. Four minute time traces are then recorded with the frequency set to to the peak value in (a) at which $\omega_{\mathrm{L}} \approx 2\pi(4.2\ \mathrm{kHz})$ with (b) the RF field amplitude on (c) the RF amplitude set at zero which represents the intrinsic noise of the OPM and (d) the electronic noise of the setup. The standard deviation of one second averages are found and the (e) Allan deviation is also calculated for the time traces.

theoretical noise floor to that found experimentally it can be seen that the result is a factor of five out, when the lower noise detector is used. In order to obtain a sensitivity closer to this noise floor, quieter electronics are required. Another major factor to this noise floor being higher is due to over half of the atoms in the setup being lost to the $F = 3$ state. This can be seen from the optical pumping predictions in Section 2.6. So, even with perfect pumping with the one laser beam it would still be expected that the experimental noise floor will always be above the theoretical noise floor. To reach the fundamental limit a second re-pump laser would be required to pump the atoms out of the $F = 3$ state. The fundamental limit of the magnetometer could be further improved by heating the vapour cell or using a vapour cell with a larger volume in order to increase the number density of caesium atoms that are probed [51, 72].

6.4.5 Non-linear Zeeman splitting

When large static magnetic fields are applied to an optically pumped magnetometer system the sub-levels are no longer equally split. Therefore, atoms in different sub-levels precess at different frequencies. This is due to the magnetic sub-levels being split by larger amounts and hence the Breit-Rabi formula now has to be used to describe the atom interaction

$$E = -\frac{h\nu_{\mathrm{hfs}}}{2(2I+1)} + (-g_I\mu_N \pm \mu_{\mathrm{eff}})Bm_F \mp \frac{\mu_{\mathrm{eff}}^2 B^2 m_F^2}{h\nu_{\mathrm{hfs}}} \pm 2\frac{\mu_{\mathrm{eff}}^3 B^3 m_F^3}{(h\nu_{\mathrm{hfs}})^2}, \qquad (6.5)$$

where $h\nu_{\mathrm{hfs}}$ is the hyperfine splitting of the ground state, $\mu_{\mathrm{eff}} = (g_s\mu_B + g_I\mu_N)/(2I+1)$, $g_s \sim 2$, μ_B is the Bohr magneton, $g_I = \mu_I/(\mu_N I)$ is the nuclear g-factor, μ_N is the nuclear magneton and μ_I is the nuclear magnetic moment [112].

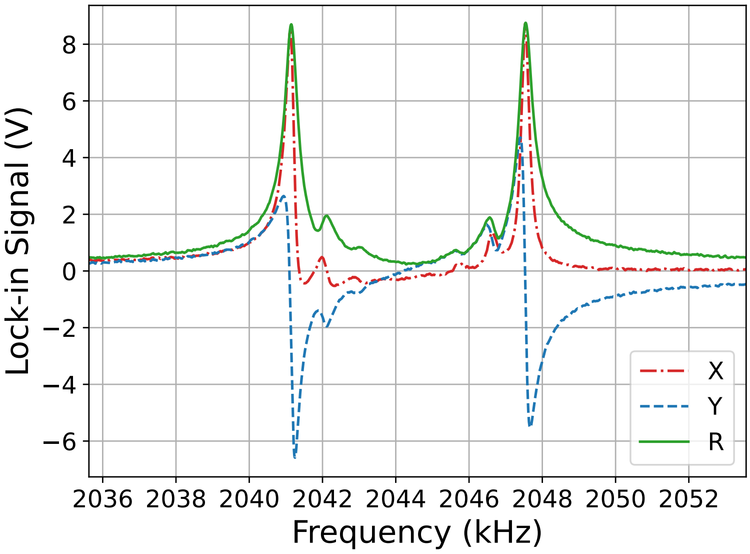

Figure 6.10: Non-linear Zeeman splitting signal for a paraffin coated caesium cell in a 584 μT static field. The first peak represents the magnetic resonance for $m = 4 \rightarrow m = 3$ and the other maximal peak represents the $m = -3 \rightarrow m = -4$ population difference.

For low static magnetic field amplitudes the linear Zeeman effect atoms experience an energy given by $E(m) = mh\nu_L$ where ν_L is the Larmor frequency (in Hz). For a caesium cell in the $F = 4$ ground state there are $2F + 1 = 9$ sublevels described by $|F, m\rangle$. Hence the sublevels are split by an equal amount given by $\Delta\nu_{m,m-1} = (E(m) - E(m-1))/h = \nu_L$. This leads to a single peak in the magnetic resonance signal at the Larmor frequency. When the atoms are placed in a large static magnetic field the splitting is no longer equal between the sublevels due to the non-linear Zeeman effect. The splittings between different sublevels can be calculated [113] by

$$\Delta\nu_{m,m-1} = \nu_L + \frac{2\nu_L^2}{\nu_{\text{hfs}}}\left(m - \frac{1}{2}\right) \tag{6.6}$$

where the prefactor $2\nu_L^2/\nu_{\text{hfs}} = \nu_{\text{split}}$ arises from the non-linear Zeeman effect. This prefactor can be left as a free fitting parameter, ν_{split}, as any stark shifts from the probe light can also have an effect on the experimentally measured value [113]. Hence, the magnetic resonance has a signal amplitude of a different form, that has a shape described by

$$R = \left|\sum_m \frac{A_{m,m-1}(1 + i(\nu_{\text{rf}} - \nu_{m,m-1})/\tilde{\gamma})}{(\nu_{\text{rf}} - \nu_{m,m-1})^2 + \gamma^2}\right|, \tag{6.7}$$

where, in the case of the caesium atoms in the $F = 4$ ground state, the sum is over the range $m = 4$ to $m = -3$ and $A_{m,m-1}$ is the amplitude of the m'th peak. The peak amplitudes are proportional to the population difference between neighbouring magnetic sublevels.

When the linewidth of the magnetometer is smaller than the non-linear Zeeman splitting, the pumping efficiency can be seen. When pumping the atoms into an aligned state, for the case of the caesium $F = 4$ state, there should be eight defined peaks [114]. Obtaining a linewidth that is smaller than the splitting can be achieved by reducing the RF power and laser light power to remove any broadening effects. The size of each peak is related to the population of atoms in each state. If optical pumping is sufficient in an alignment based magnetometer, as described here, it is expected that the signal will have two large outer peaks and the other six peaks should be small.

Figure 6.10 shows the non-linear Zeeman splitting of the paraffin cell in the experimental setup. It can be seen that there are eight peaks that are equally separated. Note that the inner two peaks are barely visible due to efficient pumping resulting in small amplitudes. By fitting Equation 6.7 to the data presented in Figure 6.10 the separation between the two outer peaks can be extracted and are found to be $7\nu_{\text{split}} \approx 6.38$ kHz and the Larmor frequency is $\nu_L \approx 2.044$ MHz. The RF field is swept from 2036 kHz to 2053 kHz. For this measurement a laser light power of 6 µW and an RF amplitude of 2 V_{rms}, which had a 3 kΩ resistor in series with the excitation coil, were chosen so that the peaks are clearly identifiable. A strong static magnetic field is applied to the system, with an amplitude of $B_0 \approx 584$ µT, using a home-made Helmholtz coil that is homogeneous over the caesium vapour cell. The Helmholtz coil is made up of a pair of square coils with a side length of 92 mm, separated by a distance of 47.9 mm and each coil has 48 windings.

6.4.6 Eddy current detection

The alignment based magnetometer, described in Section 6.2, can be used to detect conductive objects. In this case the paraffin coated cell is used to detect eddy currents that are induced in a small aluminium disk of diameter 2 cm and thickness 0.4 cm. A one-dimensional translation stage (Thorlabs MTS50-Z8) moves the object 50 mm, in the z-direction, at a distance of 5 mm above the excitation coil. Another coil, the compensation coil (diameter of 3 mm, 20 windings see Figure 6.5), is also present. The compensation coil is at the same frequency as the excitation coil and cancels the RF magnetic field at the sensing point of the atoms when no conductive object is present, i.e. $\mathbf{B}_{\text{total}}(t) = \mathbf{B}_1(t) + \mathbf{B}_2(t) \approx 0$. This method is known as the differential technique and using this technique for eddy current detection results in obtaining a better signal to noise ratio and hence the setup is sensitive to smaller oscillating magnetic fields [30]. This is due to being able to apply a larger primary RF field with the atoms still having a linear response as they only measure the induced fields. Eddy currents are induced in the aluminium sample by the excitation coil, as the compensation coil is at a large enough distance that it can be assumed the magnetic field contribution from the compensation coil is negligible. The magnetic field that the atoms measure is the secondary, induced, magnetic field as $\mathbf{B}_{\text{total}}(t) = \mathbf{B}_1(t) + \mathbf{B}_2(t) + \mathbf{B}_{\text{ec}}(t) \approx \mathbf{B}_{\text{ec}}(t)$.

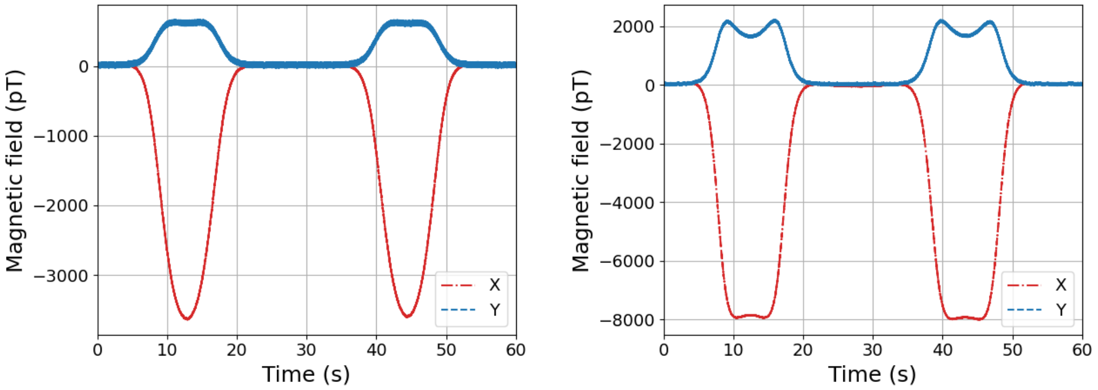

(a) (b)

Figure 6.11: Detected eddy currents signal from a small aluminium disk with a diameter of 2 cm and a thickness of 0.4 cm. The induced fields are detected using the paraffin coated caesium cell. The excitation field has an amplitude of (a) $B_1 = 16.86$ nT and (b) $B_1 = 135$ nT, at the position of the vapour cell.

Figure 6.11 shows the detection of the aluminium disk when two different RF amplitudes are applied to the excitation coil. Figure 6.11a shows the signal detected by the magnetometer when the sample is excited using an applied amplitude of 80 mV$_{\text{rms}}$ to the excitation field and 82.4 mV$_{\text{rms}}$ to the compensation coil. This corresponds to a magnetic field amplitude of $B_1 = 16.86$ nT, using the calibration in Sec. 6.4.1, at the sensing point of the atoms. When the sample is directly above the coil and the centre of the vapour cell a maximal signal is seen with the X component having an induced magnetic field measuring $|B_{\text{ec},X}| = 3.63$ nT and the Y component measuring $|B_{\text{ec},Y}| = 0.62$ nT. Hence the total magnetic field amplitude is given by $B_{\text{ec}} = \sqrt{(3.63)^2 + (0.62)^2} = 3.68$ nT. When comparing this to the excitation field it can be seen that $|B_{\mathrm{ec}}|/|B_1| \approx 0.22$. This ratio is relatively large, when compared to the eddy current detection presented in Section 5 and Section 10.7, due to the close proximity of the object to the sensing point.

Figure 6.11b shows the detection of eddy currents induced in the same aluminium disk as above but with an excitation magnetic field with a larger amplitude, B_1 = 135 nT. A double bump feature can be seen in the detected signal. This is due to the induced magnetic field amplitude being large. This causes issues as the optically pumped magnetometer no longer has a linear response to magnetic field amplitudes and hence the magnetic field conversion is no longer accurate. RF broadening causes the amplitude of the signal to drop, as can be seen in Figure 6.6c when a large RF magnetic field amplitude is applied to the setup. The magnetic field induced is a factor of 8 larger than that induced in Figure 6.11a but the detected signal only increased by just over a factor of 2.

The data presented in Figure 6.11 is the first published demonstration of eddy current detection using an alignment based magnetometer [48]. The experimental setup is similar to those in [30, 25] where larger Larmor frequencies of $\omega_L \approx 2$ MHz were used to detect salt water samples with similar conductivities to biological tissues, such as the heart. Further details on the use of optically pumped magnetometers for detecting biomedical tissues can be found in Section 3.4.

6.5 Characterisation of a 65 Torr buffer gas cell

Although vapour cells with anti-relaxation coatings, such as paraffin, result in magnetometers with high sensitivities [20, 50, 24, 23, 101], these vapour cells are not readily available and are difficult to make. Few people know how to make high quality vapour cells with anti-relaxation coatings as the cells are hand-blown. Hence for RF magnetometers to become commercially available in the future alternatives need to be found. In the literature, until now, only paraffin coated cells have been used for alignment based magnetometers to extend the spin relaxation lifetime of the alkali vapours in use [51, 64]. Buffer gas can be added to vapour cells as an alternative to anti-relaxation coatings to extend the spin relaxation lifetime. The addition of the buffer gas, e.g. nitrogen (N_2), helium (He), slows the diffusion of caesium atoms resulting in it taking longer for the atoms to reach the vapour cell walls and the spin state relaxing. Current commercially available optically pumped magnetometers use buffer gas cells [40, 42, 41, 47]. Buffer gas cells have the potential to be micro-fabricated and hence are an ideal alternative. However, the question of their use in an alignment based magnetometer is tricky as the addition of the buffer gas causes broadening and mixing of the excited states. This makes it more difficult to drive specific transitions and hence the pumping efficiency decreases. Having distinct hyperfine levels is essential in an alignment based magnetometer to produce two dark states. This will be investigated in this section using a 65 Torr buffer gas cell.

6.5.1 Absorption spectroscopy

The addition of a buffer gas, for example nitrogen, to a vapour cell with an alkali metal, in this case caesium, leads to pressure broadening. The excited states of a pure caesium or paraffin coated caesium cell have a natural lifetime of $\tau_{\mathrm{nat}} \approx 34.9$ ns for the D1 transition ($6^2P_{1/2}$) and $\tau_{\text{nat}} \approx 30.5$ ns for the D2 transition ($6^2P_{3/2}$) [68]. This results in a natural linewidth of approximately 5 MHz. When a buffer gas, N_2, is added to a caesium cell the atoms that are in the excited state collide with the buffer gas molecules. This is due to the scattering cross section of the outer caesium electron and the buffer gas molecules being much larger in the excited state [72]. This leads to rapid collisional mixing where the caesium atoms are distributed across the magnetic sublevels during their excited state. This leads to the linewidth of the absorption spectrum being broadened with the spectrum now having linewidths on the GHz scale which can far exceed the Doppler broadening. The higher the buffer gas pressure, the more the signal is broadened.

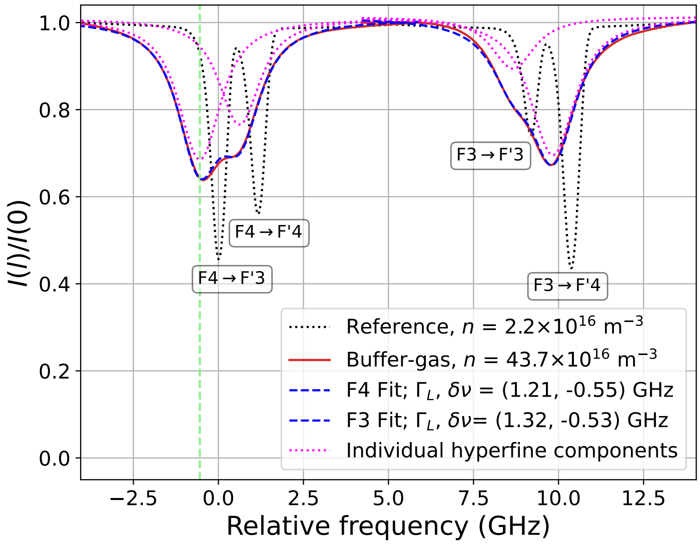

Figure 6.12: The D1 absorption spectrum for a pure caesium cell (black dotted line) and a 65 Torr buffer gas cell (red line) at a temperature of 51°C. This corresponds to a number density of atoms of 43.7×10^{16} m^{-3}. A Voigt profile is fitted to the $F = 3 \longrightarrow F' = 3, 4$ and $F = 4 \longrightarrow F' = 3, 4$ transitions with the Gaussian linewidth fixed at $\Gamma_G = 374$ MHz so the Lorentzian linewidths, Γ_L, and the pressure shifts, $\delta\nu$, can be extracted.

Figure 6.12 shows the absorption spectroscopy of two cells: a pure caesium cell (dotted black reference line) and a buffer gas cell (red line) that was stated to have a buffer gas pressure of 100 Torr by the manufacturer. The laser light is kept low during these measurements to avoid any effects of optical pumping. The reference caesium vapour cell shows the expected D1 spectroscopy with four absorption resonances separated by ground- and excited-state hyperfine splittings of 9.2 GHz and 1.2 GHz. The resonances have a lineshape that is a convolution of a Lorentzian and Gaussian, known as a Voigt lineshape. For this cell the Gaussian linewidth is much larger than the Lorentzian linewidth with a 4.6 MHz full width at half maximum of the excited state. The pressure of the buffer gas vapour cell can be determined experimentally by fitting the absorption spectroscopy to Voigt profiles [73]. The fitting of the Voigt profiles results in two ways of verifying the buffer gas pressure as both the pressure shift and pressure broadening are dependant on the collisions of the nitrogen molecules and caesium atoms. In complex form, the Voigt profile is [72]

$$\mathcal{V}(\nu-\nu_0)=\frac{2\sqrt{\ln 2/\pi}}{\Gamma_G}w\left(\frac{2\sqrt{\ln 2}((\nu-\nu_0)+i\Gamma_L/2)}{\Gamma_G}\right), \tag{6.8}$$

where Γ_G is the full width half maximum of the Gaussian profile, Γ_L is the full width half maximum of the Lorentzian profile and the complex error function is

$$w(x)=e^{-x^2}(1-\mathrm{erf}(-ix)). \tag{6.9}$$

By determining the Voigt profile, the absorption cross section can be determined by

$$\sigma_V(\nu)=\pi r_e c f \mathrm{Re}(\mathcal{V}(\nu-\nu_0)), \tag{6.10}$$

where r_e is the classical electron radius, c is the speed of light and f is the oscillator strength. The data of the buffer gas cells absorption spectrum is fitted to a number of Voigt profiles. The full width half maximum of the Lorentzian is extracted for the $F=3\longrightarrow F'=3,4$ and $F=4\longrightarrow F'=3,4$ separately with two Voigt profiles being fitted to the $F'=3$ and $F'=4$ transition using their relative hyperfine strengths of 1/4 and 3/4 respectively. The same was done for the $F=4\longrightarrow F'=3$ and the $F=4\longrightarrow F'=4$ transition with the hyperfine strengths being 7/12 and 5/12 respectively [68]. By fixing the Gaussian linewidth to $\Gamma_G=374$ MHz for a caesium cell at 51°C, the Lorentzian linewidth is found to be $\Gamma_L=1.26(5)$ GHz. Using the conversion in [73] of 19.51 MHz/Torr a buffer gas pressure of 65(3) Torr is obtained. The buffer gas pressure can also be calculated from the frequency shift of the spectrum. In Figure 6.12, a green dashed line can be seen. This shows a frequency shift from the relative zero point of $\delta\nu=-0.54(1)$ GHz for the $F=4\longrightarrow F'=3$ transition. Using the conversion to Torr from [73] of −8.23 MHz/Torr, the buffer gas pressure is calculated to be 65(1) Torr.

6.5.2 Calibrating the RF excitation coil

With the use of buffer gas cells, magnetic field gradients have more of an effect on the setup. This is due to the buffer gas slowing down the atoms and hence different atoms see different magnetic fields across the vapour cell. For the data presented for the buffer gas cell, a home-made square Helmholtz coil surrounding the vapour cell is used to apply the oscillating magnetic field. The coil is 3 cm in length and has 10 windings. A 3 kΩ resistor is placed in series with the coil. Using the procedure detailed in Section 6.4.1 the excitation coil used in the alignment magnetometer setup with the 65 Torr nitrogen buffer gas cell can be calibrated. Figure 6.13a shows the magnetometer signal response to various applied DC amplitudes. The extracted central frequency from the fits of the magnetometer signal are shown in Figure 6.13b. By using the calculations described previously (Sec. 6.4.1) a calibration of 128.89 nT/V is found for the RF coil with a 3 kΩ resistor in series. This calibration can be used to determine the smallest detectable magnetic field.

6.5.3 RF amplitude

In order to improve the sensitivity, the buffer gas cell is heated to 55°C. The power of the laser light was set to 2 μW and the amplitude of the oscillating voltage sent

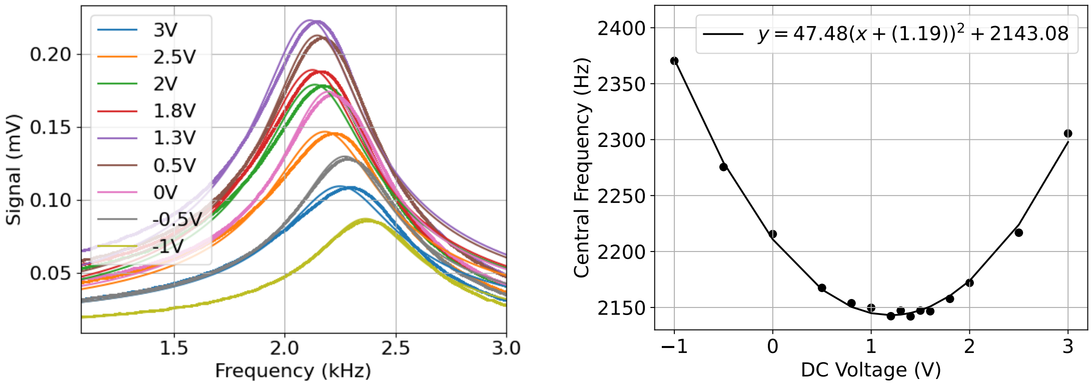

(a) (b)

Figure 6.13: Calibration of the RF magnetic field coil, used with a 65 Torr buffer gas cell, by applying various DC voltages through the coil to see how the (a) magnetic resonances (b) central frequency depend on the applied voltage.

to the RF coil was varied between 4 mV$_{\mathrm{rms}}$ and 180 mV$_{\mathrm{rms}}$. For each RF amplitude applied to the system the magnetometer signal was recorded. By fitting the recorded signals to Equation 6.3, as seen in Figure 6.14a, the signal amplitude and full width half maximum can be extracted. The sensitivity of an OPM is optimal when the amplitude to the full width half maximum is maximal. Figure 6.14b shows that this ratio is maximal in the range of 120 – 180 mV$_{\mathrm{rms}}$. However, it can be seen in Figure 6.14c that the signal amplitude is linear up to 30 mV$_{\mathrm{rms}}$. Hence, an optimal RF amplitude of 30 mV$_{\mathrm{rms}}$ is used for the buffer gas cell in the setup described in Section 6.2.

6.5.4 Optimal light power

With an RF amplitude of 4 mV$_{\mathrm{rms}}$, the optimal light power is determined for the buffer gas cell. The laser light power is varied from 1 μW to 60 μW with the demodulated magnetometer signal recorded at each light power, examples of which are shown in Figure 6.15a. Figure 6.15b shows that the amplitude to full width half maximum (FWHM) ratio is maximal for a light power of 30 – 60 μW. It is visible in Figure 6.15d that even with a light power of 30 μW the FWHM has over doubled in width from 600 Hz to ~ 1400 Hz. This is not an issue as the amplitude has also considerably increased. As it is preferable to minimise the broadening of the linewidth from the laser light power 30 μW is chosen as the optimal value.

6.5.5 Sensitivity

Figure 6.16 shows the sensitivity of the alignment magnetometer setup with the buffer gas cell using the optimised parameters of 30 mV$_{\mathrm{rms}}$ for the RF magnetic field and 30 μW of light power. As was done with the paraffin cell, four measurements were taken. All data sets had a 10 kHz sample rate. A magnetic resonance sweep is recorded with the RF field frequency being varied from 8 kHz to 13 kHz. The signal amplitude, along with the coil calibration for the RF coil, is used to determine the conversion factor of 2.33 V/nT. Three time traces of the demodulated signals are

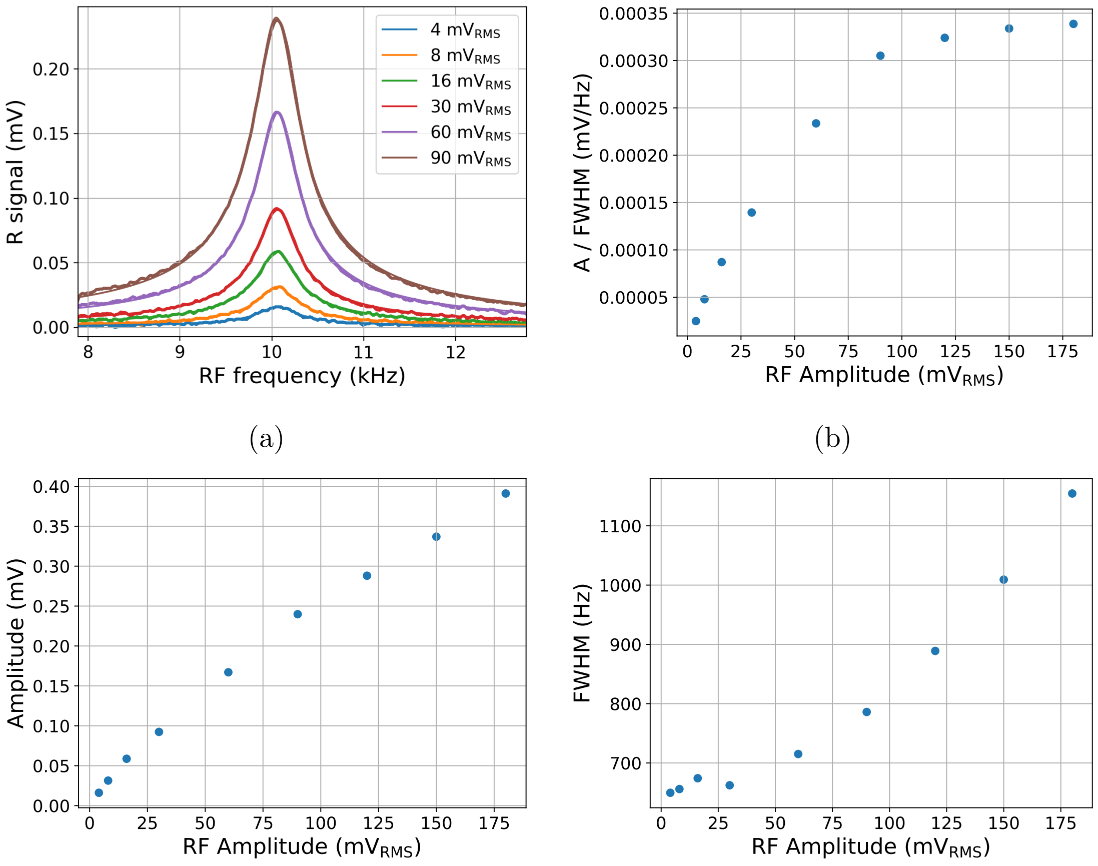

(a) (b)

(c) (d)

Figure 6.14: Characterising the amplitude of the RF magnetic field produced for the 65 Torr nitrogen buffer gas filled caesium cell. A light power of 2 μW is used. (a) The R signal of the magnetic resonance sweep is fitted to an absorptive Lorentzian to obtain (b) the amplitude/FWHM dependence on the RF amplitude applied, (c) the amplitude and (d) the full width half maximum (FWHM) of the signals are also presented.

recorded with the RF field frequency being set to the peak value, in Figure 6.16a, where $\omega_{\mathrm{rf}} = \omega_L \approx 2\pi(10\ \mathrm{kHz})$. For the first four minute time trace the RF magnetic field amplitude remained at 30 mV$_{\mathrm{rms}}$ which produces an oscillating magnetic field measuring 3.87 nT at the position of the atoms. It can be seen in Figure 6.16b that the X component of the demodulated signal is much noisier than the Y component. This is due to slight fluctuations in the temperature of the cell around 55°C. To obtain a better sensitivity the cell should be left to stabilise its temperature for longer. In order to eliminate this issue entirely a temperature controlled PID could be implemented in the setup. Both signals are noisier than the intrinsic sensitivity of the setup (Figure 6.16c) due to noise being introduced through the magnetic field coils from noisy voltage supplies. A lower noise voltage or current supply would improve the sensitivity with the RF coil on. Figure 6.16c shows the intrinsic sensitivity of the buffer gas cell in the alignment magnetometry setup. A sensitivity of 310 fT is seen using the method of calculating the standard deviation of one second averages of the data. Due to using the higher light power in comparison to that used for the paraffin coated cell, the sensitivity is the photon shot noise

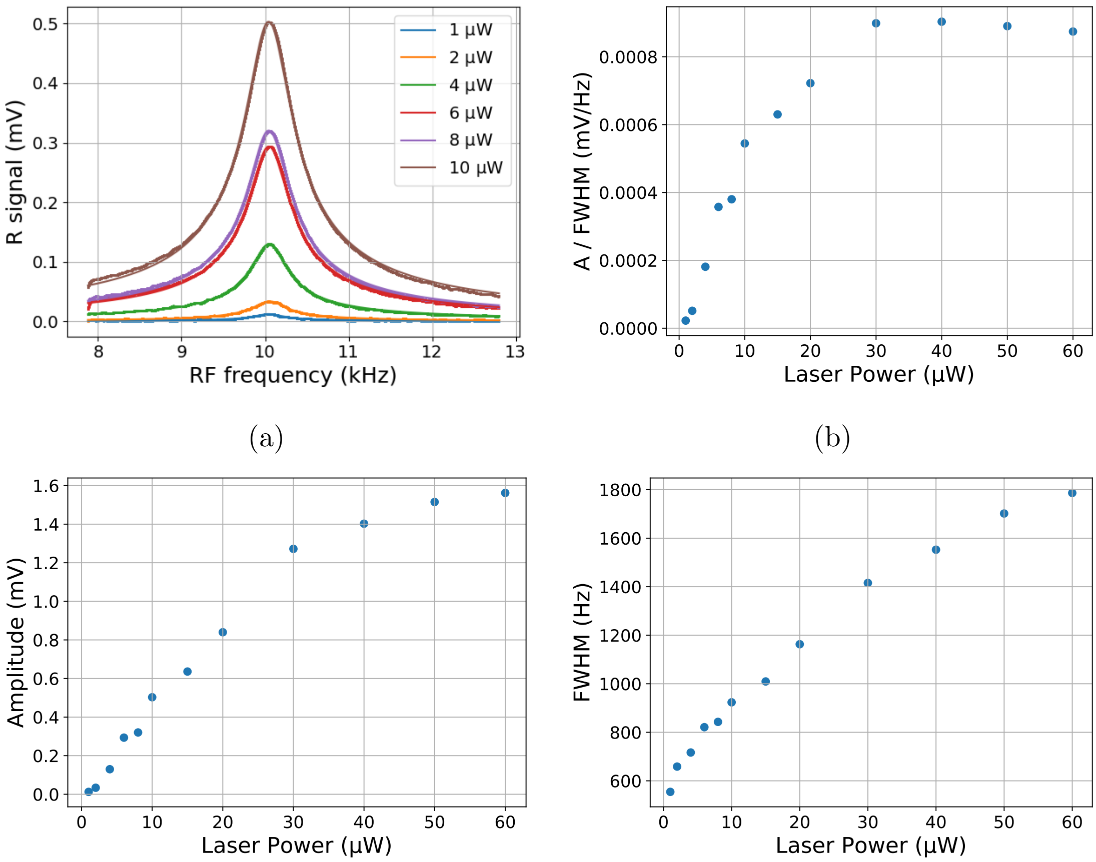

(a) (b)

(c) (d)

Figure 6.15: Characterising the optimal light power for the 65 Torr buffer gas cell, an RF amplitude of 4 $\mathrm{mV_{rms}}$ is used. (a) The $\boldsymbol{R}$ signal of the magnetic resonance sweep is fitted to an absorptive Lorentzian to obtain the (b) A/FWHM dependence on light power. The (c) amplitude and (d) full width half maximum (FWHM) of the signals are also presented.

limit. This is supported by calculating the electronic noise of the setup as shown in Figure 6.16d which shows a noise contribution of 190 fT. Hence the dominating noise from other aspects of the experiment, e.g. shot noise and atomic noise, can be calculated as $\sqrt{310^2 - 190^2} = 245$ fT. The Allan deviation for this setup can be seen in Figure 6.16e and at a gate time of a one second agrees with the standard deviation approach for calculating the sensitivity. However, it also shows that if the signal is averaged over for a longer period of time a smaller magnetic field is detectable as, apart from for the ‘X RF on’, the system is stable for even higher gate times.

Using Equation 6.4, the theoretical quantum noise limit of the buffer gas alignment magnetometer can be determined. A key difference when calculating the sensitivity for a buffer gas cell, compared to the paraffin cell, is that not all atoms are considered as being probed. Due to the T_2 being improved by slowing the atoms down, it is assumed that only the atoms that are in the laser path are probed and hence the effective volume is the volume of the beam. Hence for a beam diameter of $\sim$ 2 mm the volume of atoms probed is given by $V = V_{\mathrm{beam}} = 1.56 \times 10^{-8}$ m^3. The cell is heated to a temperature of $\sim 55^{\circ}$C which results in a number density of $n = 60 \times 10^{16}$ m^{-3}. The transverse relaxation time is given by $T_2 = 1/(\pi(800\ \mathrm{Hz}))$.

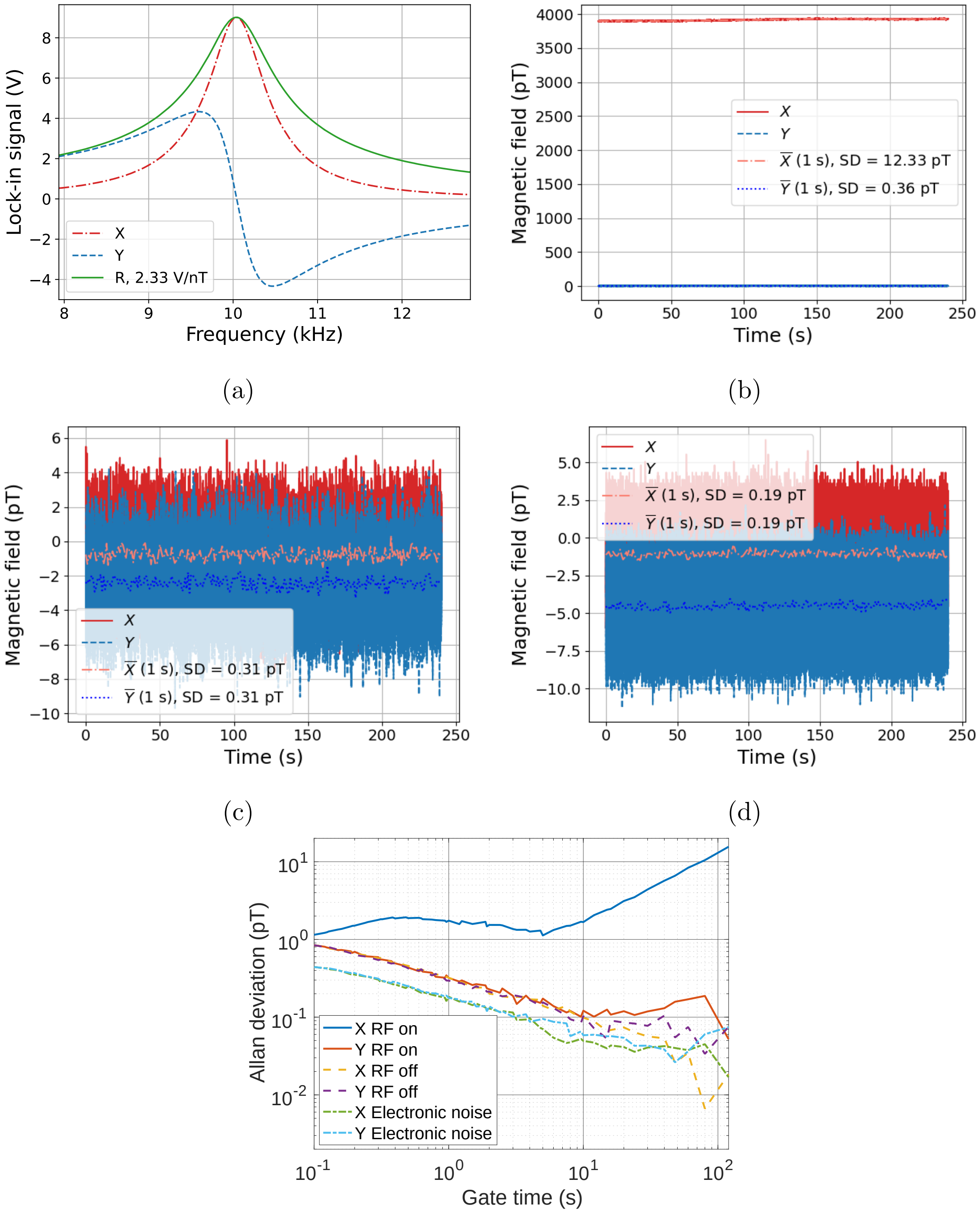

(a) (b)

(c) (d)

(e)

Figure 6.16: Sensitivity of a 5 mm diameter and 5 mm optical path length 65 Torr nitrogen buffer gas cell at a Larmor frequency of approximately 10 kHz. The cell is heated to a temperature of $\sim 55^\circ$C. (a) The magnetic resonance signal from sweeping the frequency of the RF magnetic field from 8 kHz to 13 kHz. Four minute time traces are then recorded with the frequency set to to the peak value in (a) at which $\omega_L \approx 2\pi(10\text{ kHz})$ with (b) the RF field amplitude on, (c) the RF amplitude set at zero which represents the intrinsic noise of the optically pumped magnetometer and (d) the electronic noise of the setup. The standard deviation of one second averages are found and the (e) Allan deviation is also calculated for the time traces.

Substituting these values into Equation 6.4 gives an estimate of the atomic noise to be $\delta B_{\text{spin}} \approx 50 \text{ fT}/\sqrt{\text{Hz}}$. For an ideal optically pumped magnetometer the shot noise is equal to the spin noise [115] and hence the quantum noise of the magnetometer is given by $\delta B_{\text{quantum}} = \sqrt{2}\delta B_{\text{spin}} \approx 70 \text{ fT}/\sqrt{\text{Hz}}$. It is noted that the theoretical quantum limit of the buffer gas cell matches that of the paraffin coated cell in this setup (see Section 6.4.4) as the elevated temperature counteracts the reduced probe volume and shorter T_2 time.

6.5.6 Non-linear Zeeman splitting

As was done with the paraffin coated cell, the non-linear Zeeman splitting was studied to see if a high enough pumping efficiency is achieved with the buffer gas vapour cell. Figure 6.17 shows the magnetic resonance signal when the buffer gas vapour cell is placed in a static magnetic field with a large amplitude of $B_0 = 839$ μT, using the same Helmholtz coil as in Section 6.4.5. A light power of 8 μW was used. The RF magnetic field frequency was swept from 2.921 MHz to 2.951 MHz. 8 peaks are visible in the figure with the inner most two having a small amplitude and the outer two have a much larger amplitude. Hence, this confirms that there is optical pumping to the outer two states of $m_F = \pm 4$ despite the hyperfine states partially overlapping due to the pressure broadening of the buffer gas. The difference in frequency between the outer two most peaks can be found experimentally, by fitting the data to Equation 6.7, to be $7\nu_{\text{split}} = 13.2(1)$ kHz. This is in agreement with the theoretically determined value of 13.1 kHz determined by calculating $|\Delta\nu_{4,3} - \Delta\nu_{-3,-4}|$ where these values are determined using Equation 6.6.

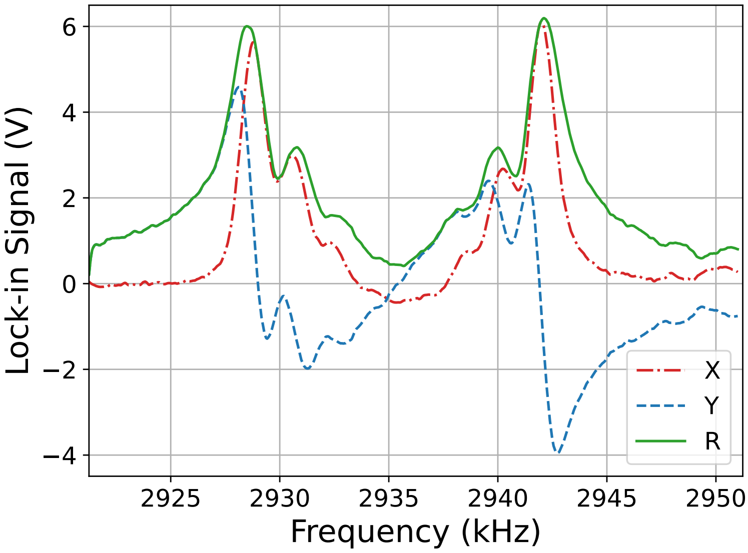

Figure 6.17: Non-linear zeeman splitting signal for a 65 Torr N_2 buffer gas caesium cell in a 839 μT static field. The first peak represents the magnetic resonance for $m = 4 \rightarrow m = 3$ and the other maximal peak represents the $m = -3 \rightarrow m = -4$ population difference.

This hence shows that a 65 Torr nitrogen buffer gas cell can be used in an alignment based magnetometer as the pumping efficiency to the outer most state is more than sufficient to create two dark states. It is noted that with a lower buffer gas pressure the overlapping of the hyperfine states would be reduced and hence it is expected that more atoms would be pumped into the dark states. However, although the pumping may improve a lower buffer gas pressure also leads to a shorter T_2 time and hence reduces the sensitivity of the optically pumped magnetometer. Further testing would be needed to see if a different buffer gas pressure would result in an improved sensitivity to that seen in Section 6.5.5. For the applications presented in this thesis the sensitivity obtained is more than sufficient.

The non-linear Zeeman splitting is important in the applications of magnetic induction tomography (MIT) of biological materials (see Section 3.4) as high frequencies and hence high magnetic fields are desired. Techniques utilising the other resonance peaks have been explored to stabilise the static magnetic field [116] and hence improve the sensitivity of magnetometers by reducing noise from magnetic field fluctuations. This technique could show its full potential in unshielded applications.

6.6 Comparison and conclusions

The results presented in this chapter show that it is possible to use a one beam, alignment configuration with a buffer gas vapour cell. Although the buffer gas cell is operated at an elevated temperature the quantum noise limit is ~ 70 fT which is the same as that of the paraffin coated cell. This is due to the reduced probe area and shorter T_2 time in the buffer gas vapour cell. A better sensitivity was achieved with the buffer gas vapour cell (310 fT) compared to the paraffin coated cell (415 fT). This is partially due to the buffer gas vapour cell requiring a higher light power for the optimal sensitivity and hence the electronic noise is, in comparison, a lower contribution to the noise floor. In the case of both of the vapour cells, low light powers (≤ 30 µW) were used to probe the atomic ensemble. The low light powers mean that low cost vertical cavity surface emitting laser (VCSEL) diodes can be used in place of the fibre coupled lasers used here [117, 118] (see Section 6.3). Both vapour cells used in this thesis are hand-blown but it is expected that a micro-fabricated buffer gas vapour cell, with the same pressure of N_2 added, would perform the same. To improve the sensitivity obtained by the paraffin coated cell the temperature could be elevated above room temperature as this results in a higher number density and hence a better sensitivity. For the buffer gas cell, a larger laser beam diameter could be used such that the atoms across the entire vapour cell are probed. The buffer gas pressure could also be further investigated to determine the optimal pressure such that the perfect balance between the rate which at caesium atoms diffuse is slow but the broadening does not affect the pumping efficiency of the system. Due to the similar sensitivities obtained between the two cells, it is believed that this pressure will be around the pressure of the vapour cell presented here. The sensitivity of both setups could be improved by using larger vapour cells.

The work presented in this chapter shows that buffer gas cells, of the correct pressure, are compatible with alignment based magnetometry. This work opens up the possibility of compact, portable and robust RF magnetometers using a single laser beam with buffer gas cells. This is a more commercially viable option than using paraffin coated cells. The use of micro-fabrication of buffer gas vapour cells would also improve the viability of RF-OPMs being able to be mass produced. OPMs, like that presented here, offer an alternative to commercially available fluxgates, e.g. Bartington magnetometers (see Figure 5.3), and induction coils for detecting oscillating, RF magnetic fields. They offer improved sensitivities and the ability to detect DC-MHz frequencies by varying the Larmor frequency.

Chapter 7

Spin noise spectroscopy

7.1 Motivation

The atoms in an optically pumped magnetometer are spin polarised using laser light through optical pumping (see Section 2.6) [39]. The polarisation of the light, used for optical pumping, depends on the type of state desired. Typically, orientation based optically pumped magnetometers use circularly polarised light [24, 23], however generating orientation from a linearly polarised beam is possible [119]. In this case, each atom is treated as a spin-$\frac{1}{2}$ particle despite the value of the total angular momentum of the ground state, F. The Bloch equations describe the evolution of the atomic spin in a magnetic field for the spin vector $\mathbf{F} = (F_x, F_y, F_z)^T$ [30]. The three components correspond to the expectation values of the angular momentum operators defined along the respective directions such that $F_\alpha = \mathrm{Tr}\{\hat{F_\alpha}\rho\}$ where $\alpha = x, y, z$ for an atomic ensemble described by a single-atom's density matrix ρ. In contrast, for an alignment based magnetometer [51, 3, 85, 64] the atoms are optically pumped using linearly polarised light. Here each atom is treated as a spin-1 particle [120]. This means that the atomic state cannot be described by a vector but instead is described using rank-2 spherical tensors with five components that describe how the atomic spin is aligned along certain axes [16].

Spin noise spectroscopy [121] is used to characterise the noise properties of a given atomic system and for the autocorrelation function that noise fluctuations exhibit in the steady state regime [122]. Only in the case of orientation based magnetometers have stochastic noise models been developed that are capable of explaining the observed noise power spectra when probing unpolarised atomic ensembles [123, 124, 125, 126], also including the effects of spin-exchange collisions [127, 128, 129]. Such models to fully characterise the spin noise spectra in the case of an alignment based magnetometer are still not complete, despite recent promising steps in that direction [130, 131, 132, 133, 134, 135].

In this chapter, methods of stochastic calculus and the formalism of spherical tensors are employed to predict the power spectral density of an alignment based magnetometer [5], similar to that described in Section 6, in the presence of a strong static magnetic field and a white noise magnetic field that is applied perpendicular to the static magnetic field. The model presented here correctly predicts the existence of peaks in the measured power spectral density at particular multiples of the Larmor frequency. It also correctly predicts the dependence of the peak amplitudes, linewidths and central frequencies on the noise intensity and input polarisation angle. The model is verified using a series of experiments where the experimental results agree very well with the theory.

The work presented here paves the way for alignment based magnetometers to be used in real time sensing tasks. Due to the spin noise being characterised in detail, the time-varying signals can be tracked beyond the nominal bandwidth of the magnetometer [136]. The alignment based magnetometer, with added noise, can be used as a scalar magnetometer to sense time-varying magnetic fields as well as having the potential to measure magnetic fields that oscillate at RF frequencies. The simplicity of only having a single beam for both pumping and probing the atomic ensembles is promising for the potential of miniaturising and commercialising RF magnetometers [137].

7.2 Theory

The theoretical predictions, found in Ref. [5], for the expected spin noise spectroscopy signals will be summarised here. In order to detect the spin noise properties of the alignment based magnetometer presented in this thesis, a noisy stochastic magnetic field $\mathbf{B}_{\text{noise}}(t)$ is applied to the system along the x-direction. The spatial configuration of the experimental setup is shown in Figure 7.1. The stochastic field introduces an additional term to the Hamiltonian presented in Section 4.2 given by

$$H_{\text{noise}}(t) = \gamma_g B_{\text{noise}}(t). \tag{7.1}$$

This noisy field is applied in place of the oscillating magnetic field. The component of the magnetic field that is in the x-direction can be written as

$$B_{\text{noise}}(t) = \frac{\Omega_{\text{noise}}}{\gamma_g}\xi(t) \approx \frac{\Omega_{\text{noise}}}{\gamma_g}\sqrt{\frac{1}{2\pi\Delta f}}\frac{dW_t}{dt}, \tag{7.2}$$

where $\mathbf{\Omega}_{\text{noise}}$ is the effective magnetic noise amplitude in units of the Larmor frequency, $\xi(t)$ is the stochastic process for the noise that is being generated. This has a constant power spectrum in a frequency range of $f \in [f_{\text{LP}}, f_{\text{cutoff}}]$ with f_{LP} being a high-pass filter that is close to zero being and is used to eliminate false signals from low frequency contributions and f_{cutoff} is a low-pass filter utilised to prevent the effects of aliasing. As $f_{\text{LP}} \approx 0$ it can be seen that $\Delta f = f_{\text{cutoff}} - f_{\text{LP}} \approx f_{\text{cutoff}}$. The white noise is interpreted as the time derivative of the Wiener process W_t [138]. Hence the Hamiltonian can be written as

$$H_{\text{noise}}(t) = \sqrt{\omega_{\text{noise}}}F_x dW_t, \tag{7.3}$$

where $\omega_{\text{noise}} = \mathbf{\Omega}^2_{\text{noise}}/(2\pi f_{\text{cutoff}})$ is the effective noise spectral density.

In the spherical tensor representation, the desired stochastic dynamical equation for the vector of the alignment coefficient is

$$d\mathbf{m_t} = \left(\mathbf{A_0} + \frac{\mathbf{A}^2_{\text{noise}}}{2}\right)\mathbf{m_t}dt + \mathbf{A}_\phi\left(\mathbf{m_t} - \mathbf{m}^{\text{ss}}\right)dt + \mathbf{A}_{\text{noise}}\mathbf{m_t}dW_t, \tag{7.4}$$

where $\mathbf{A_0} = i\Omega_L\mathbf{J}_\mathbf{z}^{(\mathbf{2})}$ is associated with the free evolution, $\mathbf{A}_\phi$ is related to the dissipative map and $\mathbf{A}_{\text{noise}} = -i\sqrt{\omega_{\text{noise}}}\mathbf{J}_\mathbf{x}^{(\mathbf{2})}$ is associated with the stochastic noise [5].

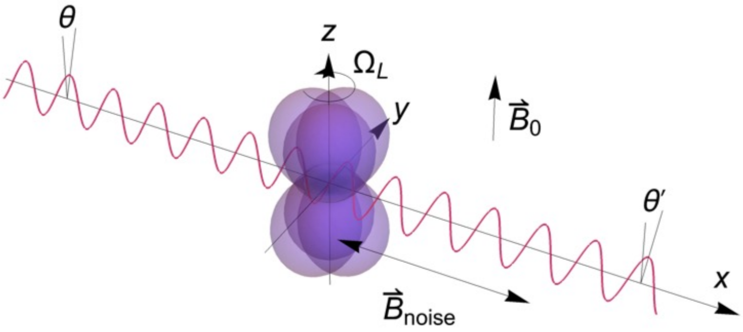

Figure 7.1: The spatial configuration of the alignment based magnetometer. The input light-beam propagates along the x-direction and is polarised at some intermediate angle $0 < \theta < \pi/2$. The atomic steady-state generally modifies the polarisation angle of the transmitted light θ'. In the experimental setup a stochastic field $\mathbf{B}_{\text{noise}}(t)$ is applied along the direction of light propagation, and induces white noise that disturbs the atomic state from equilibrium. The static magnetic field $\mathbf{B}_0$ is applied along the z-direction.

The incoming polarisation angle is rotated by an angle θ in the $z-y$-plane, as shown in Figure 7.2. Upon leaving the atomic vapour cell, the angle θ of the incoming linearly polarised light is changed to θ'. The change of the angle $\Delta\theta = \theta' - \theta$, when assuming the atomic ensemble is optically thin, obeys [16, 4]

$$\Delta\theta \propto i(\tilde{m}_{2,1} + \tilde{m}_{2,-1}). \tag{7.5}$$

The proportionality constant is dependant on a number of parameters including but not limited to the optical depth, interaction strength and light power. By rotating $\mathbf{m}_t(t) = \mathbf{m}_2(t)$ (see Equation 4.41) by the angle θ around the light propagation direction (x-axis) Equation 7.5 can be rewritten as

$$\Delta\theta \propto \mathbf{h}^{\mathrm{T}}\mathbf{D}_{\theta}^{(2)}\mathbf{m_t}, \tag{7.6}$$

where $\mathbf{h} = (0, i, 0, i, 0)^T$ and $\mathbf{D}_{\theta}^{(2)} = D_{m,m'}^{(2)}(-\pi/2, 0, \pi/2)$ is the Wigner D-matrix. Hence, the detected signal of the alignment based magnetometer may be written as

$$\begin{aligned} S(t) &= g_D \mathbf{h}^{\mathrm{T}}\mathbf{D}_{\theta}^{(2)}\mathbf{m_t} + \zeta(t) && \text{(7.7a)}\\ &= g_D \frac{1}{2}\left[\sqrt{6}m_{2,0}(t) + m_{2,2}(t) + m_{2,-2}(t)\right]\sin(2\theta) && \text{(7.7b)}\\ &+ g_D i\left[m_{2,1}(t) + m_{2,-1}(t)\right]\cos(2\theta) + \zeta(t). \end{aligned}$$

7.2.1 Spin noise spectroscopy

The power spectral density (PSD) is defined as

$$\mathrm{PSD}(\omega) = \left\langle |\delta S(\omega)|^2 \right\rangle, \tag{7.8}$$

where $\langle \ldots \rangle$ denotes the average over stochastic trajectories and $\delta S(\omega)$ is the Fourier transform of any signal. In the experiment presented here the signal is the measured current of the balanced photodetector $\delta S(t)$ and over a finite-time interval $[0, T]$ has the form

$$\delta S(\omega) = \frac{1}{\sqrt{T}} \int_0^T dt e^{-i\omega t} \delta S(t). \tag{7.9}$$

By letting $T \gg \tau_c$ where τ_c is the effective coherence time of the noisy system, it can be assured that $\delta S(t)$ is stationary and ergodic and hence the power spectrum can be rewritten in the steady state according to the Wiener-Khinchin theorem [121] as

$$\begin{aligned} \mathrm{PSD}(\omega) &= \int_0^\infty dt \cos(\omega t) \langle \delta S(t), \delta S(0) \rangle && (7.10a) \\ &= \int_0^\infty dt \cos(\omega t) \langle S(t), S(0) \rangle . && (7.10b) \end{aligned}$$

Substituting the form of the detected signal given in Equation 7.7a the power spectrum is given by

$$\mathrm{PSD}(\omega) = g_D^2 \mathbf{h}^{\mathrm{T}} \mathbf{D}_\theta^{(2)} \Xi(\omega) \mathbf{D}_\theta^{(2)T} \mathbf{h} + \left\langle |\zeta(\omega)|^2 \right\rangle, \tag{7.11}$$

where $\Xi(\omega)$ is a 5×5 matrix defined by

$$\Xi_{p,q}(\omega) = 2 \int_0^\infty dt \cos(\omega t) \left\langle m_{2,p}(t), m_{2,q}(0) \right\rangle . \tag{7.12}$$

Here $p, q = -2, ..., 2$ are the coefficients of the $\mathbf{m}_t$-vector in the steady state. The detection noise $\left\langle |\zeta(\omega)|^2 \right\rangle$ is uncorrelated from any other noise sources in the system.

For the alignment based magnetometer dynamics described by Equation 7.4, the resulting power spectral density can be calculated as a sum of absorptive and dispersive Lorentzian functions in the form [5]:

$$\mathrm{PSD}(\omega) = \sum_{j=-2,...,2} \frac{p^a_{|j|} \gamma^2_{|j|}}{(\omega - \omega_j)^2 + \gamma^2_{|j|}} + \sum_{j=\pm 1, \pm 2} \frac{\pm p^d_{|j|} \gamma_{|j|} (\omega - \omega_j)}{(\omega - \omega_j)^2 + \gamma^2_{|j|}} + \left\langle |\zeta(\omega)|^2 \right\rangle, \tag{7.13}$$

where the central frequencies ω_j read as

$$\begin{aligned} \omega_0 &= 0, && (7.14a) \\ \omega_1 &= -\omega_{-1} = \sqrt{\Omega_L^2 - \frac{9}{16} \omega^2_{\mathrm{noise}}}, && (7.14b) \\ \omega_2 &= -\omega_{-2} = 2\Omega_L - \frac{3\omega^2_{\mathrm{noise}}}{16\Omega_L}. && (7.14c) \end{aligned}$$

These central frequencies correspond to multiples of the Larmor frequency: 0, $\boldsymbol{\Omega}_L$ and $2\boldsymbol{\Omega}_L$. The linewidths take the form

$$\begin{aligned} \gamma_0 &\approx \Gamma_0 + \frac{3}{2} \omega_{\mathrm{noise}}, && (7.15a) \\ \gamma_1 &= \Gamma_1 + \frac{5}{4} \omega_{\mathrm{noise}}, && (7.15b) \\ \gamma_2 &\approx \Gamma_2 + \frac{1}{2} \omega_{\mathrm{noise}}, && (7.15c) \end{aligned}$$

where Γ_i are the dissipation rates. The full forms of ω_i and $\gamma_{|i|}$ can be found analytically [5]. For the forms presented here, the assumptions that $\boldsymbol{\Omega}_L \gg \Gamma_{|i|}$ and $\boldsymbol{\Omega}_L \gg \omega_{\text{noise}}$ must be considered. Under these assumptions the absorptive peak heights are described by

$$p_0^a = C\frac{27}{16}\omega_{\text{noise}}^2 \frac{\Gamma_0^2(2\Gamma_2 + \omega_{\text{noise}})}{(2\Gamma_0 + 3\omega_{\text{noise}})^2 G(\omega_{\text{noise}}, \boldsymbol{\Gamma})} h(\theta), \tag{7.16a}$$

$$p_1^a = C\frac{3}{4}\omega_{\text{noise}} \frac{\Gamma_0^2(2\Gamma_2 + \omega_{\text{noise}})}{(4\Gamma_1 + 5\omega_{\text{noise}}) G(\omega_{\text{noise}}, \boldsymbol{\Gamma})} g(\theta), \tag{7.16b}$$

$$p_2^a = C\frac{3}{32}\omega_{\text{noise}}^2 \frac{\Gamma_0^2}{(2\Gamma_2 + \omega_{\text{noise}}) G(\omega_{\text{noise}}, \boldsymbol{\Gamma})} h(\theta), \tag{7.16c}$$

where $C = g_{\text{D}}^2 (m_{20}^{\text{ini}})^4$ and

$$\begin{aligned} G(\omega_{\text{noise}}, \boldsymbol{\Gamma}) :=& (2\Gamma_0 + 3\omega_{\text{noise}}) \left[3\omega_{\text{noise}}^2(\Gamma_0 + 2(\Gamma_1 + \Gamma_2)) \right. \\ & \left. + 2\omega_{\text{noise}}(2\Gamma_0\Gamma_1 + 5\Gamma_0\Gamma_2 + 6\Gamma_1\Gamma_2) + 8\Gamma_0\Gamma_1\Gamma_2\right]. \end{aligned} \tag{7.17}$$

The angular dependence are given by

$$h(\theta) = [2\sin(2\theta) + 3\sin(\theta)]^2, \tag{7.18}$$

for p_0^a and p_2^a, whereas for p_1^a the angular dependence reads as

$$g(\theta) = [3 + 2\cos 2\theta + 3\cos 4\theta]^2. \tag{7.19}$$

It can be seen that in the low noise-strength regime that the peak heights obey $p_0^a \propto \omega_{\text{noise}}^2$, $p_1^a \propto \omega_{\text{noise}}$ and $p_2^a \propto \omega_{\text{noise}}^2$. Similarly, the dispersive peak heights are predicted to take the form

$$p_1^d = C\frac{3}{2}\frac{\omega_{\text{noise}}}{\Omega_L} \frac{\Gamma_0^2[16\Gamma_1^2\Gamma_2 + 8\Gamma_1(\Gamma_1 + 5\Gamma_2)\omega_{\text{noise}} + 16(\Gamma_1 + \Gamma_2)\omega_{\text{noise}}^2 + 3\omega_{\text{noise}}^3]}{(4\Gamma_1 + 5\omega_{\text{noise}})^3 G(\omega_{\text{noise}}, \boldsymbol{\Gamma})} g(\theta), \tag{7.20a}$$

$$p_2^d = C\frac{9}{64}\frac{\omega_{\text{noise}}^2}{\Omega_L} \frac{\Gamma_0^2(8\Gamma_2^2 + 8\Gamma_2\omega_{\text{noise}} + \omega_{\text{noise}}^2)}{(2\Gamma_2 + \omega_{\text{noise}})^3 G(\omega_{\text{noise}}, \boldsymbol{\Gamma})} h(\theta). \tag{7.20b}$$

7.3 Experimental setup

A schematic of the spin noise spectroscopy setup can be seen in Figure 7.2. Linearly polarised light that is resonant with the $F = 4 \longrightarrow F' = 3$ caesium D1 line (895 nm) is passed through a polarisation-maintaining fibre. The laser light has a diameter of 2 mm and an electric field amplitude $\mathbf{E_0}$ which passes through a (5 mm)^3 paraffin coated cell that is kept at room temperature and placed inside a magnetic shield (Twinleaf MS-1). The setup uses the paraffin coated vapour cell used in the table-top alignment magnetometer (see Figure 6.2a in Section 6.2). Details on the performance of the magnetometer presented here can be found in Section 6.4. Using the in-built coils in the magnetic shield, a static magnetic field $\mathbf{B_0} = B_0\hat{\mathbf{z}}$ is applied to the system. Figure 7.2 shows that a half wave plate is placed before the vapour cell and magnetic shield. This half wave plate is used to change the angle of the electric field vector of

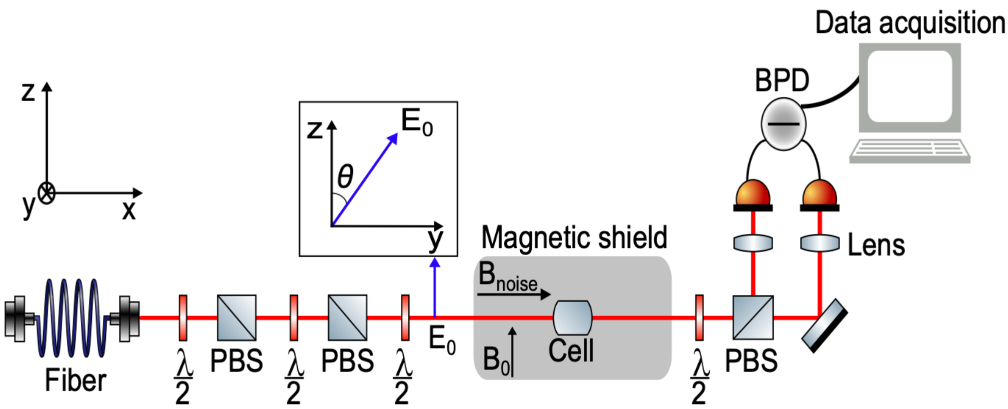

Figure 7.2: Schematic of the experimental setup implemented to study the spin noise spectroscopy of an alignment based magnetometer. A polarisation maintaining fibre is used to pass linearly polarised light, that is on resonance with the $F = 4 \longrightarrow F' = 3$ transition, to the setup. Two pairs of half wave plates ($\lambda/2$) and polarising beam splitters (PBS) are placed before the magnetic shield (marked in grey). The first pair is used to to reduce intensity fluctuations and the second pair is implemented so that the light power sent to the vapour cell can be altered. The laser light propagates along the x-axis, with the angle of its polarisation, θ, being varied in the experiment. The angle is varied in the (z, y)-plane using a third half wave plate that is placed directly before the magnetic shield. A paraffin coated caesium vapour cell is placed inside the shield. The laser light simultaneously pumps and probes the atomic ensemble. The atoms are placed in two magnetic fields: a static magnetic field, $\mathbf{B_0}$, that is applied in the z-direction and a weak noisy magnetic field, $\mathbf{B}_{\text{noise}}(t)$, that is applied in the x-direction. When the light interacts with the atoms it undergoes rotation, which is then measured by passing the output laser light through a PBS and measuring the balanced photodetection (BPD). The resulting signal is sent straight to a data acquisition card to be recorded.

the laser light with respect to the static magnetic field that is applied. The angle θ is denoted as the angle between the linear polarisation and the z-axis in the (z, y)-plane. Hence for a polarisation angle of $\theta = 0^{\circ}$ the electric field amplitude of the light is given by $\mathbf{E_0} = E_0\hat{\mathbf{z}}$ and for $\theta = 90^{\circ}$ it is given by $\mathbf{E_0} = E_0\hat{\mathbf{y}}$.

As well as the static magnetic field that is applied, a noisy magnetic field is also applied to the setup using a home-made square Helmholtz coil. This field is applied along the x-direction, such that $\mathbf{B}_{\text{noise}}(t) = B_{\text{noise}}(t)\hat{\mathbf{x}}$. The noisy magnetic field is generated using the white noise function on a function generator (RIGOL DG1032Z) with the output being attached to the Helmholtz coil. It is to be noted that a low-pass and a high-pass filter were placed between the function generator output and the home-made coil. The low-pass filter had a value of $f_{\text{cutoff}} = 1$ MHz and the high-pass filter had a value of $f_{\text{LP}} = 1$ kHz. The high-pass filter was implemented to prevent the effects of aliasing and the low-pass filter was used to remove any spurious contributions at very low frequencies.

The power spectra data that was measured as a function of the strength of the noisy magnetic field amplitude had a static magnetic field value of $B_0 = 2.7$ µT. This corresponds to a Larmor frequency of $f_L \approx 9.45$ kHz. For each dataset the strength of the noisy magnetic field amplitude was fixed in the range of 70.91 nT_{rms}

to 35.45 $\mu\mathrm{T}_{\mathrm{rms}}$. When studying the dependance of the power spectral density signal on the input polarisation angle the static field was set to $B_0 = 2.74$ μT ($f_L \approx 9.6$ kHz) and the white noise fields amplitude was fixed at $B_{\mathrm{noise}} = 1.4\ \mu\mathrm{T}_{\mathrm{rms}}$.

After the laser light has exited the cell, the polarisation rotation measurement is taken. This can be seen in Figure 7.2 as a half wave plate and a polarising beam splitter (PBS) are placed after the magnetic shield to split the components of the laser light. The light reflected and transmitted from the PBS is balanced when no magnetic fields are present in the experimental setup. The two light beams are then detected using a commercially available balanced photodetector (PDB210A/M). In order to check the linear polarisation of the setup, the ellipticity of the laser beam was measured before and after the vapour cell and it was found to be of negligible order, hence confirming the polarisation is maintained as linear in the setup. When measuring the change in the signal whilst altering the polarisation input angle the half wave plate after the shield is also rotated such that they match the polarisation angle of the transmitted light after the cell, θ'. It is noted that even if θ' is not perfectly matched, the resulting DC-component of the detected signal (Equation 7.7a) results in having a spike at zero frequency in the PSD. Within the analysis presented in this chapter this can be ignored without having any effect on the results. Hence, it is the deviations from θ' that are measured by balanced photodetection (BPD). The output voltage of the balanced photodetector is then recorded in real time using a data acquisition card (Spectrum Instrumentation M2p.5932-x4) for further analysis.

As the experimental setup in Figure 7.2 matches the theoretical spatial configuration of an alignment based magnetometer that is presented in Section 7.2, the photocurrent that is recorded can be interpreted as:

$$\delta S := S(t) - \overline{S}, \tag{7.21}$$

where $\overline{S} := \langle S_{\mathrm{ss}} \rangle$ is the time-independent mean DC component of the measured signal, which is determined by the mean of the steady-state solution, see Equation 7.4. Hence it can be seen that Equation 7.21 describes the deviations from the mean value of the detected signal which was determined in Equation 7.7a. The parameters in Equation 7.7a can be related to the experimental factors that impact their value. The effective proportionality constant g_D, which relates the instantaneous atomic state to the photocurrent signal, is dictated by a number of experimental conditions including: the power of the laser light (1 μW), the pumping efficiency, the size of the vapour cell ($(5\text{ mm})^3$), and the temperature of the cell (room temperature, $\sim 18^{\circ}$C). On the other hand, the detection noise, $\zeta(t)$, can be attributed to the photon shot noise and electronic noise arising solely due to the photodetection process that effectively leads to a background noise. Within the measured power spectral density it is seen that a DC offset is observed independently of whether the light beam interacts with the atoms or not. This results in a noise floor that depends on the frequency, partially due to the $1/f$ noise. This will be taken into account when interpreting the data and is further discussed in Section 7.5.

7.4 Calibrating the white noise amplitude

The magnitude of the noise spectral density needs to be calibrated from the white noise amplitude that is applied to the coils, i.e. $\omega_{\mathrm{noise}} = 2\pi f_{\mathrm{noise}} = 2\pi c V_{\mathrm{noise}}^2$. In order to determine the value of the calibration factor, c, the voltage in the coil that induces the noisy magnetic field is measured directly. The output signal from the function generator is first passed through a 1 MHz low-pass filter in order to prevent the effects of aliasing, and then transformed through a 1 kHz high-pass filter to remove any spurious contributions at near DC frequencies. The output of the function generator, at varying voltage amplitudes, are recorded for a duration of 0.01 seconds with 100 averages for each amplitude. The output is filtered through the same filters as used in the experiments and the data is sampled with a 40 MHz sample rate. The data is then used to compute the power spectral density of the signal sent to the coils, which is presented in Figure 7.3a, in the units of Hz (Hz^2/Hz). The units of Hz are obtained by performing adequate rescaling of the signal using the values of the coil calibration factor (10.1 nT/mV$_{\text{rms}}$) and the gyromagnetic ratio of caesium (3.5 Hz/nT). Five different amplitudes of V$_{\text{noise}}$, stated in mV$_{\text{rms}}$, are recorded.

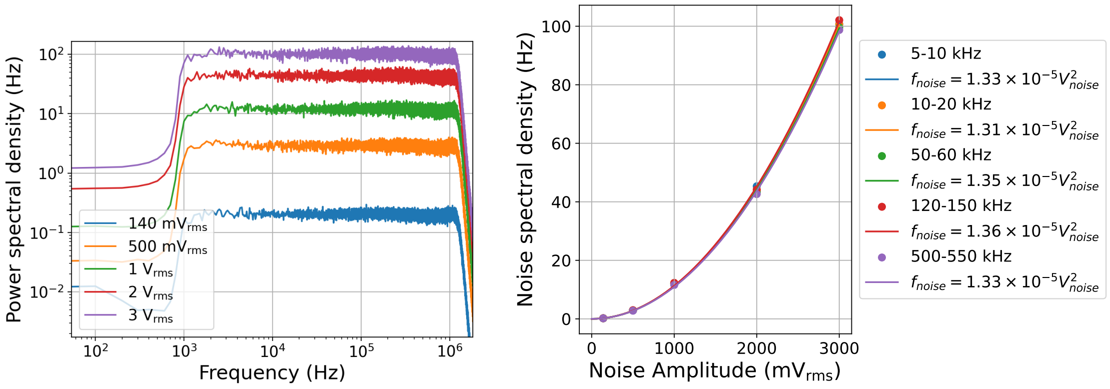

(a) (b)

Figure 7.3: Calibration of the amplitude of the white noise spectral density. (a) The output of the white noise setting on a function generator that is first passed through a 1 kHz high-pass filter and a 1 MHz low-pass filter, before being directly measured. 100 time traces of 0.01 seconds of data are recorded using a 40 MHz sample rate. The power spectral density of the data sets are then computed, which is rescaled to the units of Hz. (b) To calculate the conversion factor between the applied voltage and Hz, the effective magnitude of the noise spectral density needs to be calculated. The average value of the power spectral density is computed for five different frequency ranges, as a function of the amplitude V$_{\text{noise}}$ of the noise applied. The plot contains quadratic fits $f_{\text{noise}} = cV^2_{\text{noise}}$, applicable to each of the five frequency ranges used for averaging. These calibrations agree well and yield $c = 1.33(3) \times 10^{-5}$ Hz/mV$^2_{\text{rms}}$.

From the power spectral density, f_{noise} can be determined by seeing how the power spectral density varies with different white noise amplitudes. Areas of Figure 7.3a are averaged over in five different frequency zones (stated in Figure 7.3b) in order to obtain the effective value of f_{noise} as a function of the noise amplitude. For each of the averaged ranges, a quadratic dependence is then fitted to the data, $f_{\text{noise}} = cV^2_{\text{noise}}$. This can be used to determine the calibration factor $c = 1.33(3) \times 10^{-5}$ Hz/mV$^2_{\text{rms}}$, as shown in Figure 7.3b.

7.5 Measured Spectra

The noisy magnetic field, in the alignment based magnetometer, is varied to experimentally validate the theory outlined in Section 7.2. In the experimental data, the noise spectral density is defined in units of Hz, f_{noise}, whereas theoretically it is defined in units of rad/s, ω_{noise}. The two are related by $\omega_{\text{noise}} = 2\pi f_{\text{noise}}$. The voltage amplitude of the white noise signal that is sent to the coils is known, hence it is convenient to write the noise spectral density as $f_{\text{noise}} = cV^2_{\text{noise}}$ where the value of c was determined in the previous sub-section.

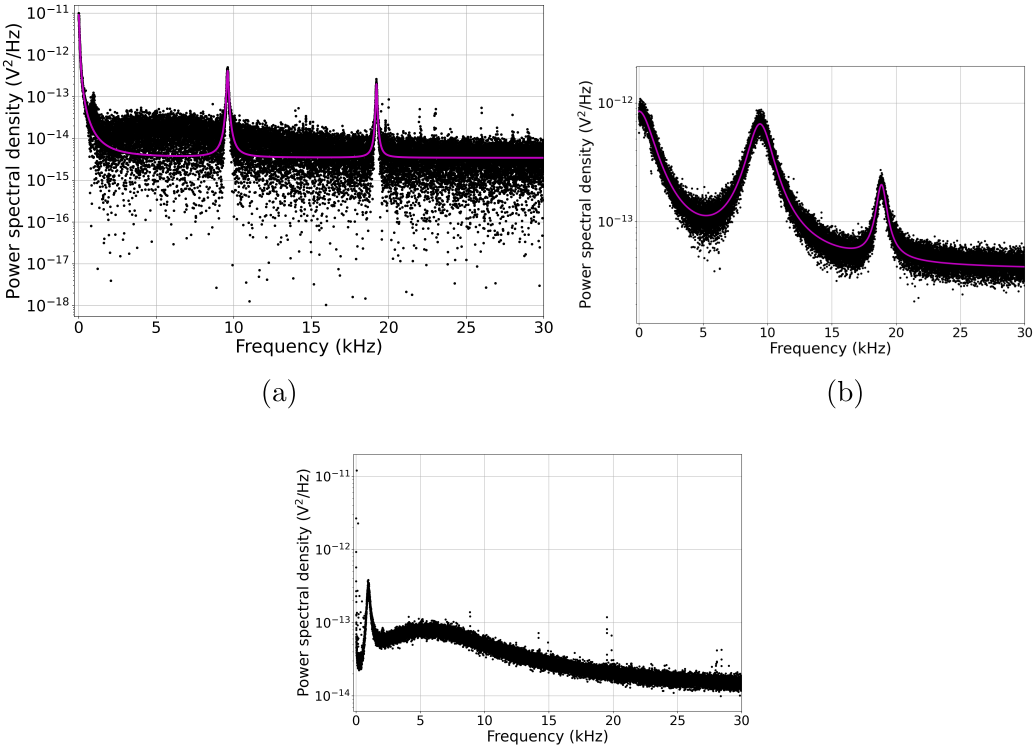

(a)

(b)

(c)

Figure 7.4: Examples of the power spectral density (PSD) for the experimental data (black dots) with the predicted theoretical fit function, Equation 7.8, plotted on top of the data (magenta line). Time traces of the magnetometer signal were recorded with 100 averages, each of which had a duration of 1 second. (a) The power spectral density of the signal when a relatively low noise spectral density of $f_{\text{noise}} = 0.26$ Hz is applied to the system and the input polarisation is set to $\theta = 40^{\circ}$. (b) The power spectral density of the magnetometer signal when a high noise spectral density is applied to the experimental setup of strength $f_{\text{noise}} = 120$ Hz with the input polarisation angle set to $\theta = 25^{\circ}$. The power spectral density for all settings have the experimental noise floors (shown in (c) subtracted and then are fitted using a single function (magenta curve)) containing three absorptive Lorentzian peaks with their centres located close to the frequencies $f = 0, f_L$ and $2f_L$. For low noise spectral density (a) the three peaks are distinguishable due to their small linewidth. At high noise spectral densities the linewidths become much larger and the three peaks significantly overlap.

For each set value of f_{noise} 100 time traces of 1 second duration were recorded, each of which were then Fourier transformed in order to measure the power spectral density. Figure 7.4a shows an example of the computed power spectral density obtained when the input polarisation angle is set to $\theta = 40^{\circ}$ and the white noise spectral density applied is relatively low, $f_{\text{noise}} = 0.26$ Hz which corresponds to $V_{\text{noise}} = 140$ mV$_{\text{rms}}$. In the power spectral density, there are three clear and distinct peaks located approximately at 0, f_L and $2f_L$ where $\Omega_L = 2\pi f_L$ which agrees with the result predicted by the theory (Equation 7.13). At low values of white noise being applied the peaks are clearly separated.

However, the noise floor between the peaks is not constant, as can be seen in Figure 7.4c. The noise floor approximately takes the value of 6.5×10^{-14} V^2/Hz for the peaks centred at $f_0 = 0$ and $f_1 \approx f_L$, while it reads approximately 2.7×10^{-14} V^2/Hz for the peak at $f_2 \approx 2f_L$. Due to this, when fitting the experimental data, the background noise floor is subtracted from each data set. This removes the detection noise (and $1/f$ noise) of different magnitudes at varying frequencies across the spectrum. This is seen in Figure 7.4a as the noise floor around the peaks is flat. A single function, containing three Lorentzian peaks, is fitted to the whole spectrum. This is the complete absorptive part of Equation 7.13. The corresponding fit parameters obtained for each of the three peaks in Figure 7.4a are listed in Table 7.1. Figure 7.4b shows the power spectral density of the magnetometry signal when high strengths of white noise are applied to the system. It can be seen in the PSD that the three peaks overlap when a high white noise is applied. This is shown explicitly for $f_{\text{noise}} = 120$ Hz. This is as expected from the theory due to an apparent increase of the peak linewidths.

In the rest of this chapter the expressions for the peak amplitudes are further studied. The dependence of the signal on the noise spectral density f_{noise} and the light polarisation angle θ is experimentally found in order to verify Equation 7.16.

j	f_j (Hz)	$\widetilde{\gamma}_j$ (Hz)	$\widetilde{p}^a_j$ (V^2/Hz)
0	0	34.9(2)	$9.03(3) \times 10^{-12}$
1	9603(1)	48.6(4)	$4.16(2) \times 10^{-13}$
2	19208(1)	37.8(6)	$1.97(2) \times 10^{-13}$

Table 7.1: Fit parameters in the low noise regime. A single function corresponding to the absorptive part of Equation 7.13 is fitted to reconstruct the PSD presented in Figure 7.4a. As it contains three Lorentzian profiles ($j = 0, 1, 2$), such a procedure yields three distinct sets of parameters: central frequencies (f_j), linewidths ($\widetilde{\gamma}_j$) and peak amplitudes ($\widetilde{p}^a_j$). The data was collected in the above measurement of the PSD (Figure 7.4a) for the Larmor frequency ~9.6 kHz, the light polarisation angle being set to $\theta = 40^{\circ}$, and the strength of applied noise set to 140 mV$_{\text{rms}}$ such that $f_{\text{noise}} = 0.26$ Hz.

7.6 Varying white noise

The amplitudes of the three peaks as a function of the applied noise spectral density f_{noise} (in Hz) is shown in Figure 7.5. For each variation, the power spectral density of the magnetometer signal is fitted to a single fit function which contained three absorptive Lorentzian peaks at $f = 0, f_L$ and $2f_L$, with the peak amplitude, linewidth and central frequency for each peak being extracted. The data was collected with the input polarisation angle fixed at $\theta = 25^{\circ}$. The applied white noise voltage was varied from 7 mV_{rms} to 3500 mV_{rms}. In order to convert the voltages to the power spectral density (in Hz) a proportionality constant is determined such that $f_{\text{noise}} = cV^2_{\text{noise}}$ where $c = 1.33(3) \times 10^{-5}$ $\text{Hz/mV}^2_{\text{rms}}$. The calibration process is described in Section 7.4.

The experimental findings for the peak amplitudes (Figure 7.5), linewidths (Figure 7.6a) and central frequencies (Figure 7.6b) are all consistent with the theoretical model. This is verified for each of the three parameters individually. In order to verify that the amplitudes match the theory, the amplitude values are plotted against the noise spectral density and fitted to Equation 7.16. When a weak noise spectral density is applied to the system it can be seen in Equation 7.16 that the dependencies show a linear or a quadratic relation, i.e. $\tilde{p}^a_0 \propto f^2_{\text{noise}}$, $\tilde{p}^a_1 \propto f_{\text{noise}}$ and $\tilde{p}^a_2 \propto f^2_{\text{noise}}$. This is verified by looking at the low white noise regime of Figure 7.5 which follows the same trend. It is noted that a tilde is used to describe the experimentally determined variables as the units are in Hz as opposed to rad/s used in the theory. This difference is the same in all cases so is absorbed by the proportionality constants, $\boldsymbol{C}$. When performing the full fitting procedure the proportionality constant at the front of each equation is allowed to differ ($\boldsymbol{C}_j$ for each p^a_j), while determining the common dissipation rates that are most consistent with the experimental data (Γ_0, Γ_1 and Γ_2). The proportionality constants are determined as $\boldsymbol{C}_0 = 2.1(2) \times 10^{-6}$ V^2, $\boldsymbol{C}_1 = 3.4(6) \times 10^{-6}$ V^2 and $\boldsymbol{C}_2 = 1.0(1) \times 10^{-6}$ V^2, respectively, which are all of the same order. The best fit dissipation rates for all three peaks read as $\tilde{\Gamma}_0 = 29(1)$ Hz, $\tilde{\Gamma}_1 = 43(4)$ Hz and $\tilde{\Gamma}_2 = 29(2)$ Hz.

The dissipation rates can also be determined from the linewidth $\tilde{\gamma}_j$ dependence on the noise spectral density. Figure 7.6a shows the linewidths, extracted from the experimental fits, against the noise spectral density. This data is fitted to Equation 7.15. A proportionality constant was added as a parameter to the theoretical equations to clearly determine how well the experimental data agrees. It can be seen that the linewidths follow the linear relationship with the slope increasing at varied rates almost perfectly. Moreover, the offsets at $f_{\text{noise}} = 0$ can be extracted and these values correspond to the dissipation rates. The dissipation rates from the linewidth fits are found to be $\tilde{\Gamma}_0 = 31(3)$ Hz, $\tilde{\Gamma}_1 = 34(1)$ Hz and $\tilde{\Gamma}_2 = 34(3)$ Hz. These are all in good agreement with those determined from the peak amplitude relation, shown in Figure 7.5.

Finally, the ability of the theoretical model to predict the relation between the central frequency and the noise spectral density needs to be studied. Figure 7.6b shows how the central frequencies vary at different noise spectral density amplitudes. The theoretically predicted relation, from Equation 7.14, is plotted over the experimental data for f_L (green dots) and $2f_L$ (blue squares). The theory is fitted to the experimental data with $f_L = \Omega_L/2\pi = 9435(1)$ Hz being the only free parameter. It can be seen that the theory agrees reasonably well with the experiment but at the values used in this experiment the change is small. It can be seen that, for the peak at f_L, the central frequency decreases in the high noise regime and mainly remains constant for the second peak. It is noted that the central frequencies stated in Figure 7.6b are within ±5 Hz. The errors on the data come from experimental imperfections, such as central frequency drifts over the time it takes to carry out the

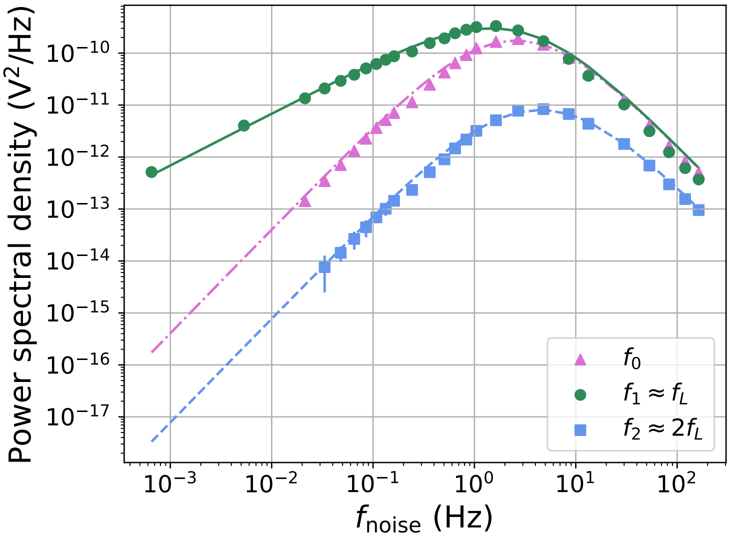

Figure 7.5: Amplitudes of the power spectral density peaks as a function of the white noise strength, which is varied from 6.53×10^{-4} Hz to 163 Hz with the light polarisation angle fixed at $\theta = 25^{\circ}$. For each value of f_{noise}, the amplitude is extracted, alongside the central frequency and linewidth, by fitting the PSD to an absorptive Lorentzian (as described in Figure 7.4). The theoretical model is fitted to the experimental data with the resulting fit plotted on top of the data for each peak at 0 Hz (pink, dotted-dashed), $\sim f_L$ (green, solid) and $\sim 2f_L$ (blue, dashed). All three peak amplitudes $\tilde{p}_j^a$ clearly follow the theoretical predictions of the form given in Equation 7.16 where the proportionality constant, C_j, for each of the three peaks is allowed to differ as well as the common values for the dissipation rates $\tilde{\Gamma}_0, \tilde{\Gamma}_1$ and $\tilde{\Gamma}_2$.

experiment and errors in fitting data. These errors have more of an impact on the peak at $2f_L$ due to the peak amplitudes being at least an order of magnitude smaller and hence closer to the experimental noise floor of the setup. Taking the errors into consideration, it can be concluded that the theory predicts the dependence of the central frequencies on the white noise strength well for both of the peaks.

It is noted that the spectrum was not fitted to the dispersive contribution of Equation 7.13. This is due to the dispersive contribution being below the experimental noise floor. It can be verified that this is as expected for a Larmor frequency of 9.45 kHz by calculating the ratio of the peak heights. Using the peak heights, p_1^a and p_2^a, and linewidths, $\tilde{\Gamma}_1 = \tilde{\Gamma}_2 = 34$ Hz, determined experimentally. p_1^d/p_1^a is determined by dividing Equation 7.20a by Equation 7.16b and p_2^d/p_2^a is determined from Equation 7.20b divided by Equation 7.16c. The calculations were done for the lowest white noise amplitude of 7 mV$_{\text{rms}}$ and the highest white noise amplitude of 3.5 V$_{\text{rms}}$. For V$_{\text{noise}}$ = 7 mV$_{\text{rms}}$ it is calculated that $p_1^d/p_1^a = 1.1 \times 10^{-4}$ and $p_2^d/p_2^a = 3.2 \times 10^{-4}$. Furthermore, when V$_{\text{noise}}$ = 3.5 V$_{\text{rms}}$ it is found that $p_1^d/p_1^a = 3.1 \times 10^{-5}$ and $p_2^d/p_2^a = 1.8 \times 10^{-4}$. Hence, the dispersive contribution is at least 4 orders of magnitude smaller than the absorptive contribution. Hence, this is significantly below the noise floor for both peaks, as seen experimentally.

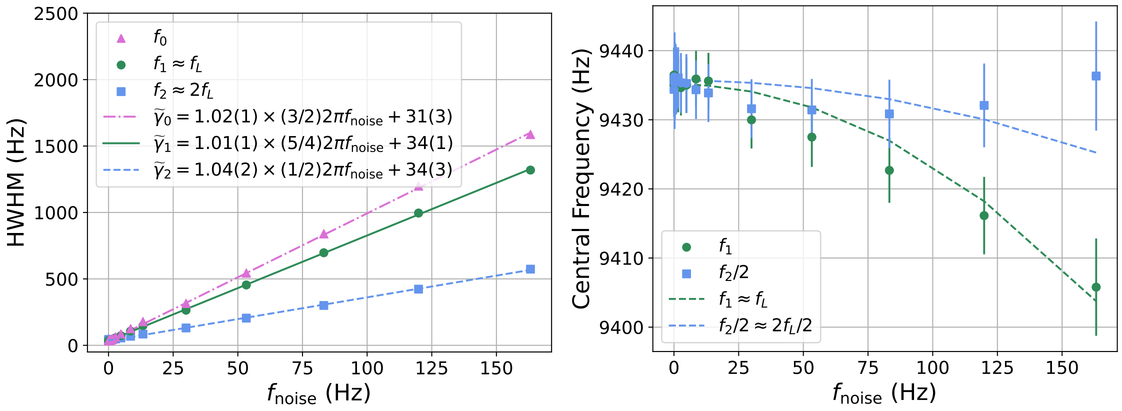

(a) (b)

Figure 7.6: The linewidth (a) and central frequency (b) of the power spectral density peaks as a function of the white noise strength (f_{noise}), which is varied from 6.53×10^{-4} Hz to 163 Hz with the light polarisation angle fixed at $\theta = 25^{\circ}$. (a) The linewidth increases linearly as a function of f_{noise} with the slope for each peak agreeing almost exactly with the proportionality constants predicted in Equation 7.15. Their offsets at $f_{\mathrm{noise}} = 0$ provide the three dissipation rates Γ_0, Γ_1 and Γ_2, which are consistent (up to $\approx$ 10 Hz) to those predicted by fitting the amplitudes (Figure 7.5). (b) The change in the central frequency is theoretically predicted in Equation 7.14. The theoretical fit is plotted on top of the experimental data (dashed lines) with $f_L = 9435(1)$ Hz is the only free parameter when fitting for $f_1 \approx f_L$ (green circles) and $f_2 \approx 2f_L$ (blue squares). The overall error in the experimentally determined central frequencies is approximately ±5 Hz, arising both from experimental imperfections (e.g., drifts, background-noise subtraction) and the fitting procedure.

7.7 Varying polarisation angle

In Equation 7.16 it can be seen that the angular dependence of the peak amplitudes can be separated from the other parameters. The angular dependence can be described by functions of the form of $h(\theta)$ (Equation 7.18) and $g(\theta)$ (Equation 7.19). This is verified explicitly in the low white noise regime with an applied noise amplitude of $V_{\mathrm{noise}} = 140\ \mathrm{mV_{rms}}$, which corresponds to $f_{\mathrm{noise}} = 0.26$ Hz, by varying the polarisation angle of the incoming light from $\theta = -20^{\circ}$ to 120°. The Larmor frequency used is $\approx$ 9.6 kHz. Figure 7.7 shows the resulting peak amplitudes as a function of the input polarisation angle. It shows the experimental results reproduce, almost exactly, the theoretically predicted angular behaviours. As expected from the theory, Figure 7.8 shows that the linewidth and central frequency remain relatively constant. The central frequency does drift over the time it takes for the data collection. The linewidth of the three peaks is determined by averaging over the linewidths of the peaks at all input angles of the polarisation, see Figure 7.8a. The linewidths are determined as $\tilde{\gamma}_0 \approx 33(2)$ Hz, $\tilde{\gamma}_1 \approx 36(1)$ Hz and $\tilde{\gamma}_2 \approx 36(3)$ Hz. By substituting these values and the known noise spectral density of $f_{\mathrm{noise}} = 0.26$ Hz into Equation 7.15 the dissipation rates are found to be $\tilde{\Gamma}_0 \approx 31(2)$ Hz, $\tilde{\Gamma}_1 \approx 34(1)$ Hz and $\tilde{\Gamma}_2 \approx 35(3)$ Hz. Using these disspation rates, the peak amplitudes shown in Figure 7.7 can be fitted to the full theoretical model using Equation 7.16. When fitting the angular dependance $h(\theta)$ and $g(\theta)$ the fitting

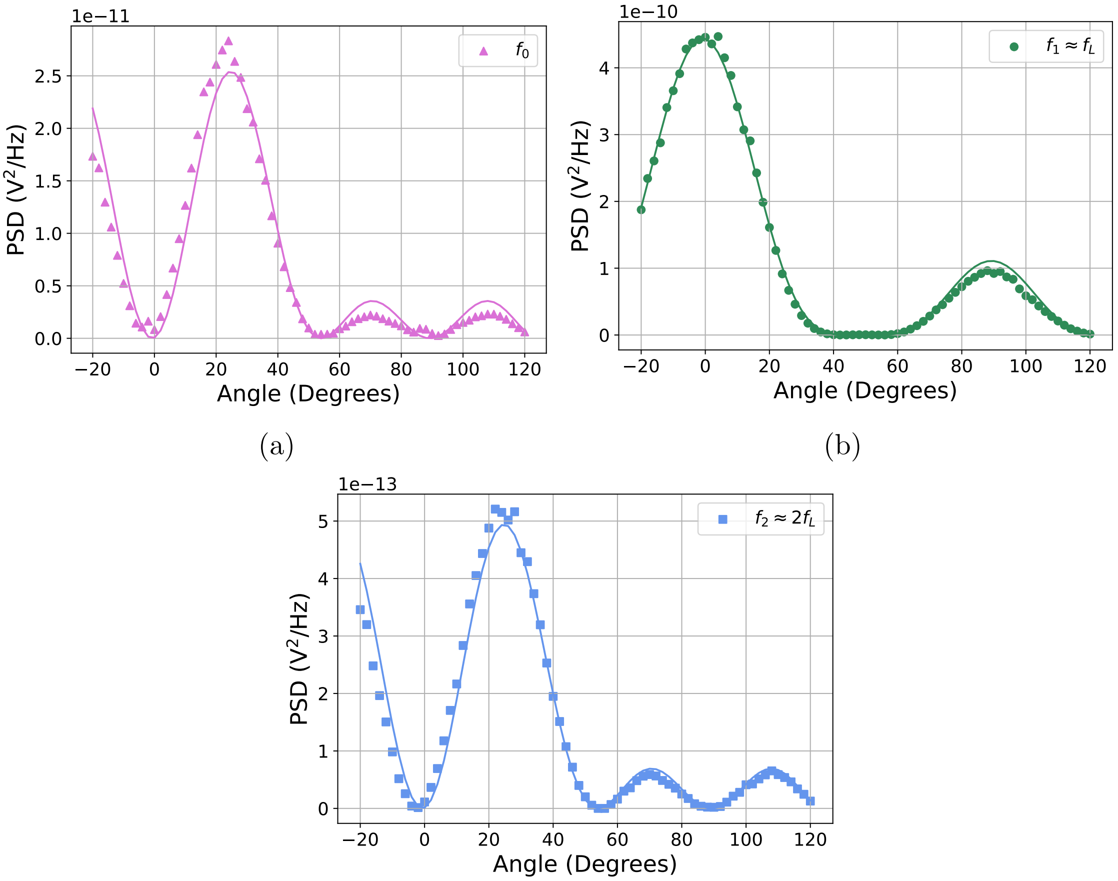

(a) (b)

(c)

Figure 7.7: The peak amplitudes of the power spectral density as a function of the input polarisation angle of the light, which is varied from $\theta = -20^{\circ}$ to 120°. The white noise strength is fixed at $V_{\text{noise}} = 140$ mV$_{\text{rms}}$, corresponding to $f_{\text{nosie}} = 0.26$ Hz. The theoretical model predictions (Equation 7.16), in particular the angular dependencies $h(\theta)$ and $g(\theta)$ (see Equations 7.18 and 7.19), are represented by the solid curves. The data is shown for the three peaks that appear in the power spectral density which have peaks centred at (a) 0 Hz, (b) f_L Hz and (c) $2f_L$. The theory is fitted using the known dissipation rates (see Figure 7.8a), with a common correction to the input angle such that $\theta \longrightarrow \theta + \delta\theta$ where $\delta\theta = 0.77(7)^{\circ}$. For each p_j^a a proportionality constant is fitted and determined to be $c_0 = 3.1(5) \times 10^{-6}$ V, $c_1 = 2.0(1) \times 10^{-6}$ V and $c_2 = 1.3(5) \times 10^{-6}$ V.

procedure accounts for a common angular offset by allowing $\theta \longrightarrow \theta + \delta\theta$. It is found that $\delta\theta = 0.77(7)^{\circ}$ for the data presented here. Similarly to the case of varying the white noise amplitude, a proportionality constant is C_j is also added to each fit function for the three peaks $\tilde{p_j^a}$ and are determined as $C_0 = 3.9(6) \times 10^{-6}$ V, $C_1 = 2.1(1) \times 10^{-6}$ V and $C_2 = 1.5(4) \times 10^{-6}$ V. These are all consistently of the same order of magnitude and very similar to the constants for each of the three peaks determined for varying the white noise strength. The experimental data agrees well with the theoretical model and the overall fit functions are plotted on top of the experimental data in Figure 7.7.

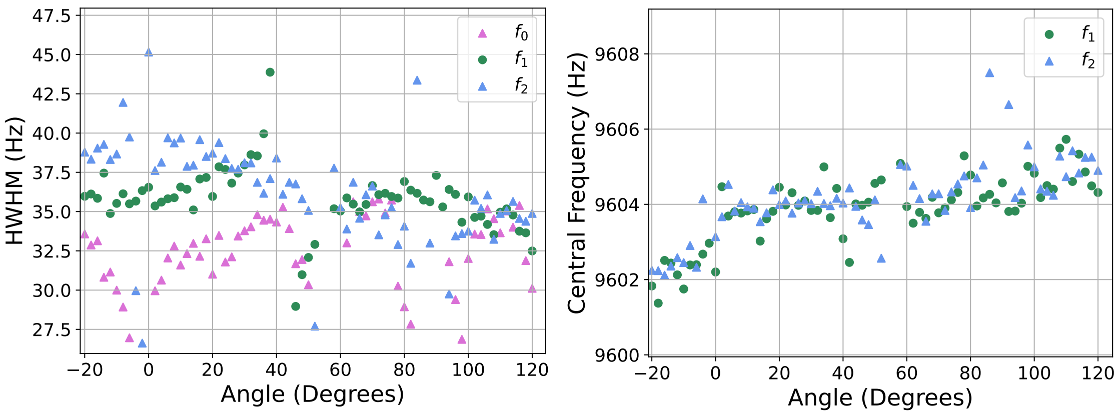

(a) (b)

Figure 7.8: The angular dependence on the (a) half width half maximum (HWHM) and the (b) central frequency for the three peaks in the power spectral density. As expected from the theory, both of these parameters are independent of the input polarisation angle and hence remain constant.

7.8 Conclusion

In this chapter experimental data is presented to verify the dynamical model that is introduced. The model allows for the spin noise spectra of an alignment based magnetometer to be predicted. These predictions are verified for various strengths of noise spectral density and a range of input polarisation angles. The experimental data and model rely on the presence of a white noise magnetic field being applied along the propagation direction of the laser beams. The added noise is used to amplify the Larmor induced peaks in the power spectral density so that they are clearly visible above the detection noise floor. The model can be used with signal processing tools to interpret the detected data better. For example, when the OPM is being operated as a scalar magnetometer, Bayesian inference methods such as a Kalman filter [136] can be used to track fast changes of the strong magnetic field in real time. This method also allows for the signal to be tracked beyond the magnetometer bandwidth [139, 140]. With the addition of the noisy magnetic field the setup could be used to perform sensing tasks in a covert manner [141]. Without having access to the pre-calibrated model an adversary who has access to the magnetometer output cannot recover the signal. In this sense, the possibility for the model to be useful for tracking time-varying signals that are encoded in oscillating magnetic fields directed perpendicularly to both the scalar magnetic field and the noisy magnetic field.

Future steps with the alignment based spin noise model here would be to generalise the model such that it describes a sensor that operates at the quantum limit [123, 125, 124], where the detection noise is small enough such that the predicted peaks in the spectrum are visible without the need to apply an artificial white noise field to amplify them. This model could then be capable of incorporating the effect of pumping and probing the ensemble with squeezed light, such that the detection noise would be reduced further, as has been done for orientation based magnetometers [126, 142, 143].

Chapter 8

Zero-field magnetometer

8.1 Motivation

Optically pumped magnetometers (OPMs) have transformed the way that magnetic fields are measured. The process is now more precise and accessible than ever before. These devices challenge alternative magnetic field sensors, such as SQUIDs [14] which are complex and expensive to operate. A number of commercially available OPMs operate exclusively near zero magnetic field [40, 42, 47] and are commonly operated in the spin-exchange relaxation-free (SERF) regime [43, 45]. This allows for one or more of the magnetic fields near zero-field to be measured with high sensitivities [133, 144]. OPMs near zero-field are extremely useful in a number of fields, especially for biomedical applications like magnetoencephalography (MEG) and magnetocardiography (MCG). For the detection of brain activity in MEG, SQUIDs have been the standard for measurements however they are large, bulky, expensive and require the patients to wear rigid helmets. The bulkiness of the helmets makes it difficult to study brain activity especially in children. Recent developments into OPM-MEG have shown promising results with them being introduced into hospitals. Optically pumped magnetometers are smaller and easier to wear when placed into a helmet configuration which makes them ideal for studying brain activity in moving individuals, including children [145, 146].

SERF magnetometers and alignment based magnetometers both have unique strengths and weaknesses when operating near zero-field. Alignment based magnetometers can operate at room temperature and have a wide frequency range. This makes them suitable for measuring a diverse range of magnetic fields, from slowly varying signals like those from a heartbeat to more rapidly changing signals such as nerve impulses and radio frequency magnetic fields [147]. SERF magnetometers typically require high temperatures of between 100°C and 200°C for optimal operation with very narrow linewidths [46]. However, they can only be operated in close to zero-field settings and require significant magnetic shielding and field compensation for optimal sensitivity. Magnetic field gradients and fluctuations significantly reduces the sensitivity of the OPMs. Hence, the process of zeroing the magnetic field in an OPM setup has a significant impact on the performance. Developing the techniques for zeroing the magnetic field has the potential to greatly improve the performance of a magnetometer near zero-field.

In the work presented in this chapter, a spin aligned atomic ensemble is utilised for zero-field magnetometry. A modulation free method for nulling the magnetic field is introduced. This technique includes studying how the linear polarisation of light is rotated after it is transmitted through an ensemble of caesium atoms. This is different to the current method used that depend on modulation [18, 106]. Analytical expressions are derived for the spin alignment and detected signals based on polarisation rotation and absorption. This is then verified using the alignment based magnetometer, shown in Section 6, near zero magnetic field. By analysing the polarisation rotation signal under different magnetic field conditions it is determined which direction the compensating magnetic field needs to be adjusted in order to decrease the overall magnetic field amplitude. This method is then used and the resulting magnetic field condition is characterised with the magnetometer's sensitivity and bandwidth being measured. Finally, it is demonstrated that the magnetometer has a sufficient performance for use in the biomedical application of magnetocardiography by measuring a synthetic cardiac signal that resembles an adult human's heart.

8.2 Magnetometry near zero-field

As derived in Section 4.8, when there is a non-zero magnetic field the signal from the alignment based magnetometer is given by

$$S^{\text{abs}} \propto m_{0,0} - \chi \frac{m_{2,0}^{\text{eq}}\{\Gamma^4 + (\omega_x^2 + \omega_y^2 - 2\omega_z^2)^2 + \Gamma^2[2(\omega_x^2 + \omega_y^2) + 5\omega_z^2]\}}{(\Gamma^2 + \omega_x^2 + \omega_y^2 + \omega_z^2)[\Gamma^2 + 4(\omega_x^2 + \omega_y^2 + \omega_z^2)]} \tag{8.1}$$

for absorption measurements and

$$S^{\text{PR}} \propto \frac{\sqrt{6} m_{2,0}^{\text{eq}}[\Gamma^3\omega_x - \Gamma^2\omega_y\omega_z + 2\omega_y\omega_z(\omega_x^2 + \omega_y^2 - 2\omega_z^2) + \Gamma\omega_x(\omega_x^2 + \omega_y^2 + 4\omega_z^2)]}{(\Gamma^2 + \omega_x^2 + \omega_y^2 + \omega_z^2)[\Gamma^2 + 4(\omega_x^2 + \omega_y^2 + \omega_z^2)]} \tag{8.2}$$

for polarisation rotation measurements of the transmitted light. In this chapter, how the magnetometer responds near zero-field is studied. The magnetometer signal can be utilised to null the magnetic field using the theoretical model. Equations 8.1 and 8.2 can be simplified near zero-field as it is instructive to Taylor expand the full formulas for the absorption and polarisation rotation hence obtaining simpler expressions for the expected signal. In order to keep the notation as simple as possible the following parameters are defined as $x = \omega_x/\Gamma$, $y = \omega_y/\Gamma$, and $z = \omega_z/\Gamma$ which are proportional to the $\boldsymbol{B}_x$, $\boldsymbol{B}_y$ and $\boldsymbol{B}_z$ components of the magnetic field, respectively.

The equation for the absorption signal will be simplified first. Begin by sweeping the $\boldsymbol{B}_x$ magnetic field and assume that $\boldsymbol{B}_y$ and $\boldsymbol{B}_z$ are close to zero (i.e. $y, z << 1$) then the expected signal equation simplifies to

$$S^{\text{abs}} \propto m_{0,0} - \chi m_{2,0}^{\text{eq}} \left[\frac{1}{1 + x^2}\right]. \tag{8.3}$$

Similarly, if sweeping the $\boldsymbol{B}_y$ magnetic field and assuming that $\boldsymbol{B}_x$ and $\boldsymbol{B}_z$ are close to zero it can be seen that

$$S^{\text{abs}} \propto m_{0,0} - \chi m_{2,0}^{\text{eq}} \left[\frac{1}{1 + y^2}\right]. \tag{8.4}$$

Finally, when sweeping the $\boldsymbol{B}_z$ magnetic field, assuming that $\boldsymbol{B}_x$ and $\boldsymbol{B}_y$ are close to zero results in a signal of the form

$$S^{\text{abs}} \propto m_{0,0} - \chi m_{2,0}^{\text{eq}} \times 1. \tag{8.5}$$

In this case the absorption signal is constant and independent of x, y, and z to first order.

The same can now be done with the signals resulting from polarisation rotation measurements. If the $\boldsymbol{B}_x$ magnetic field is being swept and it is assumed that $\boldsymbol{B}_y$ and $\boldsymbol{B}_z$ are close to zero (i.e. $y, z << 1$) then the theory estimates, to first order, the signal as

$$S^{\text{PR}} \propto \sqrt{6} m_{2,0}^{\text{eq}} \left(\frac{x}{1 + 4x^2} \right). \tag{8.6}$$

In this case, the signal does not depend on y and z to the first order and it has a dispersive lineshape as a function of x. The slope of the full signal shown in Equation 8.2 can also be calculated by taking the derivative with respect to x to second order in y and z:

$$\frac{\partial S^{\text{PR}}}{\partial x}_{|x=0} \propto \sqrt{6} m_{2,0}^{\text{eq}} \left[\frac{1 + y^2 + 4z^2}{(1 + y^2 + z^2)(1 + 4y^2 + 4z^2)} \right]. \tag{8.7}$$

From this it can be seen that the slope of the signal is maximal when $y = z = 0$. The same can now be done for simplifying the polarisation rotation signal for sweeping the $\boldsymbol{B}_y$ magnetic field, assuming the $\boldsymbol{B}_x$ and $\boldsymbol{B}_z$ magnetic fields are close to zero, then to first order in x and z the signal is of the form

$$S^{\text{PR}} \propto \sqrt{6} m_{2,0}^{\text{eq}} \left[x \frac{1}{1 + 4y^2} + z \frac{y(-1 + 2y^2)}{(1 + y^2)(1 + 4y^2)} \right]. \tag{8.8}$$

Finally, when sweeping the $\boldsymbol{B}_z$ magnetic field with $\boldsymbol{B}_x$ and $\boldsymbol{B}_y$ close to zero ($x, y << 1$) then the signal is of the form

$$S^{\text{PR}} \propto \sqrt{6} m_{2,0}^{\text{eq}} \left[x \frac{1}{1 + z^2} - y \frac{z}{1 + z^2} \right]. \tag{8.9}$$

Hence, the polarisation rotation signal, to first order, is a measure of the $\boldsymbol{B}_x$ component of the magnetic field.

From Equations 8.8 and 8.9 it can be seen that it is possible to use the polarisation rotation signals as a sensitive method for nulling the magnetic field. By using multiple magnetic fields, to sweep and apply static and sweeping fields, one can null any residual magnetic fields until the magnetic resonance signal is zero. When a zero signal is obtained when sweeping the magnetic field along the $\boldsymbol{B}_y$ and $\boldsymbol{B}_z$ direction then all three magnetic field components are zero. This procedure can be done iteratively and will be experimentally studied in the following sub-sections.

8.3 Experimental setup

The table-top magnetometer that is based on spin alignment and presented in Section 6 is modified to perform near zero-field. The schematic for the experimental setup is shown in Figure 8.1. Laser light with a wavelength of 895 nm, that is

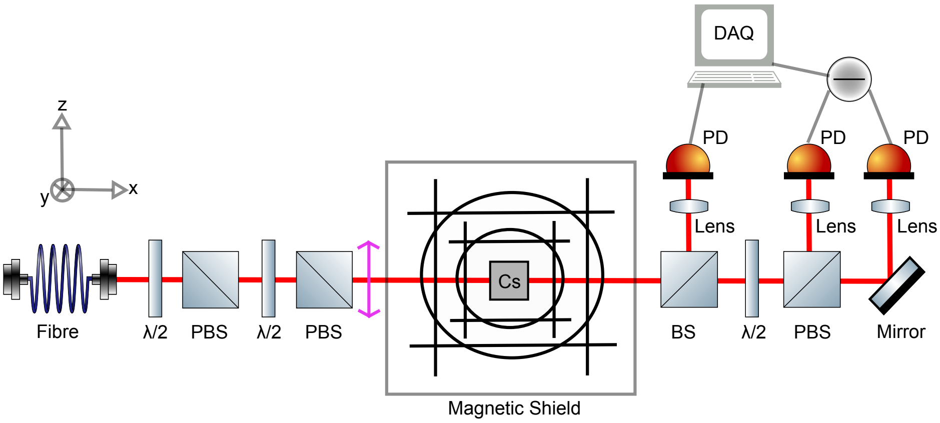

Figure 8.1: Experimental setup of utilising an alignment based magnetometer near zero magnetic field. The laser passes through a cubic vapour cell filled with caesium. There are two set of three Helmholtz coils surrounding the cell within the magnetic field. The laser light is polarised in the z-direction (magenta arrow) and propagates along the x-direction. The setup consists of a polarisation maintaining fibre, half wave plates ($\lambda/2$), polarising beam splitters (PBS), beam splitters (BS), a mirror, a single photodiode detector (PD) and a balanced photodetector consisting of two photodiodes.

resonant with the $F = 4 \rightarrow F = 3'$ caesium D1 transition, is passed through a polarisation maintaining fibre (Thorlabs DBR895PN). Two sets of a half wave plate ($\lambda/2$) and a polarising beam splitter (PBS) can be seen in Figure 8.1. The first set is used to clean up the polarisation of the light after the fibre and the second set is used to adjust the intensity of the laser light. The laser is polarised in the z-direction with a light power of 3 µW for the data presented in Figures 8.2, 8.3, 8.4 and 8.5, and 10 µW for the data presented in Figures 8.6 and 8.7. The laser is passed through a paraffin coated cell (see Figure 6.2a) placed inside a mu-metal magnetic shield (Twinleaf MS-1L). After the magnetic shield, a beam splitter is placed so that polarisation measurements and absorption measurements can be recorded. The polarisation rotation measurements are performed using a half wave plate, polarising beam splitter and balanced photodetector (Thorlabs PDB210A/M). The photodetector output is then passed through a 2 kHz low-pass filter before being recorded by the data acquisition card. It is noted that for the sensitivity and bandwidth measurements the beam splitter is removed and just the polarisation rotation measurement is studied. This is to see a larger signal as all light power transmitted through the vapour cell will hit the balanced detectors. For the absorption measurements, see Figure 8.1, the optics utilised after the magnetic shield are replaced with a single photodetector (Thorlabs PDA36A2). Similarly, in this case the data is still passed through a 2 kHz low-pass filter before being recorded.

The paraffin coated caesium cell is positioned within three sets of coils in the magnetic shield. Each set of coils can be used to apply magnetic fields in three directions ($\tilde{\mathbf{x}}$, $\tilde{\mathbf{y}}$, $\tilde{\mathbf{z}}$). When no coils are on a residual magnetic field $\mathbf{B}^{\text{residual}}$, on the order of 100 nT, is present inside the magnetic shied. The integrated coils in the magnetic shield (as standard in the Twinleaf MS-1L magnetic shield) are used to apply a static magnetic field $\mathbf{B}^{\text{DC}}$ which is used to compensate for the residual magnetic field. The larger of the two home-made three axis Helmholtz coil sets is used to generate a linearly sweeping magnetic field $\mathbf{B}^{\text{sweep}}(t)$ which is utilised in the procedure for nulling the static magnetic field. The other home-made three axis set of Helmholtz coils is used to generate different signals $\mathbf{B}^{\text{signal}}(t)$, e.g. a sinusoidal magnetic field for characterising the magnetometer response and sensitivity or a synthetic cardiac signal. Hence the total magnetic field present in the shield can be written as

$$\mathbf{B} = \mathbf{B}^{\text{residual}} + \mathbf{B}^{\text{DC}} + \mathbf{B}^{\text{sweep}}(t) + \mathbf{B}^{\text{signal}}(t). \tag{8.10}$$

8.4 Nulling the magnetic field

It will now be demonstrated how the experimentally obtained polarisation rotation signal S^{PR} can be utilised to null the total static magnetic field $\mathbf{B}^{\text{residual}} + \mathbf{B}^{\text{DC}}$. This method involves systematically sweeping the magnetic fields $\mathbf{B}^{\text{sweep}}(t)$ applied in the y- and z-direction and then varying the applied static field $\mathbf{B}^{\text{DC}}$ until a zero signal $S \approx 0$ is obtained. The total static field present in the magnetic shield should hence be $\mathbf{B}^{\text{residual}} + \mathbf{B}^{\text{DC}} \approx 0$. The procedure to null the magnetic field can be done iteratively. The results presented in this section were all produced with the total static magnetic field in the shield being close to zero. Hence the theory can be fitted to the Taylor expanded theoretically predicted lineshapes.

Figure 8.2a shows the experimental results of sweeping the magnetic field $\mathbf{B}_y^{\text{sweep}}(t)$ along the y-direction. For these measurements the static magnetic field along the x-direction was varied within the range of 10.86(1) nT to 16.86(1) nT. The static field components B_y^{DC} and B_z^{DC} were fixed at −44.00(1) nT and −97.35(1) nT, respectively. Note, the errors stated here arise from the coil calibrations used to convert from voltage applied to the field experienced at the sensing point of the atoms. The DC magnetic fields applied in the transverse directions to the static field being varied are selected such that the magnetic field in those directions are close to zero. The signals observed experimentally have a Lorentzian lineshape, as expected from the theory shown in Equation 8.8 when $x \neq 0$ and $z = 0$. When the total magnetic field in the magnetic shield is zero, which is when $B_x^{\text{DC}} = 13.82(5)$ nT, the signal transforms into a flat line which is predicted by Equation 8.8 when $x = z = 0$. This data set has an applied static magnetic field that precisely cancels the residual magnetic field leading to a net zero static field $\mathbf{B}^{\text{residual}} + \mathbf{B}^{\text{DC}} \approx 0$. Figure 8.2b shows the parameter $x \propto B_x^{\text{residual}} + B_x^{\text{DC}}$ which is determined by fitting the data in Figure 8.2a to Equation 8.8. A linear relationship can be seen between the applied static field and the fitted parameter x which represents the total static field. The fit function also fits the z parameter (see Appendix D.1) which is found to be much smaller than the values fitted for x with the results being $z \approx 0.0024$ V.

Measurements of setting the applied static field in the $\tilde{\mathbf{x}}$ component of the applied static field to $B_x^{\text{DC}} = 13.86(1)$ nT such that the overall static field is close to zero are also obtained. In this case the static magnetic field applied along the z-direction and is varied between −100.35(1) nT and −94.35(1) nT. In Figure 8.2c the signal can be seen to have more of a dispersive lineshape with the experimental data agreeing well with the theoretical predictions (see the black dotted lines). The lineshape can be seen to agree well with the theory predicted in Equation 8.8 when $x = 0$ and $z \neq 0$. Again when the applied static field compensates for the residual magnetic field in the shield the signal can be seen to be fairly constant. Figure 8.2d shows the fit

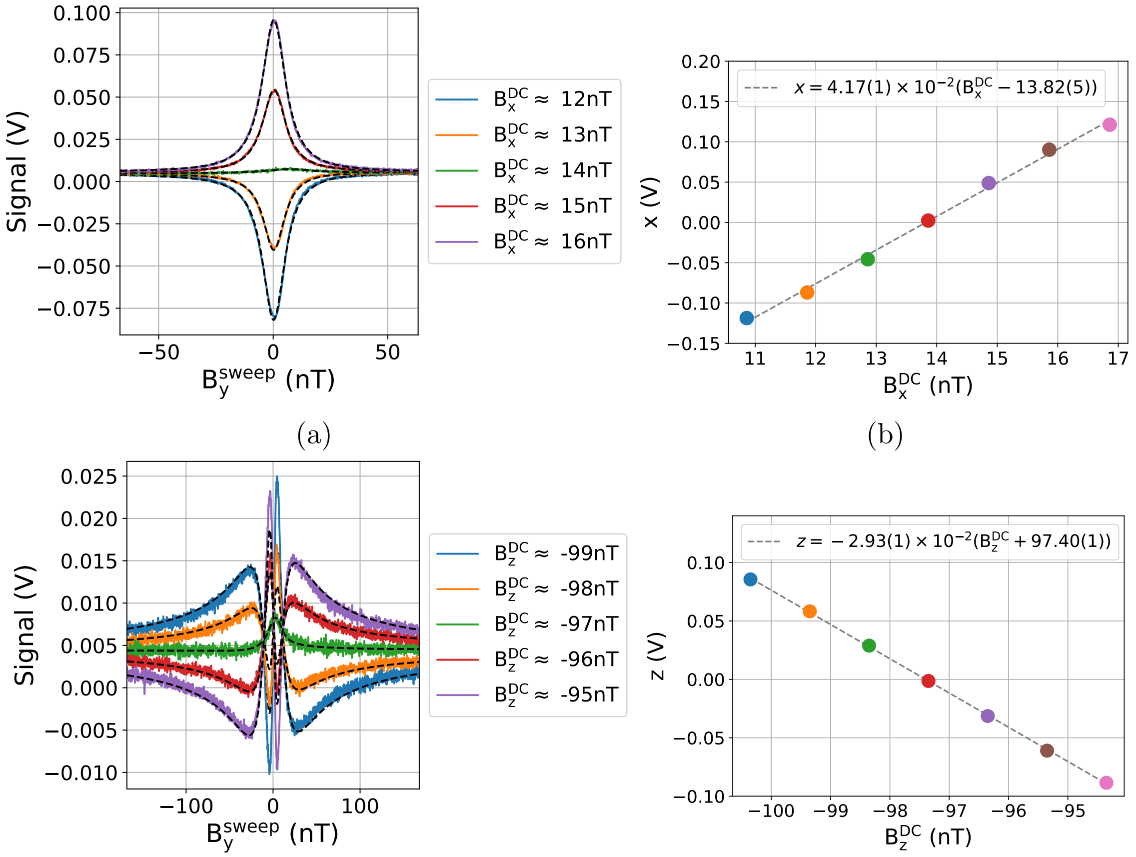

(a) (b) (c) (d)

Figure 8.2: Nulling procedure of sweeping a magnetic field $B_y^{\text{sweep}}(t)$ which is applied along the y-direction in near zero-field conditions. For each magnetic field sweep, different static fields are chosen in a set direction. For the obtained magnetic resonances the experimental data (solid, coloured lines) are fitted to the theoretical predictions shown in Equation 8.8 (black dotted lines). The varied parameter in each data set is then extracted and is fitted to a linear relation (black dotted line). (a) The magnetic resonance signals for various values of the applied static field B_x^{DC} along the x-direction where the DC magnetic field applied along the y- and z-directions are kept constant at $B_y^{\text{DC}} = -44.00(1)$ nT and $B_z^{\text{DC}} = -97.35(1)$ nT. (b) The corresponding fit parameters $x \propto (B_x^{\text{residual}} + B_x^{\text{DC}})$ extracted from (a) as a function of the applied DC field. The DC field along the z-direction is then varied with the magnetic resonances (c) being fitted and (d) the fit parameter $z \propto (B_z^{\text{residual}} + B_z^{\text{DC}})$ being shown as a function of the DC applied field. In the case of B_z^{DC} being varied the static field along the x-direction is fixed at $B_x^{\text{DC}} = 13.86(1)$ nT. For each magnetic resonance, the parameter Γ/γ was also fitted and found to be 12(1) nT for (a) and 15(1) nT for (c).

parameter $z \propto (B_z^{\text{residual}}+B_z^{\text{DC}})$ which is determined by fitting the data in Figure 8.2c. As expected, a linear relation is found between the applied static magnetic field and the total static magnetic field in the z-direction. It can be seen from the fit that the magnetic field in the mu-metal shield is nulled when $B_z^{\text{DC}} = -97.40(1)$ nT. As done previously the near zero parameter, in this case x, was also extracted from the fit (see Appendix D.1) and found to be much smaller than z with $x \approx 0.0042$ V.

The same procedure was then repeated but this time with a sweeping field B_z^{sweep} along the z-direction. Figure 8.3 shows the experimental results, along with the theoretical predictions fitted to the data, when the applied DC magnetic fields B_x^{DC} and B_y^{DC} are varied. By adjusting the values for B_x^{DC} and B_y^{DC}, it is possible to null the residual magnetic fields that are present and hence obtain a constant, zero signal. In the case of sweeping the B_z^{sweep} magnetic field, the zero-field is found when $B_x^{\text{DC}} = 13.70(5)$ nT and $B_y^{\text{DC}} = -44.01(3)$ nT as can be seen in Figures 8.3b and 8.3d, respectively. This procedure can be applied and repeated iteratively until a signal very close to zero is obtained and hence the magnetic field is nulled for specific values of B_x^{DC}, B_y^{DC} and B_z^{DC}. This method can results in the total static magnetic field being nulled to better than a small fraction of a nT. In the case presented here all three axes are nulled to within 0.06 nT of zero-field using this model. This can be seen in Figures 8.2b, 8.2d, 8.3b and 8.3d. It can also be seen that the magnetic field is nulled to a value much smaller than the linewidth of the magnetic resonance signals which is sufficient for zero-field magnetometry. Appendix D shows data where the applied static magnetic field B^{DC} is varied over a larger range from -40 nT to 40 nT and the resulting signals are fitted to Equation 8.2.

Finally, the experimental setup is utilised to show that the signal from the magnetometer is independent of B_y^{DC} and B_z^{DC} when sweeping B_x^{sweep} along the x-direction. Figure 8.4 shows the magnetometer signal when various DC magnetic fields are applied in the y- and z-directions. In both of the sub-figures the signal can be seen to have a dispersive lineshape and remains the same, hence agreeing with Equation 8.6 that, to first order, the signal is only dependent on x. When sweeping the magnetic field along the x-direction, the magnetometer is only sensitive to changes in the x component of the magnetic field along the x-direction.

8.5 Zero-field magnetometry by absorption measurements

After nulling the magnetic field using the procedure described in the previous section, the magnetometer resonance at zero-field is measured using absorption. A single photodetector is placed after the vapour cell, replacing the polarisation rotation setup, in order to measure the intensity of the transmitted light after the cell. As a magnetic field is applied to the magnetometry setup, the quantum state of the atoms in the steady state (see Equation 4.52), which in the case here are caesium, is affected. Hence the amount of light that is transmitted through the cell decreases. In the experimental setup described in Section 8.3, the atoms are only sensitive to the magnetic field components in the x- and y-directions, which are transverse to the direction in which the laser beam is polarised. A triangular ramp between -300 nT and 300 nT is used to sequentially sweep the magnetic field along the three components. Figure 8.5 shows the experimental results obtained from the

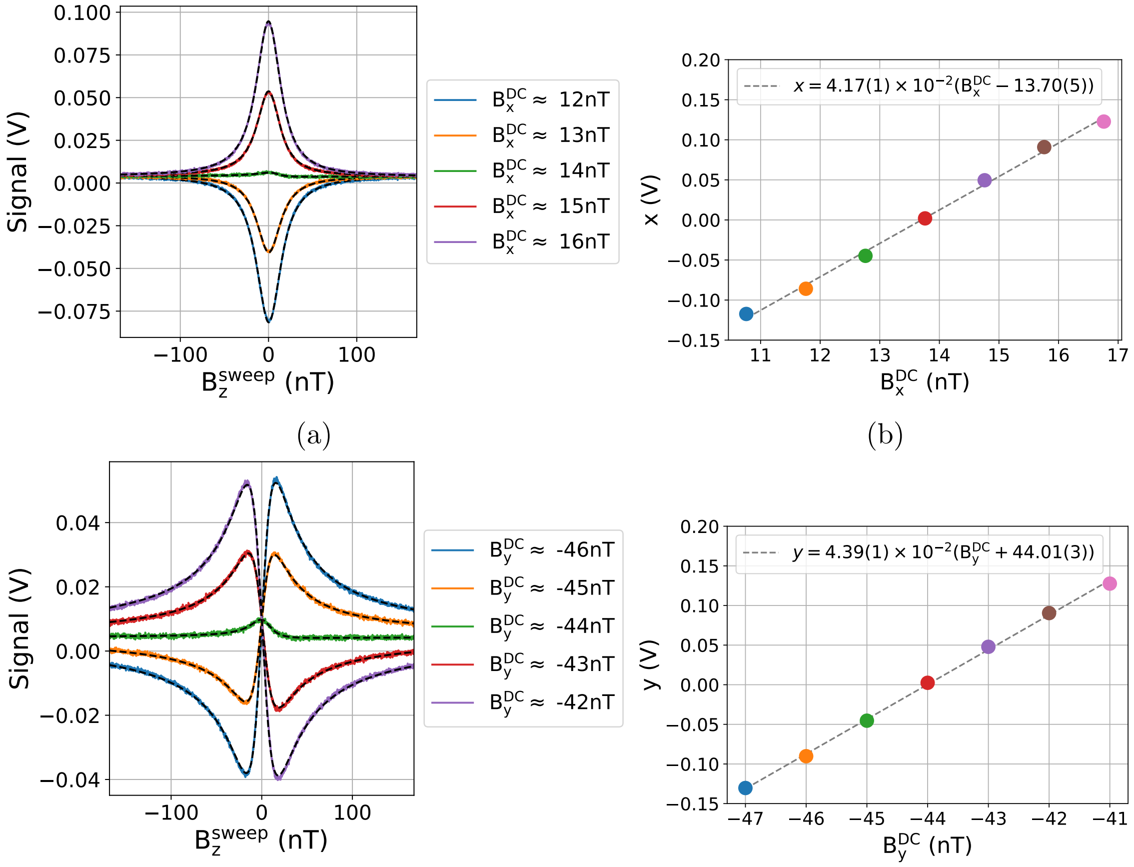

(a) (b)

(c) (d)

Figure 8.3: Nulling procedure of sweeping a magnetic field $B_z^{\text{sweep}}(t)$ which is applied along the z-direction in near zero-field conditions. For each magnetic field sweep, different static fields are chosen in a set direction. For the obtained magnetic resonances the experimental data (solid, coloured lines) are fitted to the theoretical predictions shown in Equation 8.9 (black dotted lines). The varied parameter in each data set is then extracted and is fitted to a linear relation (black dotted line). (a) The magnetic resonance signals for various values of the applied static field B_x^{DC} along the x-direction where the DC magnetic field applied along the y- and z-directions are kept constant at $B_y^{\text{DC}} = -44.00(1)$ nT and $B_z^{\text{DC}} = -97.35(1)$ nT. (b) The corresponding fit parameters $x \propto (B_x^{\text{residual}} + B_x^{\text{DC}})$ extracted from (a) as a function of the applied DC field. The DC field along the y-direction is then varied with the magnetic resonances (c) being fitted and (d) the fit parameter $z \propto (B_y^{\text{residual}} + B_y^{\text{DC}})$ being shown as a function of the applied DC field. In the case of B_y^{DC} being varied the static field along the x-direction is fixed at $B_x^{\text{DC}} = 13.76(1)$ nT. For each magnetic resonance, the parameter Γ/γ was also fitted and found to be 17(1) nT for all of the signals.

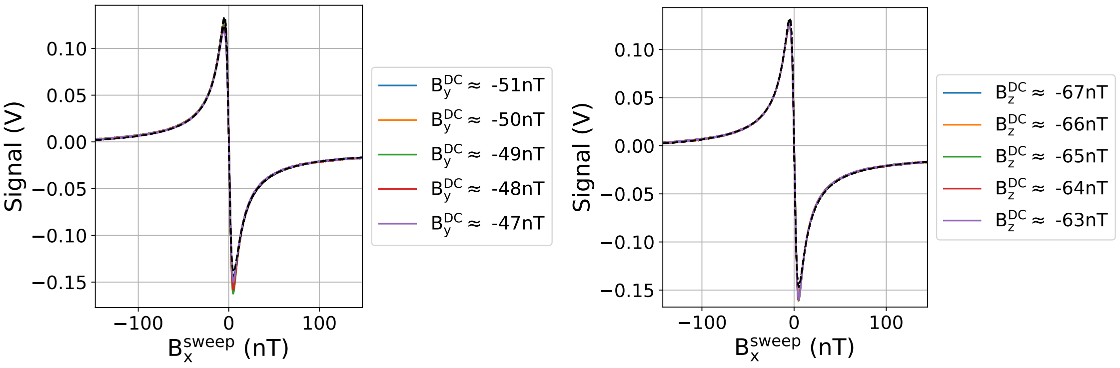

(a) (b)

Figure 8.4: Nulling procedure of sweeping a magnetic field $\boldsymbol{B}_x^{\text{sweep}}$ which is applied along the x-direction in near zero-field conditions. For each magnetic field sweep, different static fields are chosen in a set direction. For the obtained magnetic resonances the experimental data (solid, coloured lines) are fitted to the theoretical predictions shown in Equation 8.6 (black dotted lines). (a) and (b) show the magnetic resonance signals for various applied static magnetic fields along the y- and z-directions, respectively. In (a) $\boldsymbol{B}_z^{\text{DC}} = -65$ nT and in (b) $\boldsymbol{B}_y^{\text{DC}} = -49(1)$ nT. For each magnetic resonance, the parameter Γ/γ was also fitted and found to be 11(1) nT.

absorption detected using a single photodiode detector. As theoretically predicted in Equations 8.3 and 8.4, Lorentzian lineshapes are obtained when sweeping the $\boldsymbol{B}_x$ and $\boldsymbol{B}_y$ components of the magnetic field and, as seen in Equation 8.5, the signal is constant when sweeping the $\boldsymbol{B}_z$ component of the magnetic field. The Lorentzian lineshape that results from measuring the intensity of the transmitted light cannot fully determine the magnetic field components. This is due to the transmitted light being the same for a magnetic field of a certain amplitude if it is positive or negative. It is noted, however, that it is possible to measure all components of the magnetic field by implementing modulation techniques to the experiment. Several auxiliary oscillating magnetic fields are applied and the absorption measurements can then be used to determine the components of the magnetic fields present [18, 106].

8.6 Sensitivity and bandwidth

All sweeping magnetic fields are now turned off and the performance of the magnetometer at zero-field will now be studied. The bandwidth and sensitivity of the magnetometer can be determined by applying various frequency sinusoidal magnetic fields to the setup and calculating the power spectral density of the magnetometer's response signal. This is done by sequentially applying 14 different sinusoidal magnetic fields with varying frequencies between 8 Hz and 1818 Hz. Each sinusoidal wave has a fixed amplitude of 3.16 nT$_{\text{rms}}$. For each sinusoidal frequency 10 sets of 2 second time traces were recorded. Two additional sets of data were also recorded, the first was with no sinusoidal field being applied ('No RF') and the second with the balanced photodetector disconnected from the data-acquisition card ('Electronic Noise Floor'). These two data sets can be used to determine the noise floor of the magnetometer and the electronic noise that results from the data-acquisition card

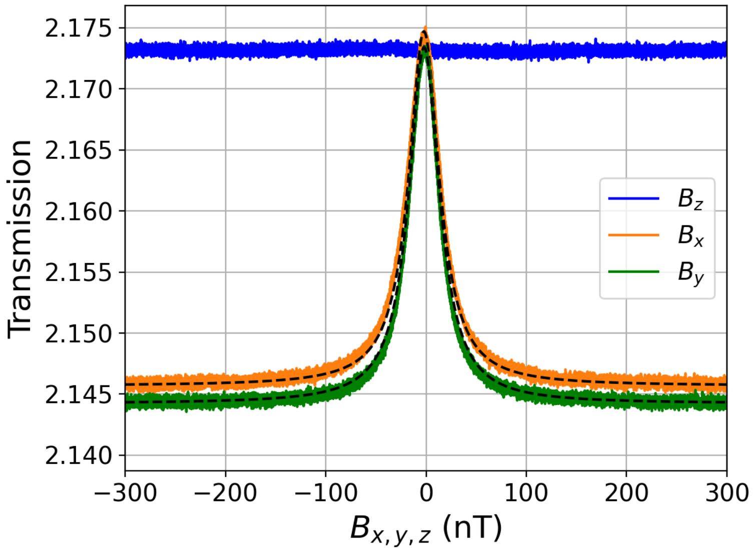

Figure 8.5: Zero-field magnetic resonance signals observed when sweeping the magnetic field from negative to positive values for B_x, B_y and B_z. These signals are observed by directly measuring the intensity of the transmitted light, i.e. absorption measurements. The half width at half maximum (Γ/γ) of the resonances was fitted and found to be 18.44(1) nT for sweeping B_x and 18.48(1) nT for sweeping B_y.

being used to record the data. For each data set, the power spectral density of the recorded data is calculated for each time trace and then averaged over. The average of the power spectral density is shown in Figure 8.6.

For each of the 14 data sets in which a sinusoidal field was applied, a sharp peak can be seen at the applied frequency. The peak heights can be used to determine the bandwidth of the magnetometer as the amplitude of the applied field remained constant for all applied frequencies. The peak heights are fitted using a formula for the response of a low-pass filter to first order which has the form $K/[1+(f/f_c)^2]^{1/2}$. Here K is the maximum amplitude of the peaks, f is the frequency dependence and f_c is the cut off frequency at 3 dB. This low-pass filter response of a magnetometer near zero-field has been derived for a zero-field OPM based on a spin oriented atomic ensemble [136] but will be used phenomenologically here to describe the spin aligned atomic ensemble. From the fit, the cut off frequency $f_c = 97(3)$ Hz can be extracted. The cut off frequency corresponds to the bandwidth of the magnetometer and it is expected that this value should be equivalent to the half width at half maximum of the magnetic resonance signals, shown in Figure 8.4. The half width at half maximum of Figure 8.4 is found to be 11 nT which is equivalent to 39 Hz. Hence, experimentally these numbers are found to differ by a factor of approximately 2.5.

When no oscillating field is applied to the setup the noise floor can be determined from the power spectral density. In Figure 8.6 the noise floor can be seen to be ≈ 2 pT/$\sqrt{\text{Hz}}$ at 1 Hz and then improves to ≈ 0.3 pT/$\sqrt{\text{Hz}}$ between 10 Hz and 100 Hz. The sensitivity of the magnetometer is mainly limited by the electronic noise of the balanced photodetector (data not shown). The noise floor of the magnetometer when taking into account the frequency response of the setup can be seen in Appendix D.3.

The fundamental limit of the magnetometer can be determined theoretically, this is when the magnetometer is limited by the quantum fluctuations in the atomic spin and the shot noise of the laser light. The total quantum noise is determined by calculating $\delta \mathrm{B}_{\mathrm{quantum}} = (\delta \mathrm{B}^2_{\mathrm{spin}} + \delta \mathrm{B}^2_{\mathrm{shot}})^{1/2}$ where the spin projection noise can be calculated as [51]

$$\delta \mathrm{B}_{\mathrm{spin}} = \frac{2\hbar}{g_F \mu_B \sqrt{nVT_2}} \tag{8.11}$$

where μ_B is the Bohr magneton, $g_F = 1/4$ for the $F = 4$ caesium ground state, $n \approx 2.2 \times 10^{16}\ \mathrm{m}^{-3}$ is the number density of caesium atoms at room temperature (18.5°C) and $V = (5\mathrm{mm})^3$ is the volume of the vapour cell. T_2 is the transverse relaxation time and is calculated by $T_2 = 1/\Gamma \approx 1/[\pi(11\ \mathrm{nT} \times 3.5\ \mathrm{Hz/nT})] \approx 4.1$ ms where Γ is determined from Figure 8.4. An ideal optically pumped magnetometer has $\delta \mathrm{B}_{\mathrm{shot}} = \delta \mathrm{B}_{\mathrm{spin}}$ and hence the total quantum noise is given by $\delta \mathrm{B}_{\mathrm{quantum}} = \sqrt{2}\mathrm{B}_{\mathrm{spin}}$ which for the magnetometer presented here is found to be $\delta \mathrm{B}_{\mathrm{quantum}} \approx 40\ \mathrm{fT}/\sqrt{\mathrm{Hz}}$. Hence with a lower noise balanced photodetector the sensitivity of the setup can be further improved.

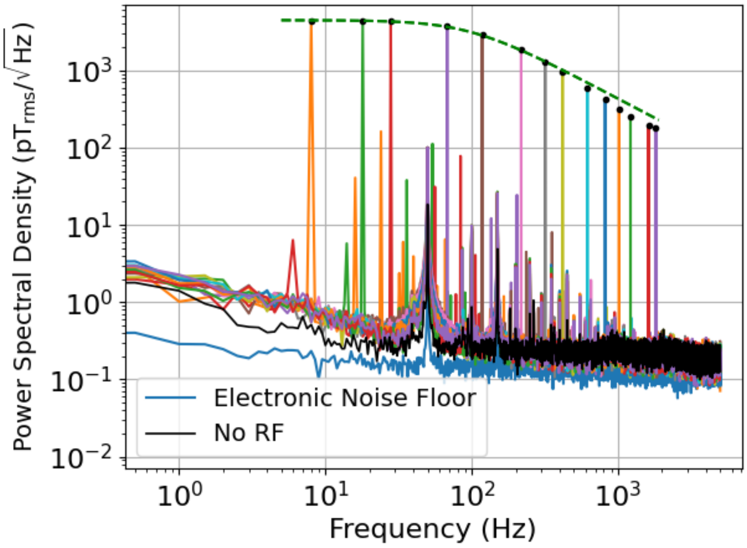

Figure 8.6: Power spectral density of the magnetometry signal using 10 time traces each of which are recorded for 2 seconds. 14 different measurement sets are calculated where sinusoidal magnetic fields are applied with various frequencies ranging from 8 Hz to 1818 Hz. Two additional measurements are taken without the sinusoidal field applied (No RF) and with the balanced photodetector disconnected from the data-acquisition card (Electronic noise floor).

8.7 Detecting a synthetic cardiac signal

In order to determine if the zero-field magnetometer presented here has a performance that is sufficient to meet the standards for biomagnetic measurements, a synthetic cardiac signal is applied along the x-direction. The applied signal had a peak to peak amplitude of 100 pT which corresponds to the magnetic field of an adult's heart at the surface of the skin [148, 149]. The magnetic field was generated using a synthetic magnetocardiogram (MCG) waveform from a function generator (RIGOL DG1032Z) connected to the larger home-made Helmholtz coil. The raw magnetometer signal can be seen in Figure 8.7(a) which contains a single time trace, no averages and no filters. The data was recorded using a 10 kHz sample rate. The signal is noisy but the larger features of an MCG waveform can still be seen. With some simple signal processing of applying a 17 Hz low-pass filter to the signal the noise drops significantly. Figure 8.7(b) shows the filtered signal. It can be seen that all of the features of an MCG are now clearly distinguishable and the signal matches that being applied to the coil, labelled 'Synthetic cardiac signal', very well. The QRS complex, which represents the depolarisation of the ventricles, the P wave, representing the depolarisation of the atria, and the T wave, which represents the repolarisation of the ventricles, are all clearly identifiable [150]. These features in a cardiogram signal are essential in the detection as they are used by medical doctors to assess the health of a heart. Hence the magnetometer presented here has a sufficient performance for the measurement of an adult human heart.

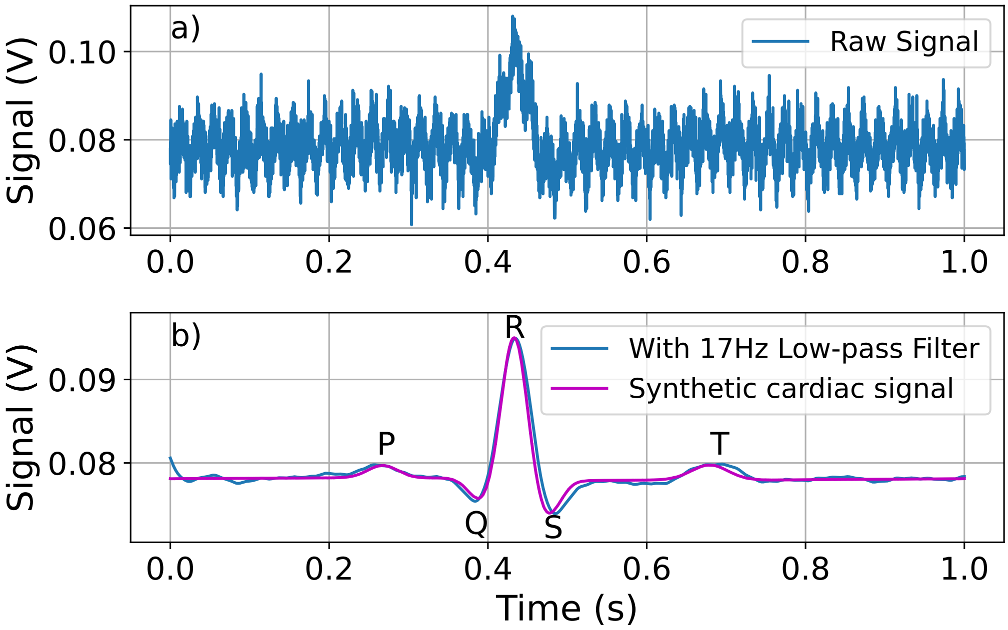

Figure 8.7: Time trace of the magnetometer signal when a synthetic cardiogram waveform is applied. (a) The raw data and (b) the data when a 17 Hz low-pass filter is applied.

8.8 Conclusion

The data presented in this chapter shows the ability for an alignment magnetometer to operate near zero-magnetic field with the polarisation rotation of the laser light being measured. By analysing the polarisation rotation signals, the residual magnetic fields can be nulled by an iterative approach. When zero magnetic field is present in all directions the signal becomes zero as predicted by the theoretical model. Achieving a zero-field environment for magnetometry is important for numerous applications including nuclear magnetic resonance (NMR) gyroscopes [151] and biomedical measurements, such as magnetoencephalography (MEG) and magnetocardiography (MCG). In these examples non-zero magnetic field components lead to artifacts or systematic errors in the signals [152]. This method shows its potential in the application of MCG as a synthetic cardiac signal is successfully detected. Unlike other methods, the method for nulling a magnetic field is modulation free. After the magnetic field is successfully nulled, the magnetometer presented here measures one component of the magnetic field using a single laser beam. If the vapour cell was replaced with a buffer gas cell this model could be extended to a vector magnetometer where three, non-overlapping, laser beams are utilised.

The magnetometer has a magnetic field sensitivity of $\sim$ 2 pT/$\sqrt{\text{Hz}}$ at 1 Hz and $\sim$ 0.3 pT/$\sqrt{\text{Hz}}$ between 10 Hz and 100 Hz. The theoretical quantum limit was calculated to be $\delta B_{\text{quantum}} \approx 40$ fT/$\sqrt{\text{Hz}}$, so with technical improvements a higher sensitivity is achievable. It is noted that commercially available OPMs, that operate in zero-field conditions, already outperform even the predicted quantum noise limit of the detector presented in this chapter with sensitivities of around $\sim$ 20 fT/$\sqrt{\text{Hz}}$ [40]. However, these detectors operate at much higher temperatures of around 150°C whereas the OPM presented in this chapter operates at room temperature ($\sim$ 18.5°C). Unlike SERF magnetometers, the same magnetometer can be tuned to operate as an RF-magnetometer by applying a static magnetic field opening up multiple applications with a single device. The use of alignment magnetometry also has the additional bonus of having minimal light-shift effects due to the low power, linearly polarised light beam that is used to pump and probe the atomic ensemble [153]. There is a number of modifications that could be made in order to enhance the sensitivity of the setup presented in this chapter, examples of which include using a reduced noise balanced photodetector, letting the laser beam pass through the vapour cell multiple times, using an elevated temperature of around 40°C and introducing a repump laser beam to transfer atoms from the 'dark' $F = 3$ ground state back into the $F = 4$ ground state which can then be probed by the laser beam.

Chapter 9

Balanced photodetector

9.1 Motivation

In order to construct a portable alignment based magnetometer (see Section 10), a low noise and high bandwidth photodetector needed to be developed. This detector also needed to be a on a small PCB in order to fit in the prototype head. For magnetic induction tomography measurements of the heart a bandwidth of 2-3 MHz is desired [30, 25]. The high bandwidth is also desired to see the non-linear Zeeman effects of caesium that can be used to confirm sufficient optical pumping of the atoms to the dark states [112]. As alignment based magnetometry is used throughout this thesis and in the portable optically pumped magnetometer, a low noise floor is needed to not be limited by the electronics of the system. The light powers typically used are in the range of 10 - 50 μW. Detecting a low powered laser beam with the dominating noise source being shot noise and not electronic noise, i.e. shot noise ≥ electronic noise, is challenging. This is due to the variance of shot noise depending linearly on the light power incident on the diodes. The variance of the shot noise i_{shot} for a photodiode is given by

$$i_{\text{shot}} = 2eI, \tag{9.1}$$

where e is the electron charge and I is the photocurrent. The photocurrent can also be written as $I = RP$ where R is the responsivity of the diode and P is the power of the laser beam that is incident on the diodes. Amplifying the photocurrent using transimpedance amplifiers helps to improve the shot noise but can introduce low-pass filters to the electronics which limits the bandwidth. Hence components and the layout of the board need to be decided carefully to obtain the best shot noise limit and bandwidth for the detector.

9.2 Testing setup

In order to test the performance of the balanced photodetectors that were designed, a test setup was used. A photograph and a simplified schematic of this setup can be seen in Figure 9.1. In order to test the performance of the detectors with as minimal external noise sources as possible, a different laser is used that is less noisy than the home-made laser system used in the other sections of this thesis. The laser used for testing is the Toptica photonics DFB pro which in this setup has a wavelength of 852 nm and is resonant with the caesium D2 line (see Section 2.1.1). The combination of a half wave plate ($\lambda/2$) and a polarising beam splitter (PBS) is used to ensure that the laser is linearly polarised. The laser light is then passed through a variable neutral density filter (VNDF) where the desired light power is fixed. For each data set in the measurements the light power is fixed at a value between 0 μW and 1 mW. The transmitted light is then split into two parts using a half wave plate and a polarising beam splitter such that 50% of the light is transmitted and 50% is reflected. The two paths of light are then directed onto the two diodes of the balanced photodetector using mirrors. The light diameter is reduced to hit the diode by placing lenses in front of the diodes. The balanced photodetectors signal is then sent straight to the data acquisition card in the computer for further analysis. The power spectral densities of the signals are then calculated.

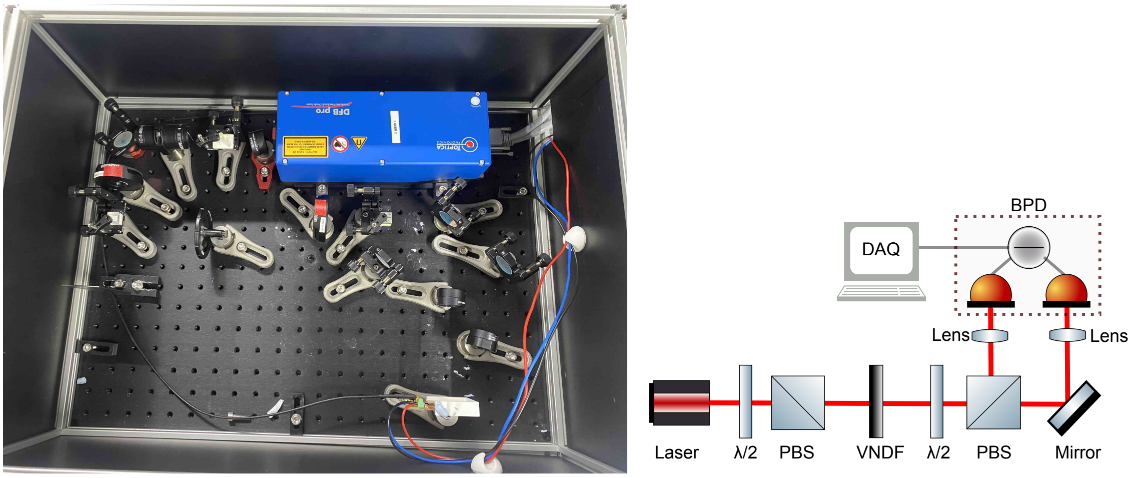

(a) (b)

Figure 9.1: The test setup used to determine the bandwidth and noise floor of a balanced photodetector. (a) An image of the test setup with the final design of the home-made detector being tested and (b) a simplified schematic of the setup. The setup consists of a laser (Toptica photonics DFB pro), half wave plates ($\lambda/2$), polarising beam splitters (PBS), variable neutral density filters (VNDF), mirrors, lenses and the balanced photodetector (BPD) that is being tested.

9.3 Thorlabs BPD

As a comparison for the detector designs being developed, a commercially available balanced photodetector (Thorlabs PDB210A/M) is tested. This detector is used in the table-top alignment based magnetometer that is described in Section 6 and utilised in Sections 7 and 8. The detector was tested using the setup described in Section 9.2 where the light power P recorded in mW is split into two beams that each hit one of the two diodes. A high sample rate of 10 MHz was used to avoid the effects of aliasing. 100 averages of 0.1 second time traces were recorded and the power spectral densities were computed. In Figure 9.2 it can be seen that the detector has a −3 dB bandwidth of 1 MHz as stated in the data sheet [154]. The detector has a low and flat noise floor. There is an increase in noise at low frequencies due to $1/f$-noise. The detector is shot noise limited at ~ 20 μW at around 10 kHz, which is the main frequency selected in Chapter 6. The linear relation across all frequency ranges in Figure 9.2b is as expected from Equation 9.1 for a shot noise limited detector. Although this detector has a low noise floor, the 1 MHz bandwidth is insufficient for MIT measurements of biological tissue, such as the heart, where typically an RF frequency of ~ 2 MHz is required for imaging [30, 25].

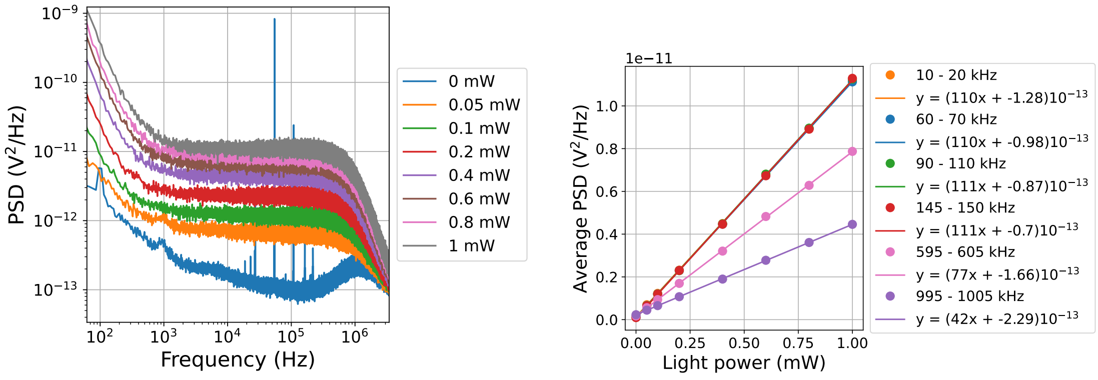

(a) (b)

Figure 9.2: Frequency response of the Thorlabs PDB210A/M as a response of various light powers incident on the photodiodes. These measurements are used to determine the bandwidth and the shot noise limit of the balanced photodetector. The power spectral density (PSD) (a) is plotted as a function of frequency for light powers between 0-1 mW. Averages over frequency ranges of the PSD are then computed and plotted as a function of light power (b).

9.4 High frequency BPD development

In order to design a balanced photodetector that has a large bandwidth, but also a low noise floor, transimpedance amplification stages need to be used. A key component of the amplification stage is the op-amp which needs to be carefully selected depending on the application of the detector. The noise floor and bandwidth are the key features looked at for the design of the balanced photodetector presented here. A feedback resistor and capacitor are placed in parallel with each other and the op-amp. This can be seen in the schematic of the detector designs (see Figures 9.3 and 9.8). The feedback resistor R_F helps to set the transimpedance gain of the stage. For example, in the most simple case when there is no resistor placed in series before the op-amp, if $R_F = 10$ kΩ the gain of the stage is given by $G = 10$ kV/A. The inverting input of a op-amp (labelled with a $-$), which the photodiode's signal is attached to, does not allow any current to flow through as it has a high input impedance. Hence, all of the current flows through the feedback resistor causing the signal amplification. In the designs used in this chapter, there is an additional resistor placed in the amplification stage. This resistor is the gain resistor R_G (R7 in Figure 9.3 and R10 in Figure 9.8) and is connected to the non-inverting input of the op-amp. When a gain resistor is present in an inverting amplification stage, the gain is set by $G = R_F/R_G$. This can be seen as the non-inverting output is connected to ground. Hence from calculating the voltage output from the amplification stage as $V_{\text{out}} = -I_{\text{in}}R_F = -V_{\text{in}}R_F/R_G$ it can be seen that the gain is given by $G = R_F/R_G$. If a second stage amplification is also implemented, which is the case here, the non-inverting input of the op-amp is utilised. In this case the gain is set differently as the amplification is from a voltage to an amplified voltage and is hence given by $G = 1 + (R_F/R_G)$.

	Component	Value
T		293 K
C_{PD}	Hamamatsu S8729	16 pF
C_{PCB}	PCB traces	~ 0.2 pF
$I_{-,\text{noise}}$	OPA657	1.3 fA/$\sqrt{\text{Hz}}$
$V_{-,\text{noise}}$	OPA657	4.8 nV/$\sqrt{\text{Hz}}$
C_{cm}	OPA657	0.7 pF
C_{dm}	OPA657	4.5 pF
GBP	OPA657	1.6 GHz
$I_{-,\text{noise}}$	OPA818	3 fA/$\sqrt{\text{Hz}}$
$V_{-,\text{noise}}$	OPA818	2.2 nV/$\sqrt{\text{Hz}}$
C_{cm}	OPA818	1.9 pF
C_{dm}	OPA818	0.5 pF
GBP	OPA818	2.7 GHz
$I_{-,\text{noise}}$	THS4021	2.3 pA/$\sqrt{\text{Hz}}$
$V_{-,\text{noise}}$	THS4021	1.2 nV/$\sqrt{\text{Hz}}$
GBP	THS4021	2 GHz

Table 9.1: Values of the noise contributing factors of components used in the home-made balanced photodetector designs.

There are a number of issues that need to be considered when designing a high bandwidth detector using transimpedance amplification stages. Many of these issues arise from voltage noise that is picked up across the circuit. Voltage noise needs to be considered as the detector being developed needs to have a low noise floor due to the low light powers inducing small photocurrents. This noise can easily become the dominating noise source in an experiment if not considered. There are four main contributors to the voltage noise [155]. The Johnson noise is one of the noise contributors which results from the feedback resistors used in the amplification stages. This noise contribution is given by $V_{\text{J,noise}}\sqrt{4k_BTR_F}$. The op-amps themselves also have an input current noise ($I_{-,\text{noise}}$) at their inverting inputs which produce a voltage noise when passing through the feedback resistor. There also exists a noise source caused by amplifying the input voltage noise $V_{\text{in,noise}}$. In an amplification circuit if there is no gain resistor present a gain still exists due to the feedback resistor being in parallel with the impedance of the circuit. The total impedance of the circuit is given by $-i/(\omega C_{\text{total}})$ where $C_{\text{total}} = 2C_{\text{PD}} + C_{\text{PCB}} + C_{\text{FR}} + C_{\text{cm}} + C_{\text{dm}}$ where C_{PD} is the capacitance of the photodiode, C_{PCB} is the capacitance of the PCB traces and C_{FR} is the parasitic capacitance from the feedback resistor. C_{cm} and C_{dm} are the capacitance of the common-mode and differential mode inputs on the op-amp, respectively. Hence this results in the voltage noise also contributing an additional noise factor of $V_{\text{in,noise}}(2\pi i f R_f C_{\text{total}})$. For the various op-amps used in this chapter the values for these capacitance noise sources can be seen in Table 9.1. Hence the overall output noise is given by

$$V_{\text{out,noise}} = \sqrt{(I_{-,\text{noise}} R_F)^2 + 4k_B T R_F + V_{\text{in,noise}}^2 + V_{\text{in,noise}}^2 \left(\frac{(2\pi f_{-3\text{dB}} R_F C_{\text{total}})}{3} \right)}. \tag{9.2}$$

Here $f_{-3\text{dB}}$ is the 3dB cut off of the frequency in the circuit which is given by

$$f_{-3\text{dB}} = \sqrt{\frac{\text{GBP}}{2\pi R_F C_{\text{total}}}}, \tag{9.3}$$

where GBP is the gain bandwidth product of the op-amp.

The final design consideration is looking at how to keep the op-amp's response stable in order to obtain a maximally flat response. As the op-amp circuits contain a number of capacitors in the design, the feedback capacitors need to be selected such that the op-amp has a second-order Butterworth frequency response. The correct feedback capacitor C_F is calculated by rearranging [155]

$$\frac{1}{2\pi R_F C_F} = \sqrt{\frac{\text{GBP}}{4\pi R_F C_{\text{total}}}}. \tag{9.4}$$

9.4.1 Initial design

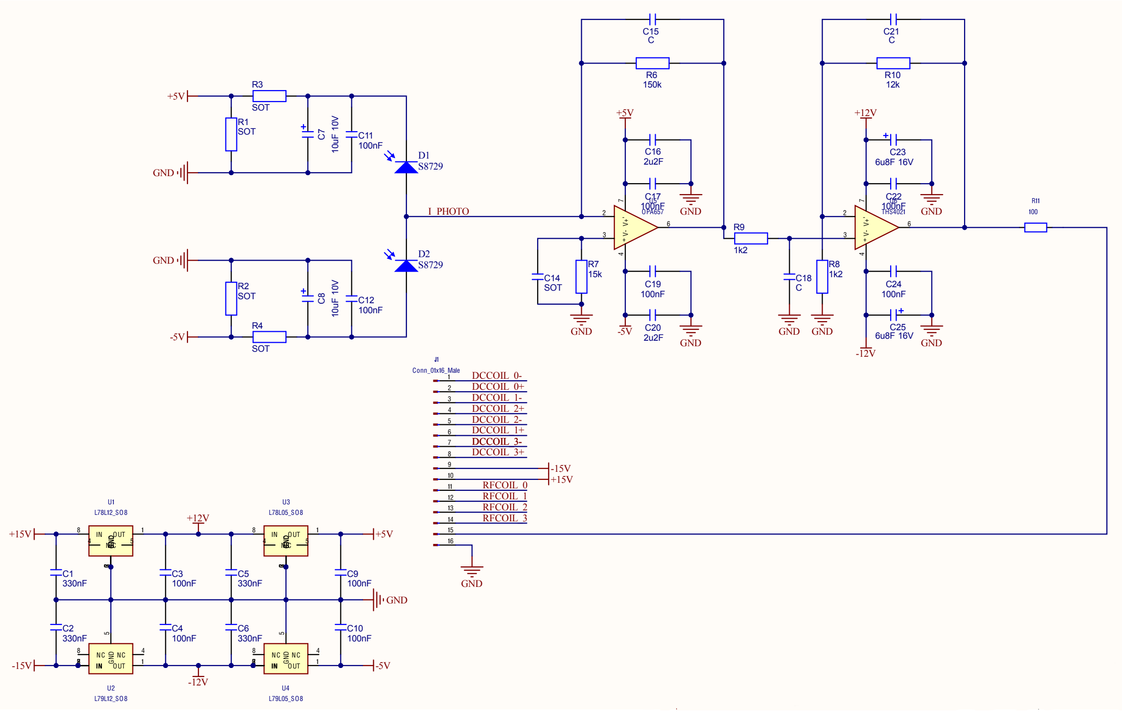

Figure 9.3: The circuit schematic of the initial home-made balanced photodetector design where a 150 kΩ feedback resistor (R6) is used on the first stage of amplification resulting in a gain of $G = 10$ V/V and a 12 kΩ feedback resistor (R10) on the second stage of amplification resulting in a further gain of $G = 11$ V/V.

The schematic of the initial balanced photodetector design is shown in Figure 9.3, which was originally designed to achieve the higher bandwidth required for the portable optically pumped magnetometer. A basic balanced photodetector design consists of two photodiodes which each generate a photocurrent when laser light is incident on the diodes. The photocurrents are then subtracted. In order to achieve a higher bandwidth, the photodiodes must be reverse biased. Each photodiode is reverse-biased by 5 V in this circuit. The photodiodes used are the Hamamatsu S8729 photodiodes which has a responsivity of ~ 0.6 A/W at 852 nm and 895 nm [156]. The two beams of light that hit the diodes are then converted into currents which are subtracted from each other. The photodiodes are balanced, so there is an equal amount of light on both diodes when there is no field, and hence a zero resultant current. When the atoms are in a magnetic field, this amount of light on each diode changes, resulting in small changes in the resultant current. As such low light powers are going to be used in the portable alignment based magnetometer for which this detector is designed for (10 - 30 μW) and a high bandwidth is desired, the photodetector signal needs to be amplified on the PCB in order to see the changes clearly. This design has a two-stage amplification. In the first stage, an operational OPA657 amplifier is used to amplify the signal with a gain of $G = 10$ and converts the current into a voltage with $R_F = 150\ k\Omega$. This amplifier was chosen due to its high gain-bandwidth-product of 1.6 GHz which gives the potential for greater than 10 MHz signal bandwidths [155]. The output voltage is then further amplified using a THS4021 voltage feedback amplifier [157]. The amount of signal amplified at this

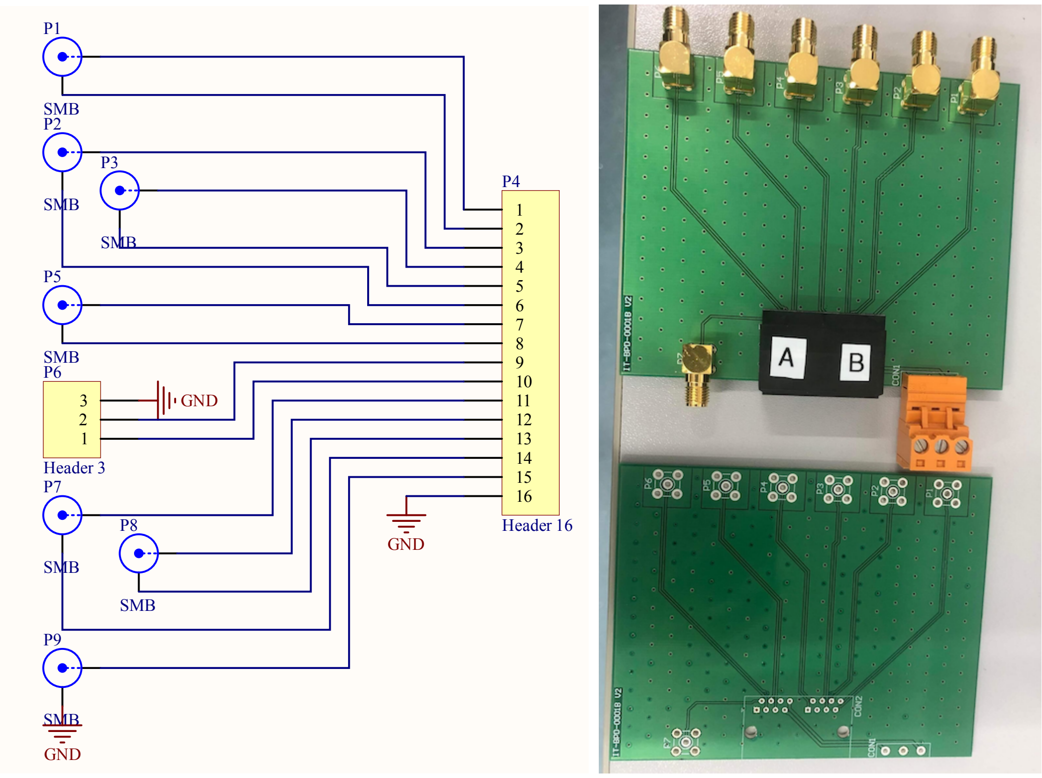

(a) (b)

Figure 9.4: The break-out box design for the balanced photodetector with (a) the circuit schematic of the board and (b) an image of the board before (bottom) and after soldering (top).

stage comes from the ratio of R9 to R10 in Figure 9.3. This gain is set to G = 11, since this is the minimum operating gain [157]. The output of the amplifier is then sent through the Ethernet adapter to a break-out box which then separates the signal off from the input signal to be analysed. The schematic and a photo of the break-out box can be seen in Figure 9.4.

The printed circuit board (PCB) design can be seen in Figures 9.5a and 9.5b (Altium Designer) alongside a photograph of the soldered board (Figure 9.5c). The PCB is a two layer board with the bottom layer being a ground plane. The amplifier output is then sent through an Ethernet cable to a break-out box (Figure 9.4). The signal is obtained from here to be analysed. The PCB has a footprint of 64 mm × 30.5 mm to fit inside the portable OPM head shown in Section 10.

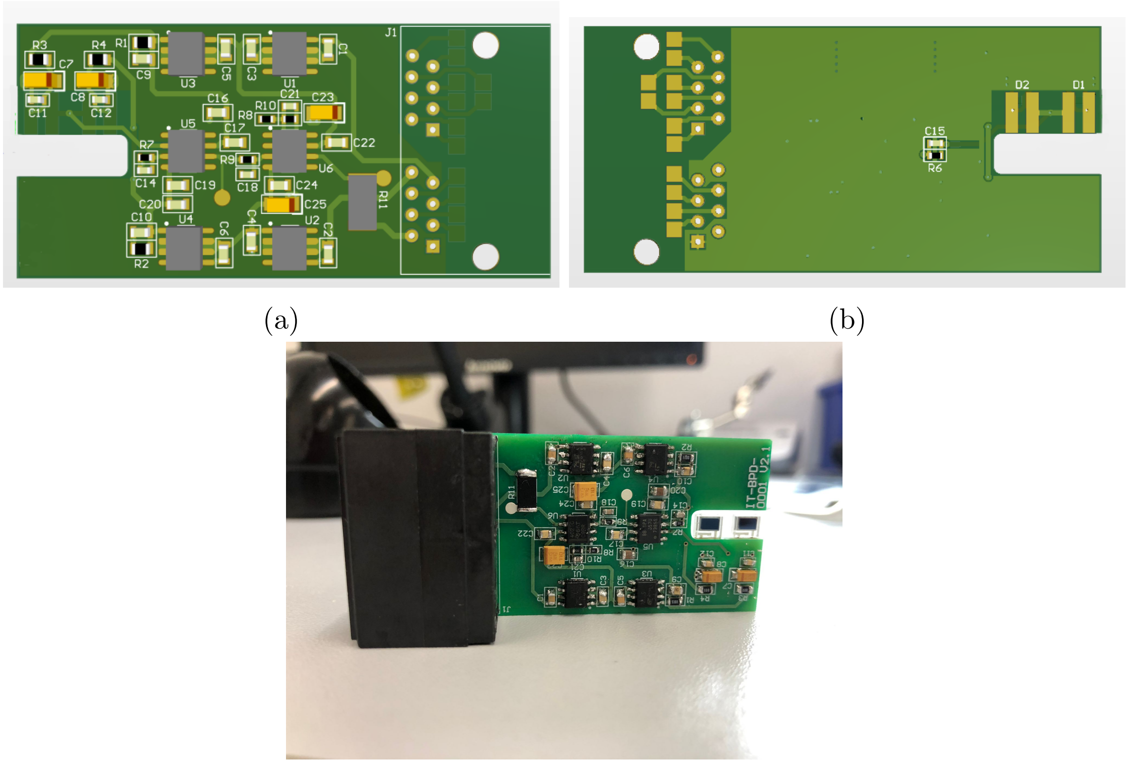

(a)

(b)

(c)

Figure 9.5: PCB board design of the initial home-made balanced photodetector design with (a) the front and (b) back design in the design program shown. (c) An image of the soldered balanced photodetector.

9.4.1.1 Performance

In order to test the balanced photodetector, various light powers were shone onto the diodes using the setup shown in Section 9.2. Data was collected for a duration of 0.01 seconds with 100 averages being recorded for each light power. To see as wide a range as possible, the maximum sample rate of the data acquisition card was used (40 MHz). These data sets were then Fourier transformed and averaged to compute the power spectral density with the results shown in Figure 9.6a. It can be seen that the BPD is shot noise limited below 10 kHz at ~ 10 μW. Between 3 kHz and 4 kHz the electronic noise is at its lowest and the detector is shot noise limited at around 3 μW. This is an excellent performance and can be seen by comparing the noise at 3 kHz to the Thorlabs detector which is shot noise limited at approximately 10 μW. Using the values given in Table 9.1, the total capacitance can be calculated as $C_{\text{total}} = 37.4$ pF when no feedback capacitor is used. This can be used to show that the detector should have a 3 dB bandwidth of 6.7 MHz. Despite predicting that the balanced photodetector design would have a bandwidth of a few MHz, when tested it could not get over 150 kHz as the cut off frequency. The bandwidth predictions were done using Equations 9.3. The noise is lowest between 3 kHz and 6 kHz where from fitting (see the orange coloured dots in Figure 9.6b) it can see that the balanced photodetector is shot nose limited from 7 μW.

To determine where the bandwidth issue are from, the gain of the amplifiers was varied and the low-pass filters on the PCB (components R9 and C18 in Figure 9.3) were also varied. This is due to the simplest explanation for the issues would be that one of these had the wrong resistor/ capacitor pairing. However, no matter how extreme these were changed, no difference to the bandwidth of the design was seen. So further testing was carried out.

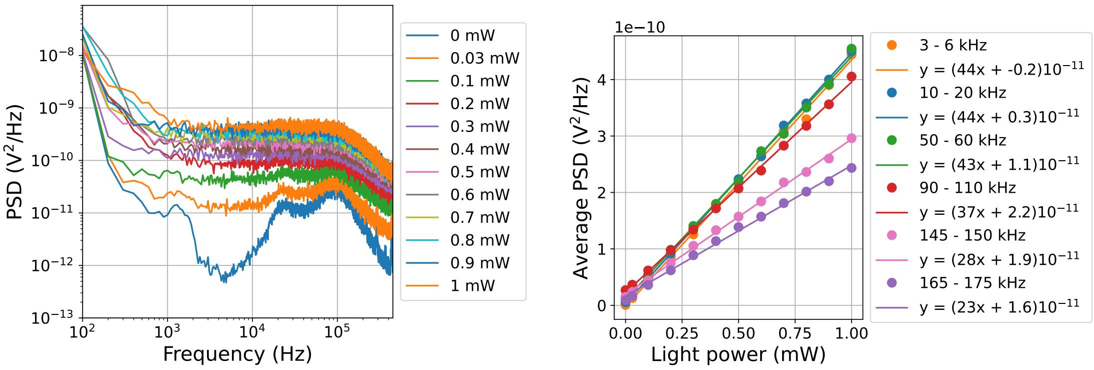

(a) (b)

Figure 9.6: Frequency response of a home-made balanced photodetector (version 1) as a response of various light powers incident on the photodiodes. The detector was designed to have a high bandwidth with a low noise floor. These measurements are used to determine the bandwidth and the shot noise limit of the balanced photodetector. The power spectral density (PSD) (a) is plotted as a function of frequency for light powers between 0 -1 mW. Averages over frequency ranges of the PSD are then computed and plotted as a function of light power (b).

9.4.1.2 Issues

It was found that despite the theoretical predictions the bandwidth of the balanced photodetector never increased above ~ 150 kHz. After investigating it was found that an issue with impedance matching was causing the problem. The break-out box does not impedance match from the 100 **Ω** impedance of the Ethernet cable to the 50 **Ω** impedance of the SMA connectors and cables. This created an artificial low-pass filter between the signal from the photodetector and the output signal from the break-out box. Figure 9.7 shows the performance of the balanced photodetector when the break-out box is removed from the setup. For simplicity the photodiodes were also removed. This was done by soldering on a BNC to the output pin, input

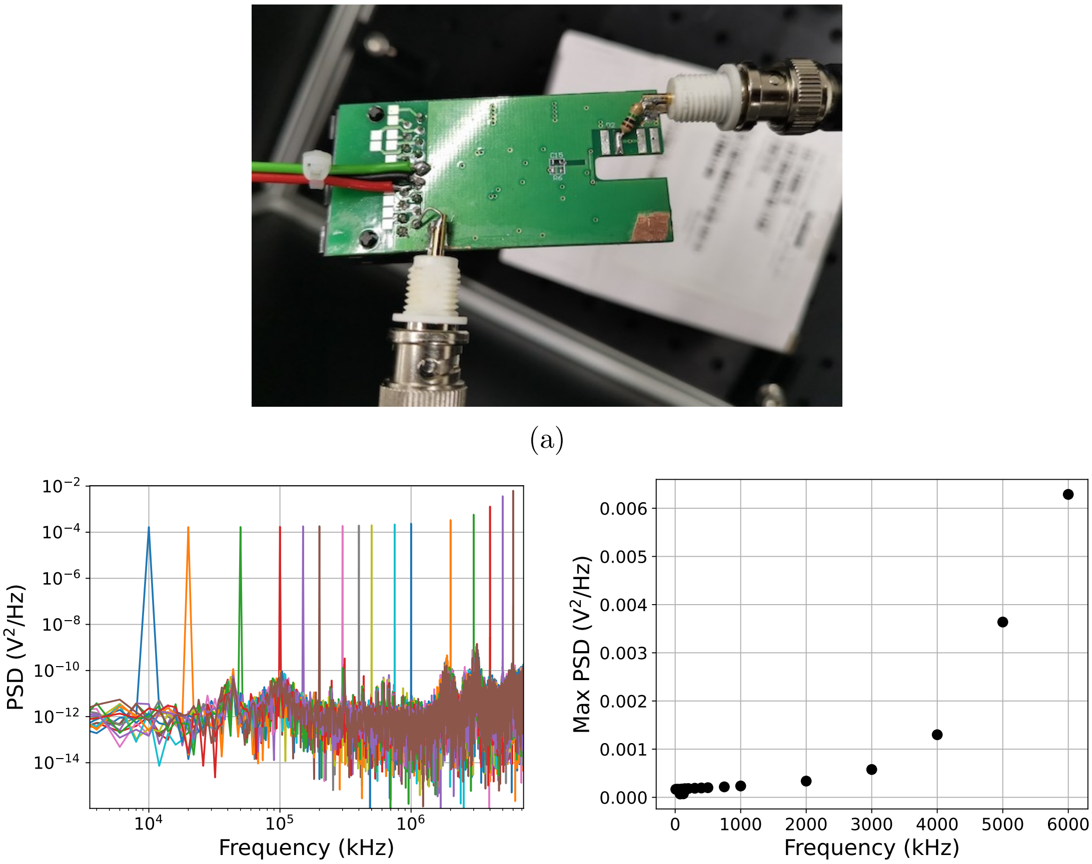

(a)

(b)

(c)

Figure 9.7: The photodiodes and break-out box were bypassed in the initial design of the balanced photodetector to identify where the bandwidth issues are from. (a) An image of the PCB with a BNC connector and a 1 MΩ resistor in place of the photodiodes, which allows voltages to be supplied to the circuit, and a BNC at the bottom of the board to carry the resultant signal to the data acquisition card. The board is powered by soldering 3 wires (black, red and green). (b) The resulting power spectral densities are computed when a 1 V_{pp} signal of a fixed frequency between 10 kHz and 6 MHz is applied to the BNC in place of the diodes. (c) The peak heights are then extracted and plotted against the corresponding frequencies.

wires to directly power the board and a BNC to apply a voltage through in place of the photodiodes, as shown in Figure 9.7a. A 1 V_{pp} sine wave of varying frequencies between 10 kHz and 6 MHz were then applied through the BNC that is in place of the photodiodes. This is supplied from a Rigol function generator through a 1 MΩ resistor such that a 1 μA current is sent to the position of the diodes. To avoid seeing affects of aliasing the maximum frequency was at 6 MHz. Using a 40 MHz sample rate, a 0.0005 second trace was taken and Fourier transformed using a one-sided periodogram function. The resultant power spectral density can be seen in Figure 9.7b where peaks at the corresponding applied frequencies can clearly be seen. The peak heights were then extracted and plotted against the applied frequency, as shown in Figure 9.7c. The cut off frequency at ~ 150 kHz is no longer present with the peaks being flat up to ~ 1 MHz. Without the break-out box, the photodetector circuit has the expected gain peak just above 1 MHz [155]. Due to data only being recorded with an applied sine wave frequency up to 6 MHz, it can not be seen if the top of the peak is at 6 MHz or at a higher frequency. This peak suggests that the detector has a large bandwidth that is at least 6 MHz. It is noted that the setup was tested without the photodiodes (data not shown) before the break-out box was bypassed. From this study it can be seen that the issue came from the break-out box. As the break-out box is the cause of the issue and provides no benefit to the circuit, a new design was developed to remove this issue.

9.4.2 Improved detector design

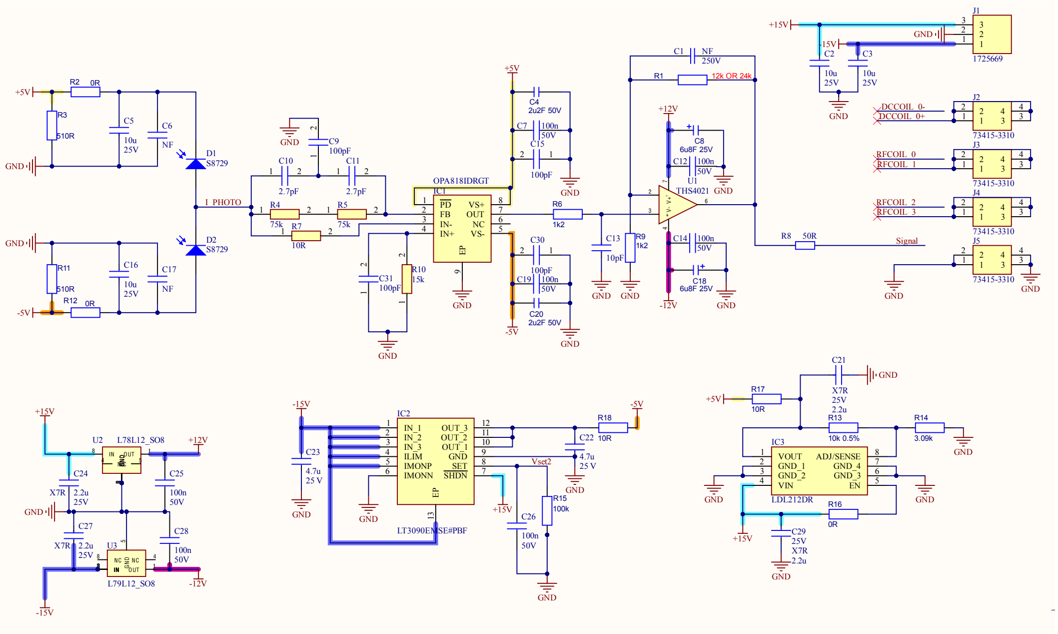

Figure 9.8: The circuit schematic of the final home-made balanced photodetector design where a 150 kΩ (R4 + R5) feedback resistor is used on the first stage of amplification resulting in a gain of $G = 10$ V/V and a 12 kΩ (R1) feedback resistor on the second stage of amplification resulting in a further gain of $G = 11$ V/V.

The schematic of the improved balanced photodetector is shown in Figure 9.8. It can be seen that most components remain the same as those used in the initial design, including the photodiodes that are used. The first stage amplification has been replaced with a op-amp that has an improved performance. The OPA818 is an updated version of the OPA657 used previously [158], with the gain bandwidth and input voltage noise showing significant improvements. The updated PCB design can be seen in Figure 9.9 alongside a photo of the new balanced photodetector. The PCB is a four layer design in order to reduce the noise floor and noise that the detector picks up from the environment. In order to accommodate the new op-amp more vias have been placed on the board to help with heat dissipation as the OPA818 has a higher working temperature. This prevents other components over heating and shutting down. The first stage of amplification has a gain of $G = 10$ with $R_F = 150$ kΩ (R4 and R5) and $R_G = 15$ kΩ (R10). The second stage of amplification has a gain of $G = 11$ with $R_F = 12$ kΩ used in the final design and $R_G = 1.2$ kΩ. It can also be seen that the Ethernet adapter has been removed and replaced with SMP connectors for the photodetector output, heater coil and two RF coils to be connected to. The voltage power inputs now also use a 3 way pluggable terminal block. These replacements are incorporated to avoid the impedance issues previously faced and removes the necessity to have a break-out box. The footprint of the PCB remains the same size as the previous design.

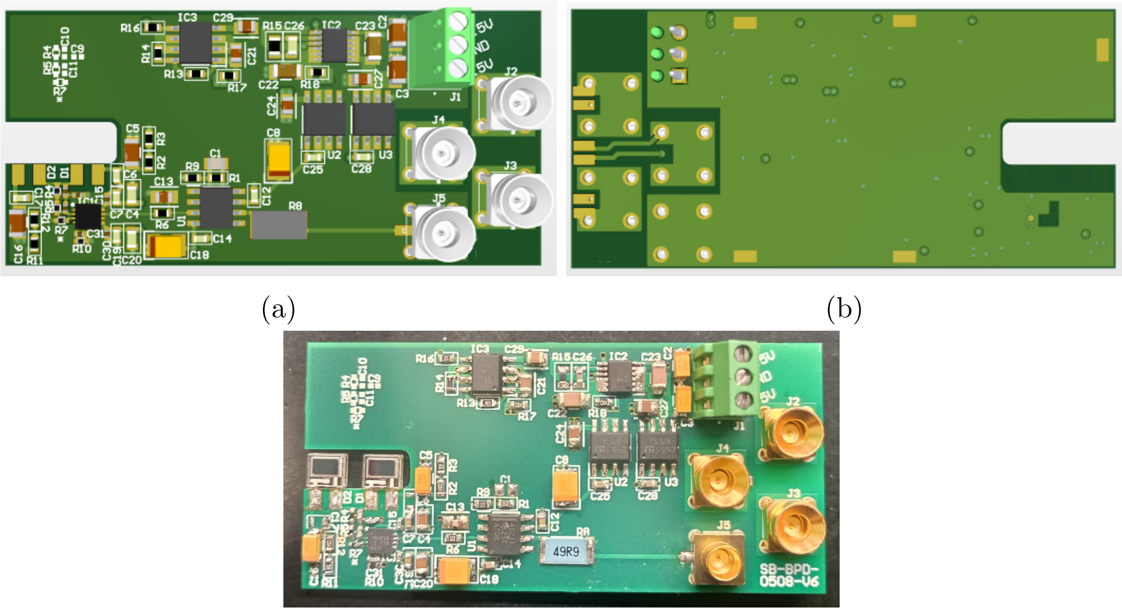

(a) (b)

(c)

Figure 9.9: PCB board design of the improved balanced photodetector design with (a) the front and (b) back design in the design program shown. (c) An image of the soldered balanced photodetector.

9.4.2.1 Performance

The balanced photodetector was tested in the same way as the initial design. A sample rate of 20 MHz was used to record 50 averages of 0.02 s time traces. The data was then Fourier transformed and averaged over to compute the power spectral density of the balanced photodetectors response to varying light powers. It can be clearly seen in Figure 9.10a that there is no longer a roll off at ∼ 170 kHz and that the detector has a much higher bandwidth. A gain peak can still be seen which is as expected from the OPA818 data sheet [158]. The peak of the gain peak can be seen to be around 4.5 MHz. It is noted that components R6 and C13 on the board create a low-pass filter with a value of ∼ 13 MHz. The noise floor of the detector, when comparing to the data set when 0.03 mW of light is split onto the two detectors, is also considerably lower and flatter than the previous design. This is due to the improved op-amp used in the first stage amplification. Below the gain peak begins (∼ 1 MHz), the detector is shot noise limited from ∼ 4 µW which is much better than the performance seen from many high performing commercially available balanced photodetectors, such as that shown in Section 9.3. The noise floor is lowest between 20 kHz and 60 kHz with the detector being shot noise limited at ~ 2 µW. For this detector design to be practical for magnetic induction tomography measurements using an alignment based magnetometer, the shot noise limit above 1 MHz needs to be investigated. Areas of the power spectral density are averaged over for a range of frequencies and the results are plotted against the light power. This data is then fitted to a linear relation. The results can be seen in Figure 9.10b. It is noted that additional noise is picked up for the higher light powers at higher frequencies so these points are excluded from the fit to obtain the correct linear relation for the data that follow this trend. Using the fit functions shown in the legend of Figure 9.10b and the noise floor at each frequency, the shot noise limit can be determined. The shot noise was calculated for the frequency ranges of 995 – 1050 MHz, 1995 – 2050 MHz and 2995 – 3050 MHz where the noise floors were found to be 1.11×10^{-11} V^2/Hz, 2.56×10^{-11} V^2/Hz and 2.73×10^{-11} V^2/Hz respectively. Hence the balanced photodetector, for the higher frequencies, is shot noise limited at ~ 21 µW around 1 MHz, ~ 53 µW around 2 MHz and ~ 60 µW around 3 MHz. This detector is therefore sufficient for MIT measurements of the heart using an alignment based magnetometer as long as a light power of at least 20 – 60 µW is used depending on the desired frequency.

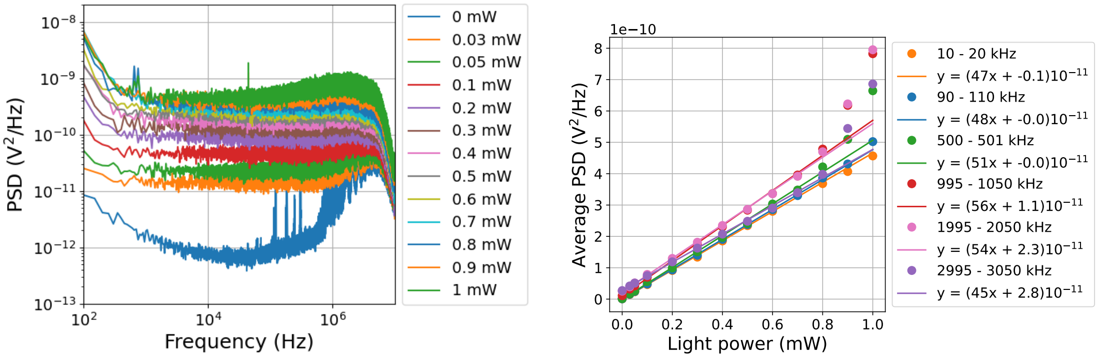

(a) (b)

Figure 9.10: Frequency response of the improved and final home-made balanced photodetector as a response of various light powers incident on the photodiodes. These measurements are used to determine the bandwidth and the shot noise limit of the balanced photodetector. The power spectral density (PSD) (a) is plotted as a function of frequency for light powers between 0-1 mW. Averages over frequency ranges of the PSD are then computed and plotted as a function of light power (b). This data shows the detector has the desired high bandwidth and low noise floor.

9.5 Conclusion

Two different home-made detectors are presented in this chapter, both of which are utilised in Section 10. Their noise floor and bandwidth are compared to a commercially available detector. Drastic improvements are seen in the performance between the initial and final design. Both detectors have frequency ranges where they out perform the commercially available Thorlabs detector. The initial balanced photodetector had a bandwidth of 150 kHz and is shot noise limited from 7 μW in the frequency range of 3 kHz to 6 kHz. The final design of the balanced photodetector, that will be used in the portable OPM, has a bandwidth of a few MHz with a gain peak being seen to start at around 1 MHz. Below this point the detector is shot noise limited from ~ 4 μW. These properties make the detector more than sufficient for the applications of alignment based magnetometry with a chosen Larmor (operational) frequency between a few kHz and a few MHz. This detector is therefore sufficient for MIT measurements of the heart using an alignment based magnetometer with a light power of approximately 35 μW. Using this light power, the detector will be shot noise limited up to ~ 1.5 MHz. If higher frequencies are required then higher light powers can be used for magnetometry, as will be discussed in Section 10.

Chapter 10

Portable buffer gas OPM

10.1 Motivation

As has been discussed, radio frequency optically pumped magnetometers can be used to detect oscillating magnetic fields in the kHz to MHz range [21, 103]. Portable RF-OPMs are not currently readily available. There have been a number of prototypes discussed in the literature [29, 2]. In unshielded conditions, the benchmark intrinsic noise is 600 fT/$\sqrt{\text{Hz}}$ [2]. These types of OPMs have already demonstrated their ability to be used for electromagnetic induction imaging [57]. An excitation coil produces a primary magnetic field $\mathbf{B}_1(t)$ which induces eddy currents in an object creating a secondary magnetic field $\mathbf{B}_{\text{ec}}(t)$. This secondary magnetic field can then be detected with a sensor [56]. The detected signal can then be used to characterise and image the objects [31, 28, 100, 29, 1]. This method can be used to image the conductivity of objects with a low conductivity, like a human heart [61, 30, 25].

Current portable prototypes are all based upon spin-oriented states which use two laser beams [29, 2]. Here the development of a portable RF-OPM is presented that is alignment based. The buffer gas cell that is characterised in Section 6.5 is used in the portable device. The sensor's performance is tested in shielded and unshielded conditions where it is seen to have a sub-pT/$\sqrt{\text{Hz}}$ sensitivity. The potential of the device for remote sensing is demonstrated by detecting aluminium disks of varying diameters. The differential technique [30] is utilised in order to gain a larger signal to noise ratio when detecting the secondary magnetic field. A 1.5 cm diameter aluminium disk is detected at a distance of 26.4 cm from the excitation coil and 23.9 cm from the sensing point of the magnetometer and is detected with a signal to noise ratio of ~ 6. This is done using the setup described in Ref. [2] showing that despite the simpler design the portable OPM presented here can perform as well as an orientation based OPM with an anti-relaxation coated cell. This shows promising results for the use of OPMs in remote sensing applications with the design presented here taking positive steps towards compact and portable RF-OPMs. Detecting highly conductive objects can be done with low frequency magnetic fields with large signals being produced from fields with a frequency of just a few Hz [1]. However, to detect and image low conductive objects the primary magnetic field needs to be at a higher frequency. The sensor developed here was designed to also be able to image low conductive objects. In order to test the capabilities, the sensitivity of the sensor is tested, in shielded conditions, at a Larmor frequency of ~ 1.5 MHz.

10.2 Design and construction of a portable OPM

Figure 10.1a shows the design of a portable optically pumped magnetometer using an alignment based magnetometry configuration and a buffer gas vapour cell. A polarisation maintaining optical fibre is used to bring linearly polarised light that is resonant with the $F = 4 \rightarrow F' = 3$ caesium D1 transition and of wavelength 895 nm into the sensor head. The light passes through a neutral density (ND) filter that attenuates the light power to $\sim$ 35 μW before the vapour cell. A linear polariser is placed before the vapour cell to clean up the light polarisation such that the light is vertically (linearly) polarised. The laser then passes through a vapour cell with a 5 mm diameter and 5 mm optical path length that contains caesium (Cs) alkali vapour and 65 Torr nitrogen (N_2) buffer gas and is heated to $\sim 50^{\circ}$C in order to increase the number density and obtain a higher sensitivity. The cell is the same as that used in the table-top setup in Section 6.5 and can be seen in Figure 6.2. The cell was characterised using a table-top setup before being placed into the portable OPM sensor head (see Section 6.5 [3]). The 3D printed sensor head can be seen in Figure 10.1b. The temperature of the vapour cell is measured using a National Instruments E-type thermocouple (purple wire in Figure 10.1b). The cell is not heated further than $\sim 50^{\circ}$C due to the sensor head being 3D printed from PLA which has a glass transition of 60°C meaning the sensor head will begin to soften. The softening of the plastic could lead to loss of alignment of the optical components. Note that increasing the temperature should result in a better sensitivity as there is a higher number density of atoms but to do this the sensor head should be printed in a more heat resistant material such as PETG. The outer casing of the portable OPM can be seen in Figures 10.1c and 10.1d. The sensor head has dimensions of 5 cm × 11.5 cm × 4 cm.

The basis of the experiment is to create an aligned state in the same way as was done using the table-top setup in Section 6. The experimental setup is very similar with the optics being replaced with smaller alternatives. The main difference arises from the applied magnetic fields in the experiment. The static magnetic field $\mathbf{B}_0$ is applied using an external coil in the y-direction. There are two 2.5 mm diameter RF coils either side of the vapour cell along the z-direction (see Figure 10.1b). Each coil has approximately 20 windings and with the centre of the coil being 1.5 cm from the centre of the vapour cell. The RF magnetic field $\mathbf{B}_{\mathrm{rf}}(t)$ causes the spin to precess around the static magnetic field with a maximal signal obtained when the frequency of the RF magnetic field ω_{rf} is equal to the Larmor frequency, $\omega_L = \gamma_{\mathrm{cs}} B_0$ with the gyromagnetic ratio of caesium being $\gamma_{\mathrm{cs}} = 2\pi(3.5 \text{ kHz}/\mu\text{T})$. After the vapour cell, polarisation rotation measurements are performed using a half wave plate, a polarising beam splitter and a balanced photodetector. Details on the balanced photodetectors used can be found in Section 9 with both of the home-made detectors being used in this chapter. It will be specified in each section which detector was used. In Figure 10.1b the initial design (BPD V1) can be seen but for higher frequency applications the final design (BPD V2) was utilised. All electronics for the sensor head, excluding the thermocouple, are controlled through the balanced photodetectors PCB.

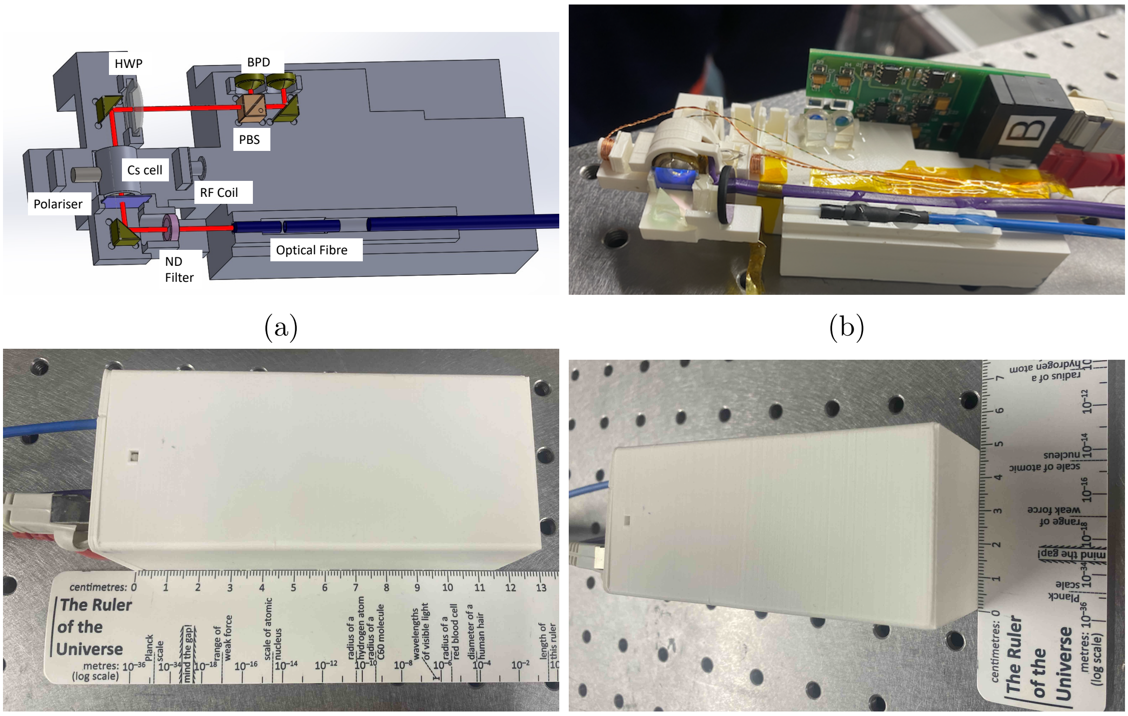

(a) (b) (c) (d)

Figure 10.1: Portable optically pumped magnetometer design that is based up on alignment using a 65 Torr buffer gas cell. (a) The design schematic of inside the OPM head and (b) an image of the constructed sensor head. The casing of the sensor head can be seen with a ruler as a size guide next to the side (c) and front (d) of the casing.

10.3 Magnetic field stabilisation for unshielded applications

For the operation of an optically pumped magnetometer, the applied static magnetic field needs to be stable. Minor fluctuations in the static field causes a noisier signal and hence a less sensitive magnetometer. Large fluctuations in the static field can cause the Larmor frequency to vary more than the signal linewidth and hence the OPM does not perform well as a magnetic field sensor. In unshielded conditions extra precautions need to be put into place in order to maintain a stable static magnetic field. For the unshielded operation of the portable OPM, a stable static magnetic field needs to be applied along the y-direction whilst any residual magnetic fields in the x- and z-directions need to be compensated for. This is done by using a three axis coil system setup with a proportional–integral–derivative (PID) feedback. A fluxgate magnetometer is used to measure the residual DC magnetic field strengths along all three axes and act as the feedback source for the coils. For low frequency applications the Bartington MAG690-FL100 is used whereas for high frequency applications the MAG690-FL1000 is chosen for its higher dynamic range. Two different feedback coil systems are used for different applications.

For the eddy current detection presented in Section 10.7 the three axis coil system used can be seen in Figure 10.2a. This coil system consists of a 3D printed cylinder that is wrapped in a solenoid coil that produces a magnetic field along the z-direction. Inside the cylinder is a flexible PCB that is wrapped and connected to the interior of the cylinder. The flexible PCB houses cosine-theta coils that are able to produce magnetic fields along the x- and y-directions. The fluxgate magnetometer and the portable OPM are placed inside the coil system with a separation of 6.25 cm between the detection points of the sensors. The $x-$, $y-$ and $z-$outputs of the fluxgate magnetometer are connected to the analogue inputs of the field-programmable gate array (sbRIO-9627) and used as the input signals for a proportional–integral–derivative feedback system that is implemented in the FPGA. This then produces a voltage that is output from the FPGA into a (LT1210) current feedback amplifier. The current output from the amplifier is then sent to the three coils in order to cancel the Earth's magnetic field at the detection point of the fluxgate magnetometer. Along the y-direction the PID system is used to set the static magnetic field, $\mathbf{B}_0$, to the desired Larmor frequency. In order to test the performance of the PID feedback system, the fluxgate magnetometer was used to measure the noise at 50 Hz along the y-direction. Without the PID system the strength of this noise measured $\sim$ 21.2 $\mathrm{nT}_{\mathrm{pp}}$. If this field strength is converted to frequency, using the gyromagnetic ratio for caesium, it corresponds to approximately 74 Hz. When the PID system is in use the noise is reduced to $\sim$ 2.5 $\mathrm{nT}_{\mathrm{pp}}$ which corresponds to a frequency of approximately 9 Hz [159, 2]. This shows the PID feedback system significantly reduces the noise and can help to stabilise the magnetic field. This coil system works well for imaging highly conductive objects however, due to the closest position the object can be placed to the OPM sensing point being 18.9 cm away from the detection point, it is not a practical design for imaging low conductivity objects such as salt water or a heart.

For imaging applications, for example MIT of the heart and low conductive objects, a different feedback coil system needed to be designed. The new design can be seen in Figures 10.2b and 10.2c. The three axis Helmholtz design was developed such that the object being imaged can be placed much closer to the detection point of the portable OPM. To create the magnetic field in the x-direction, a pair of Helmholtz coils with a diameter of 38 cm and 80 windings was used. For the y-direction a pair of Helmholtz coils with a diameter of 43 cm and 110 windings was used. Finally to produce the magnetic field along the z-direction a pair of coils with a diameter of 32 cm and 80 windings is used. In this setup the fluxgate sensing point is placed underneath the portable OPM's sensing point to allow space for the objects to be moved around in the Helmholtz coil when being imaged. The centre of the sensing points are 3.5 cm apart. The same PID feedback system using the FPGA is used here to stabilise the static magnetic field and to compensate for the Earth's magnetic field.

10.4 Characterisation

To characterise the portable magnetometer, the sensor head is placed within a magnetic shield. This makes the characterisation process easier as there are minimal external influences on the measurements. The magnetometer is characterised in order to obtain the maximal sensitivity possible with the portable OPM configuration with the hope that the same, or better, sensitivity can be obtain as was found for the buffer gas vapour cell in the table-top setup (see Section 6.5). Note, due to the miniaturisation and portability of the device the components are fixed in place and

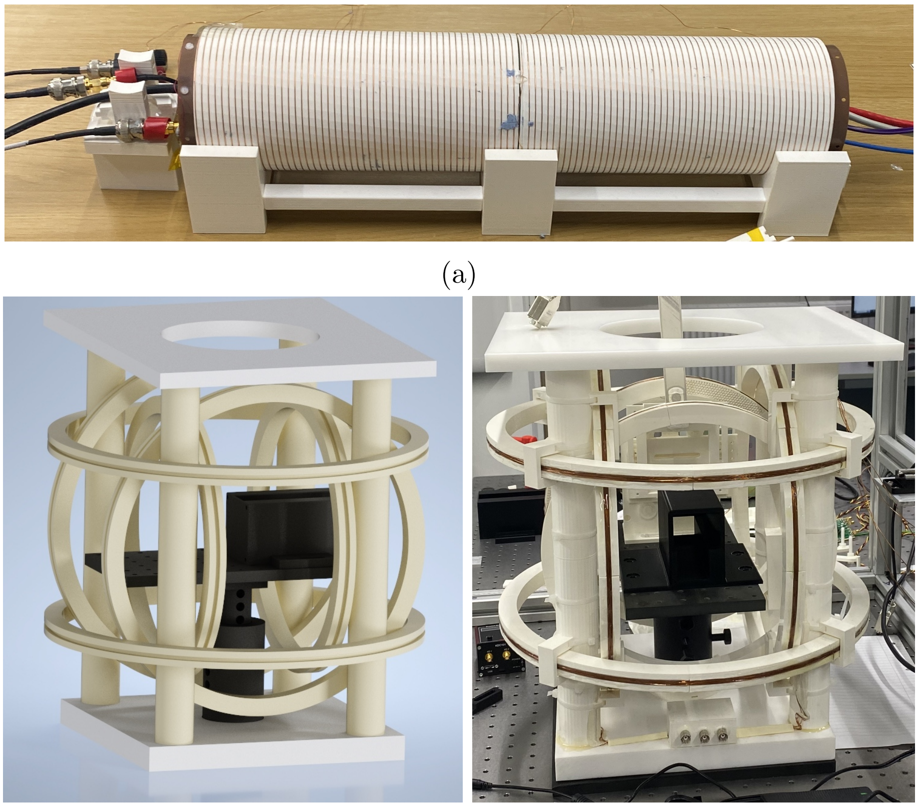

(a)

(b) (c)

Figure 10.2: Magnetic field stabilisation coil systems. (a) The initial design used for the detection of highly conductive objects in the kHz region. (b) The design and (c) an image of the constructed Helmholtz coils designed to work at frequencies in the kHz-MHz range allowing objects to be placed closer to the sensor.

light power cannot be altered to help with the sensitivity so the light power is not optimised systematically and hence is not reported on.

10.4.1 Calibrating RF coils

In order to determine the smallest detectable magnetic field by the portable OPM, the RF coils need to be calibrated. In the sensor head there are two single coils that can be used to produce the oscillating magnetic field along the z-direction. The calibration provides a conversion from the voltage applied to the coil, in Volts, to the RF magnetic field B_{rf} that the atoms see, in Tesla. Only one RF coil is used for the sensitivity measurements and this is referred to as the 'excitation' coil. A second RF coil is in the OPM head for eddy current detection and this is referred to as the 'compensation' coil. Due to both coils potentially being used in eddy current detection, both coils are calibrated and hence either can be used to obtain the sensitivity of the magnetometer. The coil calibration method used is the same as that outlined in Section 6.4.1. The basis of the calibration will be briefly outlined again here with the coil being calibrated being the excitation coil (RF0). To calibrate the excitation coil, a small oscillating magnetic field is applied to the compensation coil. This acts as the RF magnetic field with a small RF amplitude of 30 mV_{rms}. Any residual fields in the magnetic shield (Twinlief MS-2) need to be nulled using the integrated coils as $\omega_L \propto \sqrt{B_x^2 + B_y^2 + B_z^2}$. When the field is completely nulled it can be seen that $\omega_L = \gamma_{\rm cs} B_y$. With the static magnetic field equal to zero in two directions, B_x and B_z, and a static field applied along the y-direction the excitation coil can now be calibrated. DC voltages of amplitudes varying from -2 $\mathrm{V_{rms}}$ to 2 $\mathrm{V_{rms}}$ were applied to the excitation coil using a function generator (Rigol DG1032Z). The magnetic resonance signals were then recorded with the 'R' signal being fitted to a Lorentzian function as shown in Figure 10.3a. From the fit function the central frequency of the peak, $\nu_L = \omega_L/(2\pi)$, as a function of the applied DC voltage is plotted, as shown in Figure 10.3b. These were then fitted to a quadratic equation. From the fits the calibration of the coil can be determine in units of nT/V.

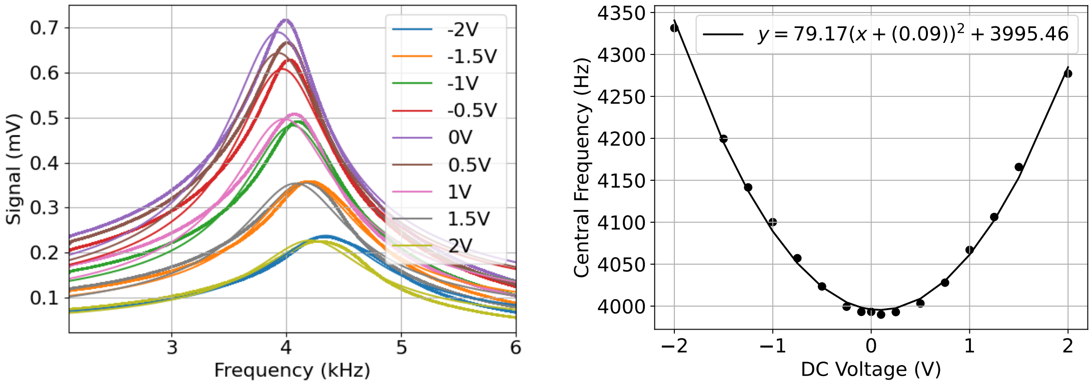

(a) (b)

Figure 10.3: Calibration of the RF magnetic field that is produced by the excitation coil, used with a 65 Torr buffer gas cell in the portable optically pumped magnetometer. This is calibrated by applying various DC voltages through the coil to see how the (a) magnetic resonances and (b) central frequency depend on the voltage applied.

In order to determine the calibration from applied voltage to magnetic field, a few assumptions need to be made. If it is assumed that $B_x \approx 0$ then the magnetic field in the magnetic shield can be written as $\nu_L = \tilde{\gamma}_{\rm cs}\sqrt{B_y^2 + B_z^2}$. Now, using the fact that $B_y > B_z$ and the binomial expansion $(1+x)^n = 1 + nx$ (to first order) when $x << n$, ν_L can be rewritten as

$$\nu_L = \tilde{\gamma}_{\rm cs}\left(1 + \frac{1}{2}\frac{B_z^2}{B_y^2}\right). \tag{10.1}$$

To fit this to the experimental data, it can be rewritten in terms of the applied DC voltage and how this affects the central frequency:

$$\nu_L = \nu_0\left(1 + \frac{1}{2}\frac{(k \times \mathrm{V_{DC}})^2}{\nu_0^2}\right), \tag{10.2}$$

where V_{DC} is the DC voltage applied to the coil being calibrated, k is the conversion factor and ν_0 is the central frequency when the magnetic field is nulled. Equation 10.2 is of the same form as the fitted parabola in Figure 10.3b. By comparison it can be seen that $\nu_0 = 3995.46$ Hz and $b_0 = k^2/2\nu_0 = 79.17$ Hz/V^2. The calibration is then found by rearranging b_0 to determine $k = \sqrt{2\nu_0 b_0} = 795.4$ Hz/V. This is equivalent to $k = 227.3$ nT/V by using the gyromagnetic ratio of caesium to convert from Hertz to Tesla ($\tilde{\gamma}_{\text{cs}} = 3.5$ kHz/μT). The same procedure can be followed to calibrate the compensation coil (RF1) by applying the oscillating magnetic field, with a 30 mV$_{\text{rms}}$ amplitude, to the excitation coil and a static magnetic field of varying amplitudes between -2 V$_{\text{rms}}$ to 2 V$_{\text{rms}}$ to the compensation coil. The results can be seen in Figure 10.4 and by substituting the fit values into Equation 10.2 the calibration of $k = 193.9$ nT/V can be found.

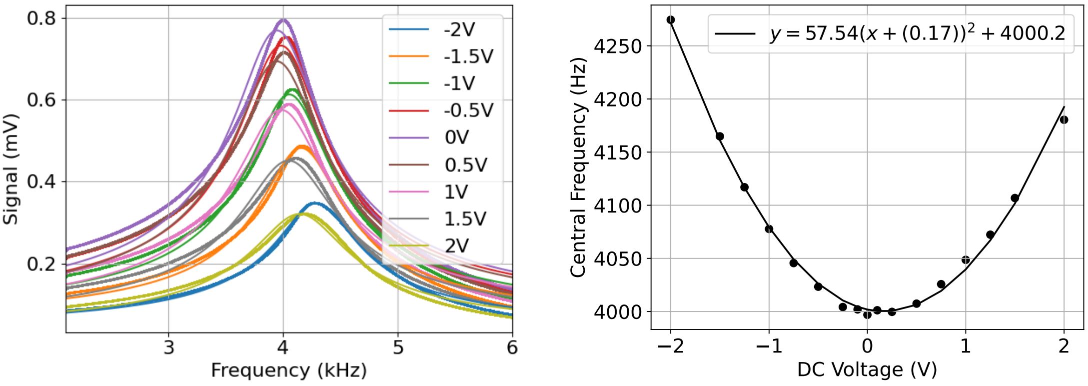

(a)

(b)

Figure 10.4: Calibration of the RF magnetic field that is produced by the compensation coil, used with a 65 Torr buffer gas cell in the portable optically pumped magnetometer. This is calibrated by applying various DC voltages through the coil to see how the (a) magnetic resonances and (b) central frequency depend on the voltage applied.

10.4.2 RF amplitude

In order to obtain the best sensitivity from an optically pumped magnetometer, the desired light power and RF amplitude need to be determined. Due to the vapour cell being at a comparable temperature to the table-top setup (see Section 6.5), the light power chosen is similar to that used in the table-top setup. Changing the light power in the portable sensor head is difficult, due to it requiring the laser current and temperature being varied together or the neutral density filter being changed, so it is not re-characterised here. As the conditions are almost identical to the table-top setup a light power of 35 μW is selected for most data sets. If a different light power is used for a data set then this is specified in the section.

Once the vapour cell was placed and aligned in the portable OPM head the last parameter that needed to be characterised was the RF magnetic field amplitude. This was done by varying the RF amplitude applied to the ‘excitation’ coil from 6 mV$_{\text{rms}}$ to 200 mV$_{\text{rms}}$ as shown in Figure 10.5. A light power of 35 μW was used here. As the amplitude of the field increases so does the amplitude and linewidth of the signal. The magnetometer resonance signals are recorded and the $R = \sqrt{X^2 + Y^2}$ is fitted to an absorptive Lorentzian curve (see Equation 6.3). Figure 10.5a shows some example traces and the corresponding fits. From these fits the full width half maximum (FWHM) and the peak amplitudes can be extracted. The optimal sensitivity point can be found at the point where the amplitude/FWHM is maximal (see Figure 10.5b). However, the response of the amplitude still needs to be linear which can be determined by looking at Figure 10.5c. It can be seen that, in the regime where the amplitude response is linear, amplitude/FWHM is maximal when the applied RF amplitude is $30 - 40$ $\mathrm{mV_{rms}}$. After testing the sensitivity for both amplitudes a better sensitivity was obtained when using 30 $\mathrm{mV_{rms}}$ so this was selected as the optimal RF amplitude.

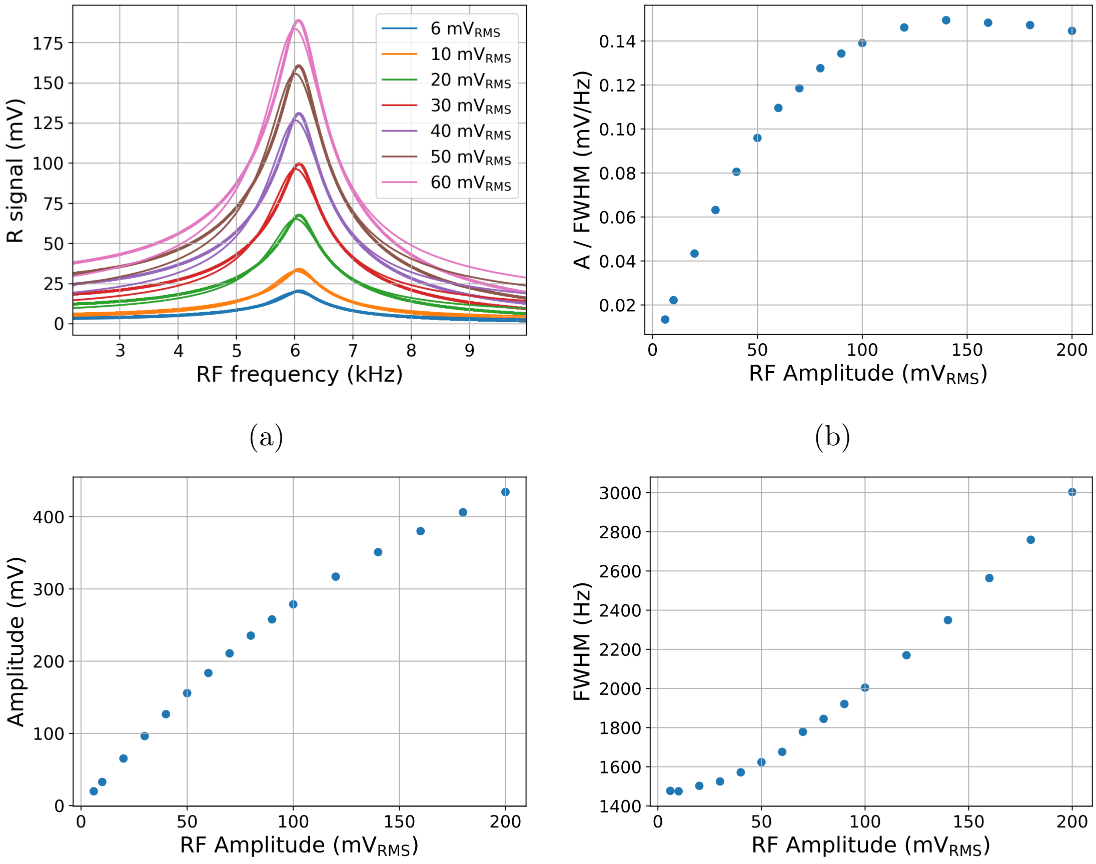

(a) (b)

(c) (d)

Figure 10.5: Characterising the amplitude of the RF magnetic field produced for the portable alignment based magnetometer which uses a 65 Torr nitrogen buffer gas filled caesium cell. A light power of 55 μW, before the vapour cell, is used and the cell is heated to $\sim 50^{\circ}$C. (a) The $\boldsymbol{R}$ signal of the magnetic resonance sweep is fitted to an absorptive Lorentzian to obtain the (b) A/FWHM dependence on the RF amplitude applied. The (c) amplitude and (d) full width half maximum (FWHM) of the signals are also presented.

How the full width half maximum and the amplitude change with increasing the RF field can be described by the following [30]

$$\mathrm{FWHM} = \mathrm{a}\sqrt{1 + \left(\frac{\mathrm{V_{rms}}}{\mathrm{V_{sat}}}\right)^2}, \tag{10.3}$$

and

$$A = \frac{a\ V_{rms}}{1 + (V_{rms}/V_{sat})^2}, \tag{10.4}$$

where V_{sat} is the voltage at which the atomic ensemble becomes saturated by the applied RF magnetic field. By fitting the data shown in Figures 10.5d and 10.5c to these equations the saturation voltage can be determined (fits not shown). The saturation voltage is found to be 0.11(1) V_{rms} when fitting the data in Figure 10.5d to Equation 10.3 and 0.237(6) V_{rms} when fitting the data in Figure 10.5c to Equation 10.4

10.5 Zero-field performance

Alongside using the portable OPM for high frequency applications of magnetic induction tomography of the heart, tuning the Larmor frequency to low frequencies opens up more potential applications for the device. By taking the Larmor frequency of the OPM to near zero-field, in a magnetic shield (Twinleaf MS-1L), it was seen that the sensor can be operated as a zero-field magnetometer. The residual magnetic fields in the shield were nulled using the methods outlined in Section 8. The bandwidth and sensitivity of the OPM were then tested. This was done by applying oscillating sine waves with frequencies from 8 Hz to 1.818 kHz. The resultant photodetector signals were then sent straight to the data acquisition card where 10 averages of 2 second time traces were recorded using a 10 kHz sample rate. The data was recorded and Fourier transformed in order to obtain the power spectral density of the signal. Figure 10.6 shows the resulting power spectral density as a function of frequency. It can be seen that, in shielded conditions, the portable OPM performs well near zero-field. The data with 'No RF' can be seen to match the base noise of the signals when an oscillating RF field of set frequency is applied. This noise floor can be used to determine the sensitivity of the sensor as 1 pT/$\sqrt{\text{Hz}}$ at 100 Hz. The bandwidth of the sensor can be determined by fitting the peak heights to the response of a first order low-pass filter, $\left(K/\sqrt{1 + (f/f_c)^2}\right)$ where f_c is the bandwidth of the magnetometer. The bandwidth was found to be 102(6) Hz. It can clearly be seen that there is a lot of $1/f$-noise and the signal has a much higher noise floor near zero frequency. Some $1/f$-noise is to be expected, but the increased amount can also result from the light hitting the balanced photodetector not being perfectly balanced. It is also noted that this data is taken using the initial balanced photodetector design (see Section 9.4.1) which similarly sees a large increase in noise as the frequency approaches zero. The data in Figure 9.6a suggests the noise at the light powers used here (~ 35 μW before the cell) is dominated by electronic noise further limiting the sensitivity. Hence the use of the improved balanced photodetector should further improve this sensitivity.

10.6 Low frequency performance

10.6.1 Shielded sensitivity

Using the optimal parameters for the portable OPM that have been found in the characterisation, the sensitivity of the device can be determined. A static magnetic

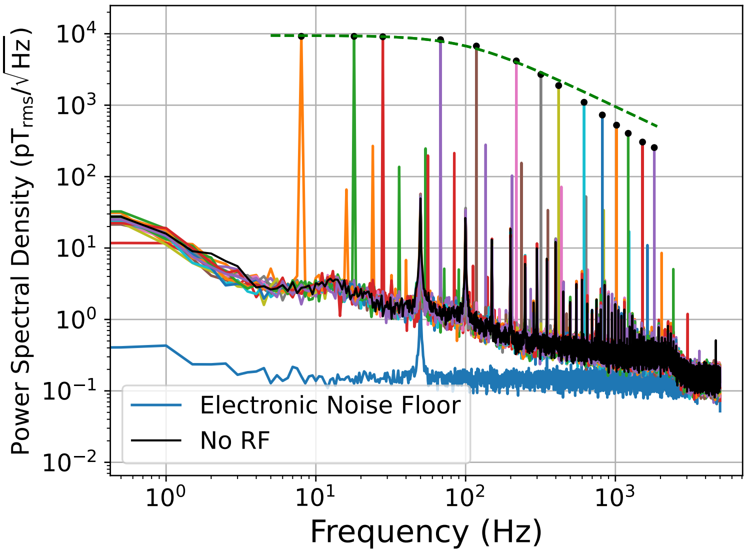

Figure 10.6: Power spectral density of the magnetometry signal from the portable optically pumped magnetometer near zero-field. 10 averages of 2 seconds time traces were recorded using a 10 kHz sample rate. 14 different measurement sets are calculated where sinusoidal magnetic fields are applied with various frequencies ranging from 8 to 1818 Hz. Two additional measurements are taken without the sinusoidal field applied (No RF) and with the balanced photodetector disconnected from the data-acquisition card (Electronic noise floor).

field of amplitude 1.73 μT is applied along the y-direction. This field corresponds to a Larmor frequency of 6042 Hz. The laser light power was set to 35 μW and the vapour cell was heated to $\sim 50^{\circ}$C. An RF amplitude of 30 mV_{rms} was applied to the excitation coil which, using the coil calibration from Section 10.4.1, is equivalent to an RF field strength of 6.82 nT_{rms} at the position of the atomic ensemble. Four different measurements were taken, all with a 10 kHz sample rate. In the first measurement, the frequency of the RF magnetic field is swept between 2 kHz and 10 kHz. This provides the magnetic resonance signal and can be seen in Figure 10.7a. The in-phase (X) component has an absorptive Lorentzian shape whilst the out-of-phase (Y) component has a dispersive lineshape. This is as expected from Equation 6.3. The peak of the amplitude signal $\left(R = \sqrt{X^2 + Y^2}\right)$ corresponds to the Larmor frequency as $\omega_L = \omega_{\text{rf}} \approx 2\pi(6 \text{ kHz})$. The peak height of the Lorentzian is used to calculate a conversion between the lock-in output voltage to the magnetic field detected. This is done by extracting the peak height and dividing it by the applied oscillating magnetic field to give a conversion factor of 0.98 V/nT. This conversion can be used to characterise the noise of the magnetometer and determine the smallest detectable field. To find the intrinsic noise of the OPM, the lock-in demodulation frequency is set at the Larmor frequency $(\omega_L = 2\pi(6.042 \text{ kHz}))$. Three sets of data were then recorded, one with the RF magnetic field amplitude on $(B_{\text{rf}} = 6.82 \text{ nT}_{\text{rms}})$, the RF field is then set to zero and finally, the laser is turned off to measure the electronic noise floor of the setup. For each data set, a four minute time trace was recorded and can be seen in Figure 10.7. The sensitivity of each time trace is then calculated by taking the average of 1 second intervals and then

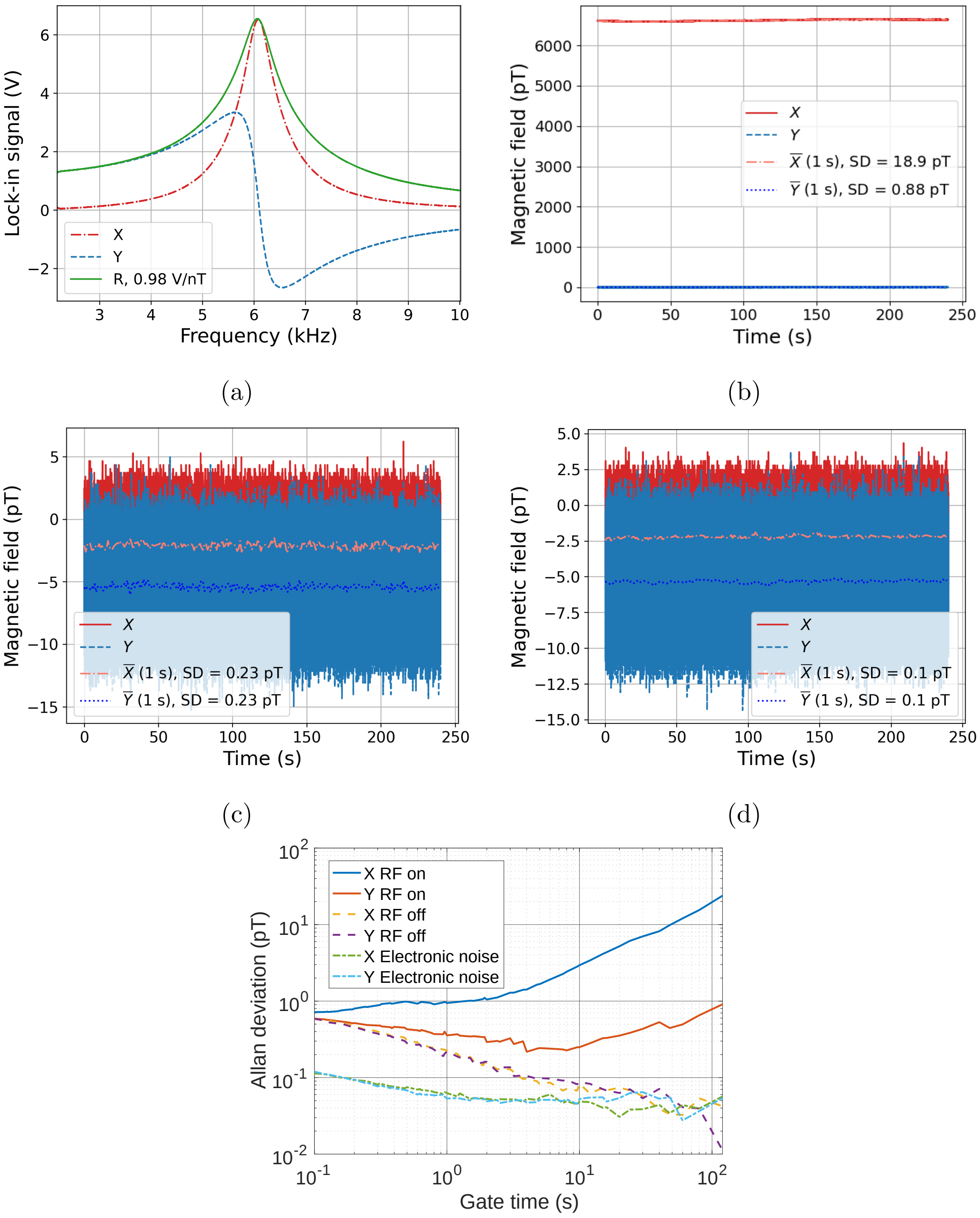

(a) (b)

(c) (d)

(e)

Figure 10.7: Sensitivity of the portable alignment based magnetometer in a magnetic shield at a Larmor frequency of approximately 6 kHz. The cell is heated to a temperature of $\sim 50^{\circ}$C. (a) The magnetic resonance signal is found from sweeping the frequency of the RF magnetic field from 2 kHz to 10 kHz. Four minute time traces are then recorded with the frequency set to the peak value in (a) at which $\omega_L \approx 2\pi(6\text{ kHz})$ with (b) the RF field amplitude on, (c) the RF amplitude set to zero which represents the intrinsic noise of the optically pumped magnetometer and (d) the electronic noise of the setup. The standard deviation of one second averages are found and the (e) Allan deviation is also calculated for the time traces.

calculating the standard deviation of these averages. The sensitivities are shown in the legends of Figure 10.7. The intrinsic sensitivity of the portable OPM can be seen in Figure 10.7c when the RF magnetic field is set to zero. The sensitivity of the OPM is 0.23 $\mathrm{pT}/\sqrt{\mathrm{Hz}}$. Figure 10.7d shows that a small contribution of this noise is from the electronic noise but the dominating factor is shot noise. The Allan deviation of all of the data sets is shown in Figure 10.7e to show the stability of the measurements. At a gate time of 1 second the deviation is found to agree with the standard deviation approach of calculating the sensitivity.

The quantum noise limit for the portable OPM can be calculated as was done for the vapour cell in the table-top setup (Section 6.5.5). There are two main fundamental limits to the sensitivity of a magnetometer which are the spin projection noise $\delta\mathrm{B}_{\mathrm{spin}}$ and the photon shot noise $\delta\mathrm{B}_{\mathrm{shot}}$. These result in a total quantum noise of $\delta\mathrm{B}_{\mathrm{quantum}} = \sqrt{\delta\mathrm{B}^2_{\mathrm{spin}} + \delta\mathrm{B}^2_{\mathrm{shot}}}$. Theoretically the spin projection noise can be calculated [51, 111]

$$\delta\mathrm{B}_{\mathrm{spin}} = \frac{2\hbar}{g_F \mu_B \sqrt{nVT_2}}, \tag{10.5}$$

where $g_F = 1/4$ for the $F = 4$ caesium ground state, n is the number density of Cs atoms, $T_2 \approx 1/(\pi(800\ \mathrm{Hz})) \approx 0.4$ ms is the transverse relaxation time. In the case of a buffer gas cell only the atoms that are inside the laser beam are probed so the volume (V) is given by the volume of the beam, $V = V_{\mathrm{beam}} = 15.6 \times 10^{-9}\mathrm{m}^{-3}$ for a beam diameter of $d_{\mathrm{beam}} \approx 2$ mm. At a temperature of 50°C the number density of Cs atoms is $n \approx 5.89 \times 10^{17}\ \mathrm{m}^{-3}$. Therefore, the spin projection noise is calculated to be $\delta\mathrm{B}_{\mathrm{spin}} \approx 47\ \mathrm{fT}/\sqrt{\mathrm{Hz}}$. An ideal optically pumped magnetometer has $\delta\mathrm{B}_{\mathrm{shot}} = \delta\mathrm{B}_{\mathrm{spin}}$ such that $\delta\mathrm{B}_{\mathrm{quantum}} = \sqrt{2}\delta\mathrm{B}_{\mathrm{spin}}$. Hence the theoretical quantum noise limit of the OPM is $\delta\mathrm{B}_{\mathrm{quantum}} \approx 66.5\ \mathrm{fT}/\sqrt{\mathrm{Hz}}$. Hence, experimentally the sensitivity is a factor of 3.5 off the theoretical limit. This factor is partially due to only using one laser beam and hence over half of the atoms are lost to the $F = 3$ state. An additional laser could improve the sensitivity of the device however this will introduce additional components to the setup making it less compact.

10.6.2 Unshielded sensitivity

Now that the intrinsic sensitivity of the OPM has been determined the performance in unshielded conditions must also be characterised. In order to characterise the noise floor of the detector in unshielded conditions the sensor head is placed inside the magnetic field stabilisation coils. For the low frequency data presented here the cylindrical coil system, shown in Figure 10.2a, was used. A higher Larmor frequency was used unshielded than in the shielded case. This was to allow the portable alignment based performance to be compared to the portable orientation based OPM previously developed [2, 48] and hence a Larmor frequency of $\omega_L \approx 2\pi(11\ \mathrm{kHz})$ was selected. The static magnetic field is set using the coil in the y-direction with the PID set to keep the magnetic field at $B_0 = 3.13\ \mu\mathrm{T}$. The magnetic resonance is initially recorded with the RF magnetic field frequency being swept between 6.5 kHz and 15 kHz with an amplitude of $B_{\mathrm{rf}} = 6.82\ \mathrm{nT}_{\mathrm{rms}}$. Figure 10.8a shows the resulting signal and the calibration from the lock-in output signal to magnetic field detected by the atoms of 1.05 V/nT. The RF frequency is then set to 10.959 kHz and a four minute time trace was recorded. As was done in the shielded case two more time

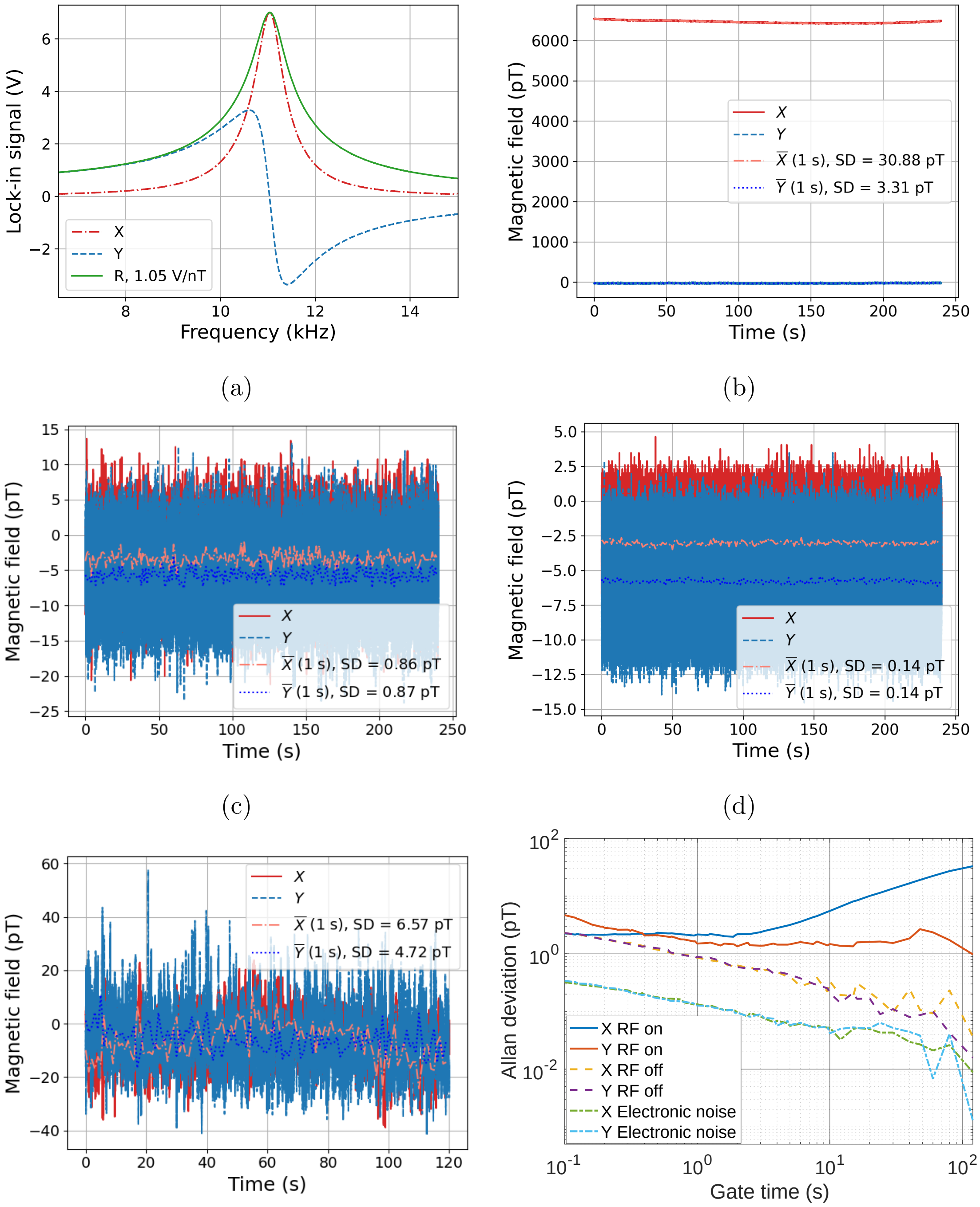

(a) (b)

(c) (d)

(e) (f)

Figure 10.8: Sensitivity of the portable alignment based magnetometer in unshielded conditions at a Larmor frequency of approximately 11 kHz. The cell is heated to a temperature of $\sim 50^{\circ}$C. (a) is the magnetic resonance signal from sweeping the frequency of the RF magnetic field from 6.5 kHz to 15 kHz. Four minute time traces are then recorded with the frequency set to to the peak value in (a) at which $\omega_L \approx 2\pi(11\text{ kHz})$ with (b) the RF field amplitude on, (c) the RF amplitude set at zero which represents the intrinsic noise of the optically pumped magnetometer, (d) the electronic noise of the setup and (e) when both the excitation coil and compensation coil are on. The standard deviation of one second averages are found and the (f) Allan deviation is also calculated for the time traces.

traces were taken: one with the magnetic field amplitude set to zero and one of the electronic noise floor. The intrinsic noise floor in unshielded conditions is higher, with a minimal detectable field of 865 fT. The increase in noise in unshielded conditions is due to a combination of environmental noise and current source noise that is used in the magnetic field stabilisation. Using a lower noise current source should reduce this noise and hence means smaller magnetic fields would be detectable by the buffer gas portable OPM in unshielded conditions. The OPM operated in unshielded conditions demonstrates comparable performance to the orientation based portable OPM presented in Ref. [2] which uses the same magnetic feedback coil system as discussed here. As the alignment based OPM presented here has a lower intrinsic noise than the unshielded result from the orientation OPM (600 fT), it should be possible with frequency filtering of the feedback system and current sources to obtain the same unshielded sensitivity.

The Allan deviation of the time traces is shown in Figure 10.8f which shows the stability of the OPM over different gate times. It can be seen that for the RF magnetic field set to zero the Allan deviation continues to decrease over longer gate times. At 100 seconds the Allan deviation measures between 25 fT and 80 fT. Hence, the intrinsic noise of the OPM is stable over longer time periods than the 1 second time interval used to define the sensitivity. With the RF magnetic field not set to zero it can be seen that, especially for the 'X' component, the signal has increased noise and does not become more stable over longer gate times.

10.7 Eddy current detection

The portable OPM's ability to detect eddy currents in unshielded conditions was tested by trying to recreate data previously collected with the fluxgate magnetometer (see Section 5.6). Two experiments were carried out. The first involved varying the position of an aluminium object between the excitation coil and the OPM. For the second experiment cylinders of varying diameters were placed at a fixed distance between the coil and the portable OPM. When moving the object the same aluminium sample as presented for the fluxgate is used (see Figure 5.1b) which is grade 6061 T6 with a radius of 2 cm and a thickness of 2 cm. When varying the diameter of the sample the same grade of aluminium is used but the samples have a smaller thickness of 4 mm. A Larmor frequency of $\omega_L \approx 2\pi(10.9 \text{ kHz})$ is used in unshielded conditions. The field stabilisation setup shown in Figure 10.2a is used to keep the static field constant. An excitation coil, with a 5 cm radius, is placed 50.3 cm away from the sensing point of the portable OPM. The setup is the same as that used in [2, 48] and is carried out to show the ability of the simplified portable OPM to compare with a more complex prototype. For each data set, the aluminium sample is placed into the setup for ~ 20 seconds and then removed for ~ 20 seconds with three averages taken. Example time traces can be seen in Figure 10.9 where, as expected from tests carried out using the fluxgate (see Section 5.5 and [1]), the signal is mainly in the in-phase (X) component. This can be further seen by calculating the skin depth for the aluminium sample at 10.9 kHz using $\delta = 1/\sqrt{\pi\mu\sigma\nu_{\text{rf}}} \approx 1$ mm which is much smaller than the 4 mm thickness of the samples being detected.

The differential method [30] is utilised in all data sets presented here by using a compensation coil, with a radius of 2.5 mm, within the sensor head. The differential method uses two magnetic fields, the primary (excitation) magnetic field $\mathbf{B_1}(t, \nu_{\text{rf}})$

and a compensation magnetic field $\mathbf{B_2}(t, \nu_{\text{rf}})$. The amplitudes of these fields are set such that $\mathbf{B_1}(t, \nu_{\text{rf}}) + \mathbf{B_2}(t, \nu_{\text{rf}}) \approx 0$ at the detection point of the atoms. When a conductive object is placed between the two coils, eddy currents are induced in the object producing a secondary induced magnetic field $\mathbf{B}_{\text{ec}}(t, \nu_{\text{rf}})$. Hence the magnetic field at the vapour cell becomes $\mathbf{B_1}(t, \nu_{\text{rf}}) + \mathbf{B_2}(t, \nu_{\text{rf}}) + \mathbf{B}_{\text{ec}}(t, \nu_{\text{rf}}) \approx \mathbf{B}_{\text{ec}}(t, \nu_{\text{rf}})$. Using the differential method improves the signal to noise ratio of the experiment and hence allows smaller signals to be detected. This comes from two factors. The first is that compensating for the magnetic field causes the system to be more sensitive than the detector with the RF magnetic field on measurements. This is shown in Figure 10.8e, where an improvement in the sensitivity of the X component can be seen. This signal is 4.74 times more sensitive. It is noted that if phase locked outputs were used to compensate for the excitation coil then the sensitivity of the setup should match the 'RF off' limit. However, in the data presented here the phase was matched manually. The second benefit of using the differential method is that a larger primary excitation field can be used without saturating the atomic ensemble. Using a single coil the applied magnetic field of 6.687 nT_{rms} is used to avoid the atoms becoming saturated whereas with a secondary compensation coil a primary field with a strength of 227.36 nT_{rms}, at the detection point, can be used. This results in a signal improvement factor of 34. Hence when comparing to the RF on sensitivity, an overall signal to noise improvement of $34 \times 4.74 \approx 160$ is achieved.

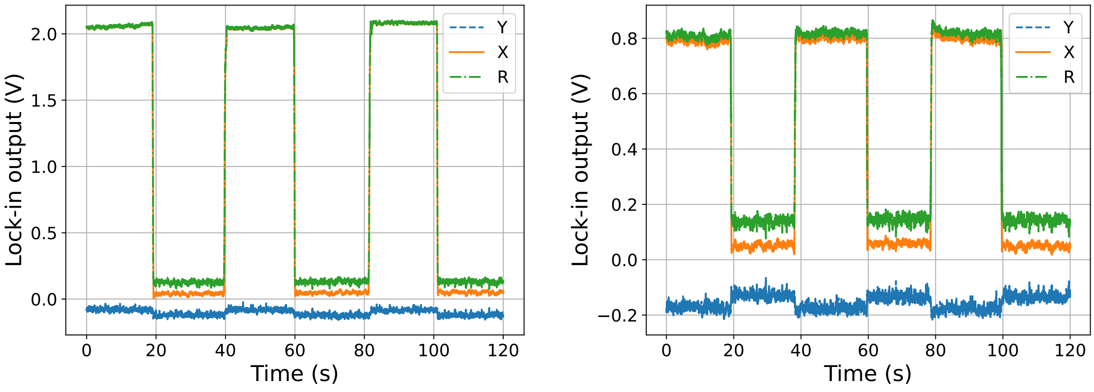

(a) (b)

Figure 10.9: Example time traces when an object is present in the setup for 20 seconds and then removed for 20 seconds. A 2 cm radius and 2 cm thickness aluminium cylinder is detected with it being placed (a) 6.4 cm and (b) 21.4 cm from the excitation coil.

Figure 10.10a shows how the detected secondary magnetic field varies as the position of the aluminium sample changes between the OPM and excitation coil. The 'R' signal is presented, however, it can be seen in the example traces (Figure 10.9) that the majority of the signal is in the in-phase (X) component of the signal. As expected, there is a quadratic dependence with the signal being lowest approximately half way between the excitation coil and sensing point of the OPM. The signal response agrees with that obtained when detecting the aluminium cylinder using the fluxgate magnetometer in Section 5.6.

How the induced magnetic field strength varies with aluminium disks of varying diameter are then studied with the results shown in Figure 10.10b. In the data shown here the cylinders were placed roughly half way between the OPM and excitation coil with a distance of 26.4 cm from the excitation coil and 23.9 cm from the sensing point of the OPM. 6061 T6 Aluminium cylinders of diameter 0.5 cm, 1 cm, 1.5 cm, 2 cm, 3 cm and 5 cm are placed in the setup with the secondary magnetic field recorded. A dotted line is shown in Figure 10.10b to show the minimal detectable field of the experimental setup. This shows that samples with a diameter as small as 1 cm can successfully be detected in the experimental configuration. The induced magnetic field is plotted against the diameter size and can be seen to follow a $1/D^3$ relation. The prefactor for the experimental data is fitted and determined to be 8.16(7) pT/cm^3. This prefactor can be compared to a theoretical prediction used in [58] and shown in Section 5.5.2. It is noted that the geometry of the object is different as the theory is for a sphere and a cylinder is used here. This is discussed in Section 5.5.2.2 and it is expected there will be a scale factor difference between the results due to the different shape geometries. However, the correct relation can still be determined. The theory shown in Section 5.5.2.2 is for a magnetic object and can be simplified further for a non-magnetic sample like the aluminium presented here. For a non-magnetic object $\mu_r = 1$ and hence the equation for the magnetic moment of the induced objects (Equation 5.7) simplifies to

$$m_{\mathrm{ec}} = \frac{2\pi r^3 B_1(z = a)}{\mu_0} \frac{j_2(kr)}{j_0(kr)}, \tag{10.6}$$

where r is the radius of the sphere and a is the distance from the excitation coil to the object. In the high frequency regime the factor containing the Bessel functions simplify as $j_2(kr)/j_0(kr) \rightarrow -1$. Hence the detected secondary magnetic field is theoretically predicted to be

$$B_{\mathrm{ec}}(z = a + a') = -\frac{r^3 B_1(z = a)}{a'^3}, \tag{10.7}$$

where a' is the distance of the object from the detection point of the OPM. Hence the induced magnetic field strength at the detection point can be written as $B_{\mathrm{ec}}(z = a + a') = \alpha D^3$ where $\alpha = B_1(z = a)/8a'^3$ and $D = 2r$ is the samples diameter. Substituting in the experimental parameters the prefactor is found to be 14.4 pT/cm^3. This agrees with theory up to a factor of 0.56(1), which agrees with the discrepancy from the different sample geometry found in Section 5.5.2.2. Using this factor it can be seen that the experimental data follows the expected theoretical trends for varying the diameter of the conductive object.

The data presented for varying the diameter of the aluminium disk can be compared to that presented in [2]. The portable OPM presented in [2] is orientation based and uses a paraffin coated cell. This OPM uses two lasers at a much higher light power than the sensor presented here. Other than the sensors used, the experimental setup and samples detected are the same so a scaling factor only needs to be considered for the differing primary magnetic fields as $\mathbf{B}_{ec} \propto \mathbf{B}_1$. Both of the portable OPM prototypes have a comparable performance in shielded and unshielded conditions for a Larmor frequency of approximately 11 kHz. In [2] an excitation field measuring 127.7 nT$_{\mathrm{rms}}$ at the vapour cell is used. The data presented in this thesis hence has an excitation field that is 78% larger and hence the detected eddy current field should also be 78% larger. Taking this factor into account it can be seen that the value of $B_{\mathrm{ec}} = 6.0D^3$ agrees well with the values presented here. A difference

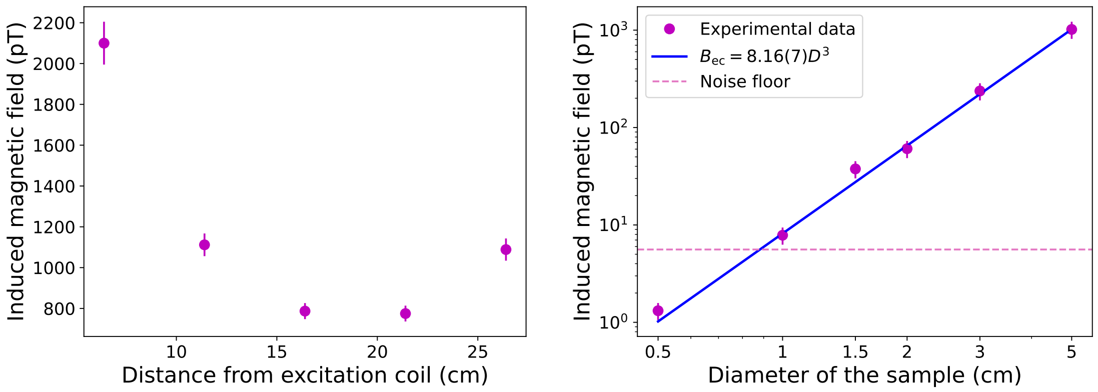

(a) (b)

Figure 10.10: Eddy current detection of 6061 T6 aluminium cylinders at (a) various distances and (b) with various diameters. (a) When varying the position of the object, the aluminium cylinder has a radius of 2 cm and a thickness of 2 cm. The distance is varied from 6.4 cm to 26.4 cm with respect to the position of the excitation coil. (b) when varying the diameter of the sample a thinner cylinder was used with a thickness of 4 mm. The diameter varied between 0.5 cm and 5 cm with the sample being placed 26.4 cm from the excitation coil.

of 31 % can be seen between the two data sets when taking into account the differing primary field. In [2] COMSOL simulated data using the model discussed in [1] and Appendix C.1 is plotted along with the experimental data. By scaling the fitted relation, which was found to be $B_{\text{ec}} = 4.5D^3$ by the 78% larger field it can be predicted from simulation that the induced magnetic field should be given by $B_{\text{ec}} = 8.01D^3$. This agrees with the experimental results presented in Figure 10.10b to within 2% and hence supports the experimental findings presented here. This shows the capabilities of the portable alignment based OPM using a buffer gas cell to perform as well as previous portable prototypes with the added benefit of a more compact setup as only a single laser is required.

10.8 High frequency performance

The future goal application of the portable OPM presented in this chapter is to image the heart using magnetic induction tomography (MIT) applications. As was outlined in Section 3.4.2, the heart has a low conductivity and hence from Equation 3.6 a higher frequency needs to be used to obtain detectable signals. Typically frequencies in the range of 1-3 MHz are used [30, 25]. Hence, here the sensitivity of the portable OPM is characterised at higher frequencies in the MHz range.

10.8.1 Shielded sensitivity

In order to characterise the intrinsic noise of the OPM at frequencies above 1 MHz, without external magnetic noise influences, the OPM was placed in a mu-metal shield. With the final design of the balanced photodetector (see Section 9.4.2) installed, the Larmor frequency was set to $\omega_L \approx 2\pi(1.495 \text{ MHz})$ by a static magnetic

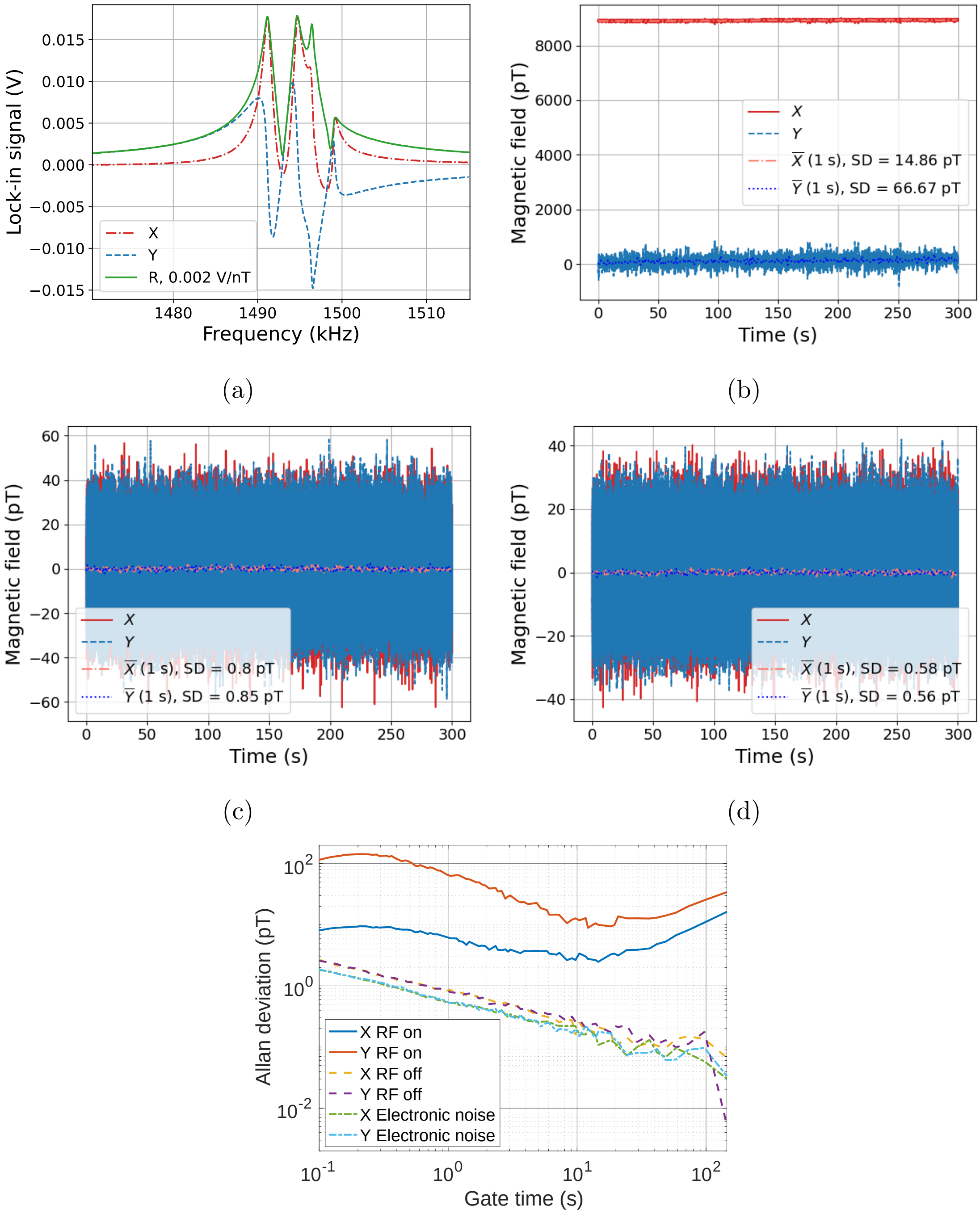

(a)

(b)

(c)

(d)

(e)

Figure 10.11: Sensitivity of the portable alignment based magnetometer at a Larmor frequency of approximately 1.5 MHz. The sensor head is placed inside a magnetic shield. The cell is heated to a temperature of ~ 50°C. (a) The magnetic resonance signal is plotted by sweeping the frequency of the RF magnetic field from 1.47 MHz to 1.515 MHz. Four minute time traces are then recorded with the frequency set to to the peak value in (a) at which $\omega_L \approx 2\pi(1.5\ \text{MHz})$ with (b) the RF field amplitude on, (c) the RF amplitude set at zero which represents the intrinsic noise of the optically pumped magnetometer and (d) the electronic noise of the setup. The standard deviation of one second averages are found and the (e) Allan deviation is also calculated for the time traces.

field of amplitude $B_0 = 427$ μT. An oscillating magnetic field is then applied with the frequency being swept form 1.47 MHz to 1.515 MHz and a fixed amplitude of $B_{\mathrm{rf}} = 8.916$ $\mathrm{nT_{rms}}$. The resulting magnetic resonance signal is shown in Figure 10.11a. The signal begins to split and two clear outer peaks can be seen. Due to the non-linear Zeeman separation not being much larger than the linewidth only the outer two peaks can be distinguished at 1.4912 MHz and 1.4947 MHz. It is noted that an additional peak at ~ 1.4964 MHz can be seen on the higher frequency peak and a second additional smaller peak at ~ 1.4992 MHz. These smaller resonances are due to the atoms trapped in the $F = 3$ hyperfine ground state. This can be shown from the ratio of the gyromagnetic ratios for the caesium ground states $\gamma_{\mathrm{F=3}}/\gamma_{\mathrm{F=4}} = -1.0032$ [68] and hence for a Larmor frequency of $\omega_L \approx 2\pi(1.495\ \mathrm{MHz})$ for the $F = 4$ state the $F = 3$ state should be shifted by ~ 5 kHz, which supports what is experimentally seen here.

To determine the noise performance of the OPM at the higher frequency, the RF magnetic field frequency is fixed to the first peak at $\omega_{rf} = \omega_L = 2\pi(1.4912\ \mathrm{MHz})$. A five minute time trace is then recorded with a sample rate of 7.196 kHz. The smallest detectable field with the RF magnetic field on is is 14.86 pT and 66.67 pT for the X and Y component, respectively. The Y component of the signal is much noisier due to the static field being noisy. This is due to the current source being noisier when supplying larger currents. The intrinsic sensitivity is then determined by setting the RF magnetic field amplitude to zero. Figure 10.11c shows the sensitivity to be 0.8 pT and 0.85 pT for the X and Y component respectively. This sensitivity is a factor of ~ 3.5 worse than at low frequencies (see Figure 10.7). There are a number of factors that contribute to the less sensitive result. The first reasoning comes from the fact that the sensitivity is a result of the signal to noise ratio. As the non-linear Zeeman splitting becomes dominant the signal amplitude begins to drop as the atoms are pumped into two dark states and, due to the use of a single laser, the optical pumping is not perfect. Another factor is from the increased sensitivity contribution from the electronic noise. In Figure 9.10a it can be seen that there is an increase in the noise floor of the balanced photodetector at and above 1 MHz. However, the electronic noise is not the dominant contributor to the overall sensitivity despite the noise significantly increasing compared to at low frequencies. A lower noise detector or use of a higher light power would help to overcome this issue. Further improvements in the sensitivity could also be seen by using a larger diameter laser light so that all atoms in the vapour cell are continuously probed. If the diameter of the light were increased from 2 mm to 5 mm the sensitivity would in theory improve by a factor of 40%. With this said, it is noted that from the simulations, a sensitivity of less than 1 pT should be sufficient for biomedical imaging of the heart.

10.9 Conclusion

Here, the development of a portable RF-OPM has been presented that operates with a single laser beam and a buffer gas cell. It operates with sub-pT/$\sqrt{\mathrm{Hz}}$ sensitivity for a Larmor frequency of 10 kHz in unshielded conditions. This performance is similar to that presented in Ref. [2] with the added benefit of only using one laser beam. The use of a buffer gas cell in this setup opens up the ability for the device to be commercialised as buffer gas cells are more readily available than anti-relaxation coated cells.

With the use of electromagnetic induction, the remote detection of electrically conductive objects was demonstrated. At a distance of 26.4 cm from the excitation coil and 23.9 cm from the sensing point of the magnetometer the smallest detectable object has a diameter of 1 cm. This detection range could be improved further by using a larger primary magnetic field or reducing the noise floor of the OPM in unshielded conditions.

The sensitivity of the magnetometer is tested at a higher Larmor frequency of ~ 1.5 MHz where, in shielded conditions, a sensitivity of 0.825 pT/$\sqrt{\text{Hz}}$ is obtained. This is sufficient for detection of low conductive object such as a human heart. This sensitivity could be further improved by increasing the beam diameter of the laser beam such that it probes the entire volume of the vapour cell. The next steps with the portable OPM is to test its sensitivity at high frequencies in unshielded conditions and demonstrate its capabilities to image low conductive phantoms.

Chapter 11

Conclusions

The results presented in this thesis have focused on the development of alignment based magnetometers and how eddy currents can be used to detect, image and characterise electrically conductive objects. Positive steps have been shown towards the miniaturisation of an alignment based magnetometer with the use of a buffer gas vapour cell.

As a point of reference, a commercially available magnetic field sensor is used to characterise the low frequency response of a non-magnetic (6061 T6 aluminium) and magnetic sample (440c steel). In Section 5, a fluxgate magnetometer is used to see how the induced eddy current signal varies with frequency between 10 Hz and 1 kHz. From this data, the electrical properties of the two samples are found. These values are then used to create COMSOL simulations to verify the experimental data. The signal response is also studied as the object's position is varied on- and off-axis. The on-axis data is also detected in Section 10 with the magnetic field sensor being replaced with a prototype portable optically pumped magnetometer.

The focus of this thesis is primarily on alignment based magnetometers. The theoretical model of an alignment based magnetometer is presented in Section 4. Typically, anti-relaxation coated vapour cells have been used to demonstrate the potential of alignment based magnetometry. The first, published, results of a buffer gas vapour cell being used in an alignment based magnetometer are presented in Section 6. A 65 Torr nitrogen buffer gas cell is placed in a table-top experimental setup. The results are then compared with a paraffin coated cell of similar dimensions. The alignment based magnetometer setup uses a single laser beam to pump and probe the atomic ensemble. The use of a single laser beam has the benefit of the OPM being able to be further miniaturised compared to setups reliant on two or three laser beams. For magnetic induction tomography where arrays of magnetometers may potentially be required the miniaturisation of the sensors is essential. The use of a buffer gas cell in place of the typical anti-relaxation coated cell is essential for commercialisation. Anti-relaxation coated cells are hand-blown and difficult to make, with few people able to produce them. However, buffer gas cells can be produced using micro-fabrication techniques and hence can be mass produced. Hence the work presented in this chapter shows positive steps towards the miniaturisation and commercialisation of an RF magnetometer.

The spin noise spectroscopy of an alignment based model is then investigated by introducing a stochastic magnetic field to the magnetometer along the light propagation axis. Previously, models have been developed to describe the spin noise dynamics of an orientation based OPM but a similar model for an alignment based magnetometer were missing. In Section 7, a model for the power spectral density of the magnetometer is predicted using methods of stochastic calculus and the formalism of spherical tensors. These predictions are then verified using the paraffin coated cell in the table-top setup presented in Section 6. This work paves the way for alignment based magnetometers to be used in real time sensing tasks. Using the characterisation of the spin noise spectroscopy, the time-varying signals can be tracked beyond the nominal bandwidth of the magnetometer.

Further characterisation of the magnetometer is carried out near zero magnetic field. By utilising the polarisation rotation signal a novel, modulation free method for nulling the magnetic field is presented. Near zero-field the magnetometer has a sensitivity of $\sim$ 300 fT/$\sqrt{\text{Hz}}$, which is sufficient for detecting a human heart beat. This is demonstrated using a synthetic cardiac signal.

In order to miniaturise the table-top alignment based magnetometer setup, a low noise and high bandwidth balanced photodetector needed to be designed with a footprint small enough to fit in the prototype sensor head. As the application goal of the portable OPM is to carry out magnetic induction tomography to map the conductivity of low conductive objects, a high bandwidth of a few MHz is required. The final balanced photodetector design is presented in Section 9 and is shot noise limited at $\sim$ 4 μW for frequencies below 1 MHz increasing to $\sim$ 21 μW around 1 MHz. The presented bandwidth is also sufficient for MIT measurements.

The buffer gas cell, which was characterised in Section 6, was then used in a prototype portable magnetometer which was designed to miniaturise the experimental setup. Section 10 shows the portable OPM setup, with a sub-pT/$\sqrt{\text{Hz}}$ sensitivity which was obtained in unshielded conditions at a Larmor frequency of $\omega_L \approx 2\pi(10 \text{ kHz})$. The shielded sensitivity was characterised at a relatively low RF frequency of $\omega_L \approx 2\pi(10 \text{ kHz})$ and a higher frequency of $\omega_L \approx 2\pi(1.5 \text{ MHz})$ with 230 fT/$\sqrt{\text{Hz}}$ and 825 fT/$\sqrt{\text{Hz}}$, respectively. The magnetometer is less sensitive at higher frequencies due to the optical pumping in a buffer gas vapour cell not being as efficient. The sensitivities could further be improved by increasing the laser beam diameter such that it probes the entire volume of the vapour cell. The potential of the OPM to be used for eddy current measurements is then demonstrated by detecting cylindrical aluminium samples. A 1.5 cm diameter sample was detected with a good signal to noise ratio at a distance of approximately 25 cm from the excitation coil and sensing point of the OPM. This shows that the portable OPM presented in this thesis performs as well as the initial OPM prototype developed by the group in Nottingham which was an orientation based magnetometer and is presented in Ref. [2]. Hence the simplified model, with a buffer gas vapour cell, shows good potential despite the design utilising a single laser beam configuration.

Future steps with the portable OPM are to image low conductive objects at high frequencies by magnetic induction tomography. This is part of an ongoing collaborative project with The Neils Bohr Institute and The University of Copenhagen, with the end goal being to image heart tissue using a portable magnetometer in unshielded conditions. This requires further characterisation of the OPM in unshielded conditions at high frequencies, with promising results already being seen with the portable alignment based magnetometer presented in this thesis. The long-term outlook of this setup would be the commercialisation of the portable OPM. The use of a buffer gas vapour cell in the prototype is a promising steps towards this goal.

Appendix A

Optically pumping rate equations

$$\frac{dp_{4,-4}}{dt} = R_p[p_{4,-3}\langle 4,1,-3,0|3',-3'\rangle^2] - \Gamma_1 p_{4,-4} + \frac{\Gamma_1}{16} \tag{A.1}$$

$$\begin{aligned}\frac{dp_{4,-3}}{dt} =& R_p[p_{4,-2}\langle 4,1,-2,0|3,-2'\rangle^2 + p_{4,-3}\langle 4,1,-3,0|3,-3'\rangle^2] \\ &- \Gamma_1 p_{4,-3} + \frac{\Gamma_1}{16} - R_p p_{4,-3}\langle 4,1,-3,0|3,-3'\rangle\end{aligned} \tag{A.2}$$

$$\begin{aligned}\frac{dp_{4,-2}}{dt} =& R_p[p_{4,-1}\langle 4,1,-1,0|3,-1'\rangle^2 + p_{4,-2}\langle 4,1,-2,0|3,-2'\rangle^2 \\ &+ p_{4,-3}\langle 4,1,-3,0|3,-3'\rangle^2] - \Gamma_1 p_{4,-2} + \frac{\Gamma_1}{16} - R_p p_{4,-2}\langle 4,1,-2,0|3,-2'\rangle\end{aligned} \tag{A.3}$$

$$\begin{aligned}\frac{dp_{4,-1}}{dt} =& R_p[p_{4,0}\langle 4,1,0,0|3,0'\rangle^2 + p_{4,-1}\langle 4,1,-1,0|3,-1'\rangle^2 \\ &+ p_{4,-2}\langle 4,1,-2,0|3,-2'\rangle^2] - \Gamma_1 p_{4,-1} + \frac{\Gamma_1}{16} - R_p p_{4,-1}\langle 4,1,-1,0|3,-1'\rangle\end{aligned} \tag{A.4}$$

$$\begin{aligned}\frac{dp_{4,0}}{dt} =& R_p[p_{4,1}\langle 4,1,1,0|3,1'\rangle^2 + p_{4,0}\langle 4,1,0,0|3,0'\rangle^2 \\ &+ p_{4,-1}\langle 4,1,-1,0|3,-1'\rangle^2] - \Gamma_1 p_{4,0} + \frac{\Gamma_1}{16} - R_p p_{4,0}\langle 4,1,0,0|3,0'\rangle\end{aligned} \tag{A.5}$$

$$\begin{aligned}\frac{dp_{4,1}}{dt} =& R_p[p_{4,0}\langle 4,1,0,0|3,0'\rangle^2 + p_{4,1}\langle 4,1,1,0|3,1'\rangle^2 \\ &+ p_{4,2}\langle 4,1,2,0|3,2'\rangle^2] - \Gamma_1 p_{4,1} + \frac{\Gamma_1}{16} - R_p p_{4,1}\langle 4,1,1,0|3,1'\rangle\end{aligned} \tag{A.6}$$

$$\begin{aligned}\frac{dp_{4,2}}{dt} =& R_p[p_{4,1}\langle 4,1,1,0|3,1'\rangle^2 + p_{4,2}\langle 4,1,2,0|3,2'\rangle^2 \\ &+ p_{4,3}\langle 4,1,3,0|3,3'\rangle^2] - \Gamma_1 p_{4,2} + \frac{\Gamma_1}{16} - R_p p_{4,2}\langle 4,1,2,0|3,2'\rangle\end{aligned} \tag{A.7}$$

$$\frac{dp_{4,3}}{dt} = R_p [p_{4,2} \langle 4,1,2,0|3,2'\rangle^2 + p_{4,3} \langle 4,1,3,0|3,3'\rangle^2] - \Gamma_1 p_{4,3} + \frac{\Gamma_1}{16} - R_p p_{4,3} \langle 4,1,3,0|3,3'\rangle \tag{A.8}$$

$$\frac{dp_{4,4}}{dt} = R_p [p_{4,3} \langle 4,1,3,0|3',3'\rangle^2] - \Gamma_1 p_{4,4} + \frac{\Gamma_1}{16} \tag{A.9}$$

$$\frac{dp_{3,-3}}{dt} = R_p [p_{4,-2} \langle 4,1,-2,0|3,-2'\rangle^2 + p_{4,-3} \langle 4,1,-3,0|3,-3'\rangle^2] - \Gamma_1 p_{3,-3} + \frac{\Gamma_1}{16} \tag{A.10}$$

$$\frac{dp_{3,-2}}{dt} = R_p [p_{4,-1} \langle 4,1,-1,0|3,-1'\rangle^2 + p_{4,-2} \langle 4,1,-2,0|3,-2'\rangle^2 + p_{4,-3} \langle 4,1,-3,0|3,-3'\rangle^2] - \Gamma_1 p_{3,-2} + \frac{\Gamma_1}{16} \tag{A.11}$$

$$\frac{dp_{3,-1}}{dt} = R_p [p_{4,0} \langle 4,1,0,0|3,0'\rangle^2 + p_{4,-1} \langle 4,1,-1,0|3,-1'\rangle^2 + p_{4,-2} \langle 4,1,-2,0|3,-2'\rangle^2] - \Gamma_1 p_{3,-1} + \frac{\Gamma_1}{16} \tag{A.12}$$

$$\frac{dp_{3,0}}{dt} = R_p [p_{4,1} \langle 4,1,1,0|3,1'\rangle^2 + p_{4,0} \langle 4,1,0,0|3,0'\rangle^2 + p_{4,-1} \langle 4,1,-1,0|3,-1'\rangle^2] - \Gamma_1 p_{3,0} + \frac{\Gamma_1}{16} \tag{A.13}$$

$$\frac{dp_{3,1}}{dt} = R_p [p_{4,0} \langle 4,1,0,0|3,0'\rangle^2 + p_{4,1} \langle 4,1,1,0|3,1'\rangle^2 + p_{4,2} \langle 4,1,2,0|3,2'\rangle^2] - \Gamma_1 p_{3,1} + \frac{\Gamma_1}{16} \tag{A.14}$$

$$\frac{dp_{3,2}}{dt} = R_p [p_{4,1} \langle 4,1,1,0|3,1'\rangle^2 + p_{4,2} \langle 4,1,2,0|3,2'\rangle^2 + p_{4,3} \langle 4,1,3,0|3,3'\rangle^2] - \Gamma_1 p_{3,2} + \frac{\Gamma_1}{16} \tag{A.15}$$

$$\frac{dp_{3,3}}{dt} = R_p [p_{4,2} \langle 4,1,2,0|3,2'\rangle^2 + p_{4,3} \langle 4,1,3,0|3,3'\rangle^2] - \Gamma_1 p_{3,3} + \frac{\Gamma_1}{16} \tag{A.16}$$

Appendix B

Eddy current detection using a fluxgate magnetometer

B.1 Allan deviation of the out-of-phase component

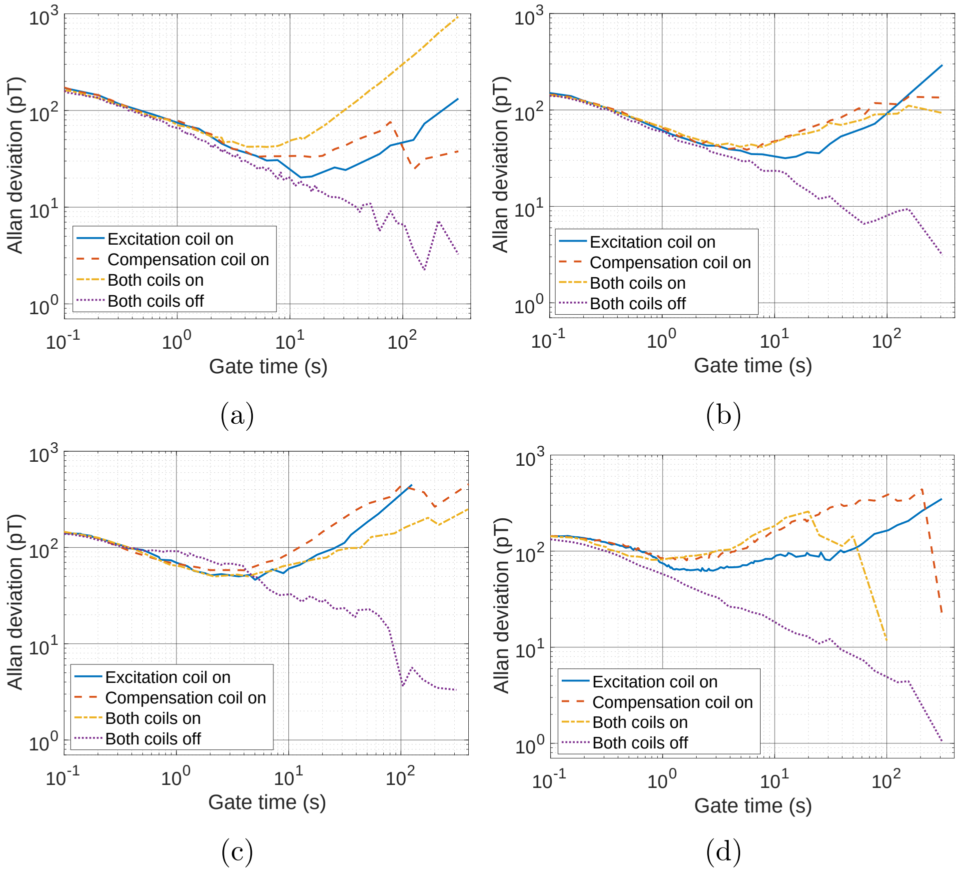

(a) (b)

(c) (d)

Figure B.1: Allan Deviation of the out-of-phase response of the fluxgate at (a) 10 Hz, (b) 120 Hz, (c) 500 Hz and (d) 1000 Hz

The stability of the out-of-phase signal is shown in Figure B.1. It can be seen that the stability and sensitivity of the signal is similar to the in-phase component (see

Figure 5.3). When both coils are on the smallest detectable field are 42 pT at 10 Hz, 42 pT at 120 Hz, 50 pT at 500 Hz and 81 pT at 1 kHz. This is in good agreement with the smallest detectable fields for the in-phase component.

Appendix C

COMSOL simulations

C.1 Fluxgate measurements

The results of the eddy current simulations, presented in Section 5, were performed using the AC/DC module in COMSOL Multiphysics 5.6. The ‘Magnetic Fields’ interface was used to compute the magnetic field and induced current distributions in and around the coils and electrically conductive samples. The default COMSOL settings were used for this interface. In order to replicate the setup, a 3D model was created (Figure C.1). The model consisted of a coil placed above a conductive object. To reduce complexity, an imaginary single-turn coil was chosen to generate the primary magnetic field. The coil and the object were then placed in the finite sphere air domain, the size of which was ten times bigger than the size of the object. The infinite element domain is included in the model (see Figure C.1). Its size is one-tenth of the overall dimensions of the model. The infinite domain ensures that the governing equations behave similarly to nature and no reflecting boundary conditions appear in the system. The finite element mesh was used to subdivide the CAD model into smaller domains, where a set of equations can be solved. As these elements are made with a refined mesh, the solution approaches the true solution. Figure C.1b shows that the finite element mesh consists of three-dimensional tetrahedral solid elements and five layers of infinite element meshes, which have been added to the spherical domain. All of the simulations were performed using a 3.60 GHz Intel(R) Xeon processor with 128 GB RAM.

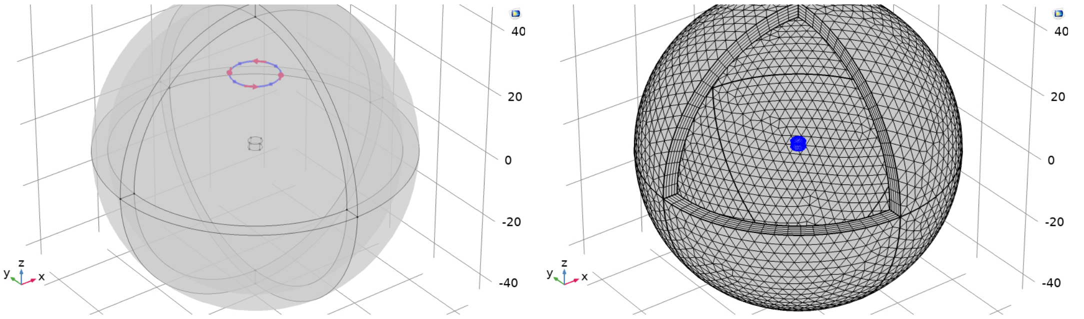

(a) (b)

Figure C.1: The 3D finite element model designed in COMSOL, showing (a) an object at the origin, the primary coil, and the boundary layer; and (b) the free tetrahedral elements for the object and for the finite domain.

In all simulations presented in Section 5, the domain was meshed with free tetrahedral elements consisting of 188,265 domain elements. Subsequent mesh refinements were performed until negligible changes occurred in the simulated curves. Figure C.2 shows the simulated magnetic field ratio ($|\mathbf{B}_{ec}|/|\mathbf{B}_1|$) for the solid aluminium cylinders with different mesh sizes for domain elements. In this figure normal = 11,394 domain elements, fine = 21,634 domain elements, finer = 55,144 domain elements and extra-fine = 188,265 domain elements. This is compared to the experimental data obtained in Section 5.5 with the results presented in Figure C.2. It can be seen that finer meshes result in the COMSOL simulation converging more closely to the experimentally obtained data.

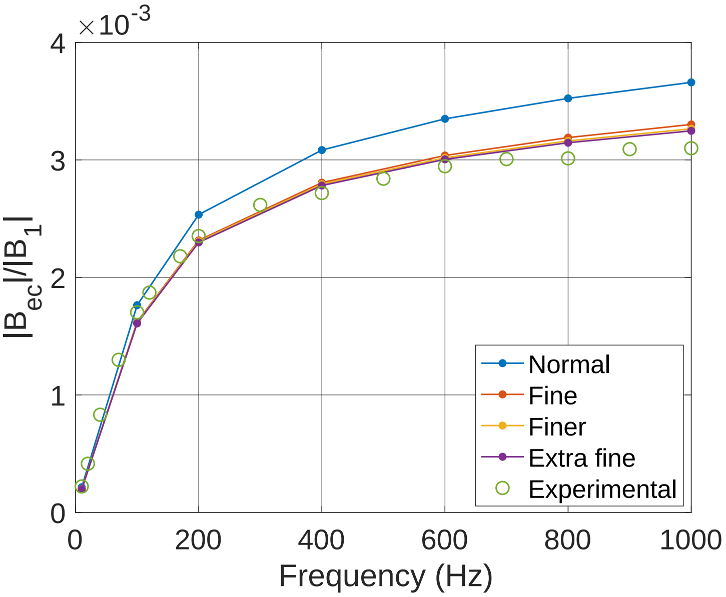

Figure C.2: Investigation of the optimal mesh type to employ. The experimental and simulated magnetic field ratio ($|\mathbf{B}_{ec}|/|\mathbf{B}_1|$) for solid aluminium cylinders were compared with different mesh sizes: normal = 11,394; fine = 21,634; finer = 55,144; extra-fine = 188,265.

For each data set, the simulation was run twice. The first run had the object present with the properties matching those used experimentally. The second run was done without the object present. Instead of removing the object from the simulation, its properties were changed to match that of the host medium (air). When using this technique, the mesh was preserved in both cases, eliminating any errors arising from the influence of the mesh on the results. The difference between these two simulation outputs is the secondary magnetic field that is induced in the object.

Figure C.3 shows the directions of the primary and secondary magnetic fields when the conductive object is placed on- and off-axis, respectively. With the object placed on-axis, the primary and secondary magnetic fields only have a z-component at the sensing point of the magnetometer. When the object is placed off-axis (in the y-z-plane), the secondary magnetic field generally has components in both the y- and z-direction. In Section 5, the z-component of the magnetic field is experimentally measured and compared to the simulation results.

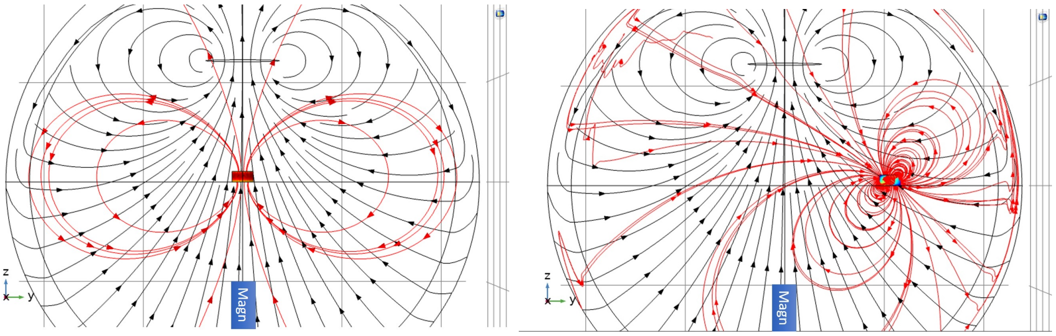

(a) (b)

Figure C.3: Simulation model results when a solid metallic cylinder is placed (a) on-axis and (b) off-axis. The magnetic moment of the primary coil (black line) is aligned along the z-axis, and stream plots of the magnetic filed lines (black lines with arrows) produced by the primary coil are shown. The induced secondary magnetic field $\mathbf{B}_{\text{ec}}(t)$ generated by eddy currents in the object are represented by the red lines with arrows on.

C.2 Imaging low conductivity samples

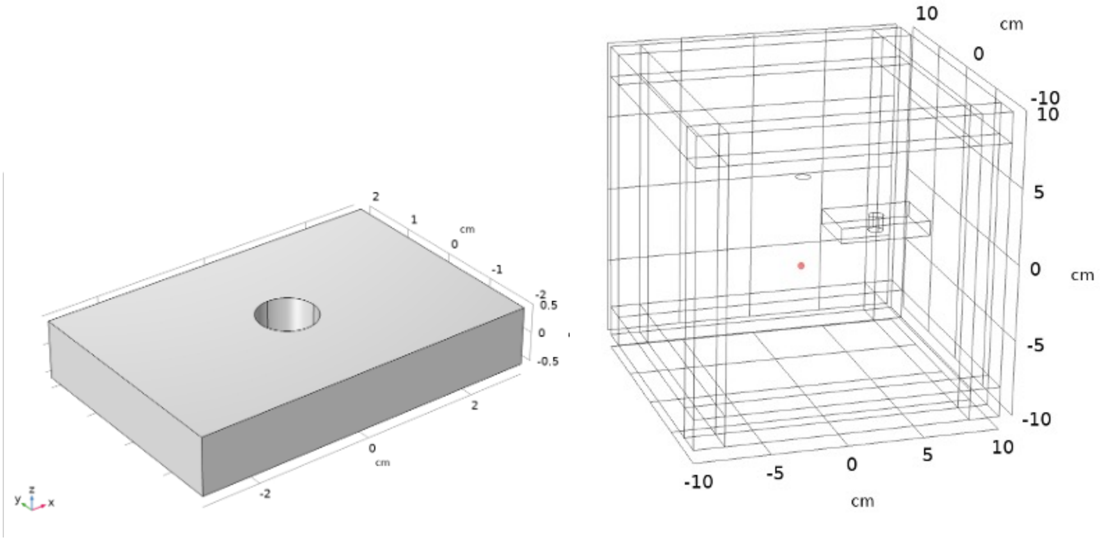

(a) (b)

Figure C.4: Simulation model design for a (a) sample of dimensions 6 cm×4 cm×1 cm with a defect at the centre with a radius of 5 mm. (b) The COMSOL model with the sample off-axis.

A similar model to that described above is employed to model the expected signal from a sample with similar electromagnetic properties to a human heart. The mesh type used is 'normal' for the data presented using this simulation model. For simplicity, the sample is given a simple rectangular prism geometry with dimensions 6 cm × 4 cm × 1 cm with a defect at the centre with a radius of 5 mm, as shown in Figure C.4a. The sample has a conductivity of 0.5 S/m and the relative permittivity was set to 1. For the defect the conductivity was set to 0 S/m, to replicate air. A coil with a radius of 5 mm was placed 3 cm from the centre of the object and the detection point of the induced magnetic fields was placed 5 cm from the centre of the sample. The coil and sensing point are on opposite sides of the sample. There are two ways that a 2D image of an object can be obtained: the first option is to keep the object at a fixed position and move the magnetic field sensing point and coil simultaneously. The other option is to move the object whilst keeping the position of the coil and sensing point fixed. The latter was chosen as in an experimental setup with an OPM moving the sensor can introduce changes in the background magnetic field. OPMs are extremely sensitive to variations in the background field, so changing the sensor's position would alter the residual fields within the experimental setup. This would result in significant noise and calibration issues. By keeping the sensor and coil stationary and moving only the sample, one preserves a stable measurement environment, ensuring reliable and repeatable data. The experimental setup in COMSOL is shown in Figure C.4b. How eddy currents are induced in the sample when the coil is at the centre of the object, over the defect, is shown in Figure C.5a. For the sample in the same position, the directions of the primary and secondary magnetic fields are shown in Figure C.5b.

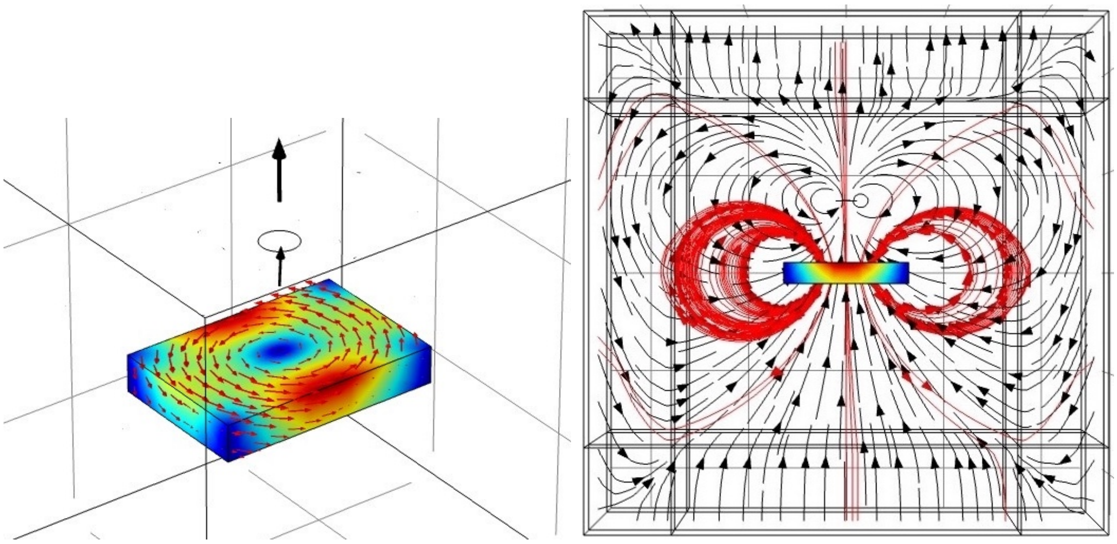

(a) (b)

Figure C.5: The (a) eddy current flow in the sample (b) the corresponding magnetic field lines produced around the sample. The magnetic moment of the primary coil (black line) is aligned along the z-axis, and stream plots of the magnetic filed lines (black lines with arrows) produced by the primary coil are shown. The induced secondary magnetic field $\mathbf{B}_{\mathrm{ec}}(t)$ generated by eddy currents in the object are represented by the red lines with arrows on.

Appendix D

Zero-field magnetometer

D.1 Near zero-field fit parameters for nulling the magnetic field

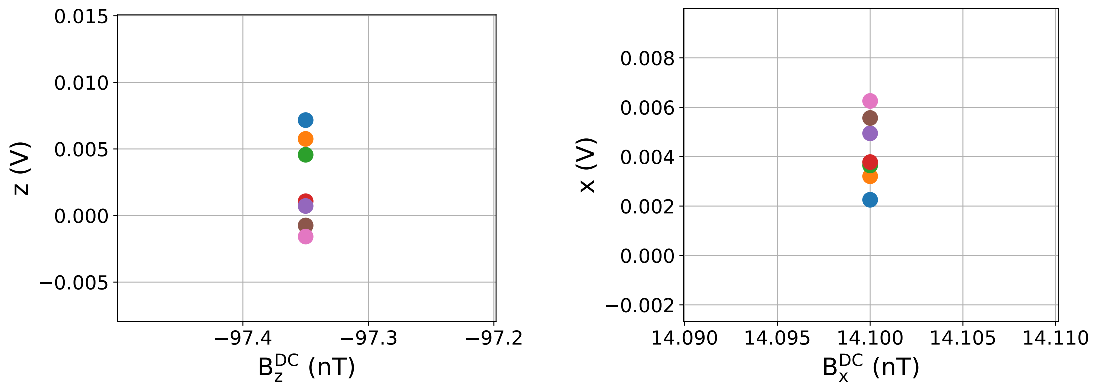

(a)

(b)

Figure D.1: Sweeping a magnetic field applied along the y-direction near zero-field condition. The fit parameters for the (a) z values when varying the value of x and (b) the x values when varying the value of z from the fits in Figure 8.2b and 8.2d, respectively.

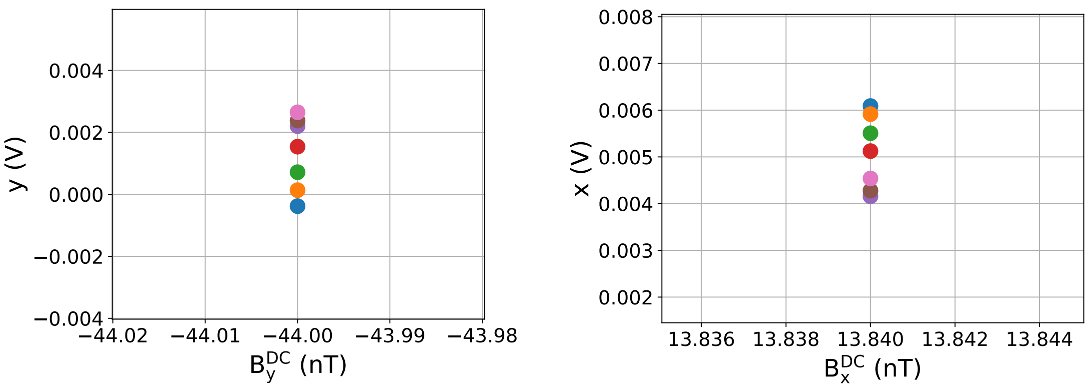

(a) (b)

Figure D.2: Sweeping a magnetic field applied along the z-direction near zero-field condition. The fit parameters for the (a) y values when varying the value of x and (b) the x values when varying the value of y from the fits in Figure 8.3b and 8.3d, respectively.

D.2 Sweeping the magnetic field over a large range

Alongside looking at how the polarisation rotation signal changes with small changes in the overall magnetic field in the magnetic shield, a range that is larger than the linewidth of the magnetometer was also studied. The field was varied such that the overall field in each direction was −40 nT to +40 nT. The results were then fitted to Equation 8.2. The fitting procedure here is different as the fit parameters for the linewidth and offset are shared between all 25 data sets. Such that when the sweeping magnetic field is in the y-direction only x and z are fitted individually for each data set. Similarly, when sweeping the z-direction field only the x and y parameters are not shared between the data sets. Figure D.3 shows the results for sweeping the $\hat{\mathbf{y}}$ component of them magnetic field. It can be seen that when fitting to the full equation a linear relationship is still obtained. Figure D.4 shows a similar relationship for when the $\hat{\mathbf{z}}$ component of the field is swept. Hence showing that the theory is not limited to the residual field being very close to zero.

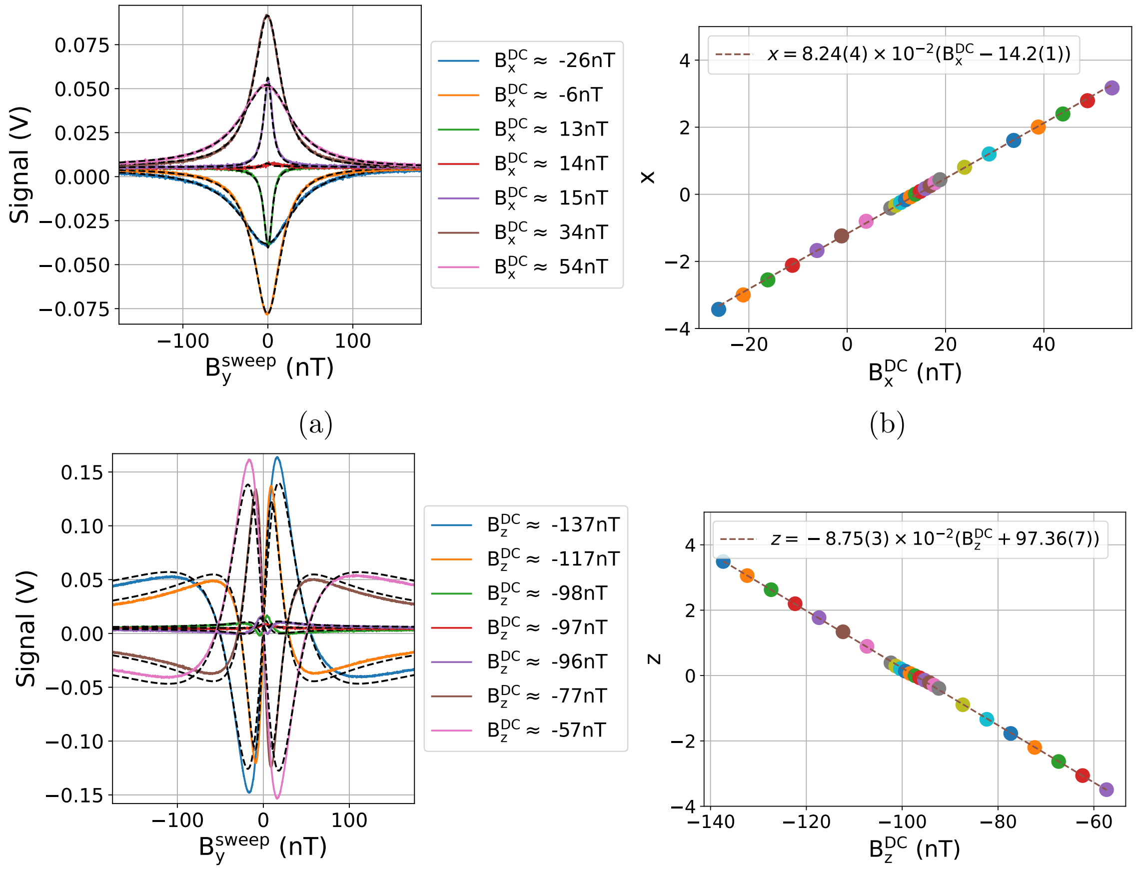

(a) (b)

(c) (d)

Figure D.3: Sweeping a magnetic field applied along the y-direction near zero-field condition. Solid lines are experimental data, and dashed lines are fits to Equation 8.2. (a) and (b) show signals for various settings of an magnetic field applied along the x- and z- directions, respectively. (c) and (d) show the corresponding fit parameters $x \propto B_x$ and $z \propto B_z$ which are proportional to different components of the net magnetic field. The DC fields are $B_y^{\mathrm{DC}} = -44.00(1)$ nT, $B_z^{\mathrm{DC}} = -97.35(1)$ nT in (a) and $B_x^{\mathrm{DC}} = 13.86(1)$ nT in (b). The parameter Γ/γ was a global fit parameter for all the resonances in (a) and was found to be 11.66(±0.03) nT. Similarly, $\Gamma/\gamma = 10.55(\pm 0.03)$ nT was found for the resonances in (b).

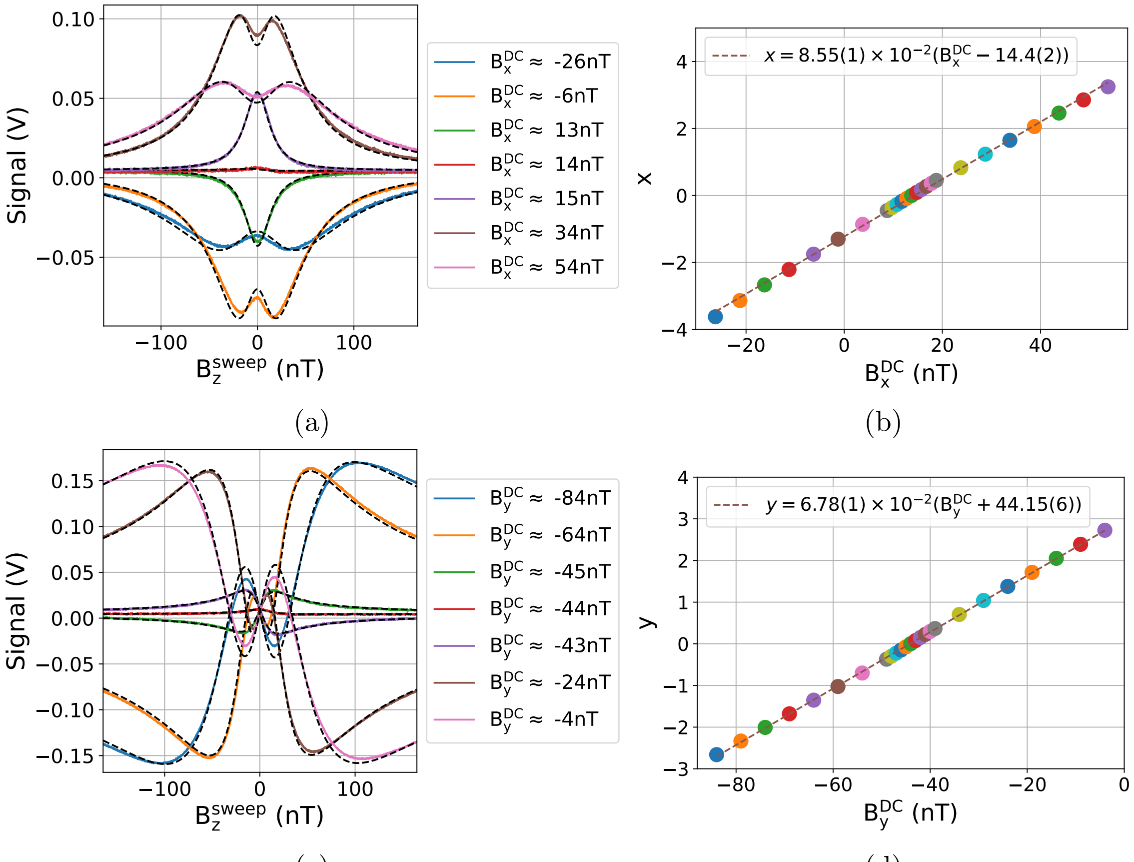

(a) (b)

(c) (d)

Figure D.4: Sweeping a magnetic field applied along the z-direction near zero-field condition. Solid lines are experimental data, and dashed lines are fits to Equation 8.2. (a) and (b) show signals for various settings of an magnetic field applied along the x- and y- directions, respectively. (c) and (d) show the corresponding fit parameters $x \propto \boldsymbol{B}_x$ and $y \propto \boldsymbol{B}_y$ which are proportional to different components of the net magnetic field. The DC fields are $\boldsymbol{B}_z^{\mathrm{DC}} = -97.35(1)$ nT, $\boldsymbol{B}_y^{\mathrm{DC}} = -44.00(1)$ nT in (a) and $\boldsymbol{B}_x^{\mathrm{DC}} = 13.76(1)$ nT in (b). The parameter Γ/γ was a global fit parameter for all the resonances in (a) and was found to be 15.88(±0.03) nT. Similarly, $\Gamma/\gamma = 17.50(\pm 0.03)$ nT was found for the resonances in (b).

D.3 Reduced sensor response sensitivity

Figure. D.5 shows a scaled version of the power spectral density (Figure 8.6). Here the data has been scaled to take into account the drop off in the magnetometer's response at higher frequencies. The noise floor shows a sensitivity of ≈ 2 pT/$\sqrt{\text{Hz}}$ at 1 Hz. The sensitivity improves to ≈ 0.3 pT/$\sqrt{\text{Hz}}$ between 10 Hz and 100 Hz before deteriorating as the magnetometers response starts to reduce.

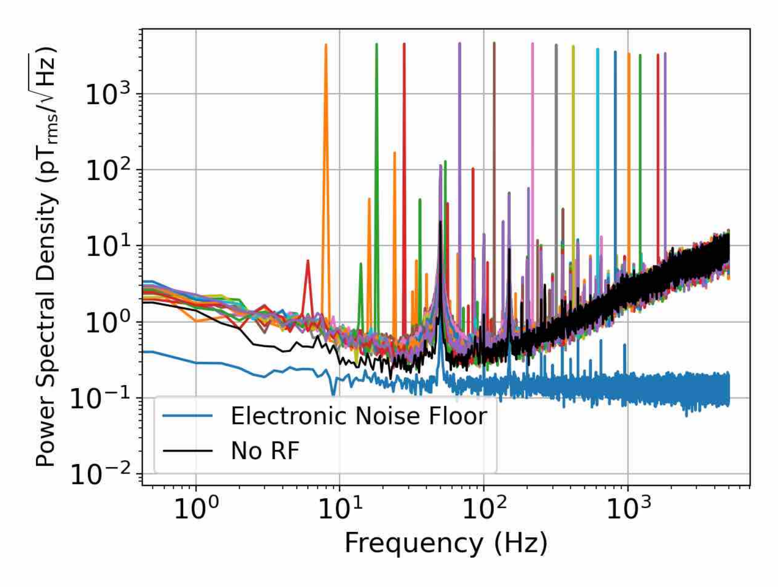

Figure D.5: Performance of the OPM at zero-field scaled to the reduced sensor response as the frequency increases.

Bibliography

[1] L. Elson, A. Meraki, L. M. Rushton, T. Pyragius, and K. Jensen. Detection and characterisation of conductive objects using electromagnetic induction and a fluxgate magnetometer. Sensors, 22(16):5934, 2022.

[2] L. M. Rushton, T. Pyragius, A. Meraki, L. Elson, and K. Jensen. Unshielded portable optically pumped magnetometer for the remote detection of conductive objects using eddy current measurements. Review of Scientific Instruments, 93(12), 2022.

[3] L. M. Rushton, L. Elson, A. Meraki, and K. Jensen. Alignment-based optically pumped magnetometer using a buffer-gas cell. Physical Review Applied, 19(6):064047, 2023.

[4] A. Meraki, L. Elson, N. Ho, A. Akbar, M. Koźbiał, J. Kołodyński, and K. Jensen. Zero-field optical magnetometer based on spin alignment. Physical Review A, 108(6):062610, 2023.

[5] M. Kozbial, L. Elson, L. M. Rushton, A. Akbar, A. Meraki, K. Jensen, and J. Kolodynski. Spin noise spectroscopy of an alignment-based atomic magnetometer. Physical Review A, 110(1):013125, 2024.

[6] A. Akbar, M. Koźbiał, L. Elson, A. Meraki, J. Kołodyński, and K. Jensen. Optimized detection modality for radio-frequency sensing with a double-resonance alignment magnetometer. Physical Review Applied, 22(5):054033, 2024.

[7] C. F. Gauss. The intensity of the earth's magnetic force reduced to absolute measurement. Royal Scientific Society, 8(3), 1832.

[8] N. Goel, A. Babuta, A. Kumar, and S. Ganguli. Hall effect instruments, evolution, implications, and future prospects. Review of Scientific Instruments, 91(7), 2020.

[9] F. Primdahl. The fluxgate magnetometer. Journal of Physics E: Scientific Instruments, 12(4):241, 1979.

[10] S. Wei, X. Liao, H. Zhang, J. Pang, and Y. Zhou. Recent progress of fluxgate magnetic sensors: Basic research and application. Sensors, 21(4):1500, 2021.

[11] S. Tumanski. Induction coil sensors—a review. Measurement Science and Technology, 18(3):31, 2007.

[12] A. Jander, C. Smith, and R. Schneider. Magnetoresistive sensors for nondestructive evaluation. Advanced Sensor Technologies for Nondestructive Evaluation and Structural Health Monitoring, 5770:1–13, 2005.

[13] J. S. Bennett, B. E. Vyhnalek, H. Greenall, E. M. Bridge, F. Gotardo, S. Forstner, G. I. Harris, F. A. Miranda, and W. P. Bowen. Precision magnetometers for aerospace applications: A review. Sensors, 21(16):5568, 2021.

[14] R. L. Fagaly. Superconducting quantum interference device instruments and applications. Rev. Sci. Instrum., 77(10):101101, 2006.

[15] D. Budker and M. Romalis. Optical magnetometry. Nature physics, 3(4):227–234, 2007.

[16] M. Auzinsh, D. Budker, and S. Rochester. Optically polarized atoms: understanding light-atom interactions. Oxford University Press, 2014.

[17] D. F. J. Kimball, E. B. Alexandrov, and D. Budker. General principles and characteristics of optical magnetometers, volume 3. Cambridge University Press: Cambridge, 2013.

[18] F. Beato, E. Belorizky, E. Labyt, M. Le Prado, and A. Palacios-Laloy. Theory of a ^{4}He parametric-resonance magnetometer based on atomic alignment. Phys. Rev. A, 98(5):053431, Nov 2018.

[19] E. Labyt, T. Sander, and R. Wakai. Flexible High Performance Magnetic Field Sensors: On-Scalp Magnetoencephalography and Other Applications. Springer Nature, 2022.

[20] I. K. Kominis, T. W. Kornack, J. C. Allred, and M. V. Romalis. A subfemtotesla multichannel atomic magnetometer. Nature, 422(6932):596–599, 2003.

[21] I. M. Savukov, S. J. Seltzer, M. V. Romalis, and K. L. Sauer. Tunable atomic magnetometer for detection of radio-frequency magnetic fields. Physical review letters, 95(6):063004, 2005.

[22] E. Boto, N. Holmes, J. Leggett, G. Roberts, V. Shah, S. S. Meyer, L. D. Muñoz, K. J. Mullinger, T. M. Tierney, S. Bestmann, G. R. Barnes, R. Bowtell, and M. J. Brookes. Moving magnetoencephalography towards real-world applications with a wearable system. Nature, 555:657–661, 2018.

[23] D. A. Keder, D. W. Prescott, A. W. Conovaloff, and K. L. Sauer. An unshielded radio-frequency atomic magnetometer with sub-femtotesla sensitivity. AIP Adv., 4(12):127159, 2014.

[24] W. Chalupczak, R. M. Godun, S. Pustelny, and W. Gawlik. Room temperature femtotesla radio-frequency atomic magnetometer. Applied Physics Letters, 100(24), 2012.

[25] C. Deans, L. Marmugi, and F. Renzoni. Sub-sm–1 electromagnetic induction imaging with an unshielded atomic magnetometer. Applied Physics Letters, 116(13), 2020.

[26] W. E. Bell and A. L. Bloom. Optical detection of magnetic resonance in alkali metal vapor. Physical Review, 107(6):1559, 1957.

[27] M. V. Romalis and H. B. Dang. Atomic magnetometers for materials characterization. Materials today, 14(6):258–262, 2011.

[28] P. Bevington, R. Gartman, and W. Chalupczak. Enhanced material defect imaging with a radio-frequency atomic magnetometer. Journal of Applied Physics, 125(9), 2019.

[29] C. Deans, Y. Cohen, H. Yao, B. Maddox, A. Vigilante, and F. Renzoni. Electromagnetic induction imaging with a scanning radio frequency atomic magnetometer. Applied Physics Letters, 119(1), 2021.

[30] K. Jensen, M. Zugenmaier, J. Arnbak, H. Stærkind, M. V. Balabas, and E. S. Polzik. Detection of low-conductivity objects using eddy current measurements with an optical magnetometer. Phys. Rev. Research, 1:033087, 2019.

[31] C. Deans, L. Marmugi, and F. Renzoni. Sub-picotesla widely tunable atomic magnetometer operating at room-temperature in unshielded environments. Review of Scientific Instruments, 89(8), 2018.

[32] J. W. Blanchard, B. Ripka, B. A. Suslick, D. Gelevski, T. Wu, K. Münnemann, D. A. Barskiy, and D. Budker. Towards large-scale steady-state enhanced nuclear magnetization with in situ detection. Magnetic Resonance in Chemistry, 59(12):1208–1215, 2021.

[33] J. H. Simpson, J. T. Fraser, and I. A. Greenwood. An optically pumped nuclear magnetic resonance gyroscope. IEEE Transactions on Aerospace, 1(2):1107–1110, 1963.

[34] T. M. Tierney, N. Holmes, S. Mellor, J. D. López, G. Roberts, R. M. Hill, E. Boto, J. Leggett, V. Shah, M. J. Brookes, et al. Optically pumped magnetometers: From quantum origins to multi-channel magnetoencephalography. NeuroImage, 199:598–608, 2019.

[35] M. J. Brookes, J. Leggett, M. Rea, R. M. Hill, N. Holmes, E. Boto, and R. Bowtell. Magnetoencephalography with optically pumped magnetometers (opm-meg): the next generation of functional neuroimaging. Trends in Neurosciences, 2022.

[36] H. Xia, A. Ben-Amar Baranga, D. Hoffman, and M. V. Romalis. Magnetoencephalography with an atomic magnetometer. Applied Physics Letters, 89(21):211104, 2006.

[37] K. Jensen, M. A. Skarsfeldt, H. Stærkind, J. Arnbak, M. V. Balabas, S. Olesen, B. H. Bentzen, and E. S. Polzik. Magnetocardiography on an isolated animal heart with a room-temperature optically pumped magnetometer. Scientific reports, 8(1):16218, 2018.

[38] R. Wyllie, M. Kauer, R. T. Wakai, and T. G. Walker. Optical magnetometer array for fetal magnetocardiography. Optics Letters, 37(12):2247–2249, 2012.

[39] W. Happer. Optical pumping. Reviews of modern physics, 44(2):169, 1972.

[40] QuSpin. `https://quspin.com`, (December 2024).

[41] Twinleaf. `https://twinleaf.com`, (December 2024).

[42] Fieldline Inc. `https://fieldlineinc.com`, (December 2024).

[43] M. P. Ledbetter, I. M. Savukov, V. M. Acosta, D. Budker, and M. V. Romalis. Spin-exchange-relaxation-free magnetometry with cs vapor. Physical Review A—Atomic, Molecular, and Optical Physics, 77(3):033408, 2008.

[44] V. Shah and M. V. Romalis. Spin-exchange relaxation-free magnetometry using elliptically polarized light. Physical Review A—Atomic, Molecular, and Optical Physics, 80(1):013416, 2009.

[45] V. K. Shah and R. T. Wakai. A compact, high performance atomic magnetometer for biomedical applications. Physics in Medicine & Biology, 58(22):8153, 2013.

[46] J. C. Allred, R. N. Lyman, T. W. Kornack, and M. V. Romalis. High-sensitivity atomic magnetometer unaffected by spin-exchange relaxation. Physical review letters, 89(13):130801, 2002.

[47] MAG4Health. `https://www.mag4health.com`, (December 2024).

[48] Lucas Martin Rushton. Radio-frequency optically pumped magnetometers for eddy current measurements. PhD thesis, University of Nottingham, 2023.

[49] J. E. Dhombridge, N. R. Claussen, J. Iivanainen, and P. D. D. Schwindt. High-sensitivity rf detection using an optically pumped comagnetometer based on natural-abundance rubidium with active ambient-field cancellation. Physical Review Applied, 18(4):044052, 2022.

[50] W. Wasilewski, K. Jensen, H. Krauter, J. J. Renema, M. V. Balabas, and E. S. Polzik. Quantum noise limited and entanglement-assisted magnetometry. Physical Review Letters, 104(13):133601, 2010.

[51] M. P. Ledbetter, V. M. Acosta, S. M. Rochester, D. Budker, S. Pustelny, and V. V. Yashchuk. Detection of radio-frequency magnetic fields using nonlinear magneto-optical rotation. Physical Review A, 75:023405, 2007.

[52] A. M. Lewis. Electromagnetic methods for nde of metal fatigue cracks: Practical techniques and theoretical models. Nondestructive Testing and Evaluation, 6(6):389–409, 1992.

[53] J. García-Martín, J. Gómez-Gil, and E. Vázquez-Sánchez. Non-destructive techniques based on eddy current testing. Sensors, 11(3):2525–2565, 2011.

[54] Y. Du, Z. Zhang, W. Yin, S. Zhu, Z. Chen, and H. Xu. Conductivity classification of non-magnetic tilting metals by eddy current sensors. Sensors, 20(9):2608, 2020.

[55] A. N. AbdAlla, M. A. Faraj, F. Samsuri, D. Rifai, K. Ali, and Y. Al-Douri. Challenges in improving the performance of eddy current testing. Measurement and Control, 52(1-2):46–64, 2019.

[56] H. Griffiths, W. R. Stewart, and W. Gough. Magnetic induction tomography: a measuring system for biological tissues. Annals of the New York Academy of Sciences, 873:335–345, 1999.

[57] A. Wickenbrock, S. Jurgilas, A. Dow, L. Marmugi, and F. Renzoni. Magnetic induction tomography using an all-optical 87 rb atomic magnetometer. Optics letters, 39(22):6367–6370, 2014.

[58] M. L. Honke and C. P. Bidinosti. The metallic sphere in a uniform ac magnetic field: A simple and precise experiment for exploring eddy currents and non-destructive testing. American Journal of Physics, 86:430–438, 2018.

[59] B. Maddox, Y. Cohen, and F. Renzoni. Through-skin pilot-hole detection and localization with a mechanically translatable atomic magnetometer. Applied Physics Letters, 120(1), 2022.

[60] C. P. Bidinosti, E. M. Chapple, and M. E. Hayden. The sphere in a uniform rf field—revisited. Concepts in Magnetic Resonance Part B: Magnetic Resonance Engineering: An Educational Journal, 31:191–202, 2007.

[61] L. Marmugi and F. Renzoni. Optical magnetic induction tomography of the heart. Scientific reports, 6(1):23962, 2016.

[62] H. L. Libby. Introduction to electromagnetic nondestructive test method. 1971.

[63] S. M. Narayan, J. Patel, S. Mulpuru, and D. E. Krummen. Focal impulse and rotor modulation ablation of sustaining rotors abruptly terminates persistent atrial fibrillation to sinus rhythm with elimination on follow-up: a video case study. Heart rhythm, 9(9):1436–1439, 2012.

[64] T. Zigdon, A. D. Wilson-Gordon, S. Guttikonda, E. J. Bahr, O. Neitzke, S. M. Rochester, and D. Budker. Nonlinear magneto-optical rotation in the presence of a radio-frequency field. Opt. Express, 18(25):25494–25508, 2010.

[65] V. Shah, S. Knappe, P. D. D. Schwindt, and J. Kitching. Subpicotesla atomic magnetometry with a microfabricated vapour cell. Nature Photonics, 1(11):649–652, 2007.

[66] S. Dyer, P. F. Griffin, A. S. Arnold, F. Mirando, D. P. Burt, E. Riis, and J. P. McGilligan. Micro-machined deep silicon atomic vapor cells. Journal of Applied Physics, 132(13), 2022.

[67] J. D. Zipfel, P. Bevington, L. Wright, W. Chalupczak, G. Quick, B. Steele, J. Nicholson, and V. Guarrera. Indirect pumping of alkali-metal gases in a miniature silicon-wafer cell. Physical Review Applied, 22(1):014056, 2024.

[68] D. A. Steck. Cesium d line data. Los Alamos National Laboratory, 2003.

[69] C. Deans. Electromagnetic Induction Imaging with Atomic Magnetometers. PhD thesis, University College London, 2018.

[70] Theo Scholtes, Stefan Woetzel, Rob IJsselsteijn, Volkmar Schultze, and Hans-Georg Meyer. Intrinsic relaxation rates of polarized cs vapor in miniaturized cells. Applied Physics B, 117:211–218, 2014.

[71] AP McWilliam, S Dyer, D Hunter, M Mrozowski, SJ Ingleby, O Sharp, DP Burt, PF Griffin, JP McGilligan, and E Riis. Optimizing longitudinal spin relaxation in miniaturized optically pumped magnetometers. Physical Review Applied, 22(6):064024, 2024.

[72] S. J. Seltzer. Developments in alkali-metal atomic magnetometry. Princeton University, 2008.

[73] A. Andalkar and R. B. Warrington. High-resolution measurement of the pressure broadening and shift of the cs d1 and d2 lines by n2 and he buffer gases. Physical review A, 65(3):032708, 2002.

[74] J. R. Wait. A conducting sphere in a time varying magnetic field. Geophysics, 16(4):666–672, 1951.

[75] J. W. Luquire, W. E. Deeds, and C. V. Dodd. Axially symmetric eddy currents in a spherical conductor. Journal of Applied Physics, 41(10):3976–3982, 1970.

[76] L. M. Rushton, L. M. Ellis, J. D. Zipfel, P. Bevington, and W. Chalupczak. Polarization of radio-frequency magnetic fields in magnetic induction measurements with an atomic magnetometer. Physical Review Applied, 22(1):014002, 2024.

[77] Y. Mamatjan. Imaging of hemorrhagic stroke in magnetic induction tomography: An in vitro study. International journal of imaging systems and technology, 24(2):161–166, 2014.

[78] L. Ma and M. Soleimani. Magnetic induction tomography methods and applications: A review. Measurement Science and Technology, 28(7):072001, 2017.

[79] M. Vaquero, D. Calvo, and J. Jalife. Cardiac fibrillation: from ion channels to rotors in the human heart. Heart rhythm, 5(6):872–879, 2008.

[80] A. E. Darby and J. P. DiMarco. Management of atrial fibrillation in patients with structural heart disease. Circulation, 125(7):945–957, 2012.

[81] T. A. R. Lankveld, S. Zeemering, H. J. G. M. Crijns, and U. Schotten. The ecg as a tool to determine atrial fibrillation complexity. Heart, 100(14):1077–1084, 2014.

[82] P. Sanders, O. Berenfeld, M. Hocini, P. Jaïs, R. Vaidyanathan, L. Hsu, S. Garrigue, Y. Takahashi, M. Rotter, F. Sacher, et al. Spectral analysis identifies sites of high-frequency activity maintaining atrial fibrillation in humans. Circulation, 112(6):789–797, 2005.

[83] S. Gabriel, R. W. Lau, and C. Gabriel. The dielectric properties of biological tissues: Iii. parametric models for the dielectric spectrum of tissues. Physics in medicine & biology, 41(11):2271, 1996.

[84] T. J. C. Faes, H. A. Van Der Meij, J. C. De Munck, and R. M. Heethaar. The electric resistivity of human tissues (100 hz-10 mhz): a meta-analysis of review studies. Physiological measurement, 20(4):R1, 1999.

[85] A. Weis, G. Bison, and A. S. Pazgalev. Theory of double resonance magnetometers based on atomic alignment. Physical Review A—Atomic, Molecular, and Optical Physics, 74(3):033401, 2006.

[86] G. Bevilacqua, E. Breschi, and A. Weis. Steady-state solutions for atomic multipole moments in an arbitrarily oriented static magnetic field. Phys. Rev. A, 89:033406, March 2014.

[87] L. Janousek, K. Capova, N. Yusa, and K. Miya. Multiprobe inspection for enhancing sizing ability in eddy current nondestructive testing. IEEE Transactions on Magnetics, 44(6):1618–1621, 2008.

[88] P. V. Czipott and W. N. Podney. Use of a superconductive gradiometer in an ultrasensitive electromagnetic metal detector. IEEE Transactions on Magnetics, 25(2):1204–1207, 1989.

[89] P. Samsonov. Nondestructive inspection of aging aircraft. In Nondestructive Inspection of Aging Aircraft, volume 2001, pages 257–261. SPIE, 1993.

[90] A. Shakoor and Z. Zhenggan. Investigation of 3d anisotropic electrical conductivity in tig welded 5a06 al alloy using eddy currents. Journal of Materials Processing Technology, 211(11):1736–1741, 2011.

[91] G. Almeida, J. Gonzalez, L. Rosado, P. Vilaça, and T. G. Santos. Advances in ndt and materials characterization by eddy currents. Procedia Cirp, 7:359–364, 2013.

[92] ETHER NDE Flaw Detection. `https://etherndE.com/applications/flaw-detection`.

[93] J. L. Rasson and T. Delipetrov. Geomagnetics for aeronautical safety: A case study in and around the Balkans. Springer Science & Business Media, 2007.

[94] X. Zhang, G. Chatzidrosos, Y. Hu, H. Zheng, A. Wickenbrock, A. Jerschow, and D. Budker. Battery characterization via eddy-current imaging with nitrogen-vacancy centers in diamond. Applied Sciences, 11(7):3069, 2021.

[95] S. D. Billings. Discrimination and classification of buried unexploded ordnance using magnetometry. IEEE Transactions on Geoscience and Remote Sensing, 42(6):1241–1251, 2004.

[96] J. R. Davis et al. Aluminum and aluminum alloys. ASM international, 1993.

[97] J. R. Davis et al. Stainless steels. ASM international, 1994.

[98] Bartington Mag690. `https://www.bartington.com/products/mag690/`, (December 2024).

[99] Bartington About Magnetometers. `https://www.bartington.com/about-magnetometers/`, (December 2024).

[100] P. Bevington, R. Gartman, and W. Chalupczak. Object detection with an alkali-metal spin maser. Journal of Applied Physics, 130(21), 2021.

[101] H. Yao, B. Maddox, and F. Renzoni. High-sensitivity operation of an unshielded single cell radio-frequency atomic magnetometer. Optics Express, 30(23):42015–42025, 2022.

[102] H. Xia, A. Ben-Amar Baranga, D. Hoffman, and M. V. Romalis. Magnetoencephalography with an atomic magnetometer. Appl. Phys. Lett., 89:211104, 2006.

[103] S-K. Lee, K. L. Sauer, S. J. Seltzer, O. Alem, and M. V. Romalis. Subfemtotesla radio-frequency atomic magnetometer for detection of nuclear quadrupole resonance. Applied Physics Letters, 89(21), 2006.

[104] R. J. Cooper, D. W. Prescott, P. Matz, K. L. Sauer, N. Dural, M. V. Romalis, E. L. Foley, T. W. Kornack, M. Monti, and J. Okamitsu. Atomic magnetometer multisensor array for rf interference mitigation and unshielded detection of nuclear quadrupole resonance. Physical Review Applied, 6(6):064014, 2016.

[105] P. Bevington and W. Chalupczak. Different configurations of radio-frequency atomic magnetometers—a comparative study. Sensors, 22(24):9741, 2022.

[106] F. Bertrand, T. Jager, A. Boness, W. Fourcault, G. Le Gal, A. Palacios-Laloy, J. Paulet, and J-M. Leger. A 4he vector zero-field optically pumped magnetometer operated in the earth-field. Review of Scientific Instruments, 92(10), 2021.

[107] B. Maddox and F. Renzoni. Two-photon electromagnetic induction imaging with an atomic magnetometer. Applied Physics Letters, 122(14), 2023.

[108] W. Li, M. Balabas, X. Peng, S. Pustelny, A. Wickenbrock, H. Guo, and D. Budker. Characterization of high-temperature performance of cesium vapor cells with anti-relaxation coating. Journal of Applied Physics, 121(6), 2017.

[109] M. V. Balabas, T. Karaulanov, M. P. Ledbetter, and D. Budker. Polarized alkali-metal vapor with minute-long transverse spin-relaxation time. Physical review letters, 105(7):070801, 2010.

[110] Red Pitaya. `https://redpitaya.com/`, (April 2025).

[111] M. T. Graf, D. F. Kimball, S. M. Rochester, K. Kerner, C. Wong, D. Budker, E. B. Alexandrov, M. V. Balabas, and V. V. Yashchuk. Relaxation of atomic polarization in paraffin-coated cesium vapor cells. Physical Review A, 72(2):023401, 2005.

[112] S. J. Seltzer, P. J. Meares, and M. V. Romalis. Synchronous optical pumping of quantum revival beats for atomic magnetometry. Physical Review A, 75:051407, 2007.

[113] B. Julsgaard. Entanglement and quantum interactions with macroscopic gas samples. PhD thesis, 2003.

[114] G. Bao, A. Wickenbrock, S. Rochester, W. Zhang, and D. Budker. Suppression of the nonlinear zeeman effect and heading error in earth-field-range alkali-vapor magnetometers. Physical Review Letters, 120:033202, 2018.

[115] M. Auzinsh, D. Budker, D. F. Kimball, S. M. Rochester, J. E. Stalnaker, A. O. Sushkov, and V. V. Yashchuk. Can a quantum nondemolition measurement improve the sensitivity of an atomic magnetometer. Physical review letters, 93(17):173002, 2004.

[116] H. Wang, M. Zugenmaier, K. Jensen, W. Zheng, and E. S. Polzik. Magnetic induction sensor based on a dual-frequency atomic magnetometer. Physical Review Applied, 22(3):034030, 2024.

[117] P .D. D. Schwindt, L. Hollberg, and J. Kitching. Self-oscillating rubidium magnetometer using nonlinear magneto-optical rotation. Review of Scientific Instruments, 76(12), 2005.

[118] R. Jiménez-Martínez and S. Knappe. Microfabricated optically-pumped magnetometers. High Sensitivity Magnetometers, pages 523–551, 2017.

[119] P. Bevington, R. Gartman, and W. Chalupczak. Generation of atomic spin orientation with a linearly polarized beam in room-temperature alkali-metal vapor. Physical Review A, 101(1):013436, 2020.

[120] G. Colangelo, R. J. Sewell, N. Behbood, F. M. Ciurana, G. Triginer, and M. W. Mitchell. Quantum atom–light interfaces in the gaussian description for spin-1 systems. New Journal of Physics, 15(10):103007, 2013.

[121] N. A. Sinitsyn and Y. V. Pershin. The theory of spin noise spectroscopy: A review. Rep. Prog. Phys., 79(10):106501, 2016.

[122] C. W. Gardiner and P. Zoller. Quantum noise, vol. 56 of springer series in synergetics. Springer–Verlag, Berlin, 97:98, 2000.

[123] V. S. Zapasskii, A. Greilich, S. A. Crooker, Y. Li, G. G. Kozlov, D. R. Yakovlev, D. Reuter, A. D. Wieck, and M. Bayer. Optical spectroscopy of spin noise. Physical review letters, 110(17):176601, 2013.

[124] V. Shah, G. Vasilakis, and M. V. Romalis. High bandwidth atomic magnetometery with continuous quantum nondemolition measurements. Physical review letters, 104(1):013601, 2010.

[125] P. Glasenapp, N. A. Sinitsyn, L. Yang, D. G. Rickel, D. Roy, A. Greilich, M. Bayer, and S. A. Crooker. Spin noise spectroscopy beyond thermal equilibrium and linear response. Physical Review Letters, 113(15):156601, 2014.

[126] V. G. Lucivero, R. Jiménez-Martínez, J. Kong, and M. W. Mitchell. Squeezed-light spin noise spectroscopy. Physical Review A, 93(5):053802, 2016.

[127] Y. Wen, X. Li, G. Zhang, and K. Zhao. Zero-field spin-noise spectrum of an alkali vapor with strong spin-exchange coupling. Physical Review A, 104(6):063708, 2021.

[128] K. Mouloudakis, G. Vasilakis, V. G. Lucivero, J. Kong, I. K. Kominis, and M. W. Mitchell. Effects of spin-exchange collisions on the fluctuation spectra of hot alkali-metal vapors. Physical Review A, 106(2):023112, 2022.

[129] K. Mouloudakis, F. Vouzinas, A. Margaritakis, A. Koutsimpela, G. Mouloudakis, V. Koutrouli, M. Skotiniotis, G. P. Tsironis, M. Loulakis, M. W. Mitchell, et al. Interspecies spin-noise correlations in hot atomic vapors. Physical Review A, 108(5):052822, 2023.

[130] A. A. Fomin, M. Y. Petrov, G. G. Kozlov, M. M. Glazov, I. I. Ryzhov, M. V. Balabas, and V. S. Zapasskii. Spin-alignment noise in atomic vapor. Physical Review Research, 2(1):012008, 2020.

[131] A. A. Fomin, M. Y. Petrov, I. I. Ryzhov, G. G. Kozlov, V. S. Zapasskii, and M. M. Glazov. Nonlinear spectroscopy of high-spin fluctuations. Physical Review A, 103(2):023104, 2021.

[132] S. Liu, P. Neveu, J. Delpy, L. Hemmen, E. Brion, E. Wu, F. Bretenaker, and F. Goldfarb. Birefringence and dichroism effects in the spin noise spectra of a spin-1 system. New Journal of Physics, 24(11):113047, 2022.

[133] S. Liu, P. Neveu, J. Delpy, E. Wu, F. Bretenaker, and F. Goldfarb. Spin-noise spectroscopy of a spin-one system. Physical Review A, 107(2):023527, 2023.

[134] J. Delpy, S. Liu, P. Neveu, E. Wu, F. Bretenaker, and F. Goldfarb. Spin-noise spectroscopy of optical light shifts. Physical Review A, 107(1):L011701, 2023.

[135] J. Delpy, S. Liu, P. Neveu, C. Roussy, T. Jolicoeur, F. Bretenaker, and F. Goldfarb. Creation and dynamics of spin fluctuations in a noisy magnetic field. New Journal of Physics, 25(9):093055, 2023.

[136] R. Jiménez-Martínez, J. Kołodyński, C. Troullinou, V. G. Lucivero, J. Kong, and M. W. Mitchell. Signal tracking beyond the time resolution of an atomic sensor by kalman filtering. Phys. Rev. Lett., 120:040503, January 2018.

[137] J. Kitching. Chip-scale atomic devices. Applied Physics Reviews, 5(3), 2018.

[138] C. W. Gardiner. Handbook of Stochastic Methods. Springer-Verlag, 3 edition, 1985.

[139] N. Wilson, C. Perrella, R. Anderson, A. Luiten, and P. Light. Wide-bandwidth atomic magnetometry via instantaneous-phase retrieval. Phys. Rev. Res., 2:013213, February 2020.

[140] R. Li, F. N. Baynes, A. N. Luiten, and C. Perrella. Continuous high-sensitivity and high-bandwidth atomic magnetometer. Phys. Rev. Appl., 14:064067, December 2020.

[141] S. Hao, H. Shi, C. N. Gagatsos, M. Mishra, B. Bash, I. Djordjevic, S. Guha, Q. Zhuang, and Z. Zhang. Demonstration of entanglement-enhanced covert sensing. Phys. Rev. Lett., 129:010501, June 2022.

[142] C. Troullinou, R. Jiménez-Martínez, J. Kong, V. G. Lucivero, and M. W. Mitchell. Squeezed-light enhancement and backaction evasion in a high sensitivity optically pumped magnetometer. Phys. Rev. Lett., 127:193601, November 2021.

[143] V. G. Lucivero, A. Dimic, J. Kong, R. Jiménez-Martínez, and M. W. Mitchell. Sensitivity, quantum limits, and quantum enhancement of noise spectroscopies. Phys. Rev. A, 95:041803(R), April 2017.

[144] G. Le Gal and A. Palacios-Laloy. Zero-field magnetometry based on the combination of atomic orientation and alignment. Physical Review A, 105(4):043114, 2022.

[145] O. Feys, P. Corvilain, A. Aeby, C. Sculier, N. Holmes, M. Brookes, S. Goldman, V. Wens, and X. De Tiège. On-scalp optically pumped magnetometers versus cryogenic magnetoencephalography for diagnostic evaluation of epilepsy in school-aged children. Radiology, 304(2):429–434, 2022.

[146] E. Boto, V. Shah, R. M. Hill, N. Rhodes, J. Osborne, C. Doyle, N. Holmes, M. Rea, J. Leggett, R. Bowtell, et al. Triaxial detection of the neuromagnetic field using optically-pumped magnetometry: feasibility and application in children. NeuroImage, 252:119027, 2022.

[147] G. Di Domenico, H. Saudan, G. Bison, P. Knowles, and A. Weis. Sensitivity of double-resonance alignment magnetometers. Physical Review A—Atomic, Molecular, and Optical Physics, 76(2):023407, 2007.

[148] G. Bison, N. Castagna, A. Hofer, P. Knowles, J-L. Schenker, M. Kasprzak, H. Saudan, and A. Weis. A room temperature 19-channel magnetic field mapping device for cardiac signals. Applied Physics Letters, 95(17), 2009.

[149] T. Sander, A. Jodko-Władzińska, S. Hartwig, R. Brühl, and T. Middelmann. Optically pumped magnetometers enable a new level of biomagnetic measurements. Advanced Optical Technologies, 9(5):247–251, 2020.

[150] W. Xiao, C. Sun, L. Shen, Y. Feng, M. Liu, Y. Wu, X. Liu, T. Wu, X. Peng, and H. Guo. A movable unshielded magnetocardiography system. Science Advances, 9(13):eadg1746, 2023.

[151] T. G. Walker and M. S. Larsen. Spin-exchange-pumped nmr gyros. Advances in atomic, molecular, and optical physics, 65:373–401, 2016.

[152] A. Borna, J. Iivanainen, T. R. Carter, J. McKay, S. Taulu, J. Stephen, and P. D. D. Schwindt. Cross-axis projection error in optically pumped magnetometers and its implication for magnetoencephalography systems. NeuroImage, 247:118818, 2022.

[153] I. M. Savukov. Spin exchange relaxation free (serf) magnetometers. High Sensitivity Magnetometers, pages 451–491, 2017.

[154] Thorlabs PDB210A/M. `https://www.thorlabs.com/thorproduct.cfm?partnumber=PDB210A/M`, (December 2024).

[155] OPA657. `https://www.ti.com/product/OPA657`, (December 2024).

[156] Hamamatsu S8729. `https://www.hamamatsu.com/eu/en/product/optical-sensors/photodiodes/si-photodiodes/S8729.html`, (December 2024).

[157] THS4021. `https://www.ti.com/product/THS4021`, (December 2024).

[158] OPA818. `https://www.ti.com/product/OPA818`, (December 2024).

[159] T. Pyragius and K. Jensen. A high performance active noise control system for magnetic fields. Review of Scientific Instruments, 92(12), 2021.